June 2017

Synthesis of heteroaromatic ruthenium dyes for use as electron reservoirs in dye-sensitized solar cells

Andrew David Basner
Syracuse University

Abstract

Increasing the usable portion of solar spectrum is a key factor in increasing the efficiency of modern solar cells. The near-IR region of the solar spectrum is often underutilized as a means of energy production, as the photons in this region do not contain enough energy to promote electrons to the conducting band of common semiconductors used in photovoltaics. To help achieve this goal, the creation of an electron reservoir was attempted. The electron reservoir would be a holding place for an electron that is excited by a sub-bandgap photon until another photon excites it to the conduction band.

The first chapter of this dissertation describes the basics of dye-sensitized solar cell technology and the requirements and characteristics of an electron reservoir. It also discusses characteristics that molecules would need to have in order to act as electron reservoirs. The electron reservoirs envisioned consist of multi-metal complexes with at least three metal centers and the presence of a near-IR absorption in the mixed-valence state.

The second chapter describes the synthesis of a number mono- and diruthenium of building blocks that were used to create larger triruthenium molecules. Most notable of these was bis(4,4'-dicarboxy-2,2'-bipyridine)(2,2'-bipyrimidine)ruthenium(II) hexafluorophosphate. The two 4,4'-dicarboxy-2,2'-bipyridine ligands allow strong attachment of the complex to TiO_2 and the 2,2'-bipyrimidine ligand allows for additional ruthenium centers to be attached.

The third chapter describes the creation of a series of triruthenium complexes. Initially, an unsuccessful combinatorial synthesis was attempted using TiO_2 as a stationary phase. Afterwards, a series of triruthenium complexes were made using the mono- and diruthenium building blocks previously made. None of the complexes synthesized had a near-IR absorption in their mixed-valence state.

The fourth chapter describes the synthesis of a cyclometalated diruthenium complex made using 2,3,5,6-tetra-(2-pyridyl)pyridine as a bridging ligand. A strong mixed-valence near-IR absorbance was seen at 1370 nm.

The fifth chapter describes the fabrication of dye-sensitized solar cells and the photovoltaic results obtained using the dyes from chapters two through four. The solar cells tested had efficiencies of 0.3% to 0.7%. However, no current was generated from photons in the near-IR region.

Synthesis of heteroaromatic ruthenium dyes for use as electron reservoirs in dye-sensitized solar cells

by

Andrew D. Basner

B.S., Indiana University-Purdue University of Indianapolis, 2007

Dissertation
Submitted in partial fulfillment of the requirements for the degree of
Doctor of Philosophy in Chemistry.

Syracuse University
May 2017

ACKNOWLEDGEMENTS

I would like to thank everyone who has helped me throughout my years at Syracuse University. First and foremost, I would like to thank Dr. Sponsler for being my research advisor. His guidance and wisdom has helped me out immensely. Without him, I would not be here today.

I would also like to thank my lab member and friends who have helped me over the years. Thank you to Amanda Lashua who I had numerous discussions and long evenings with. Thank you to Chris Petrelli and Casey Simons, who helped me stay sane while I was in graduate school. Without out our hundreds of long nights playing Settlers and Infiltration, I would have gone insane.

I would also like to thank Dr. Luk and Timothy LaBreche. Their support and guidance during the I-Corps program was invaluable. I would also like to thank Dr. Totah, Dr. Kallmerten, and Dr. Spencer for being on my committee.

Finally, I would like to thank my Family for their love and support throughout the years and for always pushing me to try and achieve great things.

TABLE OF CONTENTS

LIST OF FIGURES

LIST OF SCHEMES

LIST OF TABLES

LIST OF ABBREVIATIONS

BPY	2.2’-bipyridine
BPM	2,2’-bipyrimidine
BPM	2,2’-bipyrimidine dication
BIM	2,2’-biimidazole dianion
BIM-H_2	2,2’-biimidazole
TPY	2,2’:6’,2”-terpyridine
TPPZ	2,3,5,6-tetra-(2-pyridyl)pyrazine
TPPY	2,3,5,6-tetra-(2-pyridyl)pyridine
TPB	2,3,5,6-tetra-(2-pyridyl)benzene
TPY-TPY	6’,6”-di(2-pyridyl)-2,2’;4’,4”:2”,2”’-quaterpyridine
TPY-TBY	4’-(3,5-dipyridylphenyl)-2,2’:6’,2”-terpyridine
DHBPY	4,4’-dihydroxy-2,2’-bipyridine
DCBPY	4,4’-dicarboxy-2,2’-bipyridine
DEBPY	4,4’-dicarboethoxy-2,2’-bypyridine
TBA	tetrabutylammonium
TCO	transparent conducting oxide
ITO	indium tin oxide
FTO	fluorine doped tin oxide
MLCT	metal-to-ligand charge transfer
MMCT	metal-to-metal charge transfer
DSSC	dye-sensitized solar cells
N3	cis-bis(isothiocyanate)-bis(2,2’-bipyridyl-4,4’-dicarboxyruthenium(II)

Black Dye	tris(isothiocyanate)-4,4’,4”-tricarboxy-2,2’:6’,2”-terpyridineruthenium(III)
NIR	near-IR
CAN	ceric ammonium nitrate
CV	cyclic voltammetry
V_{oc}	open-circuit voltage
I_{sc}	short-circuit current
P_{max}	max Power
V_{max}	max voltage
I_{max}	max current
FF	Fill factor
η	Efficiency
J_{sc}	short-circuit current density
J_{max}	max current density
IF	ideality factor
DCS	dark current saturation

LIST OF COMPOUNDS

1	tris(4,4’-dihydroxy-2,2’-bypridine)ruthenium(II) chloride
2	bis(4,4’-dicarboxy-2,2’-bipyridine)dichlororuthenium(II)
3	bis(4,4’-dicarboethoxy-2,2’-bipyridine)dichlororuthenium(II)
4	tetrachloro(2,2’-bipyridine)ruthenium(IV)
5	bis(2,2’-biimidazole)(2,2’-bipridine)ruthenium(II) hexafluorophosphate
6	(2,2’-bipyridine)bis(2,2’bipyrimidine)ruthenium(II) hexafluorophosphate

7 (2,2’-biimidazole)bis(2,2’-bipyridine)ruthenium(II) hexafluorophosphate

8 bis(2,2’-bipyridine)(2,2’-bipyrimidine)ruthenium(II) hexafluorophosphate

9 dichlorobis(2,2’-bipyridine)ruthenium(II)

10 bis(4,4’-dicarboxy-2,2’-bipyridine)(2,2’-bipyrimidine)ruthenium(II) hexafluorophosphate

11 bis(bis(2,2’-bipyridine)ruthenium(II))-μ-(2,2’-biimidazole) hexafluorophosphate

12 bis(bis(2,2’-bipyridine)ruthenium(II))-μ-(2,2’-bipyrimidine) hexafluorophosphate

13 (4,4’-dihydroxy-2,2’-bipyrimidine)bis(2,2’-bipyridine) ruthenium(II) hexafluorophosphate

14 bis(2,3,5,6-tetra-(2-pyridyl)pyrazine)ruthenium(II) hexafluorophosphate

15 bis(trichlororuthenium(III))-μ-(2,3,5,6-tetra-(2-pyridyl)pyrazine)

16 tetrabutylammonium bis(trichlororuthenium(III))-μ-(2,3,5,6-tetra-(2-pyridyl)pyrazine)

17 bis(triisothiocyanateruthenium(III))-μ-(2,3,5,6-tetra-(2-pyridyl)pyrazine)

18 bis(2,2’-bipyridine)ruthenium(II)-μ-(2,2’-bipyrimidine)chlororuthenium(III)-μ-(2,3,5,6-tetra-(2-pyridyl)pyrazine)trichlororuthenium(III) hexafluorophosphate

19 bis(2,2’-bipyridine)ruthenium(II)-μ-(2,2’-bipyrimidine)chlororuthenium(III)-μ-(2,3,5,6-tetra-(2-pyridyl)pyrazine)chloro(4,4’-dihydroxy-2,2’-bipyridine)ruthenium(III) hexafluorophosphate

20 bis(2,2’-bipyridine)ruthenium(II)-μ-(2,2’-bipyrimidine)chlororuthenium(III)-μ-(2,3,5,6-tetra-(2-pyridyl)pyrazine)chloro(4,4’-dicarboethoxy-2,2’-bipyridine)ruthenium(III) hexafluorophosphate

21 bis(4,4’-dicarboxy-2,2’-bipyridine)ruthenium(II)-μ-(2,2’-bipyrimidine)isothiocyanateruthenium(III)-μ-(2,3,5,6-tetra-(2-pyridyl)pyrazine)triisothiocyanateruthenium(III) hexafluorophosphate

22 bis(trichlororuthenium(III)-μ-(2,3,5,6-tetra-(2-pyridyl)pyrazine))ruthenium(II) hexafluorophosphate

23 bis(bis(2,2'-bipyridine)ruthenium(II)-μ-(2,2'-bipyrimidine))(2,2'-bipyridine)ruthenium(II) hexafluorophosphate

24 bis(bis(4,4'-dicarbethoxy-2,2'-bipyridine)ruthenium(II)-μ-(2,2'-bipyrimidine))(2,2'-bipyridine)ruthenium(II) hexafluorophosphate

25 bis(bis(2,2'-bipyridine)ruthenium(II)-μ-(2,2'-biimidazole))(2,2'-bipyridine)ruthenium(II) hexafluorophosphate

26 bis(bis(4,4'-dicarboethoxy-2,2'-bipyridine)ruthenium(II)-μ-(2,2'-biimidazole))(2,2'-bipyridine)ruthenium(II) hexafluorophosphate

27 2,6-diamino-3,5-dibromopyridine

28 2,3,5,6-tetrabromopyridine

29 trichloro-2,2';6',2"-terpyridineruthenium

30 bis(2,2';6',2"-terpyridineruthenium)-μ-2,3,5,6-tetra-(2-pyridyl)pyridine

Chapter 1

Introduction to solar energy, dye-sensitized solar cells, and electronic reservoirs.

1.1 Introduction

The demand for renewable energy has increased dramatically in recent years. It is estimated that around 19% of final energy consumption in 2011 was a result of renewable energy sources, with around 26% of that energy coming from photovoltaics, often referred to as solar cells.[1] From 2010 to 2012, the global energy coming from solar cells increased from 40 GW to 100 GW.[1] One of the reasons for the interest in solar energy is that solar energy offers the greatest possible total energy coming from renewable energy. In Figure 1-1, a graphical representation of the maximum possible energy available in a variety of renewable sources is listed in TW/year and this is compared with the total remaining TW of energy from non-renewable sources.[1,2] The abundance of potential solar energy is one of the driving forces for solar cell research. It is estimated that if only 0.4% of the solid land area of Earth's land was covered by solar cells it would be enough to meet current global energy demands.[3]

Figure 1-1: A comparison of the available energy per year of renewable resources to the total available energy of non-renewable sources.

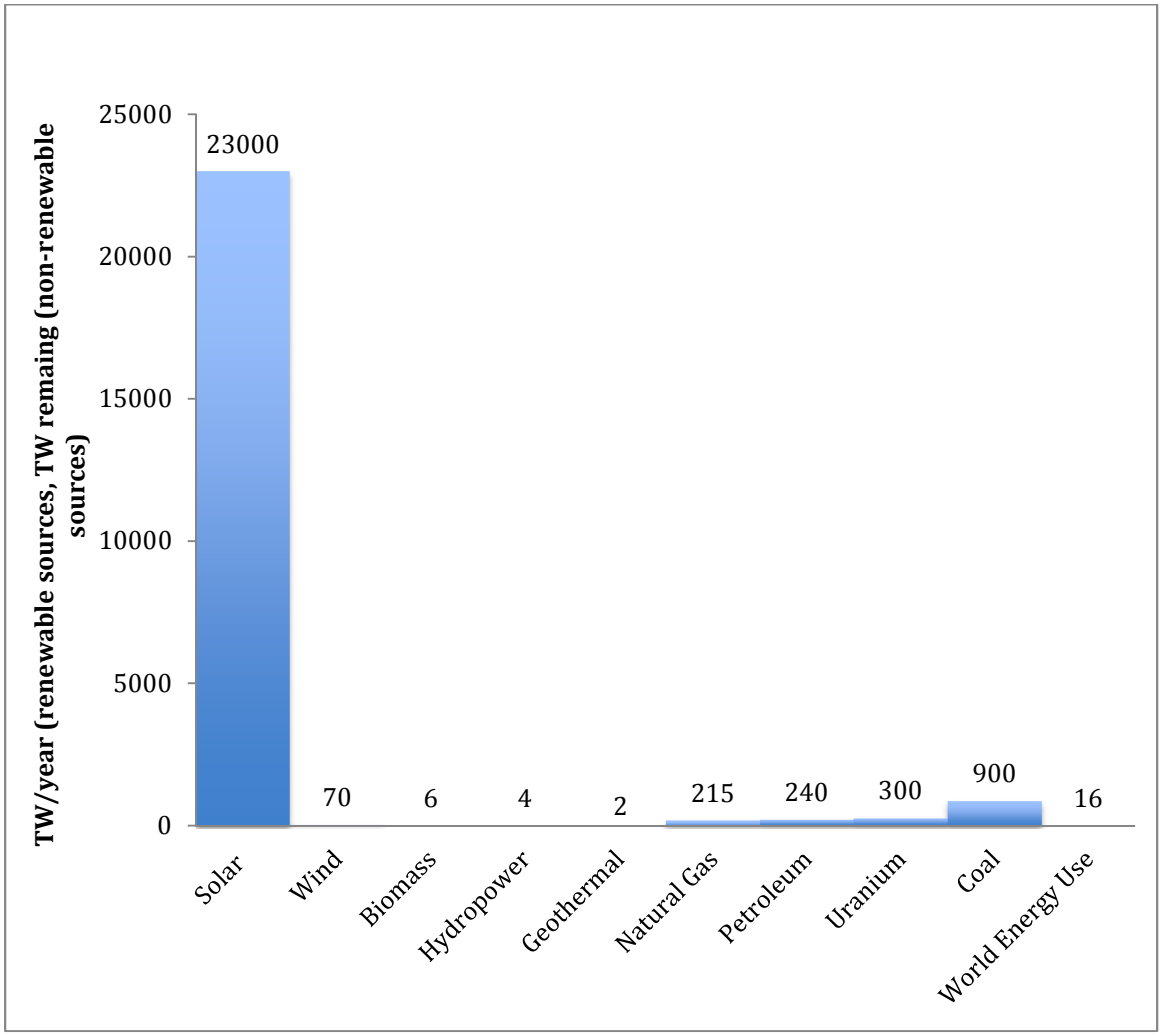

Because of the importance of solar energy research in meeting future energy demands, research on solar cell fabrication and development has also increased dramatically. The number of annual publications on solar energy has steadily increased since 1993 as seen in Figure 1-2. During this time, the overall price of solar energy has decreased, with the price of solar energy dropping from $76.67/watt in 1977 to $0.74/watt in 2013.[4]

Figure 1-2: Number of journal articles on solar energy/year. Data obtained by searching SciFinder with search term Solar Energy, and refining by year and limiting the search to journal articles, produced on Feb 24, 2014.

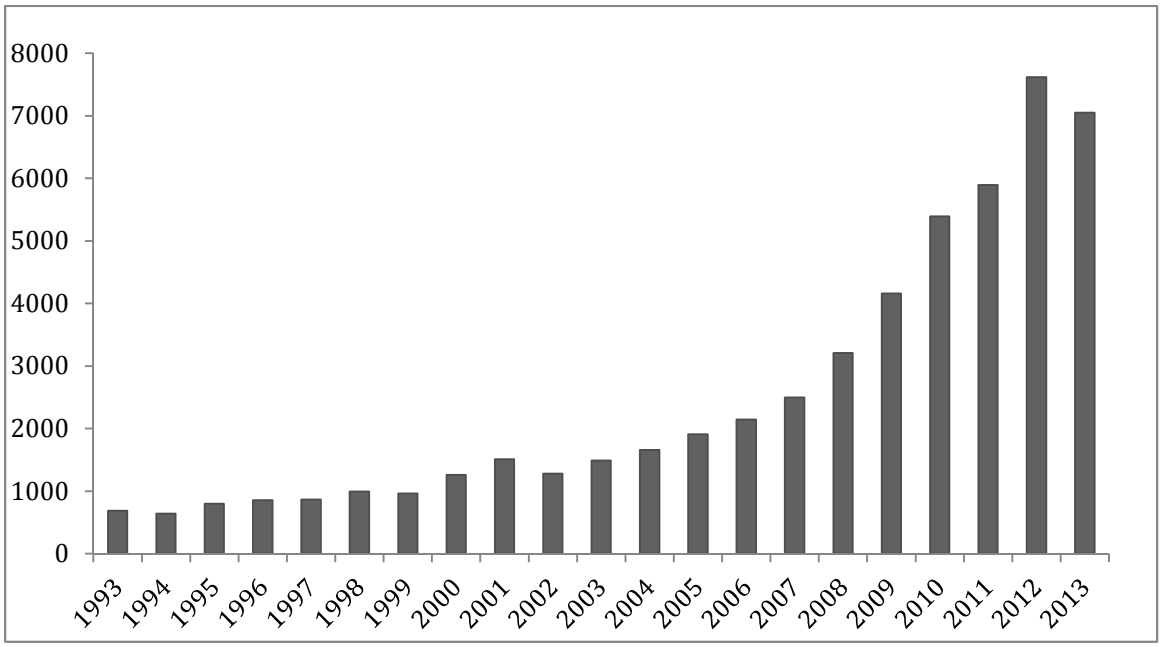

1.2 Current industry standards and types of solar cells

Currently in the market, 90% of solar cells are crystalline silicon based.[3, 5] The large abundance of silicon in the Earth's crust as well as the overall efficiency of silicon photovoltaics help make crystalline silicon solar cells the industry standard. While they are effective as solar cells, single crystal solar cells have maximum efficiency of 25%[3, 6] (14% for commercial units), which lies quite far below the theoretical maximum of around 33% for single junction, single band gap solar cells.[7] Section 1.2.1 gives a more detailed treatment of the Shockley-Queisser limit. Current efforts to improve the efficiency or cost of the solar cells include reducing the amount of semiconductor used, using less expensive semiconductors, improving manufacturing conditions, increasing photon flux, and extending the usable band gap.[8]

Making cells thinner, without having a dramatic effect on efficiency, would reduce the cost/energy output ratio. To this end, thin film solar cell technology has been an extensively studied field. Thin films[9] have been made from a variety of materials including amorphous silica (a-Si)[3,10], copper indium gallium diselenide ($Cu(InGa)Se_2$, CIGS)[11], cadmium telluride (CdTe)[12], and dye-sensitized solar cells.[3] These solar cells are considered 2nd generation solar cells, with 1st generation cells being those made of crystalline silicon.

It is also possible to use less expensive or less pure semiconductors, which lowers the overall cost of the cell at the expense of efficiency. Multicrystalline solar cells currently have a lower maximum efficiency (20% maximum, 12% commercial)[6] and only a slightly lower cost/power output ratio.[3] Dye-sensitized solar cells also fall under this category, as the TiO_2 semiconductor traditionally used is significantly cheaper than silicon.

Efforts towards increasing efficiency and simplicity of the manufacturing process also play a vital role. Reducing the number of quality control rejected cells as well as reduction of overall waste can help lower the overall cost of solar energy.

Research is also being performed to investigate ways to increase solar flux on a cell. This is done by a solar concentrator, which focuses light into an area occupied by a solar cell. While these have been effective in increasing solar efficiency, they add to the complexity to the system.[13]

1.2.1 Shockley-Queisser limit of solar cells.

In 1961, William Shockley and Hans Queisser published a paper on the theoretical limits of solar energy conversion for silicon solar cells with a band gap of 1.1 eV.[7] The Shockley-Queisser limit, as it has become to be known thereafter, deals with several assumptions that govern the overall limit of the efficiency. The assumptions are as follows:

1. There is one p-n junction per cell.
2. There is only one semiconductor present.
3. The sunlight is not concentrated, or at one sun.
4. For photons with energy in excess of the band gap the excess energy is lost as heat.
5. Photons with energy below the band gap are not strong enough to produce photocurrent.
6. Electron hole recombination is an inevitability.
7. Blackbody radiation of the cell will cause inevitable efficiency loss.
8. Each photon can only excite one electron.

For silicon solar cells with a band gap of 1.1 eV, energy losses due to the fourth assumption account for around 33% energy loss. Photons below the band gap of 1.1 eV account for another 19% loss of efficiency. Combined, this accounts for around 52% loss of efficiency due to photon wavelength issues. Blackbody radiation let off by the cell at operating temperatures accounts for another 7% loss of efficiency. Electron-hole recombination accounts for another 10-11% loss of efficiency as well. Shockley and Queisser had an initial efficiency limit around 30% listed for silicon cells with a band gap of 1.1 eV and predicted that maximum efficiencies could be achieved with cells with band gaps around 1.1-1.5 eV, with a predicted maximum efficiency around 33.7% for a solar cell with a band gap of around 1.4 eV. Their

analysis showed that silicon has nearly the optimum band gap for a single-semiconductor solar cell. The Shockley-Queisser limit has since served as an efficiency benchmark for single-semiconductor solar cells and has inspired several strategies to overcome the limitations of these cells. Some of these strategies will be discussed in section 1.4.

1.3 Dye-sensitized solar cells

Dye-sensitized solar cells are photovoltaic cells that use a wide band gap semiconductor to produce photocurrent. A simple illustration of this process is seen in Figure 1-3. While titanium dioxide, TiO_2, is typically the semiconductor of choice, zinc oxide, ZnO, and tin oxide, SnO_2, are often used as well. All semiconductors have a band gap, which is the difference between the ground or valence state for all of the electrons, and the conduction band, where electrons are free of their outer most orbital and are allowed to flow freely. TiO_2 has a band gap of 3.2 eV, which is quite large and only capable of directly harvesting high-energy photons for use as electricity. In order to utilize a larger portion of the solar spectrum in dye-sensitized solar cells, a dye is attached to the semiconductor. The ground state for the dye falls in between the valence band and the conduction band of the semiconductor. When a photon hits the dye, an electron is excited in the dye and is then injected into the conduction band of the semiconductor. This effectively lowers the band gap by increasing the ground state of the electron that is injected into the conduction band. This electron would then flow through an external circuit and back to a counter electrode. The semiconductor is attached to a piece of glass with a transparent conducting oxide (TCO) layer. This TCO layer is typically either indium tin oxide (ITO) or fluorine doped tin oxide (FTO). The counter electrode is also a TCO layered piece of glass with

a layer of platinum deposited on it. An electrolyte solution, consisting of mainly I^-/I_3^- in acetonitrile, reduces the dye back to its ground state.

Figure 1-3: The basic operating principles of a dye-sensitized solar cell.

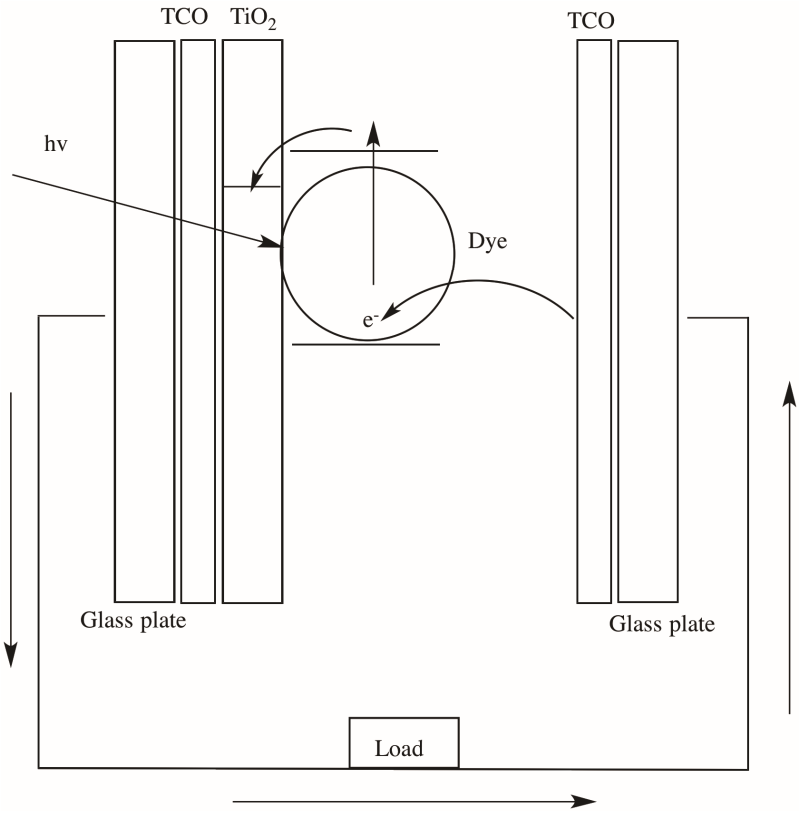

In 1991, O'Regan and Grätzel reported the first instance of an efficient dye-sensitized solar cell using the ruthenium dyes in Figure 1-4.[14, 15] Efficiencies of 7.1-7.9% were reported. Not long after, a cell was made with the now industry standard, N3, giving an efficiency of 10.4%.[16] A few years following this, another cell using another current industry standard dye, **Black Dye**, reported an efficiency of 10.4%.[17] This maximum was maintained until it was broken by Grätzel in 2013 when he obtained an efficiency of 15% using a perovskite-sensitized solar cell. In these cells, a PbI_2 solution was coated onto the TiO_2 followed by addition of CH_3NH_3I which resulted in a TiO_2 layer coated with $CH_3NH_3PbI_3$. The electrolyte was also

replaced with a solid electrolyte system of 2,2',7,7'-tetrakis(*N,N*-di-p-methoxyphenylamine)-9,9'-spirobifluorene.[20]

Figure 1-4: A trimeric ruthenium dye used in the first successful dye-sensitized solar cell, **N3**, and **Black Dye**.

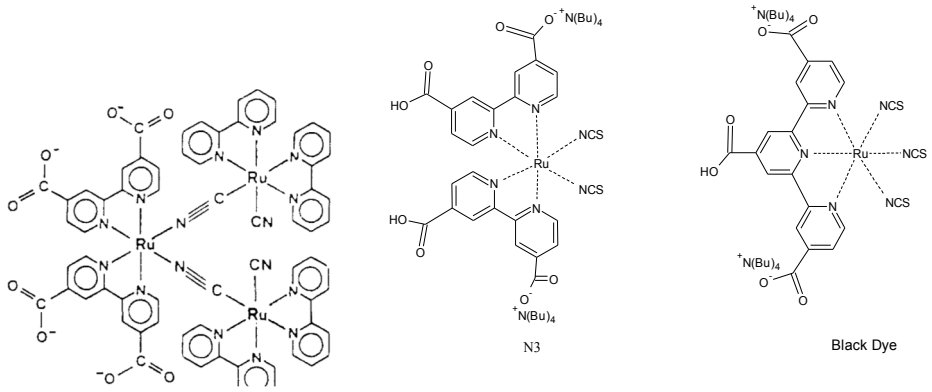

1.3.1 Advantages of dye-sensitized solar cells

Dye sensitized solar cells offer many advantages over traditional silicon based solar cells. The materials used in the construction of the cell are significantly cheaper than those in silicon solar cells. While the ruthenium is more expensive, very low quantities are needed. Another large part of the lower cost comes from the ease of assembly of these types solar cells. In fact, there are several kits anyone can buy to build their own and these have often been employed as laboratory exercises for high school or entry level college courses. Dye-sensitized solar cells can be made largely transparent and exhibit a wide variety of colors depending on the choice of dye, and these have seen interesting applications in building materials and colored glass. Figure 1.5 shows a few examples of interesting dye-sensitized solar cell applications.[18] Flexible TiO_2 coated polymers and metal foil substrates have also been employed to make flexible solar panels, a technology unavailable to other types of solar cells.[19]

Figure 1-5: This figure illustrates some interesting applications of dye-sensitized solar cells. The top left picture is a fan powered by a dye-sensitized solar cell, the top right picture displays several dye-sensitized solar cells in the shapes of leaves. These leaves power the butterflies shown in the bottom picture.

1.3.2 Disadvantages of dye-sensitized solar cells

One major disadvantage of dye-sensitized solar cells includes lower overall efficiency. Until recently, the max efficiency of a cell made using N3 was 10.4% until, Grätzel broke this barrier with the perovskite based dye-sensitized solar cell with an efficiency of 15%.[20] These values are still far below those of traditional silicon solar cells however. There are also some issues with dye stability, which also limit overall efficiency. The isothiocyanate ligand tends to be somewhat labile and can cause problems with dye degradation. The liquid electrolyte solution also limits the range of usable temperatures. Although estimates place the overall operating time of a well made cell around 10000 h, the large scale commercialization of dye-sensitized solar cells will require much better long term stability of the dye and electrolyte solution. [21]

Similar to silicon cells, one disadvantage of dye-sensitized solar cells is the overall wavelength range of absorption. While the best dyes absorb most available sunlight in the visible region, they no longer function in converting photons to current around the 800 nm mark. One study suggests that extending efficient photocurrent production to 920 nm would increase the efficiency from 11% to 14.2%.[22] This cutoff is largely controlled by the energy gap between the TiO_2 conduction band and the ground state energy level of the dye. Ruthenium dyes have been extremely successful because the energy of the metal-to-ligand charge transfer (MLCT) absorption falls in the visible region of the spectrum. Once an electron is excited to the ligand, it is easily transferred to the conduction band of the TiO_2. Lower energy photons are not energetic enough to excite this transition and are therefore unable to convert sunlight to electricity in the current model of dye-sensitized solar cells. In Figure 1-6, a solar spectrum is presented.[23] In the

Shockley-Queisser assumptions, it was estimated that 19% of the sun's energy is below the 1.1 eV threshold, which is a wavelength around 1127 nm.

Figure 1-6: A solar energy spectrum.[23]

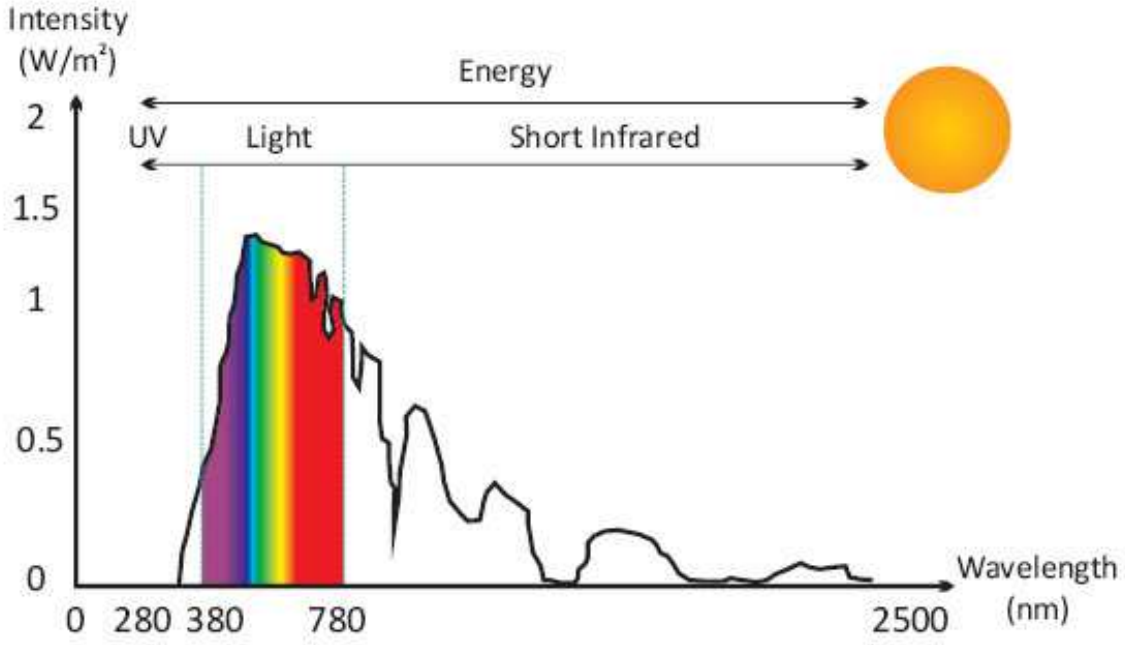

1.4 Third generation solar cells

Third generation solar cells are devices which find ways to utilize a larger portion of the electromagnetic spectrum for conversion of sunlight to electricity, effectively overcoming the Shockley-Queisser limit. [24, 25] Estimates suggest these solar cells have a theoretical maximum of around 93.3% efficiency if entropy loss could be reduced to near zero. There are several types of solar cells that fall under the category of third generation solar cells. These include tandem cells, hot carrier cells, multiple exciton per photon cells, and multiband cells.

1.4.1 Multi-junction solar cells

M multi-junction cells function by using multiple solar cells containing different band gaps. These are often stacked in order of decreasing band gap as seen in Figure 1-7. Photons that do not contain enough energy to bridge the band gap of the first cell pass through and hit another solar cell containing a semiconductor with a lower band gap. This can be repeated several times. Three-cell systems became commercially available in the late 1990s, were used as high performance cells for spacecraft, and employed high-efficiency III–V solar cells using gallium arsenide, gallium indium phosphide, and germanium.[26] Lower cost thin-films have also been used as part of multi-junction solar cells for terrestrial applications using amorphous SI:Ge:H alloys as well as crystalline silicon.[27] Multi-junction CdS quantum dot cells have also been reported.[28] Estimates place the theoretical maximum efficiency of these cells at around 86.8% with the current maximum of 38.8% belonging to a GaAs/InP bonded cell.

Figure 1-7: A simple illustration of a multi-junction solar cell.

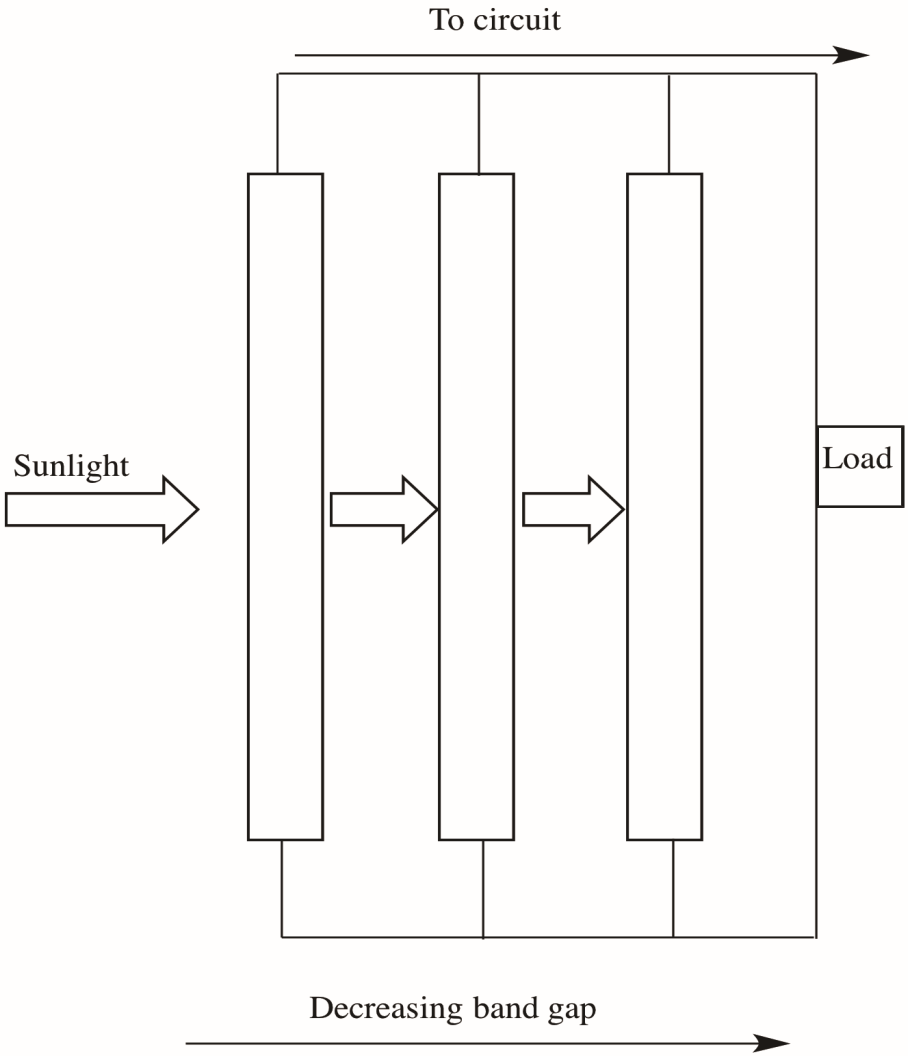

1.4.2 Hot carrier solar cells

When the absorption of a photon with more energy than required by a solar cell occurs, an electron is excited to an energy level either higher than that of the conduction band or at the upper end of it. The electron quickly relaxes to the bottom of the conduction band and the excess energy is converted to thermal energy through lattice vibrations. Hot carrier solar cells seek to extract these hot electrons in the cell before they thermalize with the lattice.[29, 30] As the relaxation time of hot electrons to the lower edge of the conduction band is on the order of

picoseconds, this process must occur quickly. One idea suggested to approach this problem is to create a bottleneck for phonon relaxation, allowing phonons time to give their energy back to electrons. Another common approach is to incorporate wide band gap semiconductors with narrow conduction and valence bands and to use very selective energy contacts to extract these cells.[29, 31] Research is largely theoretical and in the very early proof-of-concepts stages currently.[30, 32] Hot carrier cells discard one of the Shockley-Queisser assumptions, that excited electrons are at the lattice temperature.[33] As a result, it is predicted that efficiencies of around 68% are possible with hot carrier cells.[24]

1.4.3 Multiple exciton per photon solar cells

High-energy photons could be used to improve solar cell performance by creating two or more electron-hole pairs per incident photon. If a high-energy photon creates an electron-hole pair with enough energy, the excess energy can be given to the lattice and create a second electron-hole pair in the process. This would require a photon with energy at least twice that of the band gap. If a photon were three times the band gap, there would be the potential for formation of three electron-hole pairs. Experimentally, the measured increases in efficiencies due to this effect have been small. The competing processes of recombination and lattice vibrational relaxation are too efficient.

This approach discards another of the Shockley-Queisser assumptions, that a photon can only pump one electron.[34] It is estimated that a multiple exciton cell with a band gap of 0.048 eV could have a maximum efficiency of 85.9%. A cell with a band gap of 0.76 eV could have a maximum efficiency of 43.6%.

1.4.4 Multiband solar cells

Multiband solar cells are solar cells that contain an energy state lying in-between the conduction and valence band to which a photon with an energy below the band gap can excite an electron. After absorption of a second photon, the electron would then be excited into the conduction band. This was initially suggested by using a host silicon semiconductor containing defects or impurities that cause intermediate bands to be present.[35] It was initially thought that the presence of defects would enhance recombination, negating any benefits gained.[36] It appeared that minor improvements could be made after additional analysis by Keeves, Green[37] and Würfel.[38] More recent theoretical work and calculations suggested very clear improvements could be achieved if cells could operate with little recombination.[39]

Figure 1-8: A sample illustration of a multiband gap solar cell.

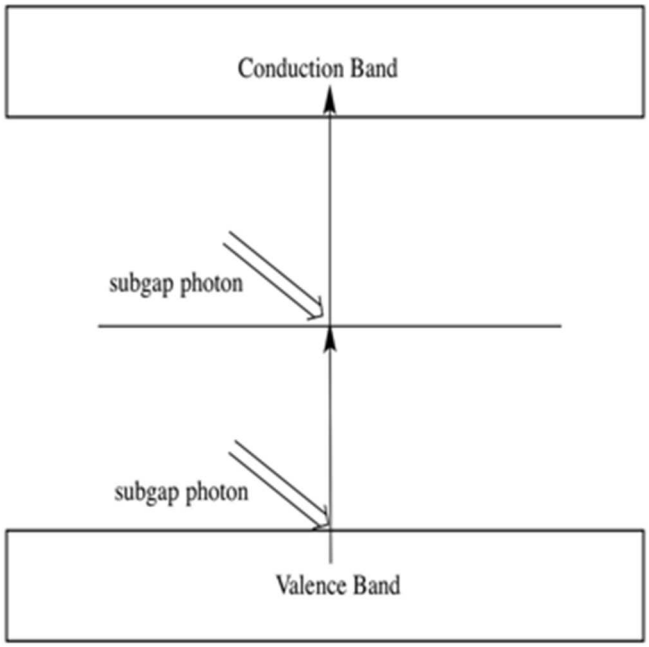

This approach disregards the Shockley-Queisser assumption that photons below the band gap are not absorbed.[40] Based on calculations performed for silicon based solar cells with an impurity band 0.7 eV above the valence band of a cell with a 1.9 eV band gap, such a cell could have a maximum efficiency of 63.7%.[24, 39] The best multiband cell made to date is an erbium doped crystalline silicon solar cell which achieved an efficiency of 3.40% at a wavelength of 1523 nm.[41, 42, 43] A multilayer DSSC made with a ytterbium and erbium doped LaF_3-TiO_2 composite attached to the back of a TiO_2 DSSC had an efficiency of 0.002% at 980 nm and another reported 0.2 mA/cm^2 at of current at 980 nm and the efficiency was not reported.[44, 45]

1.5 Reservoir model for multiband dye sensitized solar cell

This dissertation proposes an electron reservoir to act as a holding place for an electron that is excited by a sub-band-gap photon. This is different from an impurity band silicon solar cell in that the intermediate holding place is located externally to the semiconductor material.

Dye-sensitized solar cells are often considered to be third generation solar cells in addition to second generation. The dye acts as the intermediate band in-between the valence and conduction band of the TiO_2 semiconductor. In many ways, the reservoir model is similar to the functioning of a dye-sensitized solar cell. In a dye-sensitized solar cell, the dye is the intermediate level and an electron from the dye goes through the circuit and is returned to the dye. If instead the dye were acting as a reservoir, an electron would be excited to the dye from either the TiO_2 or the dye itself, and then again to the conduction band, eventually returning to the semiconductor.

It is envisioned that a reservoir can be used to create an energy level between that of the dye and the conduction band of the TiO_2. An example is seen in Figure 1-9. The reservoir would be a holding place for an electron from the dye that is excited by a sub-band-gap photon until another sub-band-gap photon excited it again to the conduction band.

There are two different ways an electron reservoir can be envisioned while being incorporated into a dye-sensitized solar cell. It is possible that an external molecule or system can act as the reservoir, or there is the possibility of the dye acting as both the dye and reservoir itself. The first situation, where an external molecule acts as the reservoir, would look similar to the right diagram in Figure 1-9. The second situation, where the dye and reservoir act as one, would look similar to the left diagram in Figure 1-9, with the exception being that the dye is also the reservoir. One of the largest problems to overcome in either case is recombination of the excited electron with the electron hole before absorption of the second photon. In order to do this, intensity of light must be increased or the lifetime of the excited state must be extended. This will be discussed more in section 1.6.1. In this dissertation, it is proposed that a mixed-valence triruthenium complex can be used which acts as both a dye and an electron reservoir.

Figure 1-9: The left figure illustrates a normal dye-sensitized solar cell and the figure on the right illustrates a simple approach to an electron reservoir.

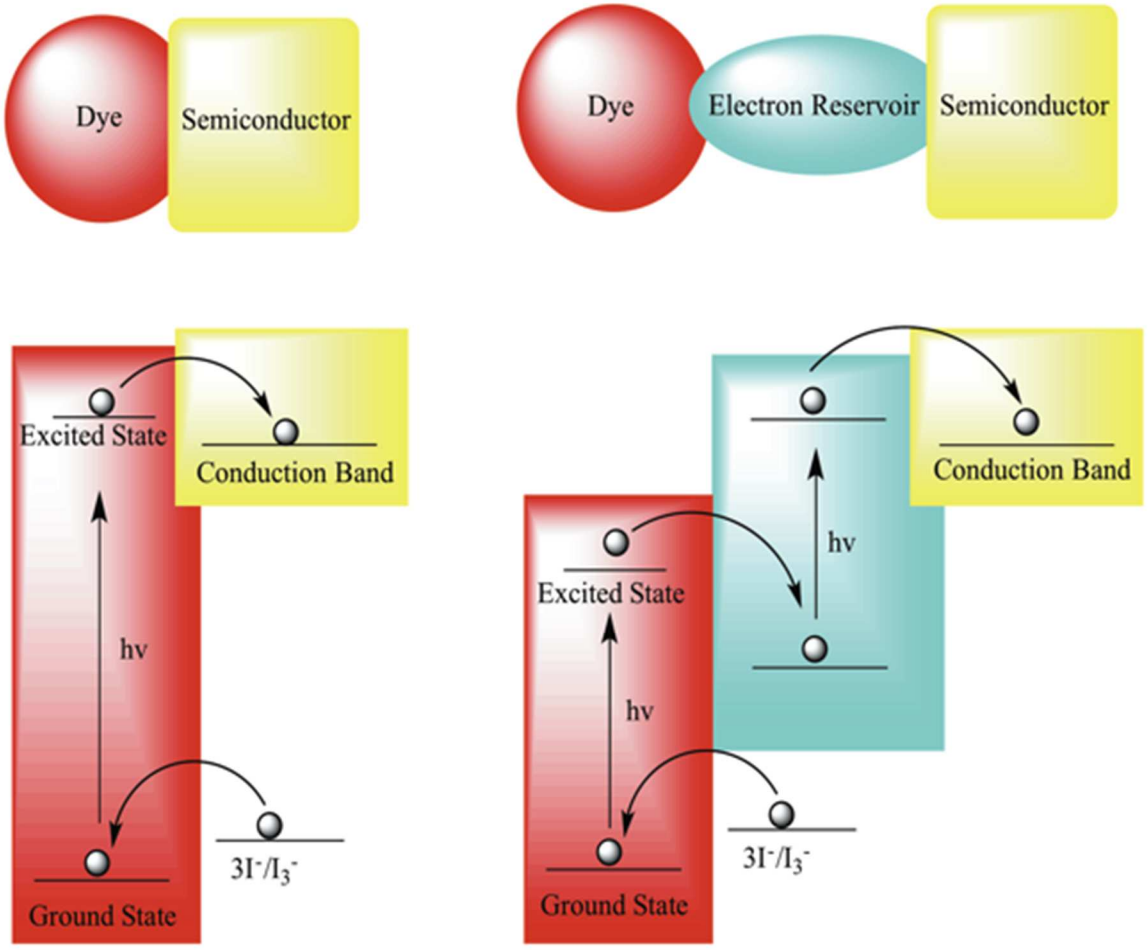

1.6 Mixed-valence complexes and systems

Mixed-valence compounds have been studied intensely due to their importance in understanding electron transfer processes.[46] Multi-metal complexes exhibiting this intermetallic electronic coupling in mixed-valence states have been the subject of numerous reviews[47, 48, 49, 50, 51] and they have seen a variety of uses in molecular electronics,[52, 53, 54, 55, 56] bioinorganic chemistry,[57, 58] solar energy,[59,] and aerospace technology.[60] The study of the Creutz-Taube ion

has led to continued research in compounds that exhibit similar properties over the past forty-five years.[61, 62, 63, 64, 65]

Figure 1-10: The Creutz-Taube ion.

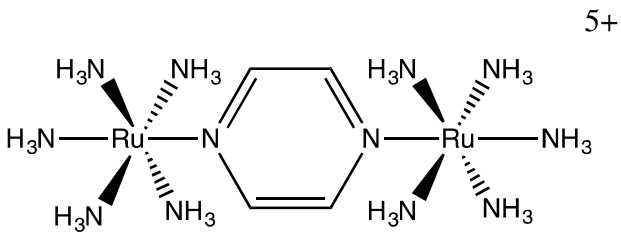

Mixed-valence compounds can be classified into three different Robin-Day classifications based on the work by M. B. Robin and P. Day.[66] In Class I systems, the unpaired electron is localized on one of the metals in the compound. In Class II systems, the electron is localized, but with sufficient interaction between metal centers that the electron can be transferred from one site to another. In Class III systems, there is complete delocalization of the unpaired electron within the molecule. Robin-Day Class II compounds have characteristically strong near-IR metal-to-metal charge transfer (MMCT) peaks in their mixed valence states. The Creutz-Taube ion, a Class II molecule, exhibits a near-IR peak at 1570 nm.[61] Because of the strong near-IR peak seen in these mixed-valence complexes, it is believed a mixed-valence triruthenium complex could produce photocurrent from light in the near-IR through the reservoir mechanism.

1.6.1 Proposed mechanism for a triruthenium electron reservoir

A proposed mechanism for a triruthenium electron reservoir is seen in Figure 1-11. An ideal triruthenium system would be in the mixed-valence state of II-III-III, or state A. Upon initial absorption of a near-IR photon, an MMCT absorption would take the dye to state B, III-II-III. There are several options at this point. Another near-IR photon could be absorbed creating state C, III-III-II, which should be energetic enough to inject an electron into the conduction band, creating state D, III-III-III. The oxidized dye would then be reduced by the electrolyte, taking it back to state A. Another option entails reduction of state B by the electrolyte to make state E, II-II-III. Subsequent absorption of a near-IR photon and an MMCT would take the dye to state F, II-III-II. Injection of the electron to the semiconductor would take the dye back to state A. There would also be the potential of reduction of state C by the electrolyte to make state F.

Figure 1-11: Proposed mechanism for a triruthenium electron reservoir.

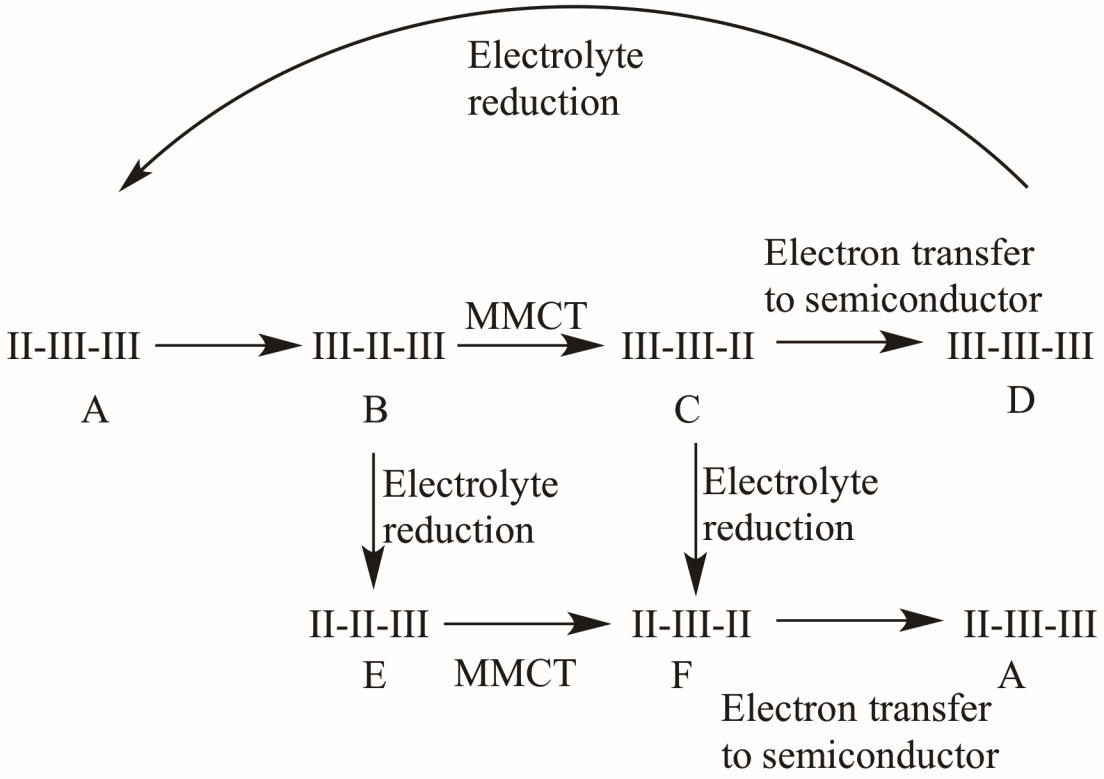

For this strategy to work, it would require a minimum of three ruthenium atoms in order to maintain a mixed valence state for both absorption steps. There also needs to be good coupling between the metal centers to have sufficient delocalization to give strong MMCT bands while maintaining localization of the charge centers. As with other intermediate band cells, limiting recombination will also be a major factor in successful operation of the reservoir. It is thus important that the lifetime of the intermediate states are long enough to allow absorption of a second photon before relaxation back to the ground state.

Figure 1-12 displays electron transfer times for various electron transfer process in a dye-sensitized solar cell.[3, 67] The relaxation time of an excited state electron in a DSSC made with N3 is roughly 10^{-8} s while the electrolyte reduction time is on the order of 10^{-6} to 10^{-8} s. These two

are typically not competing processes because the injection of an electron into the conduction band from the excited dye is on the order 10^{-10} to 10^{-12} s. Electrolyte reduction of the dye is faster than recombination by a factor of two, which creates a system where electrolyte reduction is largely diffusion controlled, although recombination can be a competing factor. The timeframe of MMCT excitation can vary depending on the metals and ligands involved but it is typically around the nanosecond to picosecond timeframe. For example, the excited state lifetime for a Co(II)-Fe(III) excited state of a Co(III)-Fe(II) cyano bridged compound is 0.8 ps.[68] Photon flux varies depending on the wavelength and intensity of light.[69] A photon of 1000 nm has a photon flux of approximately 0.06 photons per $cm^{-2}s^{-1}$ which means that a molecule with an estimated size of 1 nm^2, a rough estimate for the size of a dye, will have an estimated photon flux of 6 x 10^{12} photons per s^{-1}.[69] In 1 picosecond, approximately 6 photons will strike an area of 1 nm^2. Based on this, it is likely a second photon would strike before relaxation of a MMCT excited state would occur. The relaxation time of a MMCT is faster than a MLCT by a factor of two to four, which means MMCT relaxation can compete with injection to TiO_2 and this will likely be another major challenge in designing an electron reservoir.

Figure 1-12: Electron transfer time frames in dye-sensitized solar cells.

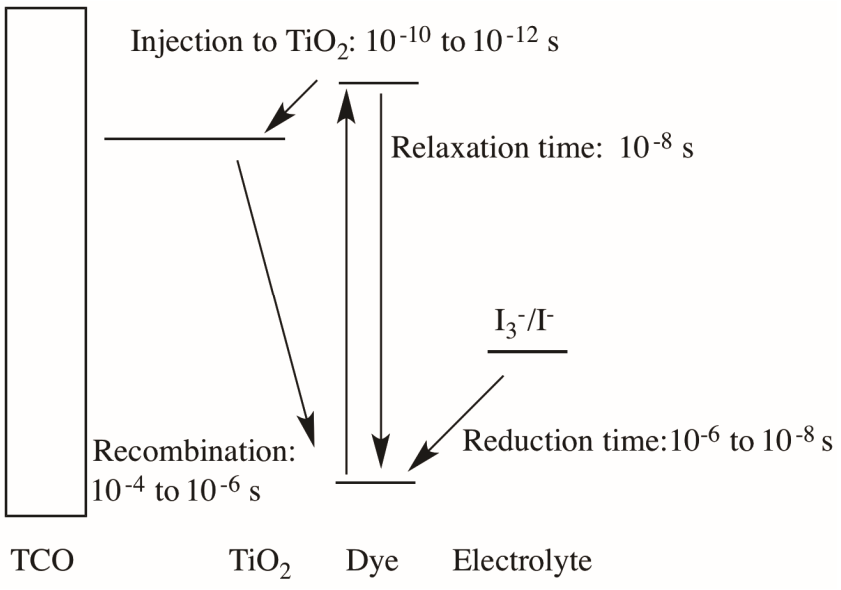

Chapter 2

Synthesis and characterization of mono and diruthenium polypyridine complexes for use in dye-sensitized solar cells

2.1 Introduction

There are several requirements that must be met to have a proper working dye for dye-sensitized solar cells.[1] The dye must not only have intense light absorption in the visible region but must also absorb over a wide range of the solar spectrum. In addition to light absorption, the compound must be stable in at least two oxidation states. The excited states must also have a long enough lifetime to transfer the excited electron to the semiconductor. Metal complexes made with polypyridine, porphyrin, and phthalocyanine systems have been shown to demonstrate all of these properties.[1] The delocalized π system of polypyridines have worked well due to their ability to complex to a variety of metals, while at the same time they are soluble in a number of solvents.[1] Ruthenium polypyridine complexes exhibit many low energy electronically excited states, which arise from π-π* transitions of the polypyridine system, d-d* metal transitions, and d-π* MLCT transitions. These transitions conveniently cover a large range of the visible light spectrum. By modifying the anchoring group of the polypyridine systems, the d-π* MLCT transitions can be tuned to easily change the absorption characteristics of complex.[1]

Polypyridine systems were chosen for the present work, since some of best dyes for dye-sensitized solar cells contain polypyridine systems. It would therefore make incorporation of multi-metal complexes into existing systems more straightforward. While developing target molecules, the plan was to not only take advantage of the proven properties of the ruthenium polypyridine systems already in use but also capitalize on the electron reservoir properties that mixed valence ruthenium complexes may have.

A generic scheme for a triruthenium complex is seen in Figure 2-1. The ligands fill two key roles in such a complex, bridging ligands and terminal ligands. A ligand that is capable of strong binding to TiO_2 is also needed. These attaching ligands are also terminal ligands here.

The key factors governing the MMCT of a multi-metal complex is the choice of the bridging and terminal ligands. By varying the bridging and terminal ligands, it would be possible to fine-tune the electronic properties of the molecules. The two bridging ligands could either be identical, making a more symmetrical molecule, or different, helping promote asymmetric electron flow.

Figure 2-1: Generic triruthenium structure.

Terminal Ligands—Ru—Bridging Ligand—Ru—Bridging Ligand—Ru—Terminal Ligands

2.1.1 Bridging Ligands

In a recent review on polynuclear transition metal complexes, well over a hundred types of bridging ligands and complexes were categorized. From this list, several potential bridging ligands were chosen.[2] The bridging ligands selected were 2,3,5,6-tetra-(2-pyridyl)pyrazine (TPPZ), 2,2'-biimidazole (BIM), and 2,2'-bipyrimidine (BPM).

Figure 2-2: Bridging ligands TPPZ, BIM, and BPM.

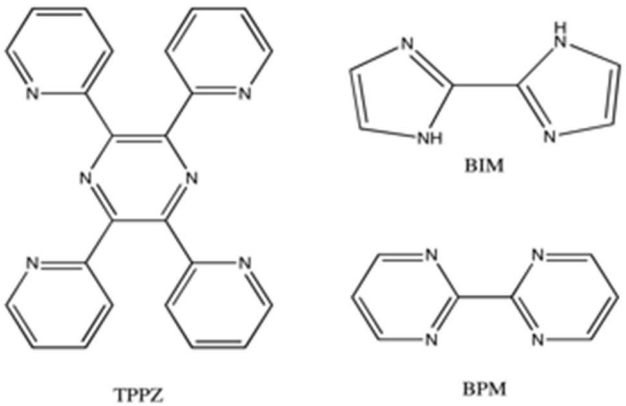

2.1.1.1 TPPZ

Bimetallic complexes containing TPPZ have received quite a bit of attention due to their similarities to the Creutz-Taube ion as seen in Figure 1-10.[3, 4, 5, 6, 7, 8, 9] The TPPZ ligand has similar spacing and coupling interactions between metal centers in bimetallic complexes while also containing a bis-tridentate coordination, providing much greater stability than seen in the Creutz-Taube ion. [6, 7] Complexes containing TPPZ as the bridging ligand tend to exhibit metal-to-metal charge transfer peaks in the near-IR when in the mixed valence state.[7, 8] In the mixed-valence state of the complex $Cl_3Ru^{(II)}(TPPZ)Ru^{(III)}Cl_3$, a NIR absorption band appears at 1785 nm.[8]

2.1.1.2 BIM

Imidazole is an aromatic molecule that is aromatic when both protonated and deprotonated. When deprotonated, imidazole is a symmetrical anion and while protonated, the imidazolium cation can act as an electron acceptor.[10] The corresponding biimidazole functions in the same manner while at the same time it is capable of being a bidentate ligand.[10, 11] The dianion of biimidazole, BIM, has been used as a bridging ligand in a number of diruthenium complexes.[12, 13, 14] One of the reasons for the interest in this bridging ligand was the relatively low oxidation potential of the diruthenium species using BIM as a bridging ligand. The first oxidation potential for the diruthenium species using BPY as the terminal ligands, $[(BPY_2Ru)_2BIM]^{+2}$, was 0.75 eV vs SCE. This would allow a complex made with BIM as a bridging ligand to easily get into a mixed-valence state. The complex $[Ru^{III}(BIM\text{-}Ru^{II}(BPY)_2)_3]^{3+}$ showed a mixed-valence absorption at 833 nm.[10] Although this wavelength is slightly lower than

desired, if the absorption was wide enough it would still prove valuable. Also, the differences in our target molecules may produce more advantageous values.[12]

Figure 2-3: Imidazole, BIM dianion, and BIM dication.

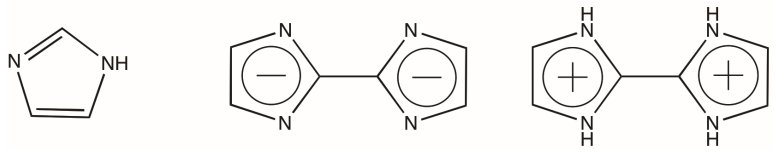

2.1.1.3 BPM

The last bridging ligand initially chosen was BPM. BPM has been used in many multi-metal ruthenium complexes.[15, 16] BPM provides a meta connection between the two ruthenium centers and when BPM was used as a bridging ligand in dendrimer complexes in solar applications, it was shown to prevent backflow of electrons, promoting net electron flow towards the semiconductor.[17, 18] It was envisioned that using a molecule with BPM would help prevent electron back transfer to the ruthenium furthest away from the TiO_2. The mixed valence complex $[(BPY)_2Ru^{II}(BPM)Ru^{III}(NH_3)_4](PF_6)_5$ does not show a NIR absorption but it is possible replacing the ammonia ligands could change that.[17, 18]

2.1.2 Terminal ligands

In the scheme in Figure 2-1, terminal ligands fill the role of both facilitating transfer of the electron from the electrolyte back to the ruthenium center and transferring excited state electrons to the semiconductor. Many complexes have been made using simple polypyridyl ligands, such as 2,2'-bipyridine (BPY) and 2,2':6',2"-terpyridine (TPY), as terminal ligands. When the terminal ligands are more π acidic than σ donor ligands such as halogens, monodentate

amines, or thiocyanates, such as in BPY and TPY, the MMCT peaks are typically at longer wavelengths.[19] There have been several examples of polypyridyl ligands used as terminal ligands in dye-sensitized solar cells.[22] While dyes made with polypyridyl terminal ligands are not as efficient as those made with σ donor terminal ligands, they do offer greater molar absorptivity.[20]

Figure 2-4: Terminal ligands BPY and TPY.

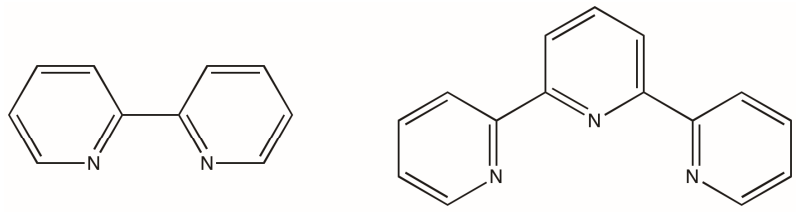

BPY TPY

When σ donor ligands such as halogens, monodentate amines, or thiocyanates are used, the MMCT peaks are typically at shorter wavelengths.[19] Higher efficiencies are seen when σ donor ligands are used in dye-sensitized solar cells. When the success N3 was first reported, using isothiocyanate over other halides showed a clear advantage in voltage and current output.[21] By using isothiocyanate instead of chloride, the open circuit voltage increased by 0.5 V and the short circuit current increased by 5 mA.[22] Evidence suggests there is a bonding interaction between the I^- of the electrolyte and the sulfur of the isothiocyanate.[23] This suggests that using isothiocyanates as terminal ligands would be a good choice.

Strong attachment of the dye to the TiO_2 is important. Among the types of functional groups that have been used to attach dye molecules to TiO_2, phosphonates, carboxylates, silyls, amides, sulfides, and alcohols have all been used successfully.[1] The two best dyes made to date, N3 and Black Dye, both use polypyridine systems with carboxylic acid anchoring groups. The

ligand 4,4'-dicarboxy-2,2'-bipydridine used in N3 would be a good choice as an attaching ligand for these complexes. It was also thought that a ligand containing hydroxyl groups would be capable of providing good binding to TiO_2. The ligand 4,4'-dihydroxy-2,2'-bipyridine was chosen as an attaching ligand because the phenoxy groups have been shown to be good anchoring groups and exhibit good binding to TiO_2. Also, the phenoxy group would be an electron-donating group, in contrast to the electron-withdrawing group of carboxylic acid, providing some design control in terms of redox potentials and electron energies.[24]

Figure 2-5: Attaching ligand DHBPY.

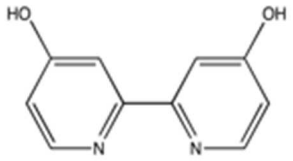

DHBPY

2.2 Target Complexes

The bridging ligands chosen offer several different ways to make triruthenium complexes. One way is by using two TPPZ ligands as seen in Figure 2-6. In this example, the terminal ligands could either be TPY, halogens, or isothiocyanates.

Figure 2-6: Illustration of triruthenium complex using two TPPZ bridges.

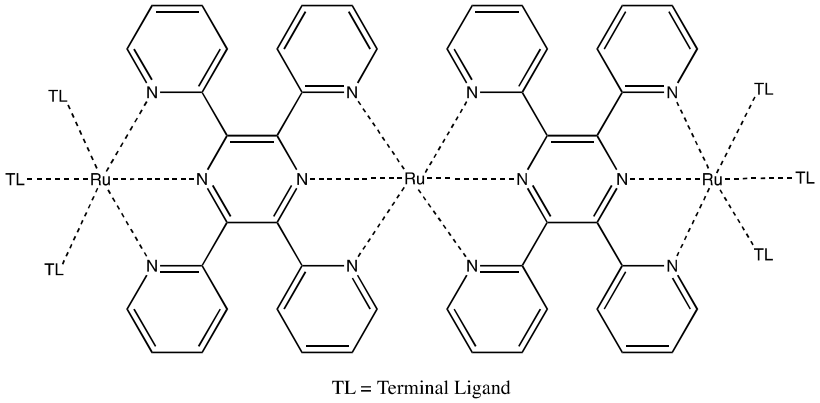

Alternatively, two BIM or two BPM bridges could be used as seen in Figure 2-7 and 2-8 respectively. In either of these, the terminal ligands could be BPY, DHBPY, or a polypyridyl carboxylic acid such as DCBPY. In the complexes of Figures 2-6, 2-7, and 2-8, introduction of end-to-end asymmetry depends on the terminal ligands.

Figure 2-7: Illustration of triruthenium complex using two BIM bridges.

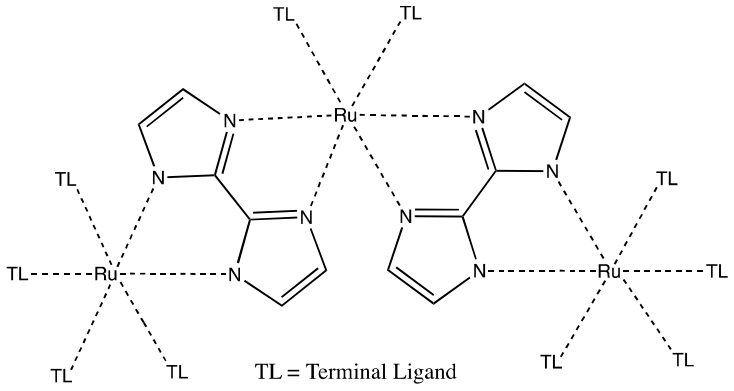

Figure 2-8: Illustration of triruthenium complex using two BPM bridges.

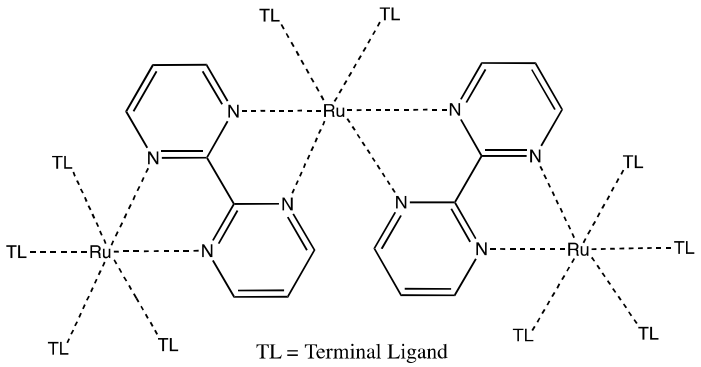

Using two different bridging ligands would allow easier synthesis of an asymmetric complex. For example, one side of the complex could be bridged by a TPPY ligand while the other side could be bridged by a BPM ligand as seen in Figure 2-9. Here, the terminal ligands could be changed depending on the asymmetry desired in the molecule.

Figure 2-9: Illustration of triruthenium complex using one TPPZ bridge and one BPM bridge.

.

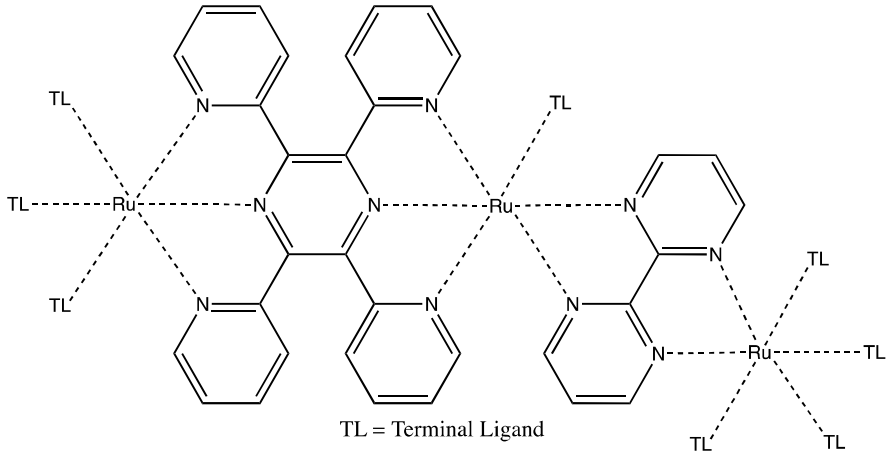

These potential triruthenium complexes were broken down into several smaller building blocks. By combining these building blocks, different triruthenium complexes could be made. Initially, it was thought that once several these smaller building blocks were made, mixing and matching these building blocks would allow a wide variety of complexes to be made. Also, it was thought that a combinatorial approach to building these complexes could be performed by building complexes directly onto the TiO_2. Building complexes directly onto the TiO_2 would help greatly in the building of asymmetric complexes. If the combinatorial method were unsuccessful, a traditional solution based chemistry approach would be used to combine the building blocks.

2.2.1 Building blocks needed to make bis-TPPZ bridged complexes

To make a bis-TPPZ complex (Figure 2-6), a natural starting point would be the monoruthenium building block $[(TPPZ)_2Ru]^{2+}$ (Figure 2-10). TPPZ is commercially available and synthesis of the monoruthenium building block has already been reported in a number of publications.[3, 6] This complex is typically reported as a hexafluorophosphate salt.[3] Adding monoruthenium fragments to each side of this building block would provide triruthenium complexes like those seen in Figure 2-11. The terminal ligands could be σ donor ligands like isothiocyanate or polypyridyl ligands like TPY.

Figure 2-10: Bis-TPPZ ion, $[(TPPZ)_2Ru]^{2+}$.

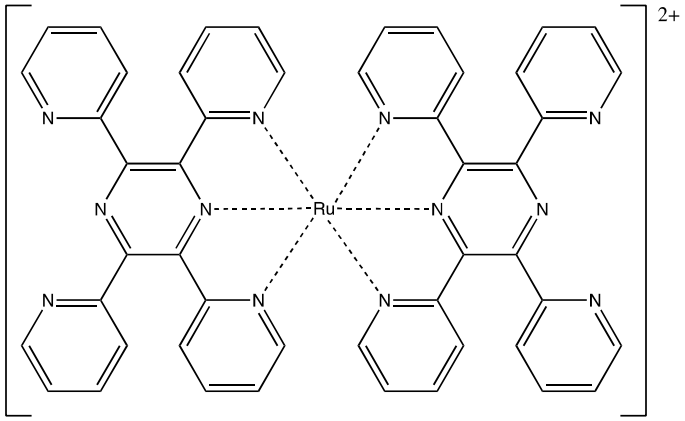

Figure 2-11: Potential triruthenium complexes that could be made with $[(TPPZ)_2Ru]^{2+}$.

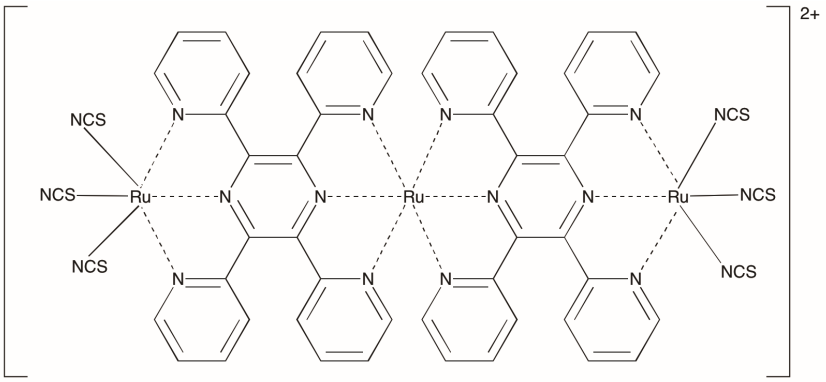

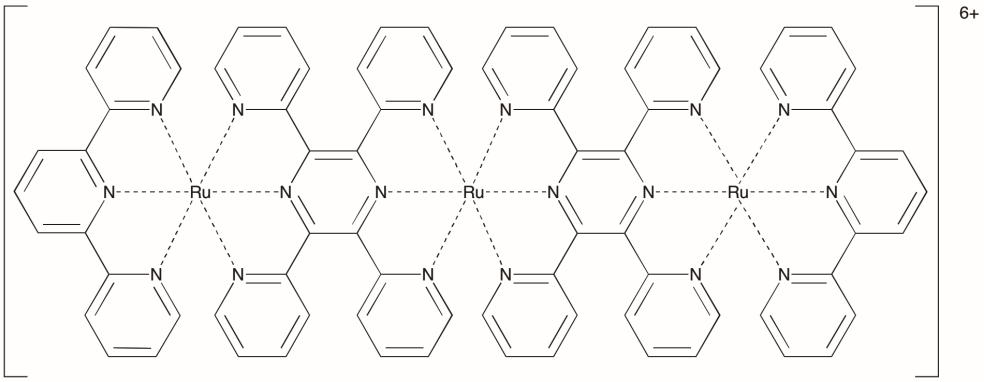

2.2.2 Building blocks needed to make bis-BIM bridged complexes

A bis-BIM bridged complex (Figure 2-7) could be made by starting with a bis-BIM monoruthenium building block, $[(BIM)_2RuBPY]^{2+}$ (Figure 2-12), most likely as a hexafluorophosphate salt. A number of monoruthenium building blocks, such as $(DHBPY)_2RuCl_2$, $(BPY)_2RuCl_2$, $(DCBPY)_2RuCl_2$ or bis(4,4'-dicarboethoxy-2,2'-bipyridine)dichlororuthenium(II) $(DEBPY)_2RuCl_2$, could be added to this to create triruthenium complexes (Figure 2-13).

Figure 2-12: Bis-BIM ion, $[(BIM)_2RuBPY]^{2+}$.

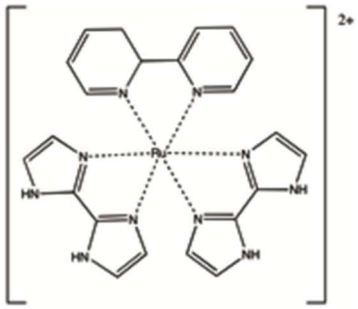

Figure 2-13: Potential triruthenium complexes that could be made with $[(BIM)_2RuBPY]^{2+}$.

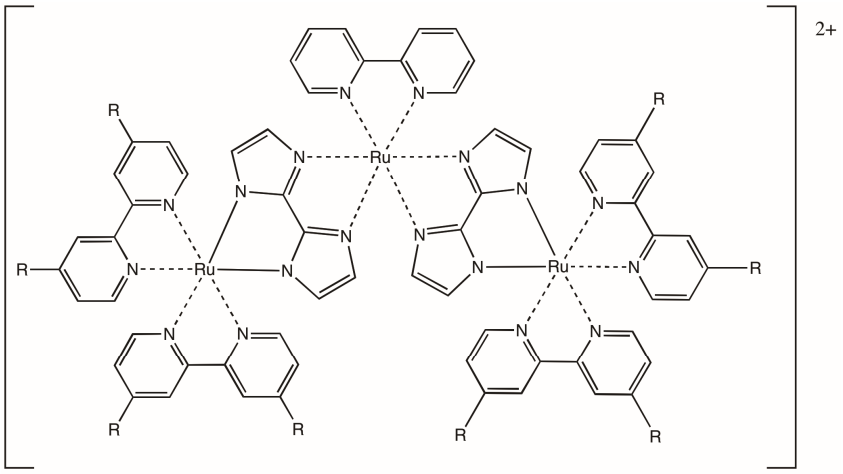

R =H, OH, CO_2H, CO_2Et,

2.2.3 Building blocks needed to make bis-BPM bridged complexes

A strategy similar to the one for the bis-BIM bridged complexes could be applied for the double BPM-bridged complexes (Figure 2-8) as well. A bis-BPM monoruthenium center, $[(BPM)_2RuBPY]^{2+}$ (Figure 2-13), could be made analogous to $[(BIM)_2RuBPY]^{2+}$. The building blocks $(DHBPY)_2RuCl_2$, $(BPY)_2RuCl_2$, $(DCBPY)_2RuCl_2$, or $(DEBPY)_2RuCl_2$,could also be added to this center building block to make triruthenium complexes (Figure 2-14). These would also most likely be hexafluorophosphate salts.

Figure 2-14: Bis-BPM ion, $[(BPM)_2RuBPY]^{2+}$.

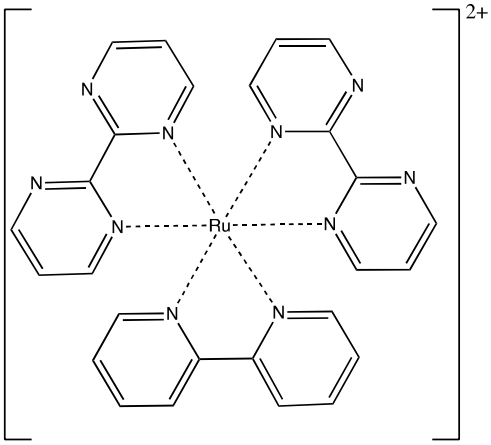

Figure 2-15: Potential triruthenium complexes that could be made with $[(BPM)_2RuBPY]^{2+}$.

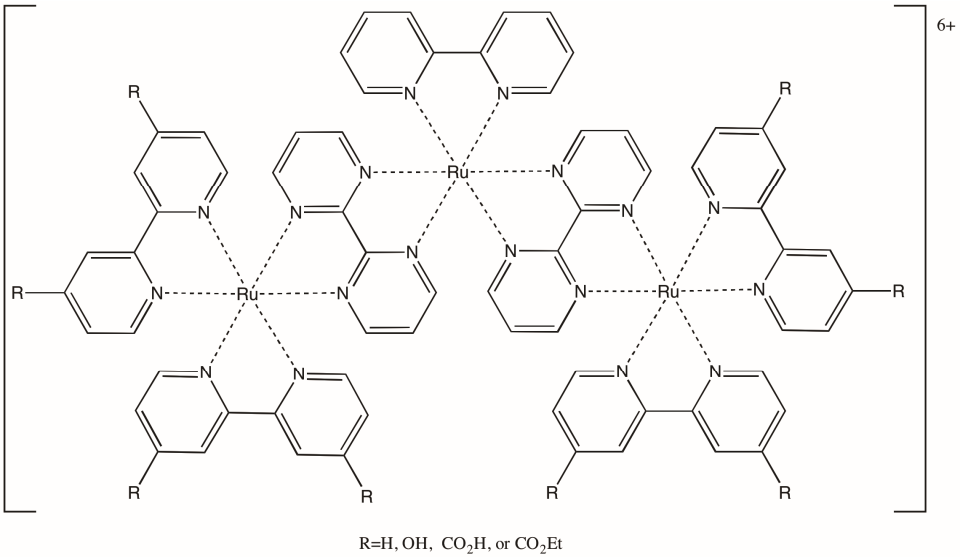

2.2.4 Building blocks needed to make a BPM and TPPZ bridged complex

Complexes made with mixed bridges are a bit more complicated. A different route could be taken depending on the directionality of the complex. A complex with TPPZ closer to the TiO_2 could be made by adding a bis-BPY ruthenium complex with a single BPM, $[(BPY)_2Ru(BPM)]^{2+}$, to a diruthenium bridged TPPZ complex, $(TPPZ)(RuCl_3)_2$ as seen in Figure 2-15. Adding an additional attaching ligand to the other end of the TPPZ bridged complex would result in a mixed-bridge triruthenium complex with the TPPZ bridge closer to the titanium (Figure 2-16).

Figure 2-16: Two building blocks, $[(BPY)_2RuBPM]^{2+}$ and **15**, needed to make mixed bridge triruthenium complexes.

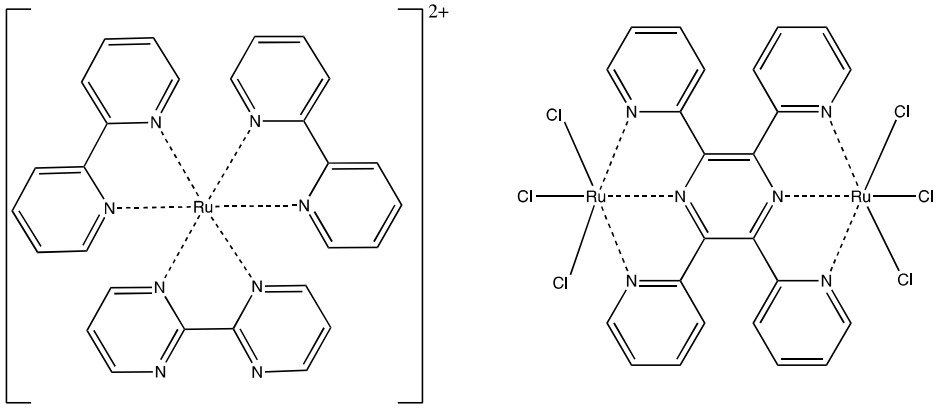

Figure 2-17: Potential mixed bridge triruthenium complexes.

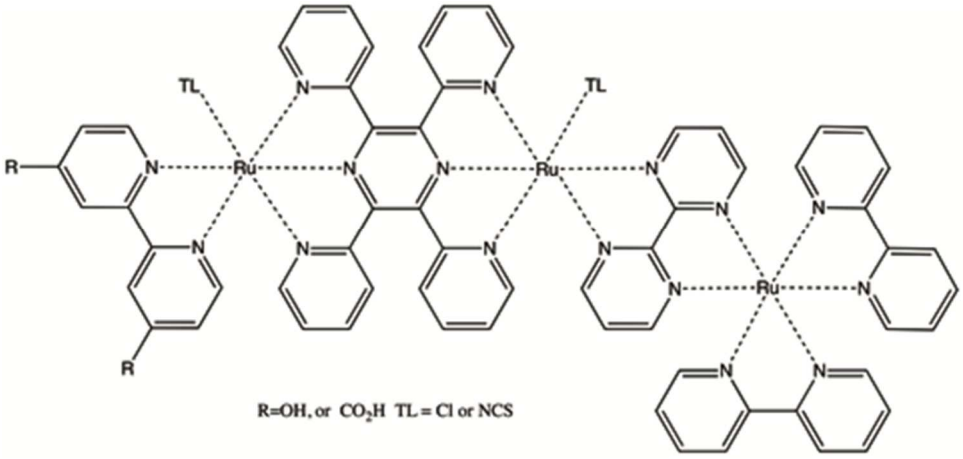

Alternatively, a bis-attaching ligand complex such $[(DCBPY)_2Ru(BPM)]^{2+}$ (Figure 2-17) could be added to $Cl_3Ru(TPPZ)RuCl_3$ to make a triruthenium complex with the BPM bridge closer to the TiO_2 (Figure 2-18). In a complex such as this, the chlorines could be left in place or they could be replaced with isothiocyanate or TPY.

Figure 2-18: Building block with bis-DCBPY attaching groups, $[(DCBPY)_2Ru(BPM)]^{2+}$.

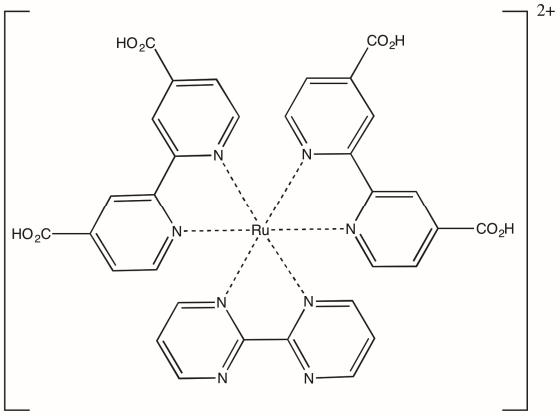

Figure 2-19: Potential mixed bridge tri ruthenium complex made with $[(DCBPY)_2Ru(BPM)]^{2+}$.

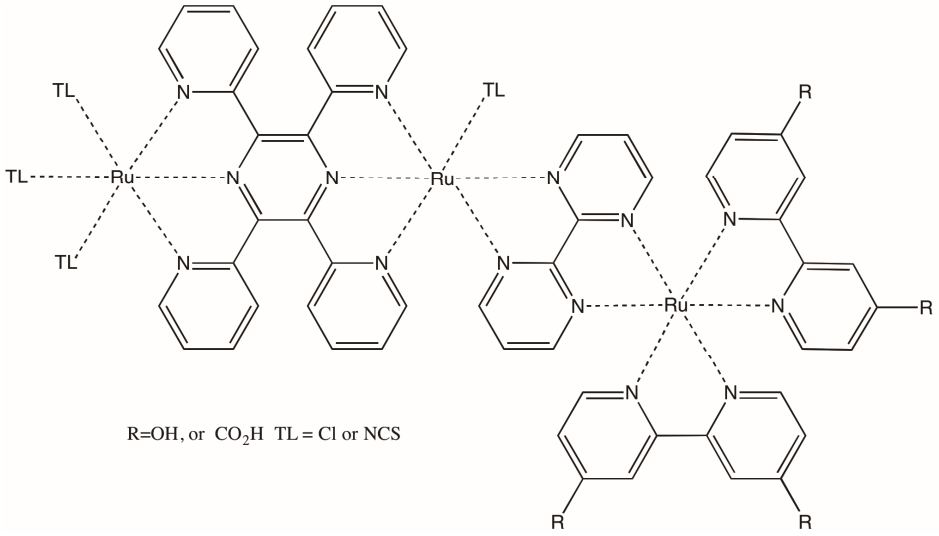

The remainder of this chapter describes the synthesis and characterization of a wide variety of these building blocks. Testing their ability to make triruthenium complexes along with attempting combinatorial synthesis of the triruthenium building blocks will be presented in Chapter 3.

2.3 Experimental Data

All reactions were carried out under an atmosphere of dry nitrogen or in a glovebox unless otherwise noted. All NMR spectra were run using a 300 or 400 MHz Bruker NMR. All UV/Vis measurements were performed on a Perkin Elmer Lambda 950 UV/Vis spectrometer. All IR measurements were taken on a Thermo Nicolet IR200 FT-IR.

2.3.1 Synthesis of 4,4'-dihydroxy-2,2'-bipyridine, DHBPY

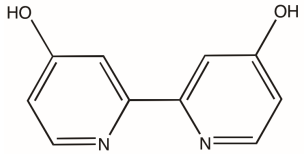

DHBPY was prepared using a modified literature procedure.[25, 26] 4,4'-Dimethoxy-2,2'-bipyridine (0.261 g, 1.21 mmol) was added to glacial acetic acid (12 mL). Excess hydrobromic acid (2 mL, 48%) was added and the reaction mixture was heated under reflux for 18 h. The solvent was removed in vacuo and a small portion of DI water (10 mL) was added to the white/pink solid to dissolve it. The pH was adjusted to 7 by slow addition of a 0.1 M NaOH solution to make a white precipitate that was collected by vacuum filtration. The solid was placed on a high vacuum line overnight. The white precipitate was then recrystallized in boiling H_2O and collected by vacuum filtration. A total of 0.177 g was collected for a yield of 77.7%. The ^{1}H NMR agrees with the literature spectrum. ^{1}H NMR (300 MHz, DMSO-d_6) δ 10.90 (s, 2H), 8.50 (d, J = 6.0 Hz, 2H), 7.93 (d, J = 2.0 Hz, 2H), 7.04 (dd, J = 6.0 Hz, 2.0 Hz, 2H).

2.3.2 Synthesis of tris(4,4'-dihydroxy-2,2'-bypridine)ruthenium(II) chloride, 1

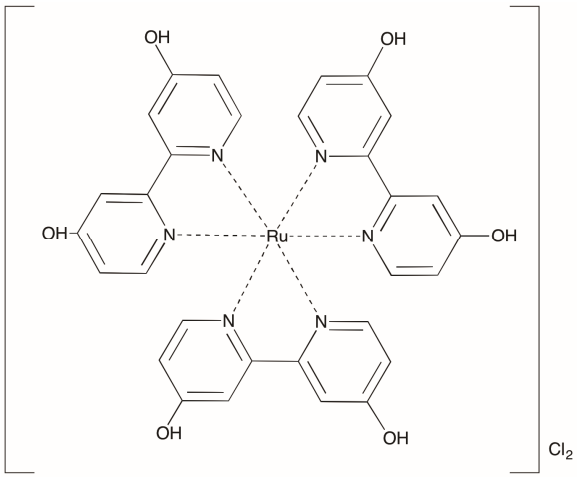

This complex was formed trying to make the bis-4,4'-dihyroxy-2.2'-bypridine product $DHBPY_2RuCl_2$. A typical example is as follows. DHBPY (0.224 g, 1.04 mmol) and $RuCl_3$ (0.102 g, 0.493 mmol) were added to 25 mL DMF and the reaction was refluxed for 8 h under nitrogen. After removing most of solvent in vacuo, acetone was added to precipitate an orange product, which was collected by vacuum filtration. A total of 0.222 g was collected for a yield of 39.1%. ^{1}H NMR (300 MHz, DMSO-d_6): δ 8.15 (d, J = 6.0 Hz, 6H), 7.21 (s, 6H), 6.85 (br. s, 6H), 4.05 (s, 6H) (the presence of three aromatic peaks instead of six suggested that the tris complex was formed instead of the bis product); IR (cm^{-1}): 3568 (br), 3429, 3054, 2918, 1701, 1655, 1637, 1608, 1545, 1438, 1405, 1377, 1313, 1260, 1228, 1126, 1017, 898, 809, 768, 768, 718, 662.

2.3.3 Synthesis of 2,2'-dicarboxy-4,4'-bypridine, DCBPY

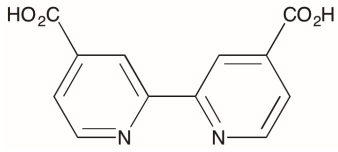

This compound was synthesized per a literature procedure.[27] The total mass collected was 0.590 g for a yield of 60.1%. The ^{1}H NMR agrees with the literature spectrum. ^{1}H NMR (300 MHz, DMSO-d_6): δ 8.91 (d, J = 4.8 Hz, 2H), 8.84, (s, 2H), 7.91 (d, J = 4.8 Hz, 2H).

2.3.4 Synthesis of bis(4,4'- dicarboxy -2,2'-bipyridine)dichlororuthenium(II), 2

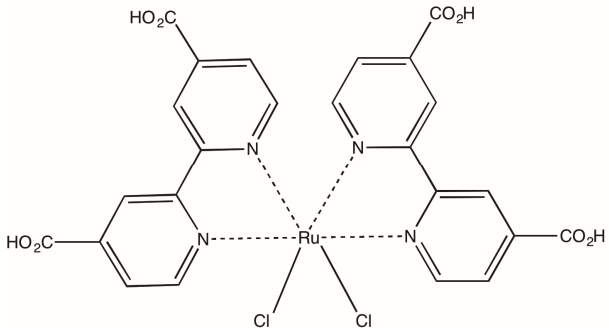

This compound was synthesized per a literature procedure.[28] A total of 0.102 g was collected for a yield of 27.4% yield. The ^{1}H NMR agrees with the literature spectrum.[28] ^{1}H NMR (300 MHz, DMSO-d_6): δ 9.86 (d, J = 8.0 Hz, 2H), 9.13 (d, J = 8.0 Hz, 2H), 8.95 (s, 2H), 8.81 (s, 2H), 8.12 (d, J = 5.0 Hz, 2H), 7.93 (d, J = 5.0 Hz, 2H).

2.3.5 Synthesis of 4,4'-dicarboethoxy-2,2'-bipyridine, DEBPY

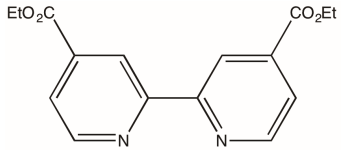

This compound was synthesized per a literature procedure.[29, 30, 31]. The total mass collected was 0.789 g for a yield of 55.2%. The ^{1}H NMR agrees with the literature spectrum. ^{1}H NMR (400 MHz, $CDCl_3$): δ 8.97 (s, 1H), 8.89, (d, *J* = 8.0 Hz, 1H), 7.92 (d, *J* = 8.0 Hz, 1H).

2.3.6 Synthesis of dichlorobis(4,4'-dicarboethoxy-2,2'-bipyridine)ruthenium(II), 3

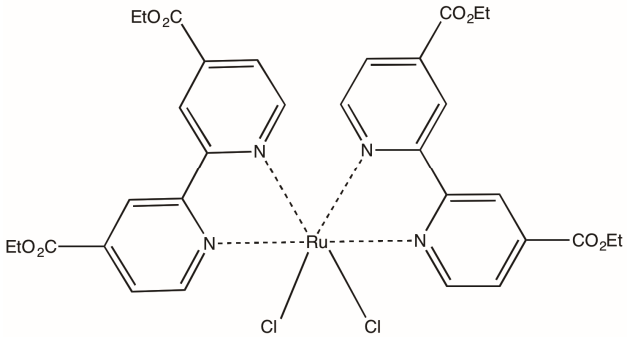

This compound was synthesized with a modified version of a literature procedure.[29] To $RuCl_3$ (0.180 g, 0.866 mmol) in 50 mL of ethanol was added DEBPY (0.524 g, 1.75 mmol) and the reaction was refluxed for 72 h under nitrogen. After removing most of the solvent in vacuo, acetone was added to precipitate a purple product. A total of 0.320 g was collected for a 47.7%. The ^{1}H NMR agrees with the literature spectrum.[28] ^{1}H NMR (400 MHz, DMSO-d_6): δ 10.10 (d, *J* = 5.8 Hz, 2H), 9.12 (s, 2H), 8.94 (s, 2H), 8.26 (d, *J* = 5.3, Hz 2H), 7.76 (d, *J* = 5.9 Hz, 2H), 7.49 (d, *J* = 5.6 Hz, 2H), 4.52 (q, *J* = 6.8 Hz, 4H) 4.36 (q, *J* = 7.0 Hz, 4H), 1.45 (t, *J* = 7.0 Hz, 6H) 1.31 (t, *J* = 7.0 Hz, 6H).

2.3.7 Synthesis of tetrachloro(2,2'-bipyridine)ruthenium(IV), 4

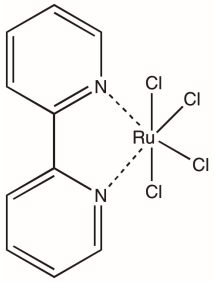

This compound was synthesized per a literature procedure.[32] A total of 0.473 g was collected for a yield of 49%. No NMR or characterization was given in the literature, but the appearance of the black solid matched the description given. The NMR shows the expected BPY peaks, which are slightly shifted downfield because of binding to Ru. ^{1}H NMR (300 MHz, DMSO-d_6): δ 8.83 (d, J = 7.6 Hz, 2H), 8.58 (d, J = 7.8 Hz, 2H), 8.27 (t, J = 7.5 Hz, 2H), 7.75 (t, J = 7.7 Hz, 2H).

2.3.8 Synthesis of bis(2,2'-biimidazole)(2,2'-bipridine)ruthenium(II) hexafluorophosphate, 5

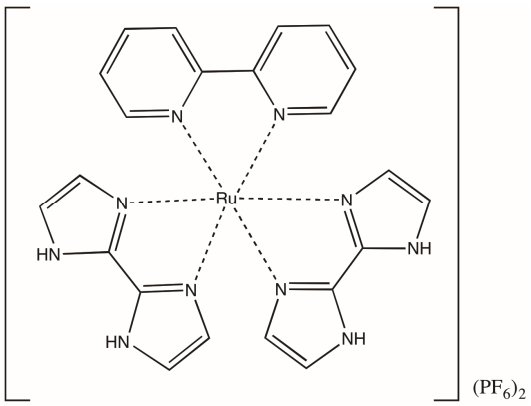

This compound was synthesized with a modified version of a literature procedure.[12] To 100 mL ethylene glycol was added **4** (0.671 g, 1.68 mmol). This was heated at 150 °C for 1 h under nitrogen and then biimidazole (0.574 g, 4.27 mmol) was added. The mixture was heated

for 24 h at 150 °C under nitrogen. After cooling, excess NH_4PF_6 was added and the solution was stirred for another 1 h. A red precipitate (1.14 g) was collected by vacuum filtration for a yield of 77.3%. NMR data was not presented in the literature. ^{1}H NMR (300 MHz, acetone-d_6): δ 13.12 (s, 4H), 8.57 (d, *J* = 7.8 Hz, 2H), 8.13 (d, *J* = 4.2 Hz, 2H), 7.91 (t, *J* = 8.1 Hz, 2H), 7.39 (t, *J* = 6.6 Hz, 2H), 7.36 (s, 2H), 7.28 (s, 2H), 6.58 (s, 2H) 6.45 (s, 2H).

2.3.9 Synthesis of (2,2'-bipyridine)bis(2,2'bipyrimidine)ruthenium(II) hexafluorophosphate, 6

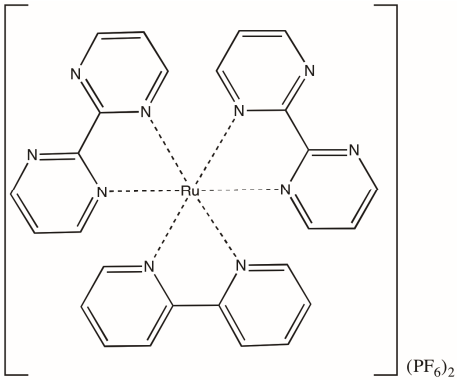

To a solution BPM (0.086 g, 0.540 mmol) in 100 mL of EtOH:H_2O (1:1) was added **4** (0.111 g, 0.279 mmol) and the solution was heated at reflux for 8 h under nitrogen. After cooling, 10 mL of a saturated solution of KPF_6 in H_2O was added and the solution was stirred for 12 h. A brown precipitate was collected by vacuum filtration. A total of 0.653 g was collected giving a 44.3% yield. This was rinsed 3 times with 10 mL of acetone and 3 times with 10 mL of ether. NMR data was not presented in the literature. ^{1}H NMR (300 MHz, acetone-d_6): δ 9.21 (m, 4H), 8.81 (d, *J* = 8.4 Hz, 2H), 8.71 (dd, *J* = 5.7 Hz, 1.8 Hz, 2H), 8.45 (dd, *J* = 5.7 Hz, 1.8 Hz, 2H), 8.25 (m, 4H), 7.73 (m, 4H), 7.60 (t, *J* = 8.4 Hz, 2H).

2.3.10 Synthesis of (2,2'-biimidazole)bis(2,2'-bipyridine)ruthenium(II) hexafluorophosphate, 7

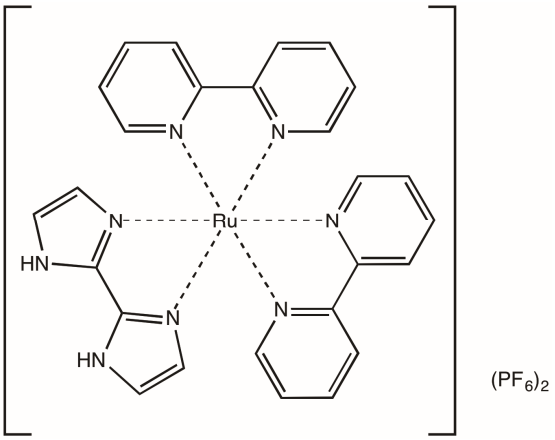

To a solution of **4** (0.384 g, 0.793 mmol) in 100 mL H_2O:EtOH (1:1) was added BIM (0.106 g, 0.793 mmol). This was refluxed for 8 h. After cooling, 3 mL of a saturated NH_4PF_6 solution was added. A red precipitate was collected by vacuum filtration. A total of 0.441 g was collected for a yield of 63.3%. ^{1}H NMR (400 MHz, acetone-d_6): δ 8.76 (m, 4H), 8.68 (d, J =1.4 Hz, 2H), 8.15 (m, 8H), 7.64 (td, J = 5.6 Hz, 1.3 Hz, 2H), 7.52 (td, J = 5.7 Hz, 1.3 Hz, 4H).

2.3.11 Synthesis of bis(2,2'-bipyridine)(2,2'-bipyrimidine)ruthenium(II) hexafluorophosphate, 8

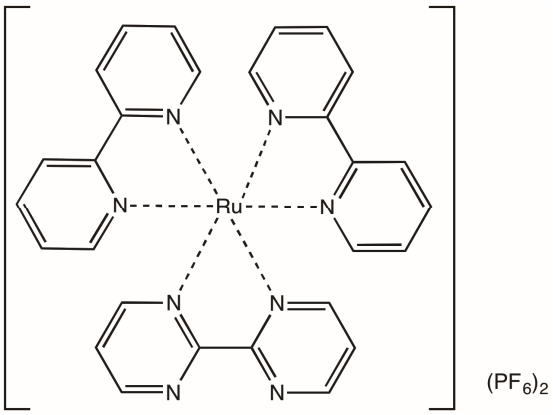

This compound was synthesized with a modified version of a literature procedure.[16] To a solution of BPM (0.0855 g, 0.540 mmol) in 100 mL of EtOH:H_2O (1:1) was added **4** (0.265 g, 0.548 mmol) and the solution was heated at reflux for 24 h under nitrogen. After cooling, 5 mL of a saturated solution of NH_4PF_6 in H_2O was added and the solution was stirred for 12 h. A brown precipitate was collected by vacuum filtration. The brown precipitate was dissolved in acetone and filtered. Most of the acetone was removed by vacuum and then a brown solid was re-precipitated by slow addition of ether. This brown solid was collected by vacuum filtration and rinsed with ether. A total of 0.350 g was collected for a yield of 86.1%. ^{1}H NMR (300 MHz, aceteonitrile-d_3): δ 9.09 (dd, *J* = 4.8, 2.4 Hz, 2H), 8.50 (dd, *J* = 7.5, 1.5 Hz, 4H), 8.07(m, 6H), 7.87 (qd, *J* = 7.5, 1.5, 2H), 7.69 (*J* = 7.5, 1.5, 2H) 7.51 (t, *J* = 5.0 Hz, 2H), 7.42 (m, 4H).

2.3.12 Synthesis of 2,2'-biimidazole, BIM-H_2

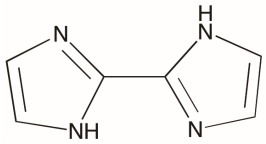

This compound was synthesized with a modified version of a literature procedure and a typical reaction follows.[33] Glyoxal (113 mL, 2.47 mol) was cooled to 0 °C under nitrogen. To this was added excess NH_4OH (200 mL) dropwise. The mixture slowly turned yellow and was stirred for 18 h at room temperature. A grey solid was collected by vacuum filtration. This solid was dissolved in 1 M HCl and the solution was heated at 100 °C for 15 min. After cooling, the solution was neutralized with aqueous K_2CO_3. A white precipitate was collected by vacuum filtration. A total of 19.0 g was collected for yield of 17.2%, based on glyoxal. The ^{1}H NMR agrees with the literature. ^{1}H NMR (300 MHz, DMSO-d_6): δ 12.64 (s, 2H), 7.06 (s, 4H).

2.3.13 Synthesis of dichlorobis(2,2'-bipyridine)ruthenium(II), 9

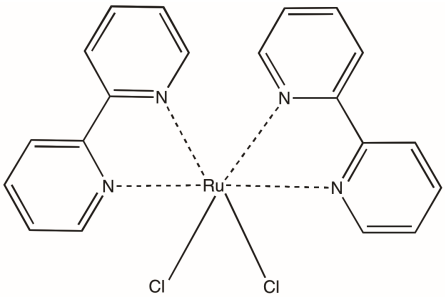

This compound was synthesized with a modified version of a literature procedure.[34,35,36] Dimethylformamide (15 mL) was placed in a round bottom flask and was purged with nitrogen for 15 min. Ruthenium chloride hydrate (0.215 g, 1.04 mmol), bipyridine (0.320 g, 2.05 mmol), and lithium chloride (0.465 g, 11.0 mmol) were added to the flask. The solution was heated under reflux for 6 h while under nitrogen. After cooling to room temperature, the mixture was poured into 100 mL reagent grade acetone and placed into a refrigerator overnight for 12 h at 5°C. A greenish black ppt. was seen the following morning. This was collected by vacuum filtration and rinsed with three 10 mL portions of DI water, followed by washing with three 10 mL portions of diethyl ether. This was carried on without further purification and 0.276 g was collected for a yield of 55.6%. The ^{1}H NMR agreed with the literature spectrum. ^{1}H NMR (300 MHz, DMSO-d_6): δ 9.96 (d, J = 4.8 Hz, 2H), 8.63 (d, J = 8.0 Hz, 2H), 8.47 (d, J = 8.0 Hz, 2H), 8.06 (t, J = 6.6 Hz, 2H), 7.76 (t, J = 6.0 Hz, 2H), 7.67 (t, J = 7.5 Hz, 2H), 7.51 (d, J = 6 Hz, 2H), 7.09 (t, J = 6.0 Hz, 2H).

2.3.14 Synthesis of bis(4,4'-dicarboxy-2,2'-bipyridine)(2,2'-bipyrimidine)ruthenium(II) hexafluorophosphate, 10

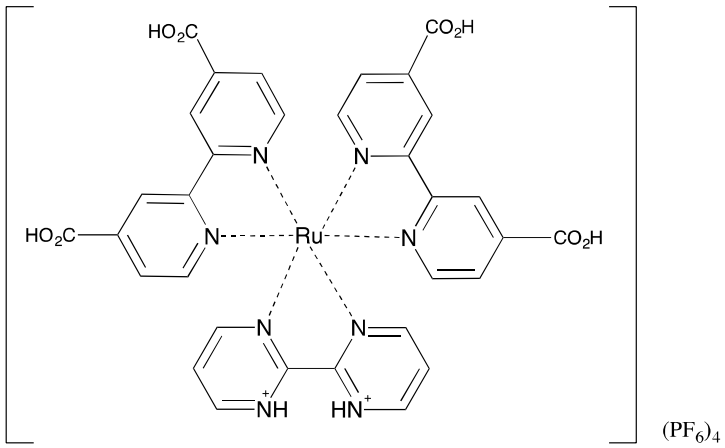

To a solution of **2** (0.531 g, 0.804 mmol) in EtOH/H_2O (1:1, 150 mL) was added 6 eq of NaOH. To this was added BPM (0.129 g, 0.815 mmol). The reaction was stirred under nitrogen for 24 h at reflux. After cooling, the solution was acidified with 1 M HCl until the pH reached 4 and then 10 mL of saturated NH_4PF_6 was added. A red solid was collected and a column was performed on silica gel using H_2O as the eluent. A red band eluted and 0.611 g was collected for a yield of 57.2%. ^{1}H NMR (300 MHz, D_2O): δ 9.08 (d, J = 3 Hz, 2H), 8.90 (d, J = 3.9 Hz, 4H), 8.17 (dd, J = 5.7 Hz, 1.5 Hz, 2H), 8.03 (d, J = 6 Hz, 2H), 7.86 (d, J = 5.7 Hz, 2H), 7.74 (d, J = 4.2 Hz, 2H), 7.70 (d, J = 4.5 Hz, 2H), 7.59 (t, J = 5.1 Hz, 2H). IR (cm^{-1}): 3127 (br), 3030, 1995, 1721, 1636, 1578, 1554, 1406, 1315, 1229, 1138, 1023, 841, 767, 748, 665, 557, 495.

2.3.15 Synthesis of bis(4,4'-dicarboxy-2,2'-bipyridine)diisothiocyanateruthenium(II), N3

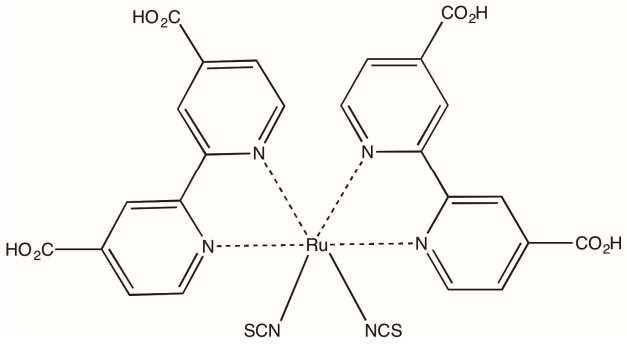

The synthesis of **N3** began by dissolving **2** (0.1108 g, 0.1668 mmol) in 30 mL of DMF. To this solution was added 0.1 M aqueous NaOH (10 mL) to deprotonate the carboxy groups. Potassium thiocyanate (0.2294 g, 2.361 mmol) was separately dissolved in 2 mL of DI H_2O and added to the above solution. This was heated to reflux for 6 h under N_2. Once cooled, the solvent was removed in vacuo and the residual solid was dissolved in DI H_2O and filtered through a sintered funnel to remove any undissolved particles. The pH of the filtrate was adjusted to 3 by adding 0.1 M sulfuric acid and the solution was placed in the refrigerator for 12 h. A dark purple solid was then collected by vacuum filtration and washed with 3 portions of 10 mL acetone and 3 portions of 10 mL diethyl ether. A total of 74.7 mg was collected for a yield of 63.1%. ^{1}H NMR (300 MHz, DMSO-d_6): δ 9.43 (d, J = 5.7 Hz, 2H), 9.19 (s, 2H), 9.02 (s, 2H), 8.38 (d, J = 5.7 Hz, 2H), 7.79 (d, J = 6.0 Hz, 2H), 7.59 (d, J = 6.6 Hz, 2H).

2.3.16 Synthesis of bis(bis(2,2'-bipyridine)ruthenium(II))-μ-(2,2'-biimidazole) hexafluorophosphate, 11

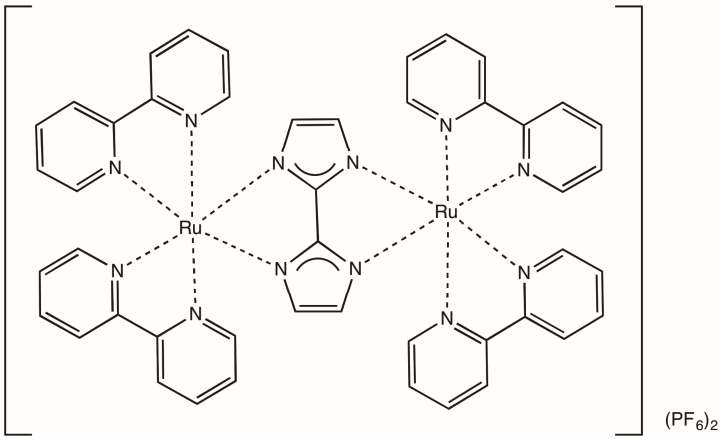

This compound was synthesized with a modified version of a literature procedure.[12] To a solution of **7** (0.100 g, 0.207 mmol) in DI H_2O, was added aqueous 1.0 M NaOH until the solution turned from orange to purple, indicating the biimidazole ligand was deprotonated. Afterwards, solid **9** (0.172 g, 0.207 mmol) was added and the solution was heated at reflux for 72 h. After cooling, 2 mL of a saturated aqueous NH_4PF_6 solution was added to make the red hexafluorophosphate salt precipitate. This was collected by vacuum filtration and rinsed with 3 portions of 10 mL of ether. A total of 0.246 g was collected for a yield of 94.9%. ^{1}H NMR (400 MHz, acetone-d_6) δ 8.75 (d, *J* = 6.1 Hz, 2H), 8.68 (m, 6H), 8.30 (d, *J* =4.9 Hz, 2H) 8.11 (td, *J* = 7.8 Hz, 1.3 Hz, 2H), 8.04 (td, *J* = 7.8 Hz, 1.2 Hz, 2H) 7.95 (m, 4H), 7.88 (d, *J* = 5.6 Hz, 2H), 7.80 (t, *J* = 5.6 Hz, 2H), 7.74 (m, 4H), 7.37 (m, 6H) 6.00 (d, *J* = 8.2 Hz, 4H).

2.3.17 Synthesis of bis(bis(2,2'-bipyridine)ruthenium(II))-μ-(2,2'-bipyrimidine) hexafluorophosphate, 12

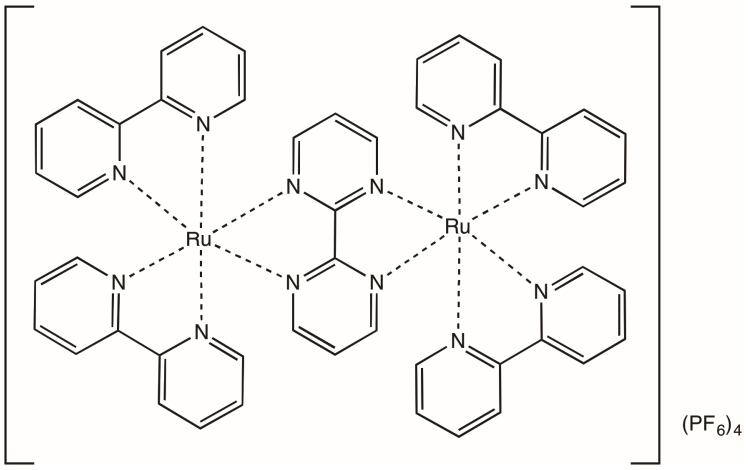

This compound was synthesized with a modified version of a literature procedure.[37] To a solution of **8** (0.158 g, 0.183 mmol) in 100 mL of EtOH:H_2O (1:1) was added **9** (0.08 g, 0.184 mmol). This was heated under reflux for 18 h and the solution turned from an orange/red color to a green color, similar to what was described in the literature. After cooling, 3 mL of a saturated KPF_6 solution was added to make a dark brown precipitate. This was placed in the refrigerator for 24 h and then the brown product was collected by vacuum filtration. A total of 0.228 g was collected for a yield of 79.4%. ^{1}H NMR (300 MHz, acetone-d_6): δ 8.82 (d, J = 8.4 Hz, 8H), 8.60 (d, J = 7.2 Hz, 4H), 8.58 (d, J = 6.0 Hz, 4H), 8.30 (m, 8H), 8.04 (d, J = 5.7 Hz, 4H) 7.83 (t, J = 6.3 Hz, 4H) 7.72 (t, J = 5.7 Hz, 2H), 7.61 (t, J = 5.7 Hz, 4H).

2.3.18 Synthesis of (4,4'-dihydroxy-2,2'-bipyrimidine)bis(2,2'-bipyridine) ruthenium(II) hexafluorophosphate, 13

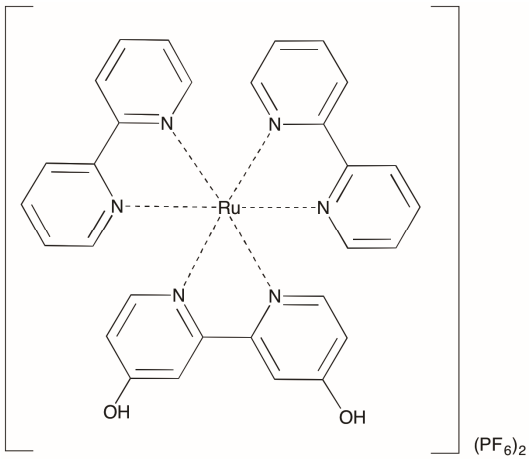

This complex was prepared by dissolving **9** (0.2186 g, 0.4512 mmol) in EtOH (12 mL). To this, DHBPY (0.0916 g, 0.487 mmol) was added and the solution was refluxed for 6 h. The solution was initially a dark purple and turned orange over the course of the reaction. Once cooled, an aqueous solution of NH_4PF_6 was added and an orange precipitate was formed. The precipitate was collected by vacuum filtration and rinsed with diethyl ether. A total of 0.228 g was collected for a yield of 56.6%. ^{1}H NMR (300 MHz, acetone-d_6): δ 8.79 (d, J = 6.0 Hz, 2H), 8.76 (d, J = 6.0Hz, 2H), 8.16 (m, 6H), 8.05 (s, 2H), 8.01 (d, J = 6.0 Hz, 2H), 7.60 (t, J = 6.0 Hz, 4H), 7.52 (t, J=6 Hz, 2H), 6.99 (dd, J = 6 Hz, 1 Hz, 2H), 3.55 (s, 2H).

2.3.19 Synthesis of bis(2,3,5,6-tetra-(2-pyridyl)pyrazine)ruthenium(II) hexafluorophosphate, 14

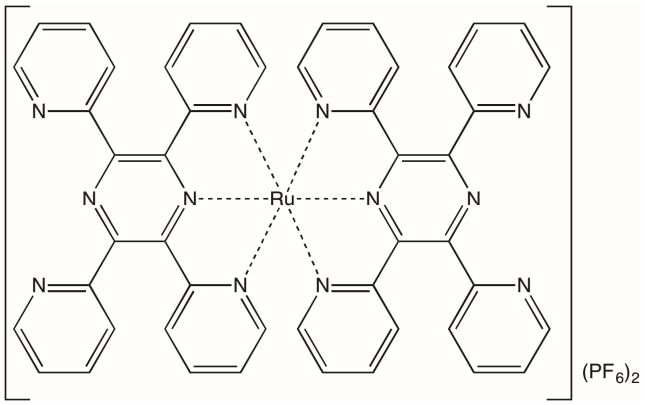

This compound was synthesized per a literature procedure.[3]. A total of 0.142 g of product was collected for a yield of 43.3%. The ^{1}H NMR agrees with the literature spectrum. ^{1}H NMR (300 MHz, acetone-d_6): δ 8.81 (dd, J=5, 4H), 8.58 (dd, J=8, 4H), 8.35 (dd, J=8, 4H), 8.12 (dd, J=7.5, 4H), 7.89 (dd, J=7, 8H), 7.80 (dd, J=8, 4H), 7.41 (dd, J=7, 4H), IR (cm^{-1}): 3030, 1677, 1587, 1567, 1520, 1471, 1401, 838, 788, 753, 669, 556, 551.

2.3.20 Synthesis of bis(trichlororuthenium(III))-μ-(2,3,5,6-tetra-(2-pyridyl)pyrazine), 15

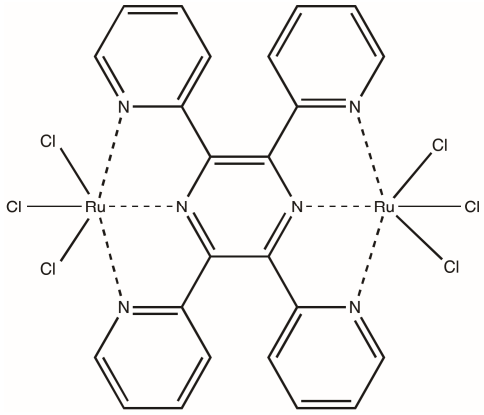

This compound was synthesized per a literature procedure.[38] A total of 0.389 g was collected for a yield of 95.6%. The ^{1}H NMR had a very low signal to noise ratio and was not very clear due to the product being paramagnetic. There were broad, very low intensity multiplets downfield of where normal TPPZ peaks would occur. ^{1}H NMR (300 MHz, DMSO-d_6): It is believed that the paramagnetic Ru(III) caused significant line broadening, and a very low signal to noise ratio was seen; UV (EtOH) λ_{max} 255, 300, 390, 650 nm; IR (cm^{-1}): 3068, 1592, 1518, 1464, 1423, 1297.

2.3.21 Synthesis of tetrabutylammonium bid(trichlororuthenium(III))-μ-(2,3,5,6-tetra-(2-pyridyl)pyrazine), 16

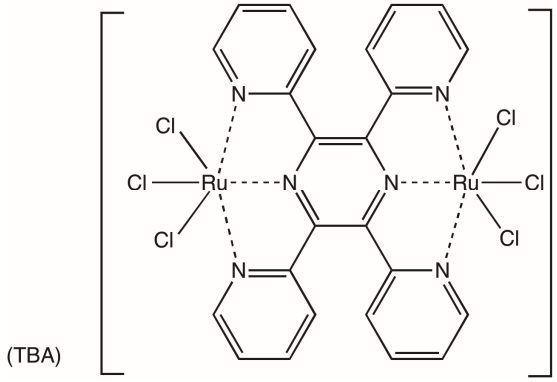

This compound was synthesized per a literature procedure.[8] A total of 0.511 g was collected for a yield of 90.2%. The ^{1}H NMR had a very low signal to noise ratio and was not very clear due to the product being paramagnetic. There were broad, very low intensity multiplets downfield of where normal TPPZ peaks would occur. ^{1}H NMR (300 MHz, DMSO-d_6): It is believed that the paramagnetic Ru(III) caused significant line broadening. and a very low signal to noise ratio was seen; UV (EtOH) λ_{max} 476, 644, 1706 nm.

2.3.22 Synthesis of bis(triisothiocyanateruthenium(III))-μ-(2,3,5,6-tetra-(2-pyridyl)pyrazine), 17

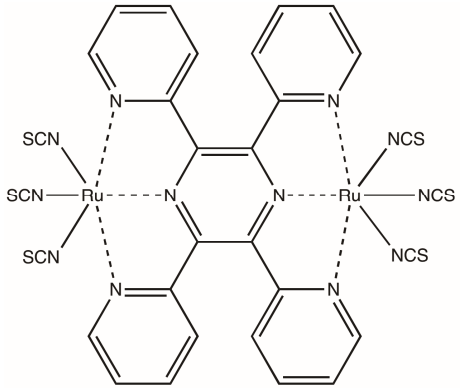

To a solution of **15** (0.104 g, 0.130 mmol) in 100 ml DI water was added AgOTf (0.280 g, 1.09 mmol). This was stirred for 5 h at 70 °C under nitrogen and the solution turned from green to a royal blue and a white precipitate formed. The white precipitate, AgCl, was filtered by vacuum filtration and the blue solution was returned to a round bottom flask. To this solution was added KSCN (0.129 g, 1.34 mmol) and the reaction was stirred under nitrogen at 70 °C for 5 h. The solution turned from blue/black to a dark green solution. After cooling, a green precipitate was collected by vacuum filtration. Column chromatography was performed on aluminum oxide using acetone to elute a green band which was **17**. A total of 0.501 g was collected for a yield of 98.1%. ^{1}H NMR (300 MHz, acetone-d_6): δ 9.19 (m, 4H), 8.90 (m, 4H), 8.06 (m, 8H); IR (cm^{-1}): 3050, 2360 (bound NCS), 1699, 1652, 1592, 1457, 1417, 1350, 1247, 1187, 1060, 1010, 794, 775, 749, 692, 581, 555.

2.4 Results and Discussion

Synthesis of the building blocks began with the hydrolysis of 4,4'-dimethoxy-2,2'-bipyridine with glacial acetic acid and 48% HBr, and this is seen in Scheme 2-1. DHBPY was obtained in a 77.7% yield. The ^{1}H NMR showed two doublets, which were the two hydrogens between the N and the OH group. Meta coupling was seen between both hydrogens ortho to the OH and the OH signal was seen at 10.90 ppm.

Several attempts were made towards the synthesis of $(DHBPY)_2RuCl_2$ but were largely met with failure. When DHBPY was treated with 0.5 eq of $RuCl_3$, a bright orange product was obtained. ^{1}H NMR analysis showed three distinct peaks while a bis-DHBPY product would be expected to have 6 peaks. This indicated either a mono-DHBPY substituted product or a tris-DHBPY substituted product, **1**, was being formed. Most tris-bipyridine complexes tend to have an orange/red color and the compound formed was similar in color, suggesting that the tris product was being formed. In contrast, most complexes with the general formula L_2RuCl_2 (L = a bipyridyl ligand) tend to have a dark purple color. The mono BPY complex, **4**, was a dark black color, with an appearance similar to ruthenium chloride.

Scheme 2-1: Synthesis of **1**.

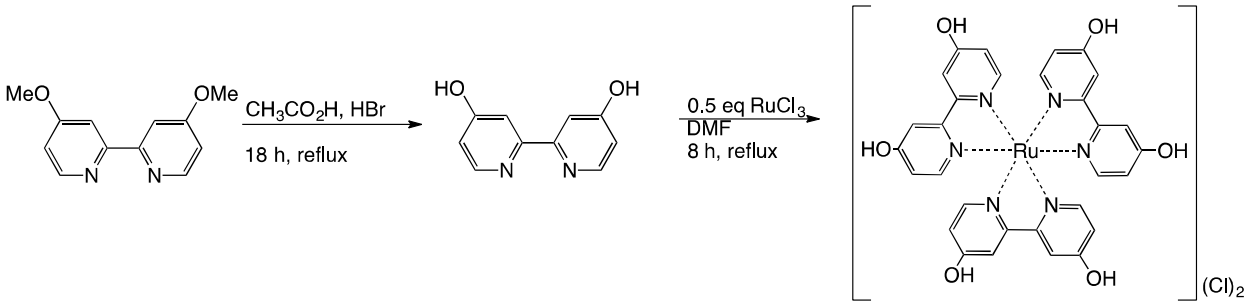

DHBPY
77.7% Yield

1
39.1% Yield

A variety of conditions were tried to see if $(DHBPY)_2RuCl_2$ could be made. Reactions times of 8 h, 24 h, and 48 h were tested in addition to many different solvent systems including DMF, EtOH, EtOH/H_2O, and DMF/H_2O, all with similar results. A patent was released in 1992 describing a way to make a similar complex using osmium instead of ruthenium.[39] The method used in the patent is outlined in Scheme 2-2. Attempting to do the analogous procedure with $RuCl_3$ instead of K_2OsCl_6 was unsuccessful. According to the patent, the osmium product was precipitated from the solution by addition of acetone after the reaction was complete. The ruthenium products were soluble in both acetone and ethylene glycol. Tris-BPY complexes tend to be soluble in acetone, which is probably the cause of this phenomenon. The reaction was tried at reaction times of 8 hr, 24 hr, and 48 hr. In all cases, the ^1H NMR again showed 3 peaks in the aromatic region as well as the hydrogens on the methoxy carbon that were not hydrolyzed.

Scheme 2-2: Synthesis of $(DHBPY)_2OsCl_2$.

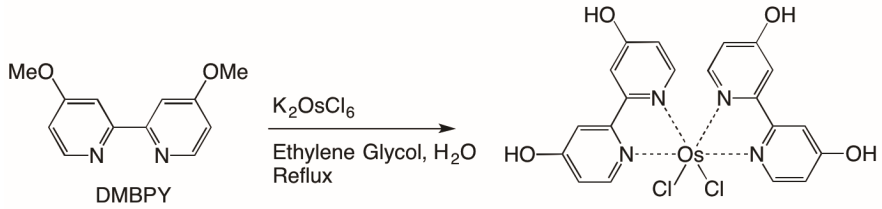

At the Fall 2012 ACS National meeting, a conversation was had with Dr. Jared Paul from the Paul group at Villanova University. He recently reported on the structural and electronic properties of **1** and $[(DHBPY)Ru(BPY)_2]Cl_2$.[40, 41] When asked about the bis-DHBPY product, he mentioned that he too was unable to make it and that it was unclear why it would not form.

Oxidation of 4,4'-dimethyl-2,2'-bipyridine gave DCBPY in 60.1% yield and refluxing DCBPY with sodium dichromate in sulfuric acid produced **2** in 27.6% yield, as shown in

Scheme 2-3. The ^{1}H NMR agrees with the literature spectrum, although the carboxylic acid hydrogen was not observed, likely due to some residual water in the DMSO solvent. The same splitting pattern was seen was in DHBPY, although slightly downfield due to the electron withdrawing carboxylic acid group. The ^{1}H NMR of **2** had six peaks, including four doublets and two singlets which is what was expected (two doublets and one singlet per pyridine ring of DCBPY). One of the pyridine rings on each DCBPY is oriented in-plane cis to the other DCBPY while the other pyridine ring is oriented in-plane cis to chlorine. While both rings are technically always cis to both a chlorine and DCBPY, "in-plane cis" specifically refers to the ligand cis while being in plane with the aromatic ring. Figure 2-16 illustrates this better. It is likely the pyridine ring in-plane-cis to the other DCBPY is experiencing a shielding effect due to magnetic anisotropy in the face of the aromatic ring, causing the double from the hydrogen ortho to the nitrogen to be further upfield than the other peaks.

Scheme 2-3: Synthesis of **2**.

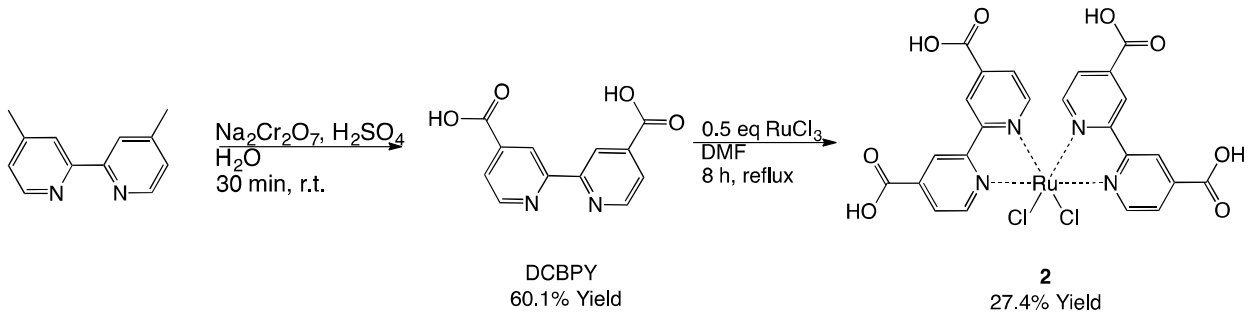

Figure 2-20: Illustration of hydrogen interactions in **2**.

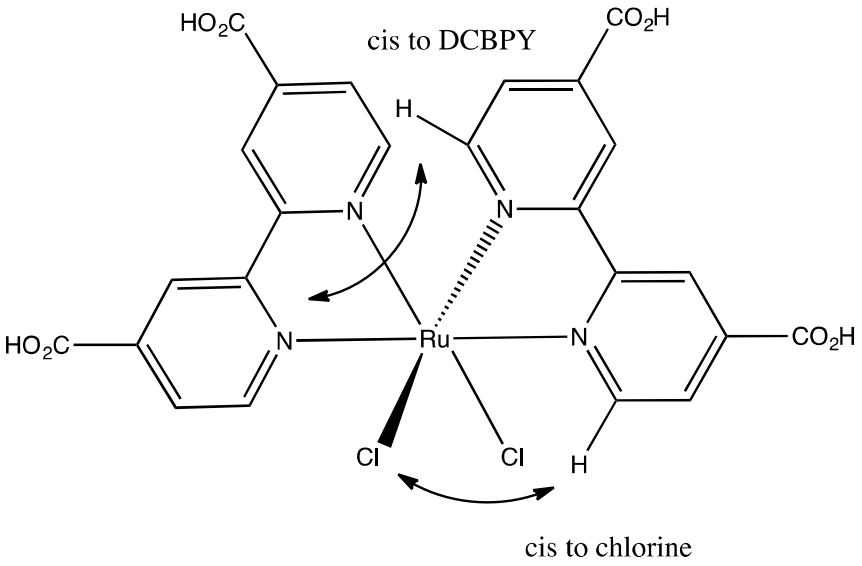

Esterification of DCBPY with ethanol and sulfuric acid proceeded with 60.1% yield. Formation of **3** was achieved with 47.8% yield. These are seen in Scheme 2-4. Six peaks were seen in the aromatic region as with **2**, and the ^{1}H NMR of **3** also displayed two ethyl peaks. Similar to **2**, the peaks on one ring of DEBPY are further upfield, presumably due to magnetic anisotropy, as in **2**.

Scheme 2-4: Synthesis of **3**.

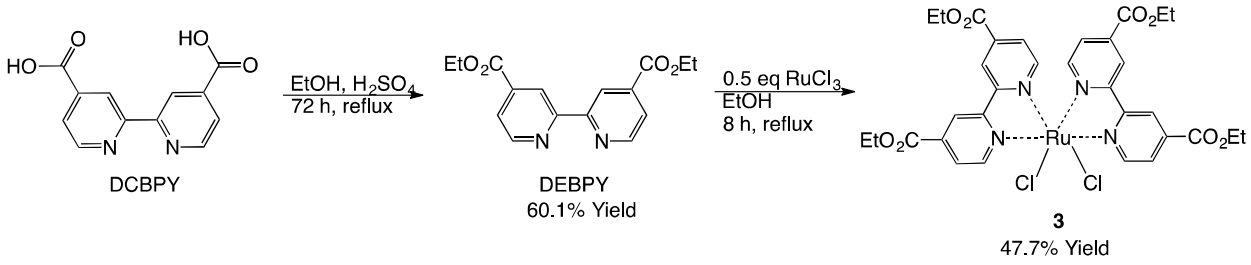

Formation of **4** was achieved in 49% yield and is seen in Scheme 2-5. After adding all the reagents, the mixture was stirred open to air and was then capped and allowed to sit for 3 weeks. According to the literature, the reaction is complete after 1 week, but yields increased from roughly 50% to around 90% by letting it sit for up to 3 weeks.[32] No additional yield was noticed by waiting additional time however. While originally reported as a Ru(IV) species, a more recent paper suggests it is actually a Ru(III) negatively charged species with a counter ion of (BPY+H).[42] Using **4** to make the bis-BIM and bis-BPM products **5** and **6** always resulted in the formation of a portion of the mono-BIM and mono-BPM products **7** and **8**, suggesting that it is product formed was the Ru(III) species and that the extra BPY from Ru(III) is being used to make the mono products.

Scheme 2-5: Synthesis of **4**.

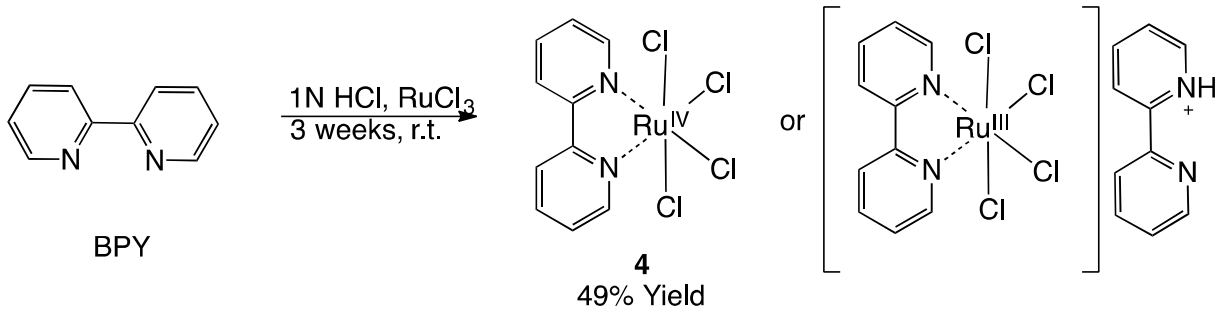

Formation of BIM-H_2 by condensation of glyoxal with NH_4OH was achieved in 17.9% yield and is seen in Scheme 2-6. Two peaks are seen in the ^1H NMR, one for the NH hydrogen and one for the electronically equivalent C–H hydrogens. In the literature procedure, a solution of the product was filtered through activated carbon. Instead, the product was dissolved by

addition of aqueous NaOH, filtered, and then precipitated by addition of HCl. The product was then collected by vacuum filtration.

Scheme 2-6: Synthesis of BIM-H_2.

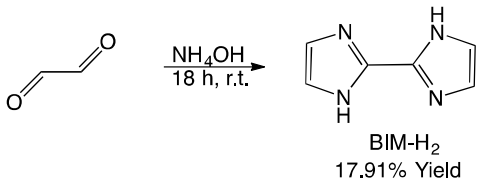

The synthesis of **9** is seen in Scheme 2-7 and proceeded in 53.6% yield. The ^{1}H NMR had eight distinct peaks, four doublets four triplets. Similar to the analysis of the peaks in **2** (Figure 2-20), placement of one pyridine ring in-plane cis to chlorine and one in-plane cis to the other bipyridine ring likely causes a shielding difference in each pyridine ring.

Scheme 2-7: Synthesis of **9**.

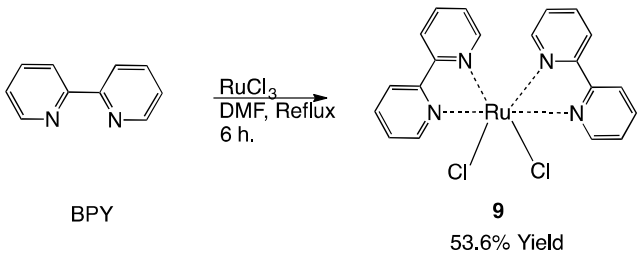

The synthesis of **10** is seen in Scheme 2-8. After deprotonating **2**, BPM was added and the solution was refluxed for 24 h, followed by acidification and precipitation with hexafluorophosphate.

Scheme 2-8: Synthesis of **10**.

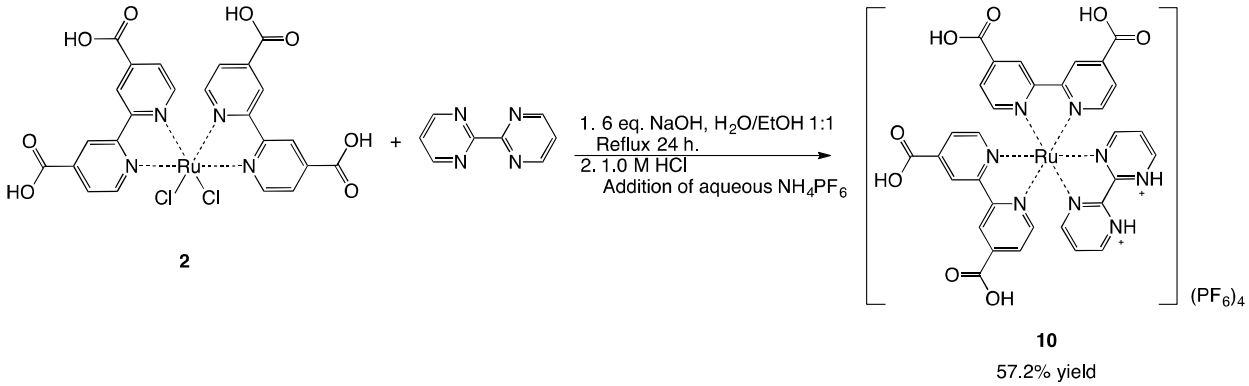

2 **10**

57.2% yield

The first time the synthesis was attempted, the solution was left basic instead of acidifying. Tetrabutylammonium hexafluorophosphate was added in an attempt to make the tetrabutylammonium salts of the carboxylic acids. At first it was thought that the tetrabutylammonium ions would form an ion pair with the deprotonated carboxylate groups, and the hexafluorophosphate ions would balance the charge on the ruthenium which would be in the +2 oxidation state. However, it would also be possible to have two or three of the carboxylate groups in an ion pair with tetrabutylammonium and the other two or one remaining with a negative charge to counter the charge on the ruthenium center forming a zwitterion. Mass spectrometry was performed using MALDI and a peak was seen at m/z=748. The isotopic distribution matched the predicted distribution and the mass corresponds to a complex with three tetrabutylammonium ions and one sodium ion with an overall charge of +2. Figure 2-17 displays this complex. However, it was easier to acidify the complex, eliminating any uncertainty as to the number of tetrabutylammonium ions. In subsequent trials, this was performed.

Figure 2-21: Illustration of a deprotonated **10** with tetrabutylammonium ion counter ions.

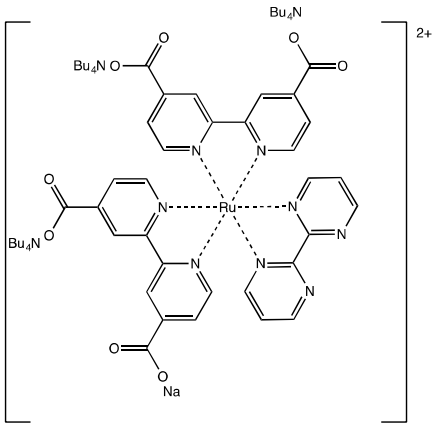

All peaks were identified and assigned using ^{1}H-^{1}H COSY in D_2O and the COSY analysis is seen in Figure 2-18 and Figure 2-19. The IR also showed stretching for the carboxylic acid functional groups as well. The shift at 9.08 ppm correlates to the shift at 7.59 ppm, which in turn correlates to the shift at 8.17 ppm. This was determined to be the 3 hydrogens on the BPM ring. C_2 symmetry in the molecules makes the two rings of BPM equivalent. The peak at 9.08 ppm is most likely the hydrogen that is para to the ruthenium. This hydrogen would be less shielded than the ortho hydrogen facing towards the DCBPY rings, which is at 8.17 ppm. The triplet at 7.59 ppm would be the hydrogen in between these two. This is seen in Figure 2-18. The peak at 8.98 ppm is not correlated to any others, which indicates it is the hydrogen ortho to both the carboxylic group on DCBPY and the carbon-carbon bridge between the rings. The doublet at 8.03 ppm is coupled to the doublet at 7.74 ppm and the doublet at 7.86 ppm is coupled to the doublet at 7.70 ppm. This is illustrated in Figure 2-19. The peaks at 8.03 ppm and 7.86 ppm correspond the hydrogens on DCBPY that are ortho to the nitrogen, since hydrogens ortho to nitrogen usually occur further downfield. The peaks at 7.74 ppm and 7.70 ppm correspond to the peaks ortho to the carboxylic acid and meta to the nitrogen. This is

seen in Figure 2-19. It was not determined which set of peaks is on the ring that is in-plane cis to the BPM and which is in-plane cis to the other DCBPY.

Figure 2-22: COSY analysis of BPM ligand in **10**.

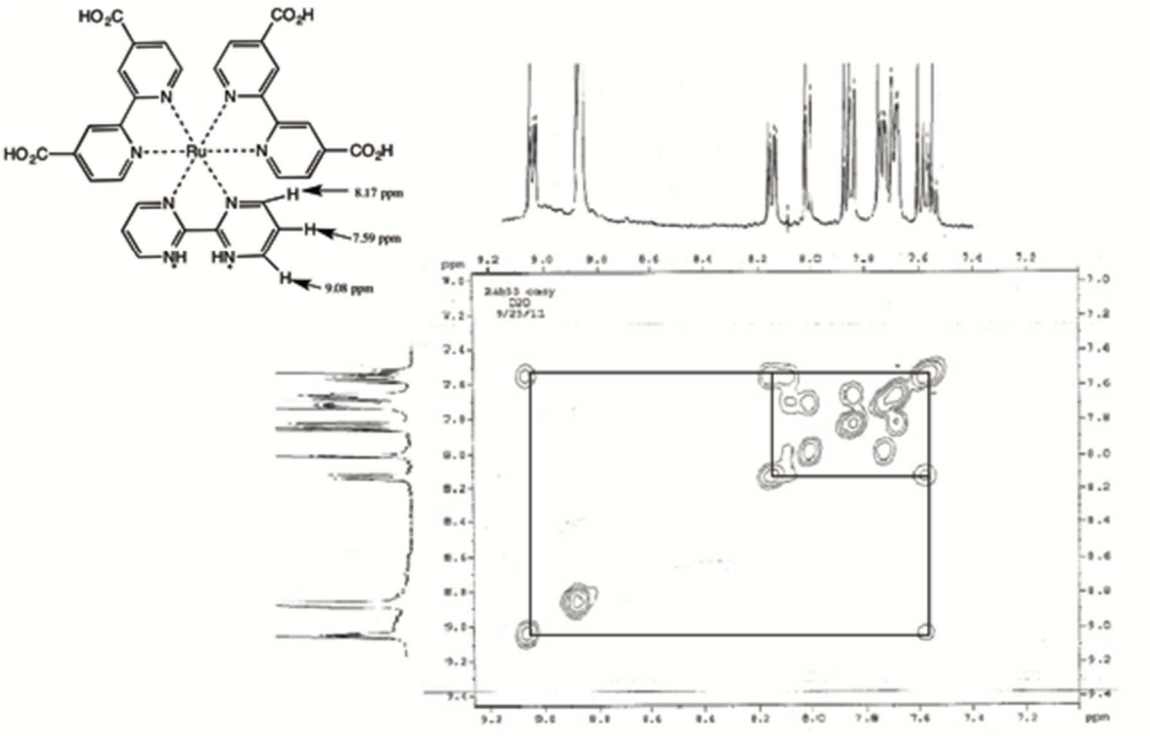

Figure 2-23: COSY analysis of DCBPY ligand in **10**.

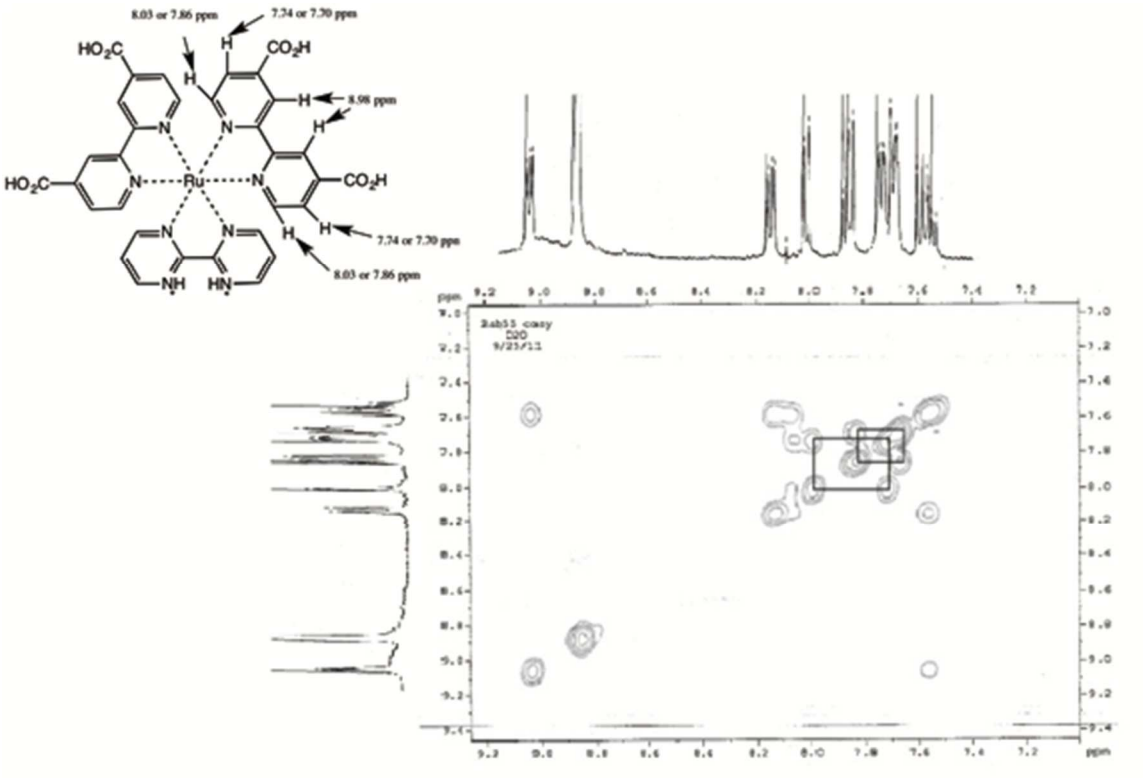

The synthesis of **N3** was achieved by refluxing **2** with KSCN in DMF and is seen in Scheme 2-9. During the initial synthesis of N3, Grätzel determined that the thiocyanate is bound to the ruthenium through N as opposed to S.[43] The authors noted that peaks appears in the IR at 2126 and 2093 cm^{-1}, characteristic of cis isothiocyanates. The IR obtained experimentally displayed these peaks as well. Grätzel reported that the IR also showed a peak corresponding to C=S bending at 770 cm^{-1}.[43] He noted that this peak would not be present if the SCN was bound through the sulfur, and would instead show a weak peak near 700 cm^{-1}. The IR of N3 obtained experimentally had a peak at 775 cm^{-1}, corresponding to C=S bending and an N bound isothiocyanate.

Scheme 2-9: Synthesis of **N3**.

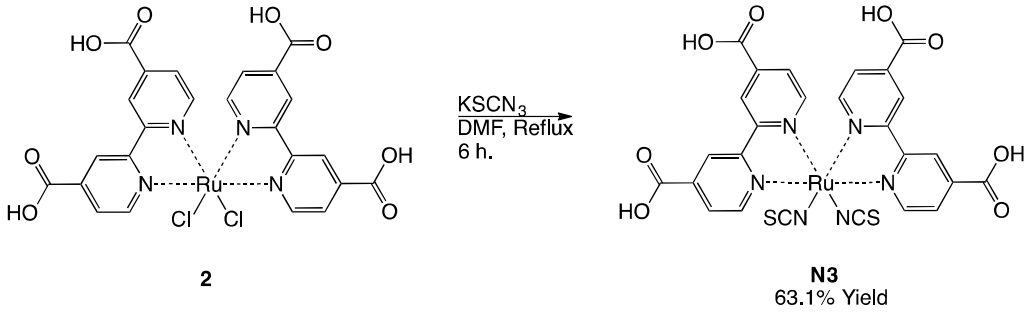

Compound **5** was obtained in 77.3% yield by heating BIM and **4** in ethylene glycol at 150 °C for 24 h as seen in Scheme 2-10. The product was a bright orange and could be deprotonated with NaOH or NaOEt changing the color to purple. In the ^{1}H NMR, four bipyrdine peaks were seen, two doublets and two triplets. An additional four singlets were observed for the four hydrogens of the bimidazoles upfield from the pyridine peaks at 7.36, 7.28, 6.58, and 6.45 ppm. The NH peak appeared at 13.12 and showed integration of four hydrogens. The four peaks from the bipyridine, a doublet, triplet, triplet, and doublet at 8.57, 8.13, 7.91, and 7.39 respectively, showed an integration of two hydrogens each.

Scheme 2-10: Synthesis of **4**.

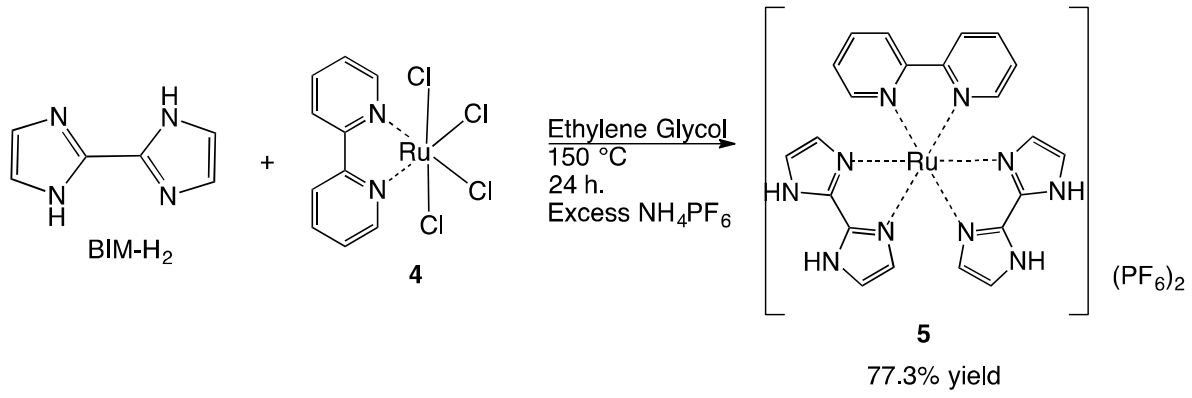

Compound **6** was made by refluxing **4** with BPM in ethanol/water (1:1) and was obtained in 44.3% yield. The ^{1}H NMR was integrated to twenty hydrogens as would be expected, eight hydrogens from the BPY ligand and twelve hydrogens from the BPM. The peaks from the BPM ligand were integrated into four doublets and two triplets, with each peak integrating to two hydrogens. The BPY ligand followed the two doublet, two triplet pattern, with each peak integrating to two.

Scheme 2-11: Synthesis of **6**.

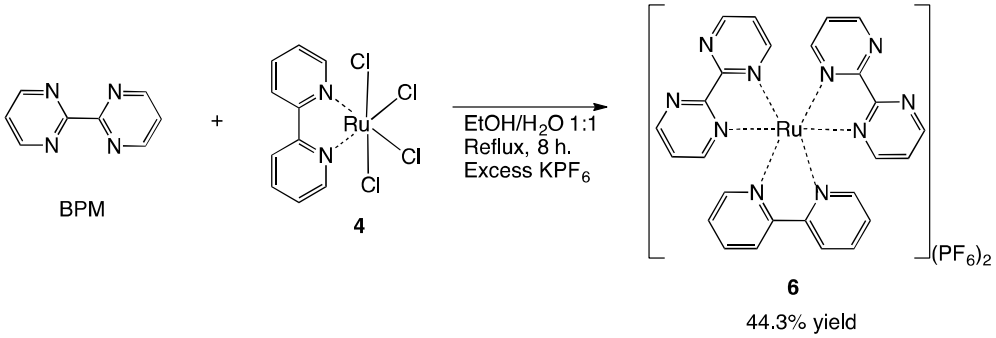

Compound **7** was made by adding BIM-H_2 to **9** and refluxing in ethanol for 3 h. A yield of 63.3% was obtained. ^{1}H NMR in acetone-d_6 showed five peaks present. Three of those are from the bipyridine ligand at 8.76, 8.15, and 7.52 ppm. While normally four peaks would be expected, in this compound two peaks overlap at 8.15 ppm. The other two peaks are from the imidazole, at 7.64 and 8.68 ppm. NH peaks were not observed in the NMR.

Scheme 2-12: Synthesis of **7**.

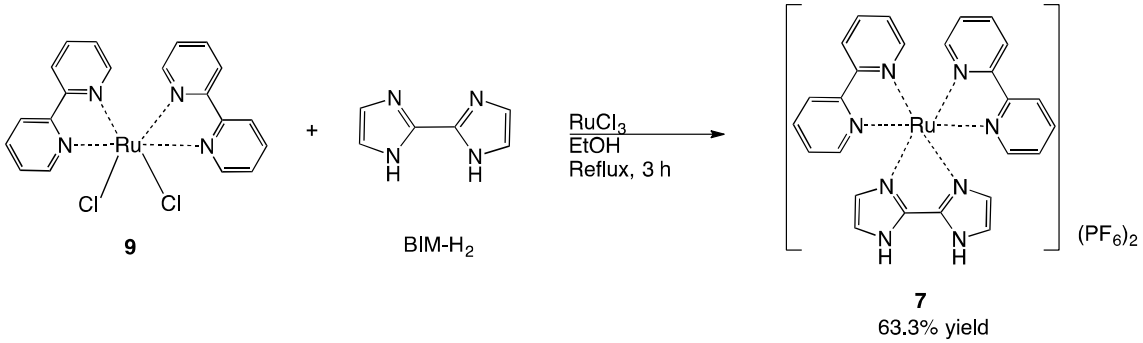

9 BIM-H_2 **7**
63.3% yield

Compound **8** was made in a manner similar to **7**, although a longer reaction time was needed. This reaction is seen in Scheme 2-13. The ^{1}H NMR showed total integration of 22 hydrogens, with eight peaks for the bipyridine ring and three for the bipyrimidine, as expected.

Scheme 2-13: Synthesis of **8**.

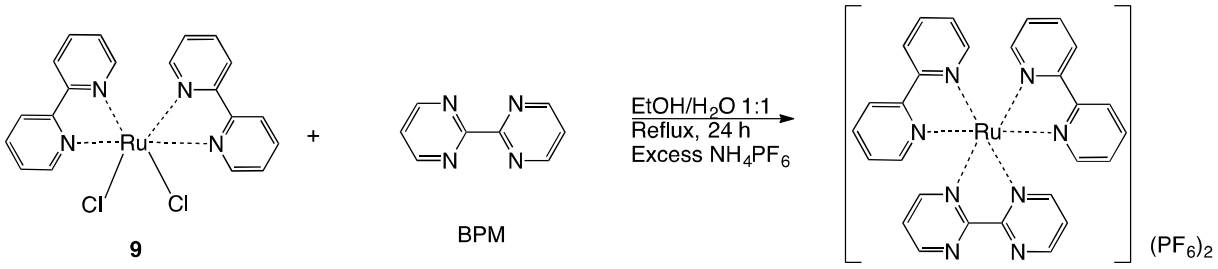

9 BPM **8**
86.1% yield

Synthesis of the diruthenium **11** and **12** were similar to each other and are shown in Schemes 2-14 and 2-15. NaOH was needed to deprotonate the NH groups on **7** before the reaction. These were both refluxed until a color change occurred in the solution. Compound **11** product was a dark red color while compound **12** was a green/brown color. The appearance of both BIM and BPM complexes match the color of the complexes seen in the literature.[12, 37] The

^{1}H NMR of the **11** displayed 36 hydrogens relative to the lowest integration peaks of 2H, which is consistent with symmetry along the Ru–Ru axis. There would be four diasteromers in all diruthenium complexes, which were not possible to separate. They hydrogens are expected to be chemically equivalent however. The ^{1}H NMR of **12** displayed 38 hydrogens relative to 2H signals, which is consistent with symmetry along the Ru-Ru axis.

Scheme 2-14: Synthesis of **11**.

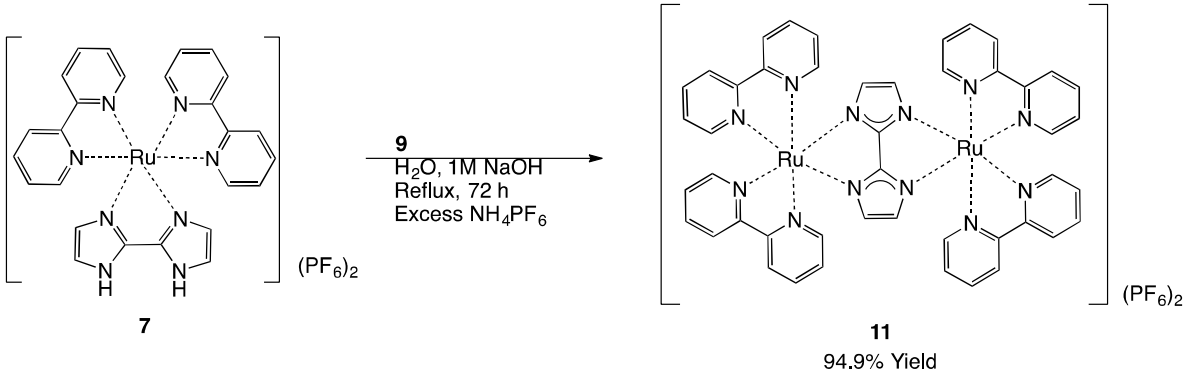

7 **11**
94.9% Yield

Scheme 2-15: Synthesis of **12**.

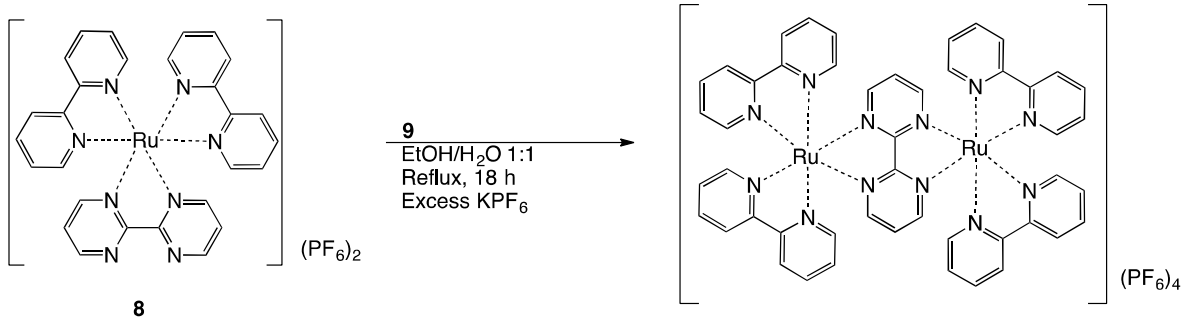

8 **12**
79.4% Yield

In order to test the ability of DHBPY to bind to the TiO_2 layer, **13** was synthesized as seen in Scheme 2-16 and was obtained in 56.6% yield. A 0.2 mM solution of **13** in acetonitrile was prepared and a TiO_2 electrode was soaked in the solution for 24 hours.[1] The solution, which was a dark orange/red color, left the TiO_2 layer an intensely colored orange after washing with ethanol and acetone, indicating that the complex was tightly bound.

Scheme 2-16: Synthesis of **13**.

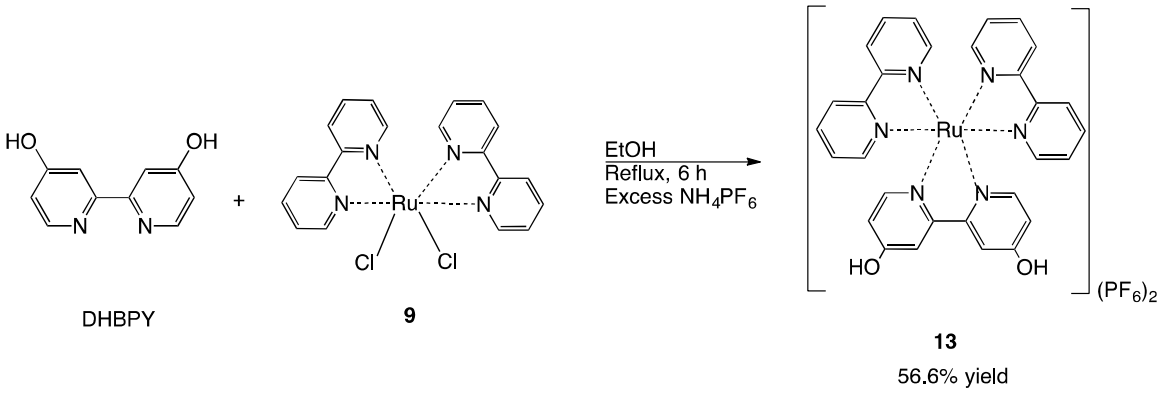

DHBPY **9** **13**

56.6% yield

Synthesis of **14** was achieved by refluxing TPPZ with $RuCl_3$ for two days as seen in Scheme 2-17.[3] A 43.3% yield was obtained and the product was a red/orange color.

[1] TiO_2 electrode preparation is reported in Chapter 5.

Scheme 2-17: Synthesis of **14**.

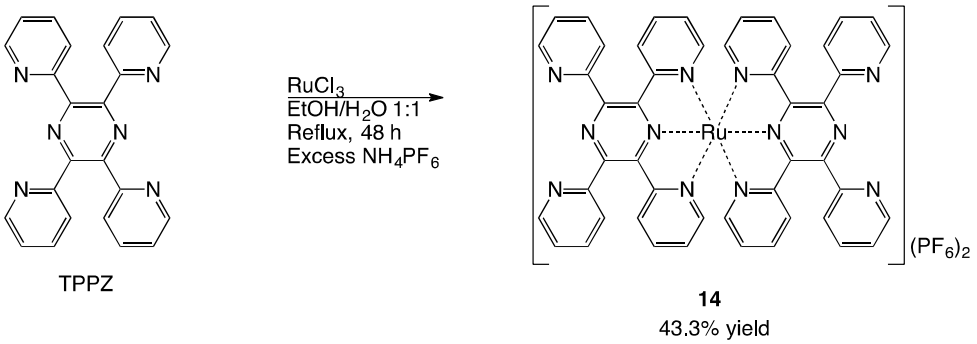

TPPZ

14
43.3% yield

TPPZ was also used as a bridging ligand to build a number of diruthenium products. Refluxing TPPZ in ethanol with two equivalents of $RuCl_3$ gave the diruthenium product **15**. This could be reduced from the Ru^{III}/Ru^{III} system to the Ru^{III}/Ru^{II} system, **16**, by refluxing with tetrabutylammonium chloride, lithium chloride and acetone.[8] The excess lithium chloride is used as a reducing agent. Alternatively, silver trifluoromethanesulfonate could be added to precipitate silver chloride making $(TfO)_3Ru(TPPZ)Ru(OTf)_3$, followed by addition of KSCN to make **17**. During the synthesis of N3, it was determined that the thiocyanate is bound to the ruthenium through the N bond as opposed to the S bond. While Grätzel reported two IR peaks for the cis product, 2126 and 2093 cm^{-1}, in **Black Dye** where three isothiocyanates are present, only one peak is seen at 2106 cm^{-1}.[44] The IR spectrum of **17** displayed a single peak at 2093 cm^{-1}. The IR spectrum of **17** also had a peak at 775 cm^{-1}, corresponding to C=S bending and a nitrogen bound isothiocyanate as in N3.

Scheme 2-18: Synthesis of **15**, **16**, and **17**.

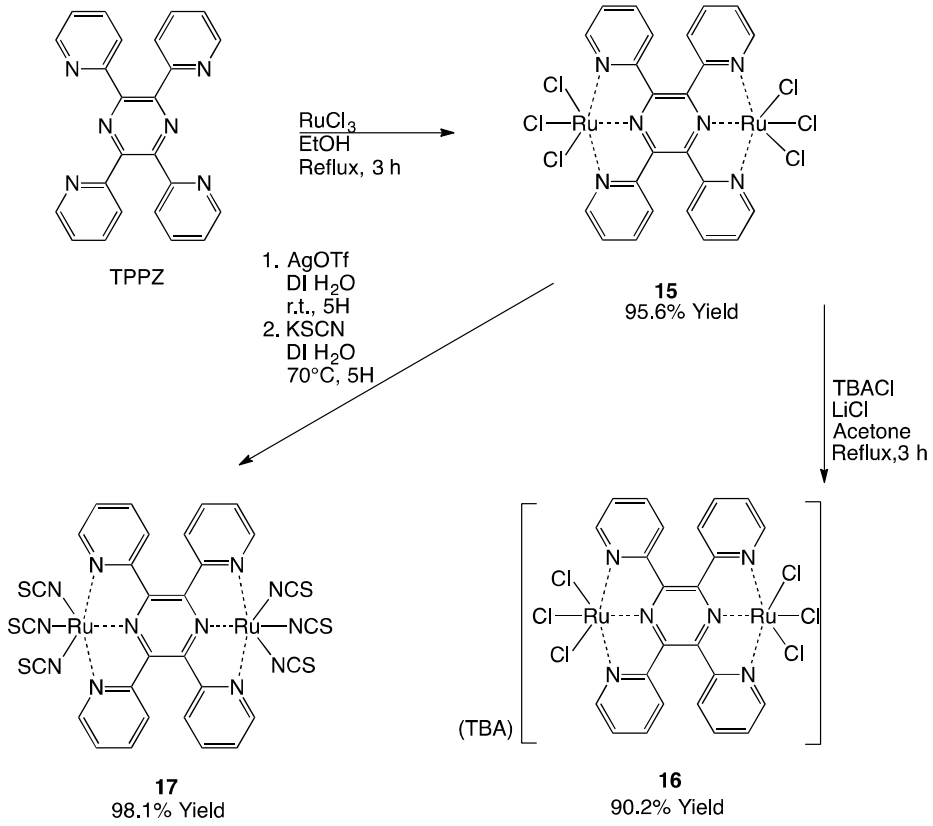

2.5 Conclusions

A wide variety of mono- and disubstituted complexes were prepared. Two new complexes were prepared, **10** which contains two DCBPY groups and a BPM which is capable of further metal addition, and **17**. The solar cell capability of these two complexes are reported in Chapter 5. ^{1}H NMR data for a number of mono- and diruthenium products were also obtained where none was available in the previous literature. Chapter 3 describes the attempts to combine these building blocks into triruthenium complexes along with a study on their ability to form mixed-valence compounds.

Chapter 3

Synthesis and characterization of triruthenium complexes and testing combinatorial synthesis on TiO_2

3.1 Introduction

In the previous chapter, the synthesis of a variety of mono- and diruthenium complexes was described. This chapter describes the attempts to combine these building blocks into triruthenium complexes for use as electron reservoirs.

Combinatorial chemistry has made it possible to make a large number of compounds, or libraries, out a large number of smaller different but similar molecules.[1] This makes it possible to make several large but different molecules, such as peptides or proteins, very rapidly. When performing reversible reactions under thermodynamic control, such as those often employed in coordination chemistry, the process is called dynamic combinatorial chemistry, DCC. Dynamic combinatorial chemistry has been used to make a wide variety of metal-ligand libraries.[2] Metal-ligands interactions in DCC require the ligand substitution to be fast, which often depends on factors such as the metal, charge, steric, and electronic properties of the ligands. Labile ligands tend to work best in DCC. The kinetics of this exchange depends on the ligand-field stabilization energy, the Jahn-Teller distortion, and ligand characteristics.[2] Figure 3-1 lists the water exchange rate constants (k) and mean lifetime (τ) in the first coordination sphere of metal ions at 25 °C.[2] At first glance, Ru^{III} and Ru^{II} species appear on the slower end of the water exchange process. Ruthenium complexes have been made via dynamic combinatorial chemistry previously, incorporating Ru-porphyrin complexes[3, 4] as well as triruthenium macrocycles such as the complex in Figure 3-2.[5] Iron tripeptide-bipyridine complexes have been made using dynamic combinatorial chemistry[6] but the ruthenium-bipyridne complexes to date have not had the favorable equilibrium required for dynamic combinatorial chemistry[7, 8] and ru-bipyridine complexes have been largely inert.[2] A combinatorial chemistry synthesis on titanium dioxide could not be found.

Figure 3-1: Water exchange rate constants (k) and mean lifetime (τ) in the first coordination sphere of metal ions at 25 °C.[5]

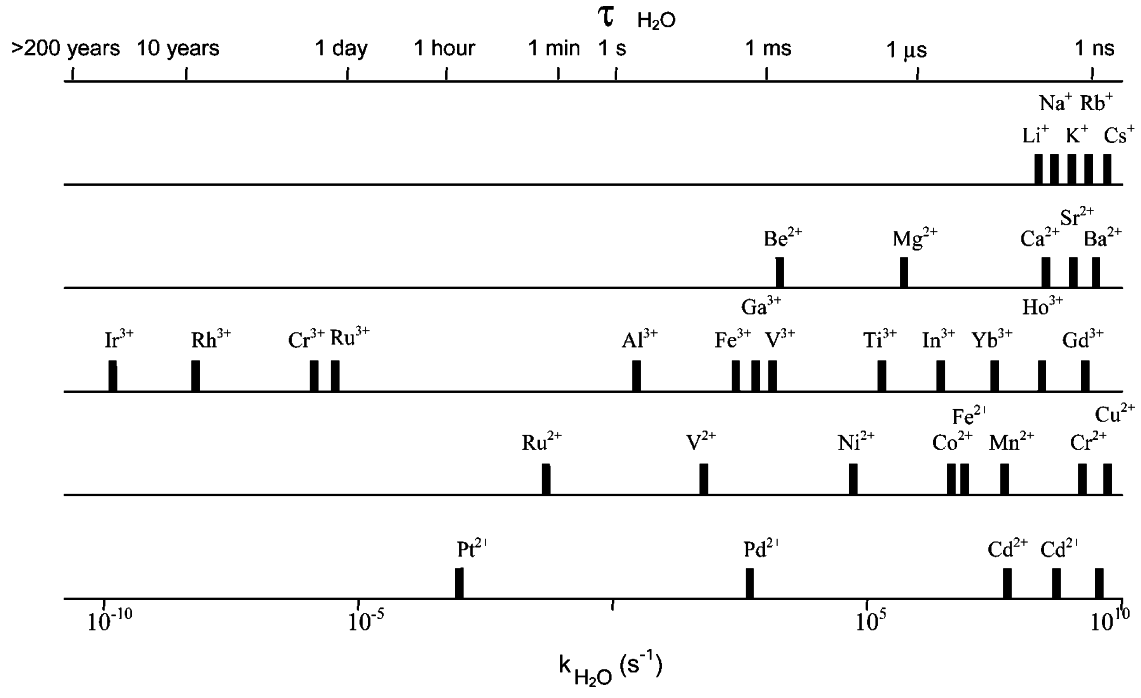

Figure 3-2: A triruthenium macrocycle made via dynamic combinatorial chemistry.

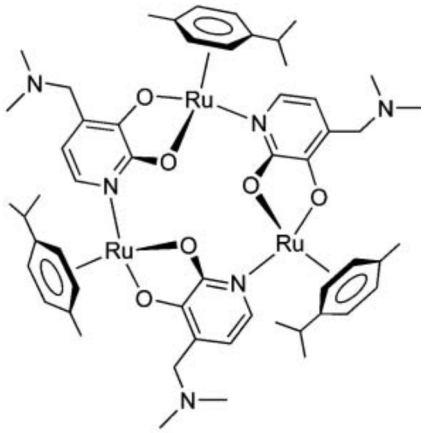

This chapter describes an attempt to use combinatorial chemistry to combine the building blocks made in Chapter 2 directly onto a titanium dioxide coated piece of glass as an attaching point. In the event that this was unsuccessful, traditional solution phase chemistry would be attempted to combine these building blocks. The ability to synthesize multi-metal complexes directly on the TiO_2 would speed up synthesis of the triruthenium molecules and also aid in the isolating and purifying of the complexes. It would also help building asymmetric molecules.

Figure 3-3: Generic diagram of a combinatorial chemistry procedure on TiO_2.

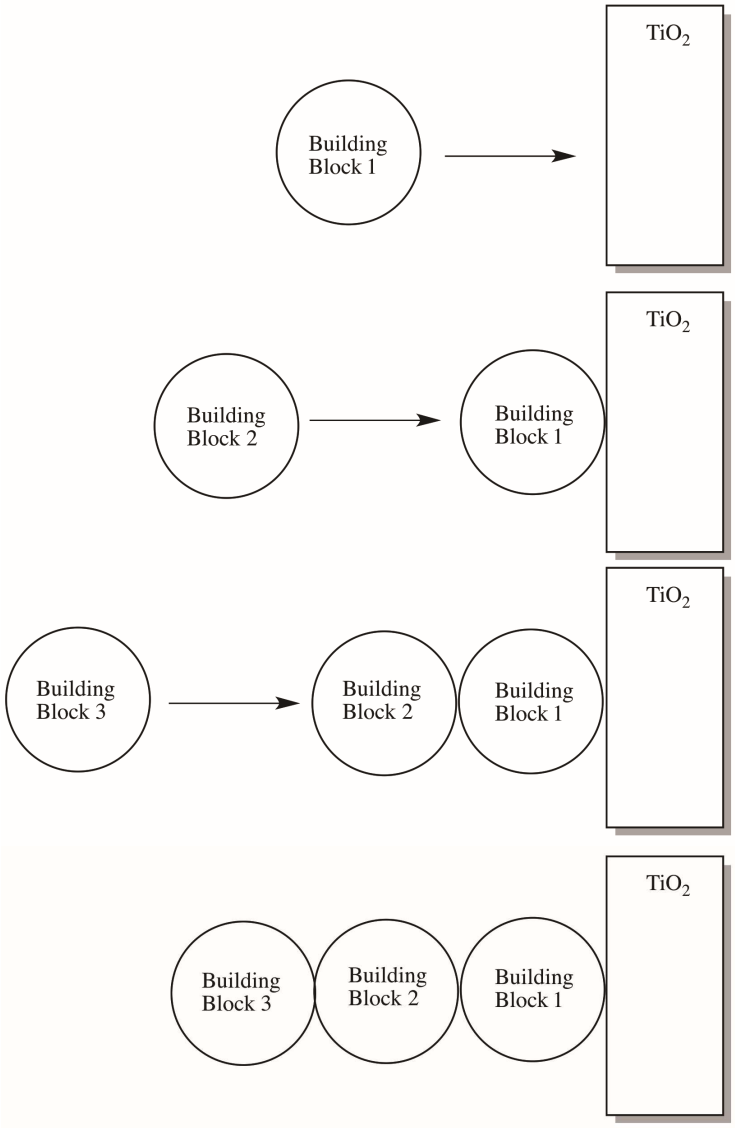

3.1.1 Triruthenium target molecules

In Chapter 2, a number of triruthenium frameworks were presented with different bridging ligands between the ruthenium centers. Figures 3-5 and 3-6 display target molecules containing the mixed BPM and TPPZ bridge system. Depending on where the attaching ligand is attached, the TPPZ bridge can be in closer proximity to the TiO_2 layer, as in Figure 3-4, or BPM can be in closer proximity to the TiO_2 as in Figure 3-5. The molecule in 3-4 can be made via combing an attaching ligand, **15** and **8**. The attaching ligand can be either DHBPY or DCBPY. The chlorines of **15** could eventually be replaced with NCS as in **N3** and **Black Dye**.

Figure 3-4: Potential triruthenium targets with a TPPZ and BPM bridge and the attaching ligand closer to the TPPZ bridge.

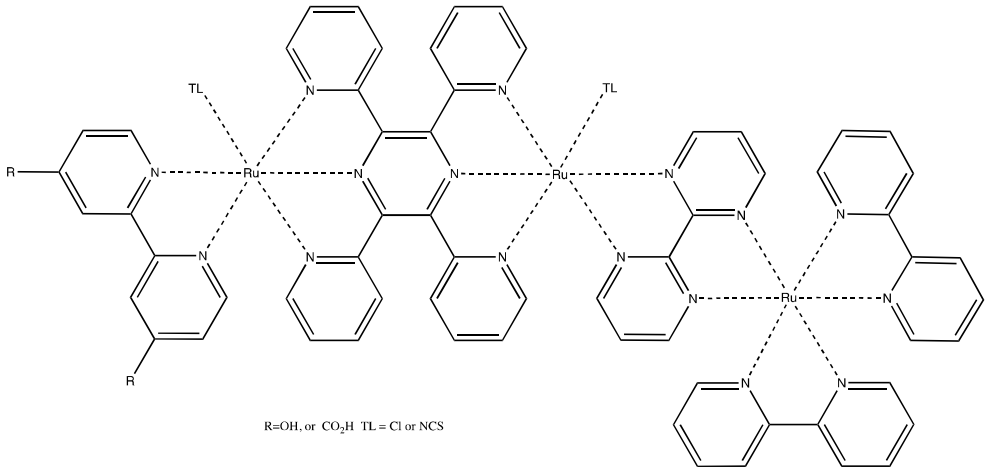

The complexes in Figure 3-5 could be made by combining **10** or $(DHBPY)_2RuCl_2$, and **15**. As before, the attaching ligands might be DHBPY or DCBPY. The chlorines could also be replaced with NCS.

Figure 3-6 displays the target complexes with two BIM bridges. In this example, one side would have attaching ligands DHCBPY or DHBPY and the other side would have BPY

ligands attached. These complexes could be made by joining the building blocks $(DHBPY)_2RuCl_2$ or **2** with **5**, and **9**.

Figure 3-5: Potential triruthenium targets with a TPPZ and BPM bridge and the attaching ligands closer to the BPM bridge.

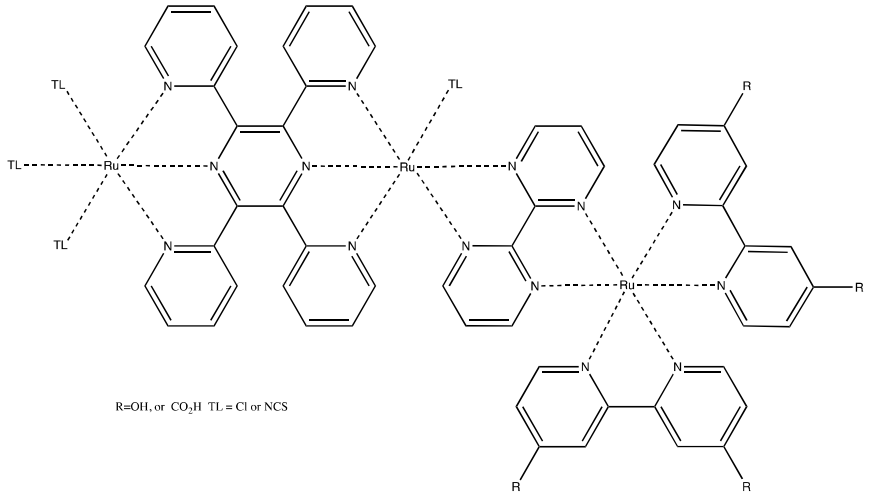

Figure 3-6: Potential triruthenium targets with two BIM bridges.

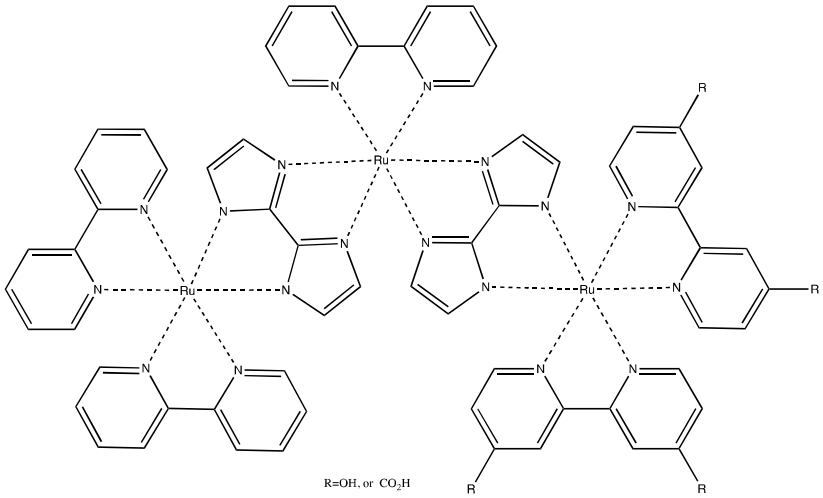

Figure 3-7 displays the target complexes with two BPM Bridges. As in the double BIM bridged complexes, the attaching ligands would be DHCBPY or DHBPY. These could be made by combing the building blocks $(DHBPY)_2RuCl_2$ or **2** with **6**, and **9**. A double TPPZ bridge like the one seen in Figure 3-8 could be made with the building blocks DHBPY or DCBPY with **14** and two additions of $RuCl_3$.

Figure 3-7: Potential triruthenium targets with two BPM bridges.

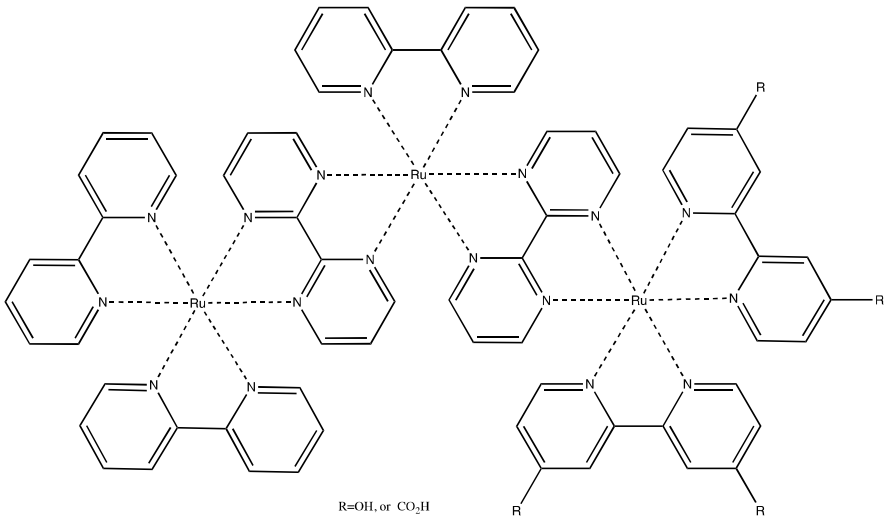

Figure 3-8: Potential triruthenium targets with two TPPZ bridges.

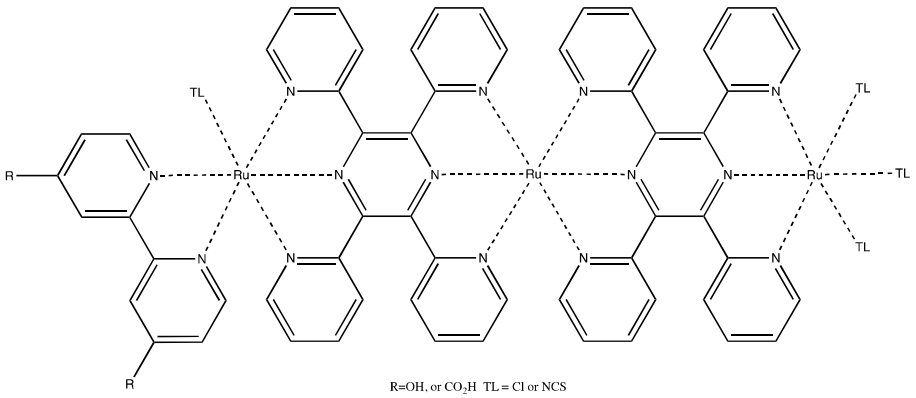

The remainder of this chapter describes the attempts to creating tri-ruthenium complexes via combinatorial synthesis on TiO_2 and solution phase synthesis of a number of tri-ruthenium complexes.

3.2 Experimental

All reactions were carried out under an atmosphere of dry nitrogen or in a glovebox unless otherwise noted. All NMR spectra were run using a 300 or 400 MHz Bruker NMR. All UV/Vis measurements were performed on a Perkin Elmer Lambda 950 UV/Vis spectrometer. All IR measurements were taken on a Thermo Nicolet IR200 FT-IR.

3.2.1 Synthesis of bis(2,2'-bipyridine)ruthenium(II)-μ-(2,2'-bipyrimidine)chlororuthenium(III)-μ-(2,3,5,6-tetra-(2-pyridyl)pyrazine)trichlororuthenium(III) hexafluorophosphate, 18

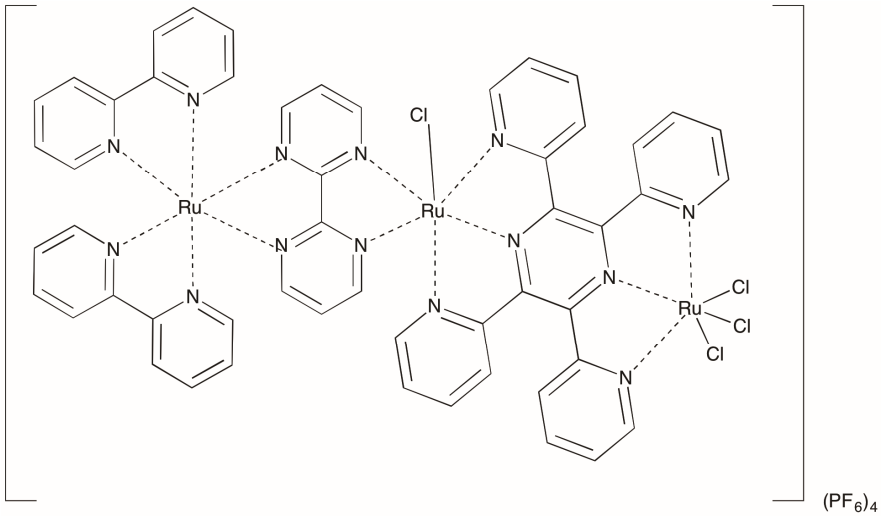

To a mixture of EtOH/H_2O (50 mL, 2:1), **8** (0.200 g, 0.232 mmol) and **15** (0.181 g, 0.244 mmol) were added. The mixture was refluxed for 6 h. After cooling to room temperature, the EtOH was removed in vacuo and a saturated aqueous solution of NH_4PF_6 (10 mL) was added to create a dark green/black ppt. The solid was collected by vacuum filtration and rinsed with three portions of 10 mL of diethyl ether. A total of 0.331 g was collected for a yield of 66%. The solid was placed on a high vacuum line for 12 h. ^{1}H NMR (300 MHz, acetone-d_3): δ 9.30-7.00 (m, broad) It is believed that the paramagnetic Ru(III) caused significant line broadening; UV (EtOH) λ_{max} 245, 290, 399, 610 nm.

3.2.2 Synthesis of bis(2,2'-bipyridine)ruthenium(II)-μ-(2,2'-bipyrimidine)chlororuthenium(III)-μ-(2,3,5,6-tetra-(2-pyridyl)pyrazine)chloro(4,4'-dihydroxy-2,2'-bipyridine)ruthenium(III) hexafluorophosphate, 19

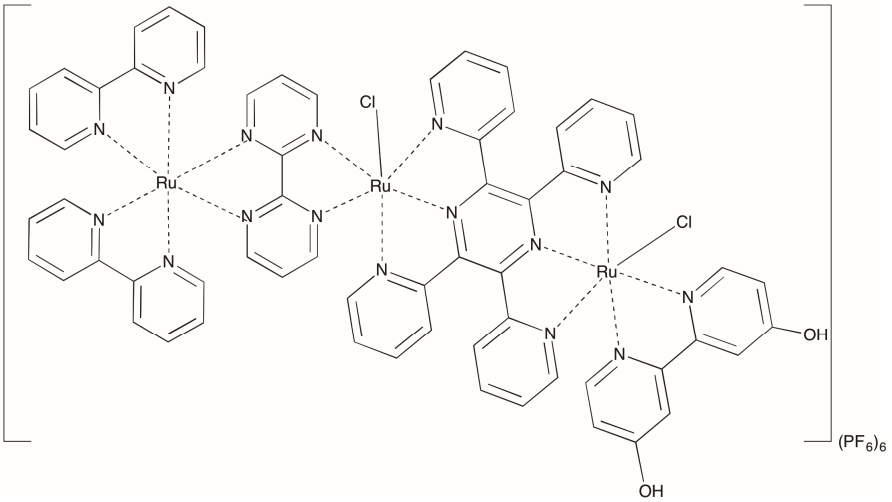

To a mixture of EtOH/H_2O (25 mL, 2:1), **18** (0.163 g, 0.0695 mmol) and DHBPY (0.0188 g, 0.0793 mmol) were added. The mixture was heated under reflux for 6 h. The EtOH was removed in vacuo, and a saturated aqueous solution of NH_4PF_6 (10 mL) was added to create a dark green/dark black ppt. The solid was collected by vacuum filtration and rinsed with three portions of 10 mL of diethyl ether. A total of 0.126 g was collected for a yield of 79%. The solid was placed on a high vacuum line for 12 h. ^{1}H NMR (300 MHz, acetonitrile-d_3): δ 9.30-7.00 (m, broad), 5.85 (t, J = 45 Hz) It is believed that the paramagnetic Ru(III) caused significant line broadening as it had an appearance of a very broad triplet spanning 2 ppm. It was nearly identical to **18** except for the appearance of a new triplet at 5.85 ppm with a J value of around 45 Hz (which appears to be from the OH groups on DHBPY) which has been significantly broadened due to the Ru (III); UV (EtOH) λ_{max} 245, 290, 399, 610 nm.

3.2.3 Synthesis of bis(2,2'-bipyridine)ruthenium(II)-μ-(2,2'-bipyrimidine)chlororuthenium(III)-μ-(2,3,5,6-tetra-(2-pyridyl)pyrazine)chloro(4,4'-dicarboxy -2,2'-bipyridine)ruthenium(III) hexafluorophosphate, 20

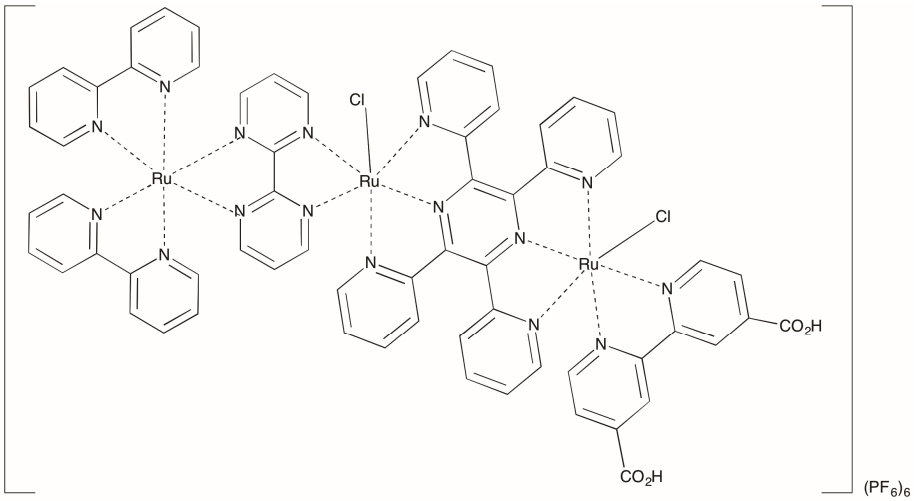

To a mixture of EtOH/H_2O (25 mL, 2:1), **18** (0.154 g, 0.0695 mmol) and DCBPY (0.0174 g, 0.0794 mmol) were added. The mixture was heated under reflux for 6 h. The EtOH was removed in vacuo and a saturated aqueous solution of NH_4PF_6 (10 mL) was added to create a dark black ppt. The solid was collected by vacuum filtration and rinsed with three portions of 10 mL of diethyl ether. A total of 0.0785 g was collected for a yield of 75%. The solid was placed on a high vacuum line for 12 h. ^{1}H NMR (300 MHz, acetonitrile-d_3): δ 9.30-7.00 (m, broad) It is believed that the paramagnetic Ru(III) caused significant line broadening as it had an appearance of a very broad triplet spanning 2 ppm; UV (EtOH) λ_{max} 205, 249, 295, 390, 605 nm.

3.2.4 Synthesis of bis(4,4'-dicarboxy-2,2'-bipyridine)ruthenium(II)-μ-(2,2'-bipyrimidine)isothiocyanateruthenium(III)-μ-(2,3,5,6-tetra-(2-pyridyl)pyrazine)triisothiocyanateruthenium(III) hexafluorophosphate, 21

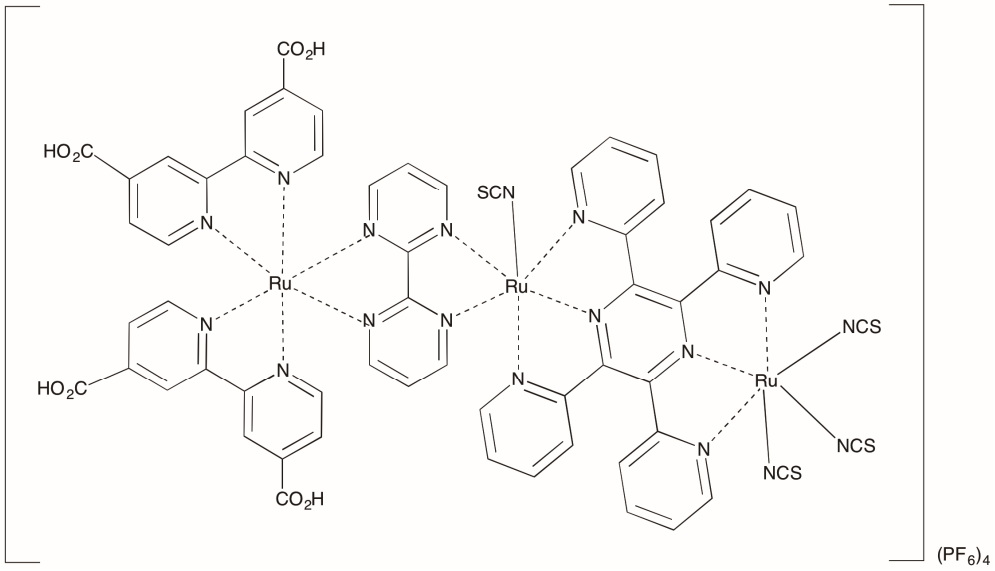

To a solution of **15** (0.152g, 0.189 mmol) in H_2O (100 mL) was added AgOTf (0.533 g, 2.07 mmol). The mixture was stirred at 70 °C for 5 h. The blue solution was then filtered to remove the excess AgCl. To this solution was added **10** (0.254 g, 0.191 mmol) and 0.1 M NaOH until the pH reached 10. The mixture was heated at 70 °C for 72 h. During this time, the solution changed from blue to a dark red/purple color. After 72 h, KSCN (0.425 g, 4.37 mmol) was added and the solution was stirred for another 24 h. After this 24 h, 1 M HCl was added until the pH reached 4 and then excess NH_4PF_6 was added. After cooling, dark red/purple solid was collected by vacuum filtration and this was rinsed with 3 portions of 10 mL of ether. A total of 0.274 g was collected for a yield of 67%. The ^{1}H NMR was not very clear due to the product being paramagnetic and no peaks were seen. IR (cm^{-1}): 3030, 2107, 1888, 1591, 1419, 1352, 1191, 775; UV (EtOH) λ_{max} 446, 605 nm.

3.2.5 Synthesis of bis(trichlororuthenium(III)-μ-(2,3,5,6-tetra-(2-pyridyl)pyrazine))ruthenium(II) hexafluorophosphate, 22

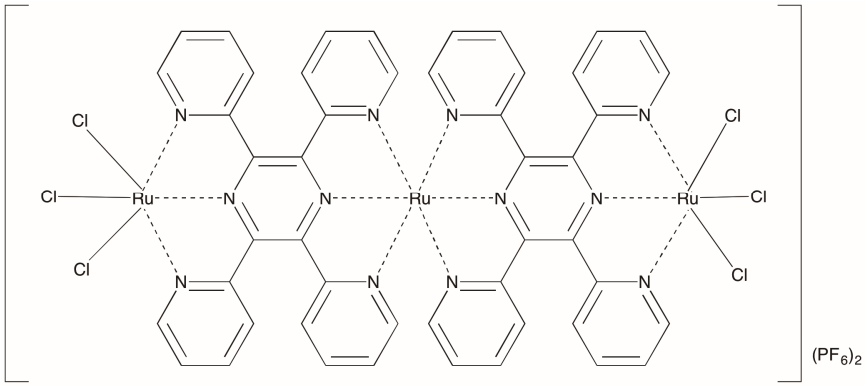

To a solution of acetone/EtOH (1:1, 100 mL) was added **14** (0.2663 g, 0.2195 mmol) and $RuCl_3$ (0.1493 g, 0.7198 mmol). This was refluxed for 48 h under nitrogen. After cooling, a blue precipitate was found in the flask. This was collected by vacuum filtration and rinsed with 3 portions of 10 mL of ether. A total of 0.300 g was collected for a yield of 87%. The ^1H NMR was not very clear due to the product being paramagnetic and no peaks were seen. IR (cm^{-1}): 3339, 3025, 1593, 1415, 1357, 1298, 1245, 1188, 1158, 1101, 778; UV (EtOH) λ_{max} 473, 599, 668 nm.

3.2.6 Synthesis of bis(bis(2,2'-bipyridine)ruthenium(II)-μ-(2,2'-bipyrimidine))(2,2'-bipyridine)ruthenium(II) hexafluorophosphate, 23

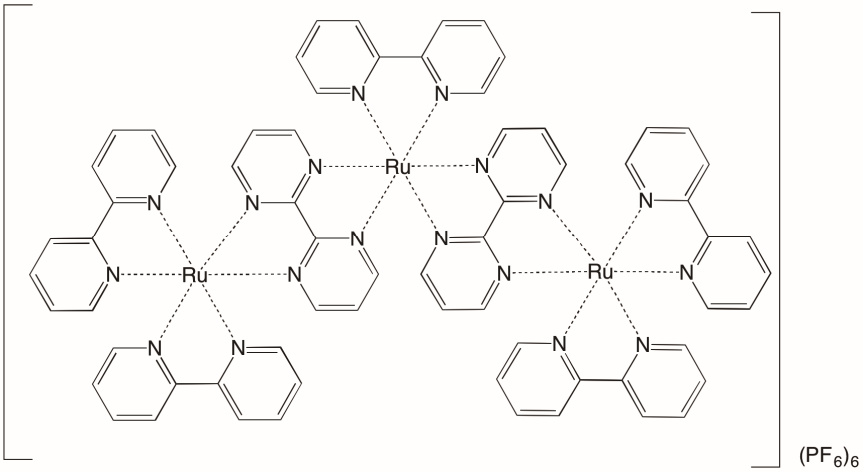

To a solution of acetone/EtOH (1:1, 50 mL) was added **6** (0.153 g, 0.177 mmol) and **9** (0.200 g, 0.412 mmol) and the mixture was then heated under reflux for 72 h. Column chromatography was performed on alumina using an eluent mixture of 100:10:1 $CHCl_3$:MeOH:NH_3. After collecting the product, 10 mL of a saturated NH_4PF_6 solution was added to precipitate an olive green/black solid and this was collected by vacuum filtration. This solid was dissolved in acetone and then re-precipitated by addition of ether. The olive green/black solid was again collected by vacuum filtration and rinsed with 3 portions of 10 mL ether. A yield of 43% was obtained. ^{1}H NMR (300 MHz, acetone-d_6): δ 8.57 (m), 8.07 (m), 7.31 (m); IR (cm^{-1}): 3110, 3090, 2958, 2929, 2859, 1727, 1604, 1466, 1448, 1422, 1404, 1272, 1123, 1072, 839, 768, 728, 557; UV (EtOH) λ_{max} 495, 575, 675 nm.

3.2.7 Synthesis of bis(bis(4,4'-dicarbethoxy-2,2'-bipyridine)ruthenium(II)-μ-(2,2'-bipyrimidine))(2,2'-bipyridine)ruthenium(II) hexafluorophosphate, 24

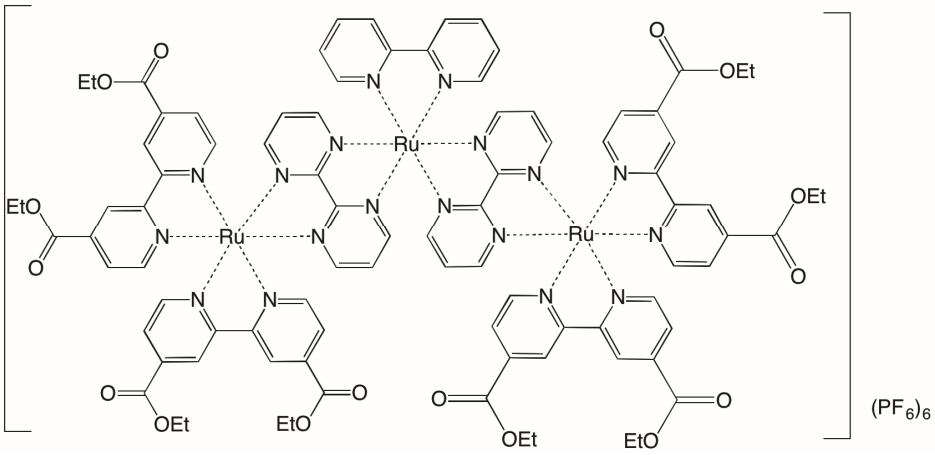

To a solution of acetone/EtOH (1:1, 50 mL) was added **6** (0.0520 g, 0.0602 mmol). To this was added **3** (0.0765 g, 0.122 mmol) and the mixture was then heated under reflux for 72 h. Column chromatography was performed on alumina using an eluent mixture of 100:10:1 $CHCl_3$:MeOH:NH_3. After collecting the product, 10 mL of a saturated NH_4PF_6 solution was added to precipitate an olive green/black solid and this was collected by vacuum filtration. This solid was dissolved in acetone and then re-precipitated by addition of ether. The olive green/black solid was again collected by vacuum filtration and rinsed with 3 portions of 10 mL ether. A total of 0.117 g was collected for a yield of 68%. ^{1}H NMR (300 MHz, acetone-d_6): 9.23 (m, 6H), 8.83 (d, J = 8.0, 6H), 8.73 (dd, J = 8.0, 2.0, 2H), 8.47 (m, 4H), 8.23 (m, 12H), 8.0 (m, 2H), 7.77 (m, 6H), 7.62 (m, 6H), 4.48 (m, 16H), 1.75 (m, 24H); IR (cm^{-1}): 3080, 2950, 2850, 1720, 1611, 1550, 1406, 1230, 1129, 1019, 898, 840, 768, 768, 719, 675, 557, 496; UV (EtOH) λ_{max} 563 nm.

3.2.8 Synthesis of bis(bis(2,2'-bipyridine)ruthenium(II)-μ-(2,2'-biimidazole))(2,2'-bipyridine)ruthenium(II) hexafluorophosphate, 25

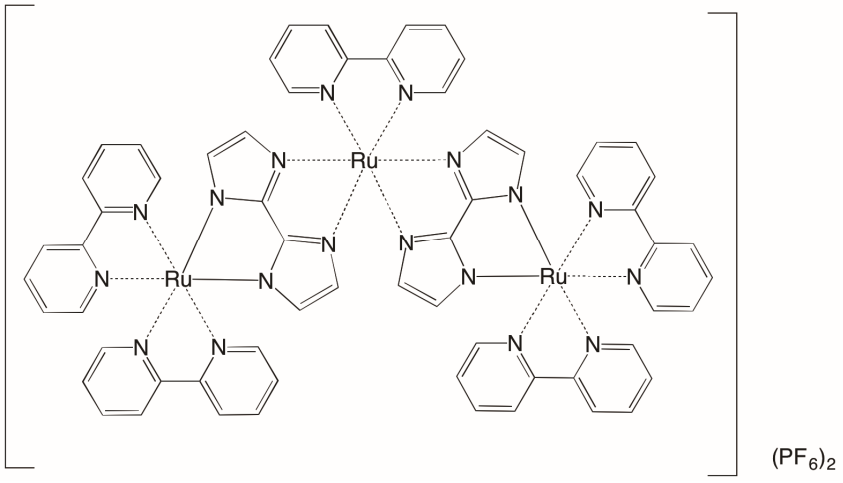

To a solution of acetone/EtOH (1:1, 50 mL) was added **5** (0.136 g, 0.1670 mmol) and NaOH (0.0432 g, 1.08 mmol). This was stirred at room temperature for 10 min. To this was added **9** (0.182 g, 0.376 mmol) and the mixture was then heated under reflux for 72 h. Column chromatography was performed on alumina using an eluent mixture of 100:10:1 $CHCl_3$:MeOH:NH_3. After collecting the product, 10 mL of a saturated NH_4PF_6 solution was added to precipitate a red/purple solid and this was collected by vacuum filtration. This solid was dissolved in acetone and then re-precipitated by addition of ether. The red/purple solid was again collected by vacuum filtration and rinsed with 3 portions of 10 mL ether. A total of 0.192 g was collected for a yield of 70%. ^{1}H NMR (300 MHz, acetone-d_6): δ 8.58 (m), 8.05 (m), 7.39 (m); IR (cm^{-1}): 3114, 3090, 1602, 1465, 1445, 1420, 840, 761, 728, 657, 559; UV (EtOH) λ_{max} 465, 510 nm.

3.2.9 Synthesis of bis(bis(4,4'-dicarboethoxy-2,2'-bipyridine)ruthenium(II)-μ-(2,2'-biimidazole))(2,2'-bipyridine)ruthenium(II) hexafluorophosphate, 26

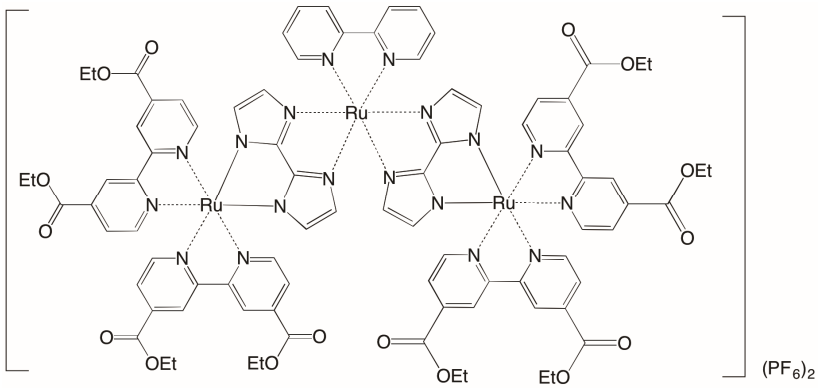

To a solution of acetone/EtOH (1:1, 50 mL) was added **5** (0.0533 g, 0.0654 mmol) and NaOH (0.0160 g, 0.401 mmol). This was stirred at room temperature for 10 min. To this was added **23** (0.100 g, 0.129 mmol) and the mixture was then heated under reflux for 72 h. Column chromatography was performed on alumina using an eluent mixture of 100:10:1 $CHCl_3$:MeOH:NH_3. After collecting the product, 10 mL of a saturated NH_4PF_6 solution was added to precipitate a red/purple solid and this was collected by vacuum filtration. This solid was dissolved in acetone and then re-precipitated by addition of ether. The red/purple solid was again collected by vacuum filtration and rinsed with 3 portions of 10 mL ether. A total of 0.132 g was collected for a yield of 71%. ^{1}H NMR (300 MHz, DMSO-d_6): δ 9.30-6.70 (m, 40 H), 4.47 (m, 16H), 1.43 (m, 24H); IR (cm^{-1}):3384 (br), 3030, 1716, 1603, 1541, 1405, 1363, 1313, 1260, 1231, 842, 766; UV (EtOH) λ_{max} 465, 505 nm.

3.3 Results and Discussion

3.3.1 Combinatorial synthesis of triruthenium complexes on TiO_2

To see if triruthenium complexes could be made via combinatorial synthesis on TiO_2, synthesis of **19** and **20** on TiO_2 was attempted. Both of these began with solution phase synthesis which began with the creation of a common building block **18**. This is outlined in Scheme 3-1. After **18** was made, either DCBPY or DHBPY to a solution **18** to create the respective triruthenium complexes. This is outline in Scheme 3-2. Both compounds were a dark green/black color.

Scheme 3-1: Synthesis of **18**.

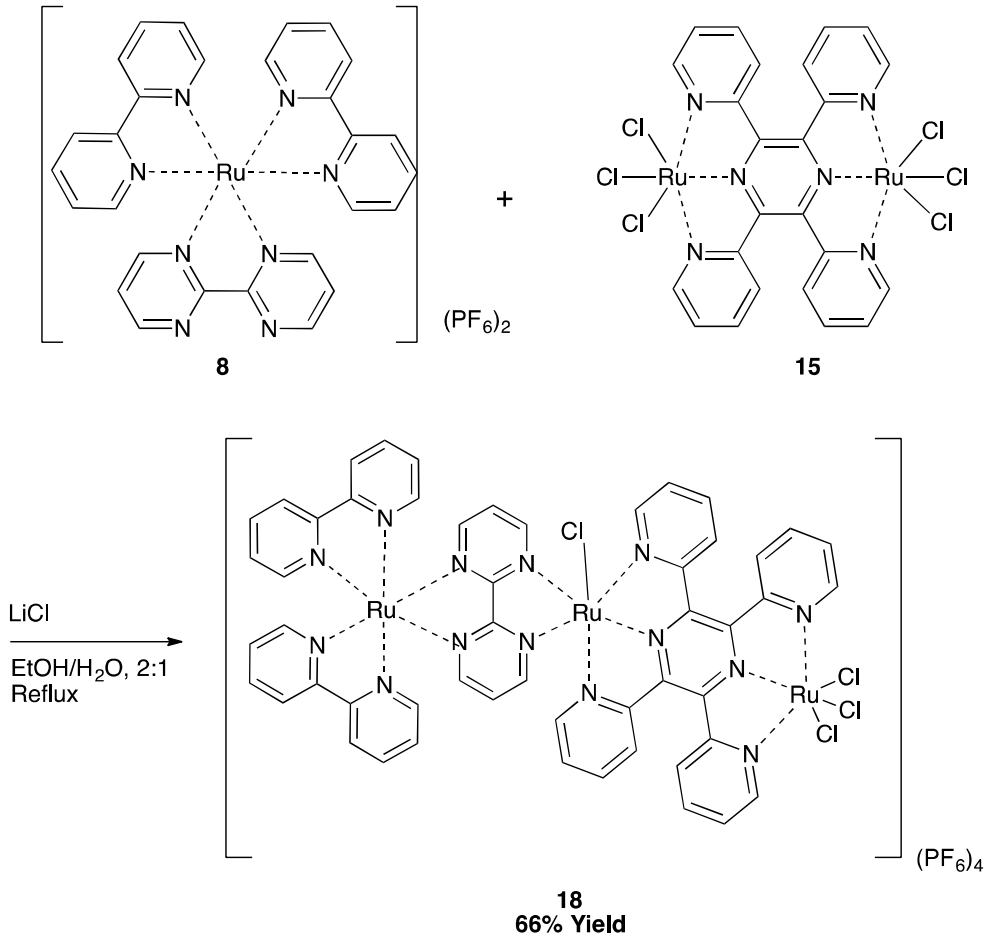

8 + **15** → **18**
66% Yield

Scheme 3-2: Synthesis of **19** and **20.**

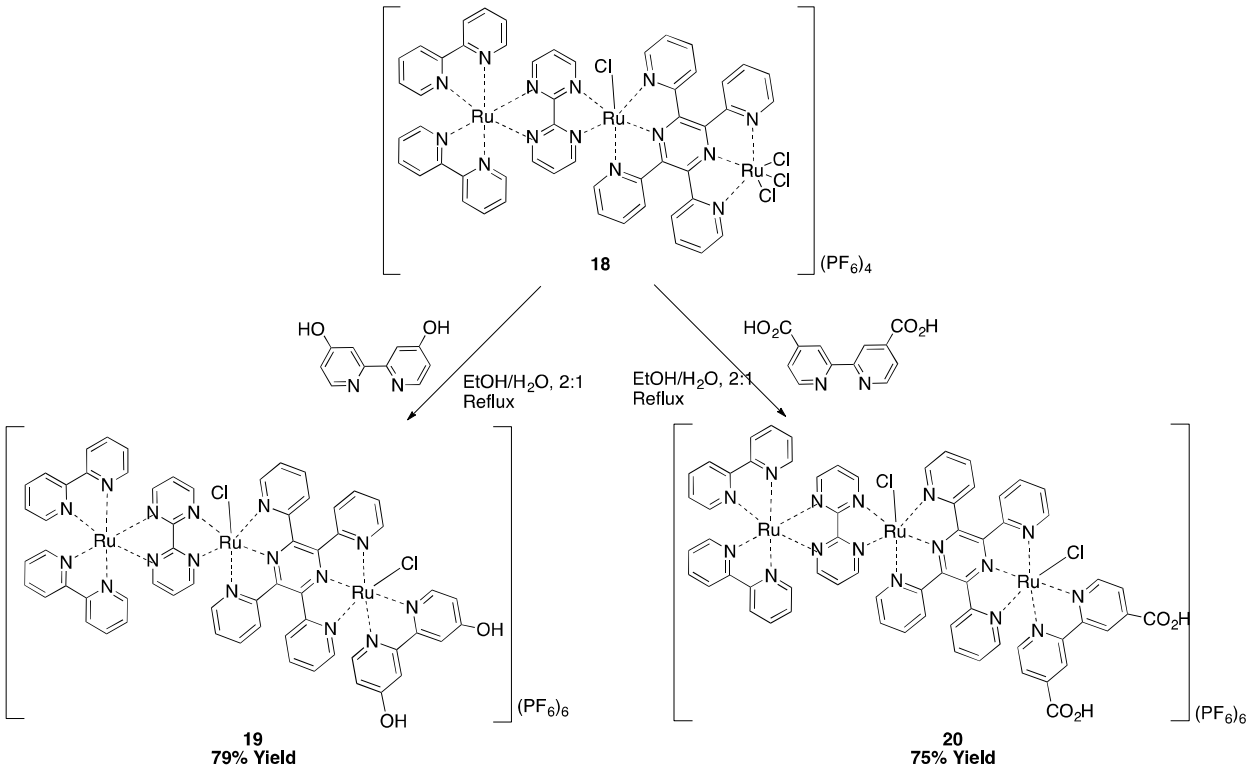

Monitoring the by ^{1}H NMR was difficult, as there was paramagnetic ruthenium (III) in both the reactants and products. Also, triruthenium complexes tend to have very low solubility in most solvents, which results in a low signal to noise ratio. ^{13}C NMR was also performed on each sample, but in most cases, no peaks appeared after eight hours of scanning. It is likely the low concentrations and low signal to noise ratio are the cause. This was also true for the remaining triruthenium complexes in this chapter.

UV-Vis was used to monitor the reaction, since solid state UV-Vis can be used to monitor the progress of the combinatorial synthesis on the TiO_2. The UV-Vis spectrum of the starting materials and products of the **18** synthesis is seen in Figure 3-9. The peaks at 399 and 610 nm were roughly the same as those in **15**, except the 399 peak was red shifted around 30 nm and the 610 nm peak was blue shifted by about the same amount. These peaks are from the π orbital absorptions of TPPZ and the MLCT absorptions respectively. Replacing two of the

chlorine ligands with **8** would likely decrease the electron density on one of the rutheniums attached to the TPPZ, likely causing these changes.

Figure 3-9: The UV-Vis spectra of the reactants and products involved in the synthesis of **18**.

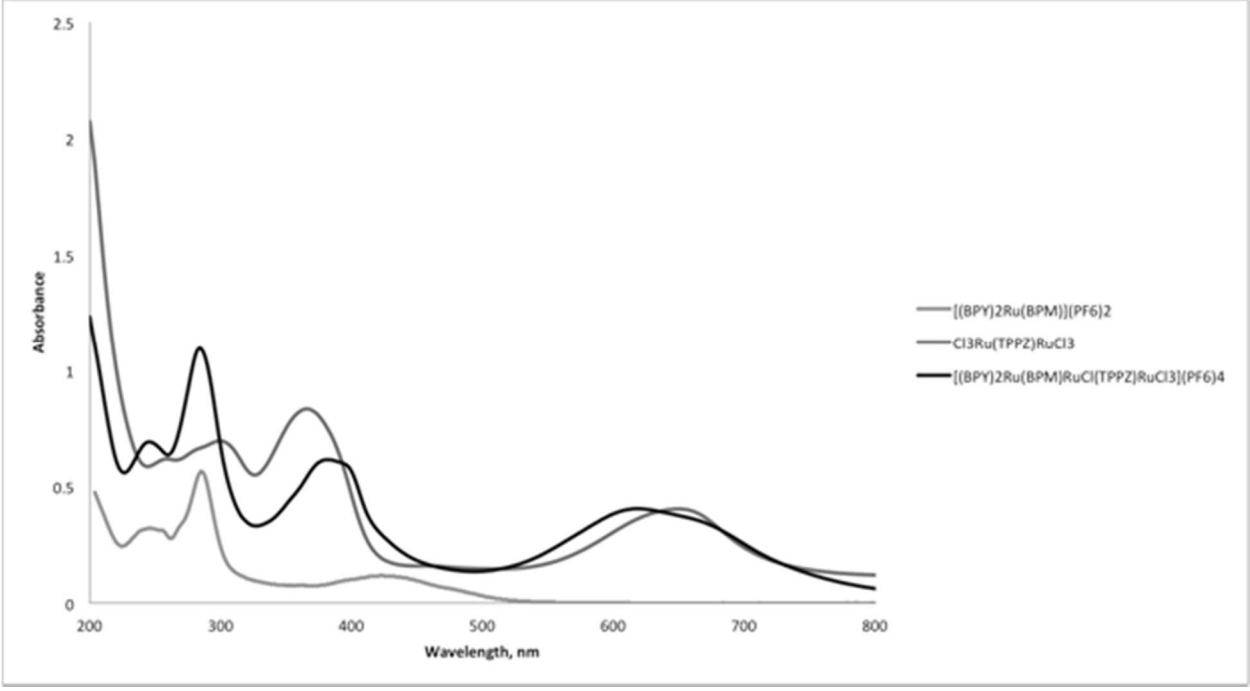

The UV-Vis spectra of **19** and **20** are seen in Figure 3-10. The only major difference between the two is the presence of a peak at 235 nm in **20**. Electron withdrawing groups, like the carboxylic acid group on DCBPY, are known the cause red shifts in aromatic rings. In all three complexes, there is a shoulder at roughly 675 nm. This is a common feature in triruthenium complexes and it is attributed to a higher population of singlet-triplet transitions, which are seen when the number of metal centers is greater than two.[9]

Figure 3-10: The UV-Vis spectra of **18, 19,** and **20**.

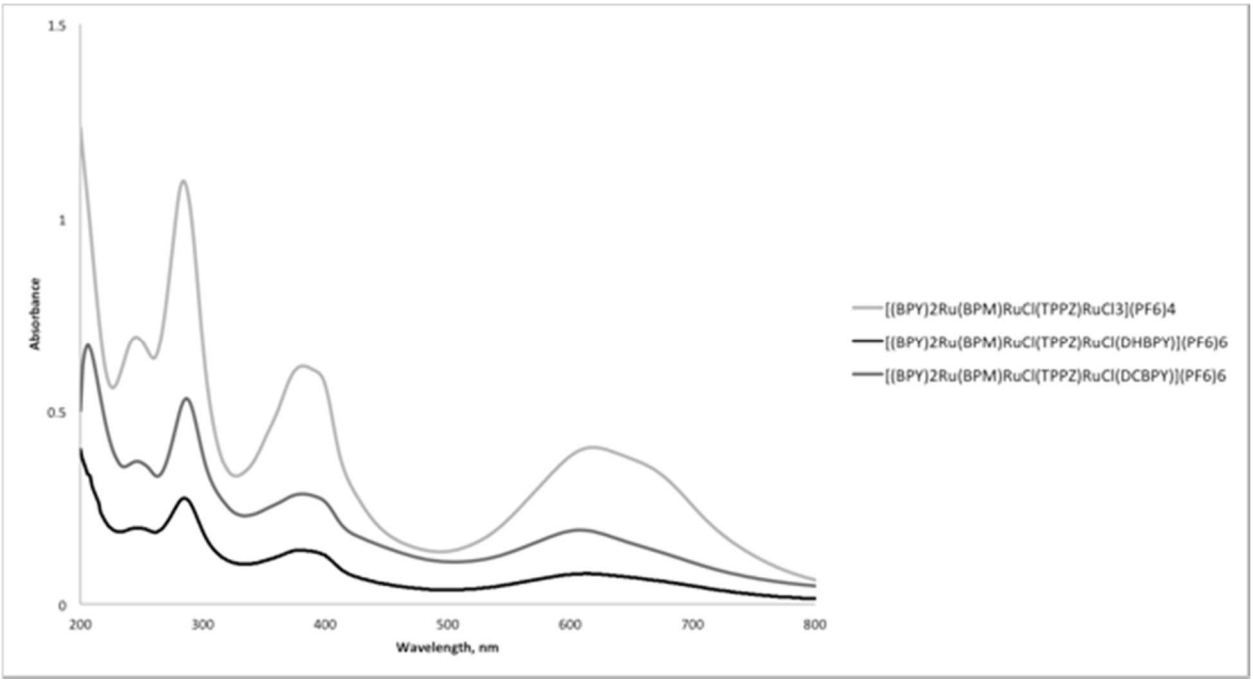

Combinatorial synthesis of **19** began by adding DHBPY to the TiO_2, followed by **15**, and finally **8**. This was initially performed using the same conditions as the solution phase synthesis, EtOH/H_2O in a 2:1 ratio. The solid state UV-Vis results are seen in Figure 3-11. There was no presence of the building blocks in the UV-Vis. The TiO_2 plate appeared to degrade during the course of the synthesis and no major color changes were seen. It was assumed the boiling solvent was causing the TiO_2 to degrade. This was problematic as higher temperatures are needed for the reaction.

Figure 3-11: Solid state UV-Vis of the first attempt at combinatorial synthesis of **19** on TiO_2.

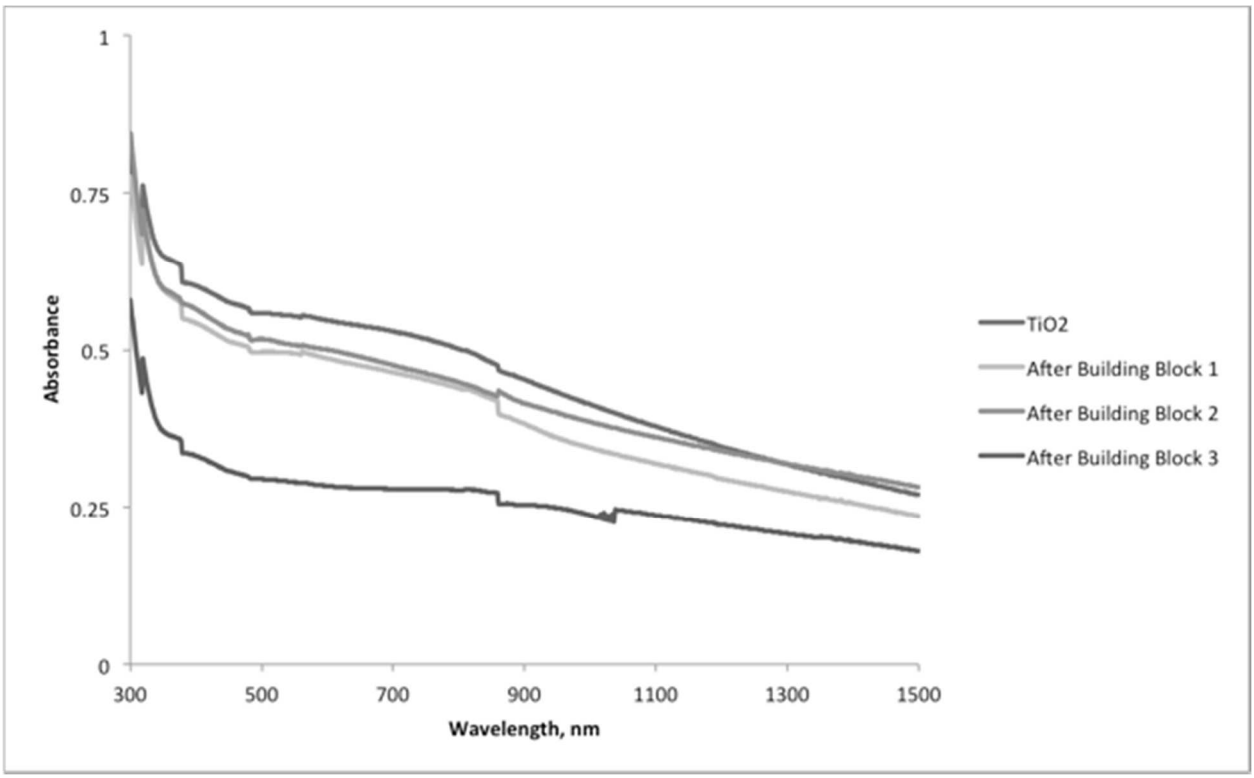

In order to get perform the reaction at lower temperature, the chlorines of **15** were replaced with triflates. The combinatorial synthesis of **19** was attempted again at both 20 °C and 50 °C in the exact same manner as before, except $(TfO)_3Ru(TPPZ)Ru(OTf)_3$ was used as the second building block. The results were the same as before, the TiO_2 appeared to degrade and tiny holes appeared in the TiO_2 layer. No noticeable attachment of the building blocks was seen. The final UV-Vis results of the second combinatorial attempt are seen in Figure 3-12. There was no major difference between the 20 °C and 50 °C trials. There is also no apparent absorption around 600 nm, which typically results from the MLCT transitions in ruthenium polypyridine complexes. A TiO_2 electrode was soaked in **19** to use as a frame of reference. The UV-Vis of this electrode, in addition to a solution phase UV-Vis of **19**, is included in Figure 3-12. The absorption of the triruthenium complex while on TiO_2 is red shifted slighted, which is common for ruthenium complexes on TiO_2.[10]

Figure 3-12: Solid state UV-Vis of the second attempt at combinatorial synthesis of **19**.

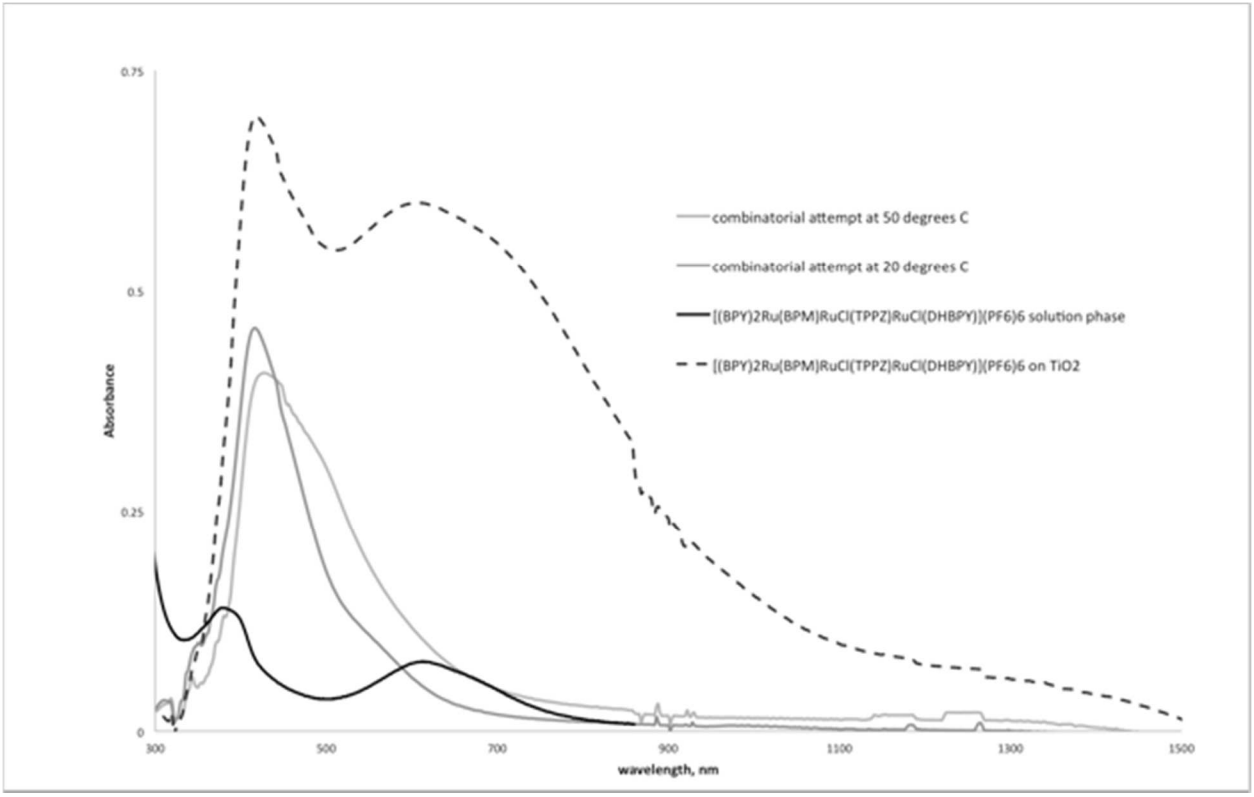

In section 3.1, it was mentioned that ruthenium-bipyrdine complexes are largely inert and have not been successfully used in dynamic combinatorial chemistry due to their slow ligand substitutions. It is likely the case with these complexes as well, as not evidence of a reaction was seen, even with highly labile triflate groups on the ruthenium centers.

3.3.2 Solution phase synthesis of triruthenium complexes

Since combinatorial synthesis was not working, the targets were modified slightly and solution phase chemistry was attempted on the remaining targets. It was decided to make symmetrical complexes instead of asymmetric complexes at first to see if the proposed bridges would produce a NIR absorption in the mixed valence states. The ancillary ligands do have some effect on where the NIR peak is located, but they tend not to affect whether or not a peak will be seen.[11]

The mixed bridge **21** was made by refluxing a solution of $(TfO)_3Ru(TPPZ)Ru(OTf)_3$ and **10**. This is outlined in scheme 3-3. The chlorines of **15** were replaced with triflate groups to facilitate the reaction. Similar to the previous triruthenium complexes, analysis by ^1H NMR was not possible, as there was paramagnetic ruthenium (III) in both the reactants and products. The IR spectra of **21** had a shift 2107 cm^{-1} caused by the isothiocyanate group and a shift at 1888 cm^{-1} caused by the carboxylic acid group in DCBPY. This complex was a dark green/black color.

Scheme 3-3: Synthesis of **21.**

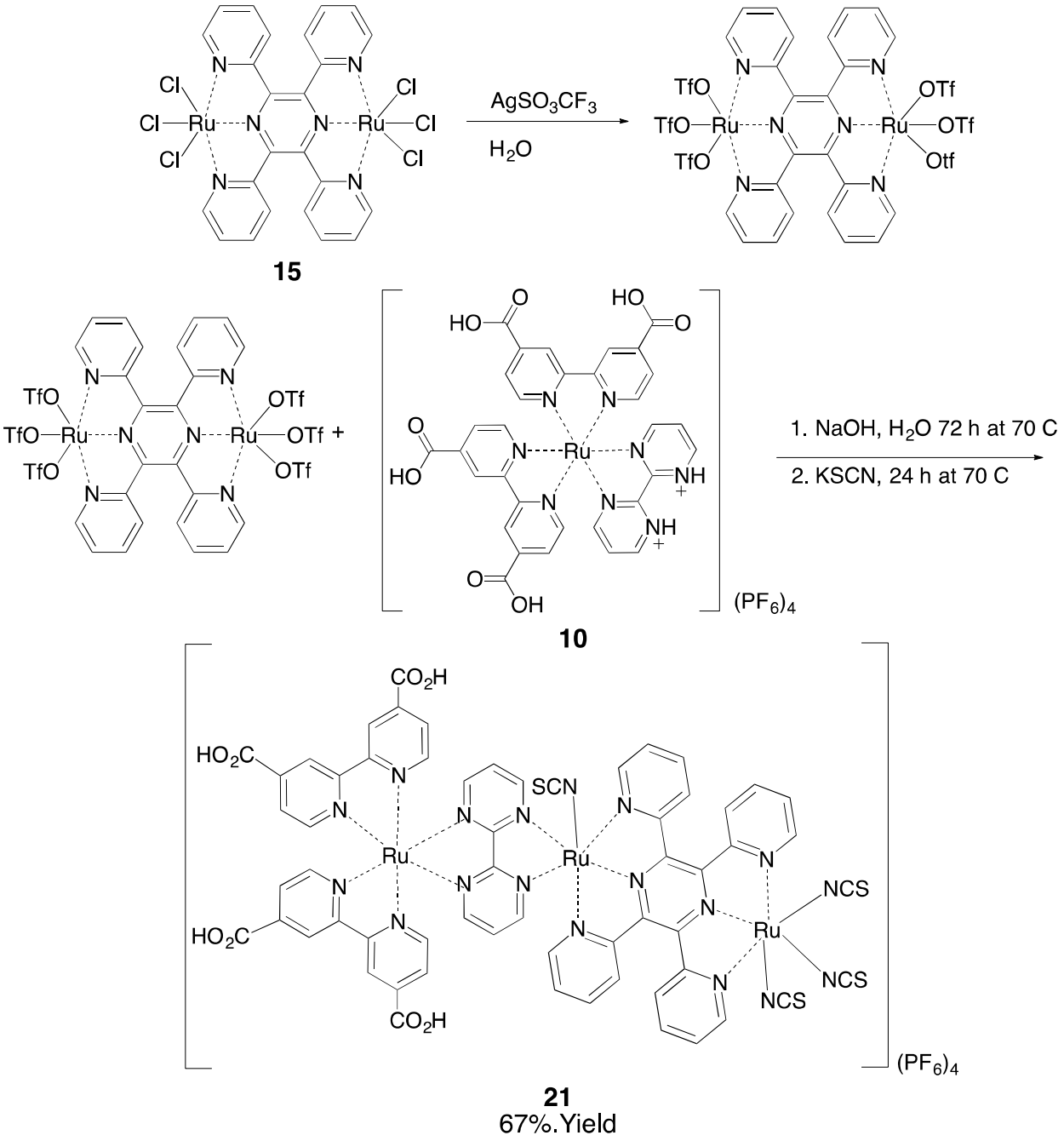

A bis-TPPZ bridged complex, **22**, was made by adding $RuCl_3$ to **14**. The synthesis is seen in Scheme 3-4. Analysis by ^1H NMR was not possible, as there was paramagnetic ruthenium (III) in the products. The UV-Vis spectrum was similar to that of **15**, except the TPPZ π absorptions in **22** were more intense. This complex had blue/green color to it, similar to **15.**

Scheme 3-4: Synthesis of **22**.

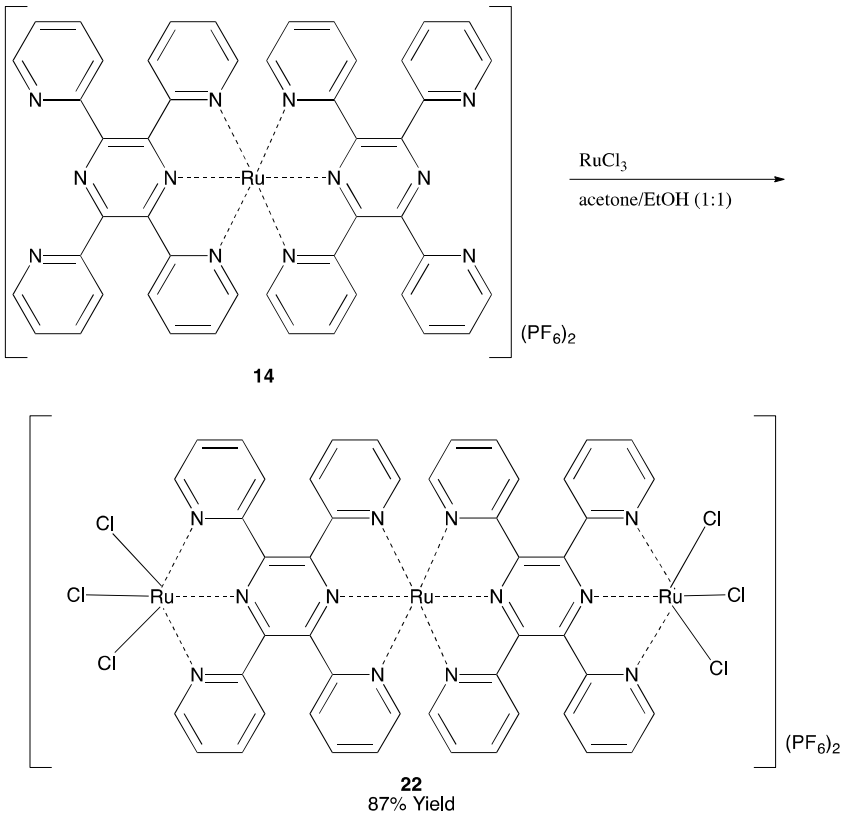

Two bis-BPM bridged complexes were made by adding **6** to either **9** or **3** to make **23** and **24** respectively. Both of these complexes were an olive green/black color. The synthesis is seen in Scheme 3-5. The carbonyl of the DEBPY ligands causes an absorption peak to appear at 1720 cm^{-1} in the IR of **24**, which is absent in **23**. In many polypyridine multiruthenium complexes, the ^1H NMR gets difficult to analyze once there are three or more ruthenium centers. The same is seen in the ^1H NMR of these two complexes. Because there are eight possible stereoisomers and almost all hydrogens are in the 7-9 ppm range, there were a large number of overlapping peaks and it was not possible to assign all of the hydrogens. In the ^1H NMR of **24**, the ethoxy group of DEBPY were present at 4.48 and 1.75 ppm in the appropriate 2:3 ratio.

Scheme 3-5: Synthesis of **23** and **24**.

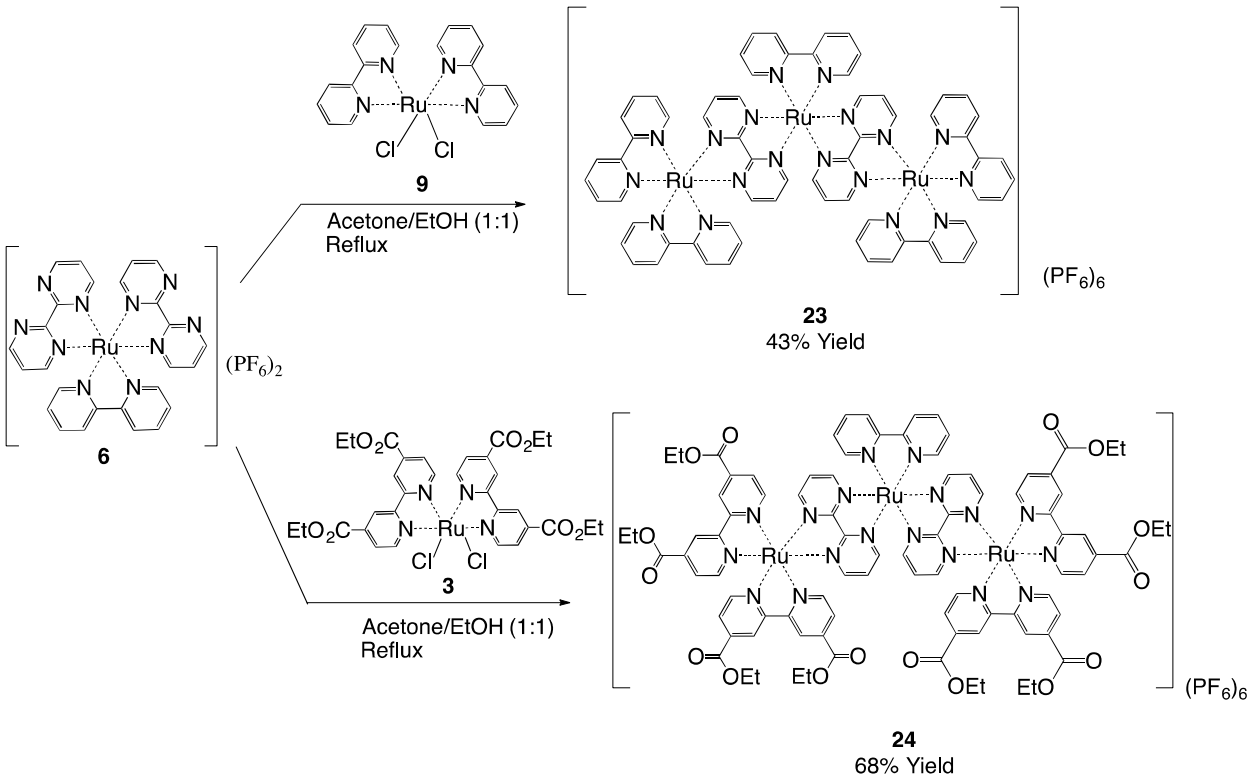

Two bis-BIM bridged complexes were made in a manner similar to the bis-BPM bridged complexes. **5** to either **9** or **3** made **25** and **26** respectively. The synthesis is seen in Scheme 3-6. While the bis-BPM bridged complexes were an olive green color, these two were dark red/purple. The ^{1}H NMR of these two complexes was similar to those of the bis-BPM bridged complexes. There were a large number of overlapping peaks and it was not possible to assign all of the hydrogens. In the ^{1}H NMR of **26**, the carboethoxy group of DEBPY were present at 4.47 and 1.43 ppm in the appropriate 2:3 ratio. A carbonyl peak was seen in the IR of **26** at 1716 cm^{-1}.

Scheme 3-6: Synthesis of **25** and **26**.

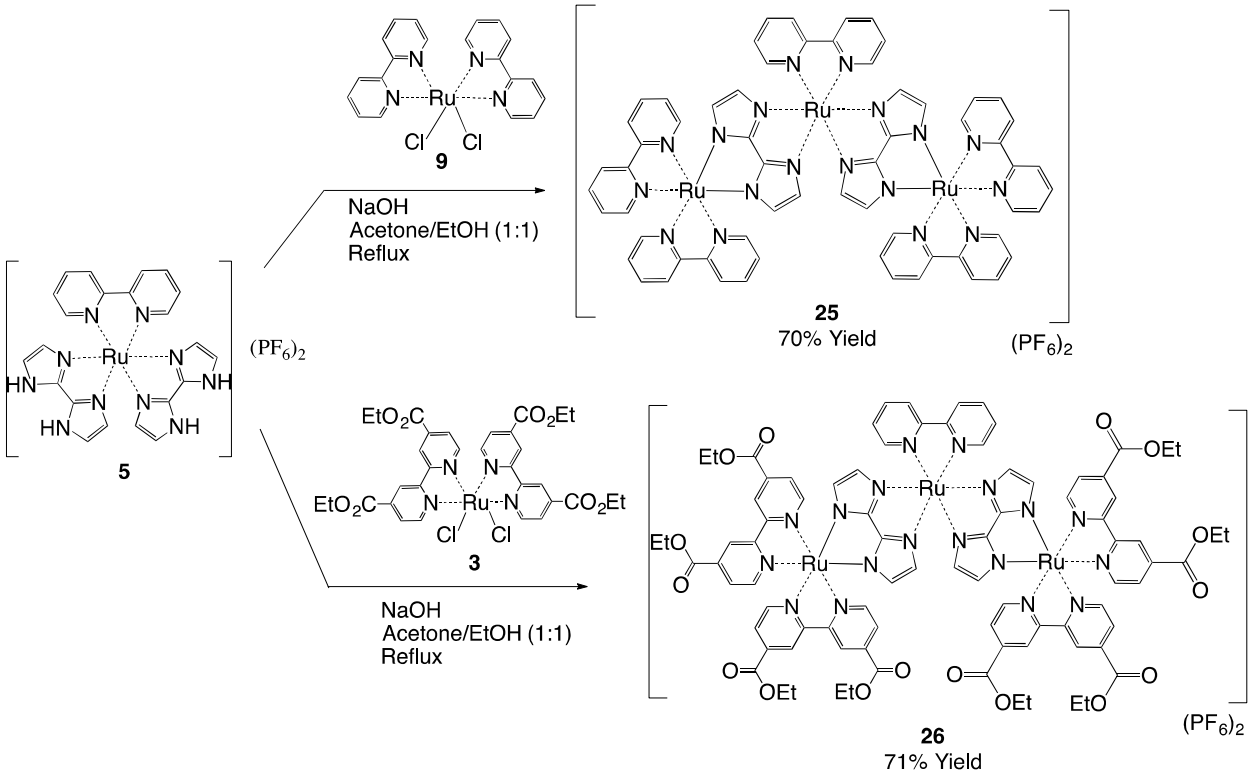

3.3.3 Elemental analysis of triruthenium complexes

An elemental analysis was performed on the eight triruthenium complexes described in this chapter and the results are seen in Table 3-1. Analysis was performed by Intertek Pharmaceuticals in Whitehouse, NJ. In most complexes, the experimental carbon, hydrogen, and nitrogen content was significantly lower than the expected values. During the synthesis of these complexes, excess hexafluorophosphate salt was added to precipitate a product. It is likely a significant amount of excess salt was present in the sample. This would not show up in the ^{1}H NMR or UV-Vis of the complexes. This in turn would cause the experimental values for carbon, hydrogen, and nitrogen to be significantly lower as is seen in the elemental analysis.

Table 3-1: Elemental analysis of triruthenium complexes

Complex	Anal. Calcd.	Found
19	C, 33.12; H, 2.26: N, 9.66	C, 23.23; H, 3.44: N, 8.64
20	C, 33.35; H, 2.26: N, 9.43	C, 9.41; H, 4.32: N, 10.09
21	C, 33.51; H, 1.78: N, 11.72	C, 29.47; H, 1.41: N, 11.95
22	C, 36.43; H, 2.04; N, 10.62	C, 36.96; H, 3.02; N, 8.87
23	C, 34.92; H, 2.31; N, 11.11	C, 0.47; H, <0.10; N, 0.12
24	C, 37.97; H, 2.97; N,8.86	C, 7.14; H, 0.46; N, 2.86
25	C, 45.45; H, 2.95; N, 15.39	C, 37.52; H, 2.84; N, 10.84
26	C, 46.64; H,3.64; N, 11.38	C, 30.59; H, 1.22; N, 13.95

3.3.4 UV-Vis and ceric ammonium nitrate oxidation spectral data

In order to see if a NIR peak would appear in the mixed-valence state of the compounds, ceric ammonium nitrate titrations, CAN, were performed. A UV-Vis of each triruthenium sample, and a few diruthenium samples, were taken. After this, a solution of 0.25 equivalents of CAN was added and the UV-Vis was retaken. This was repeated until a total of 2 equivalents of CAN was added to the diruthenium complexes and a total of 3 equivalents of CAN was added to the triruthenium complexes.

The CAN titrations of BIM-bridged complexes **11**, **25**, and **26** are seen in Figures 3-13, 3-14, and 3-15 respectively. All three complexes exhibit the same general pattern. A MCLT absorbance at roughly 500 nm slowly decreases as more CAN is added. Around 550-600 nm, an inflection point is seen and the absorbance increases as more CAN is added. In **11** the absorbance continues throughout the NIR. In **25**, and **26**, the increase in absorbance is only seen until roughly 800 nm. As CAN is added, the ruthenium centers are oxidized from Ru(II) to Ru(III). It is likely this is why the MLCT absorbance drops around 500 nm. The increase in absorbance from 600 to 800 nm most likely comes from a mixed-valance MMCT that arises when there is one Ru(II) center and one or more Ru(III) center. Since this does not disappear once 3 equivalents of CAN is added, this might suggest not all of the metals centers are being

oxidized. As mentioned in Chapter 2 of this dissertation, the complex $[Ru^{III}(BIM)Ru^{II}(BPY)_2)_3]^{3+}$ showed a mixed-valence absorption at 833 nm.[12] The wavelength is a bit higher than the mixed-valence absorbance seen in $[((BPY)_2Ru(BIM))_2Ru(BPY)](PF_6)_2$, and $[((DEBPY)_2Ru(BIM))_2Ru(BPY)](PF_6)_2$.

Figure 3-13: CAN titration of **11**.

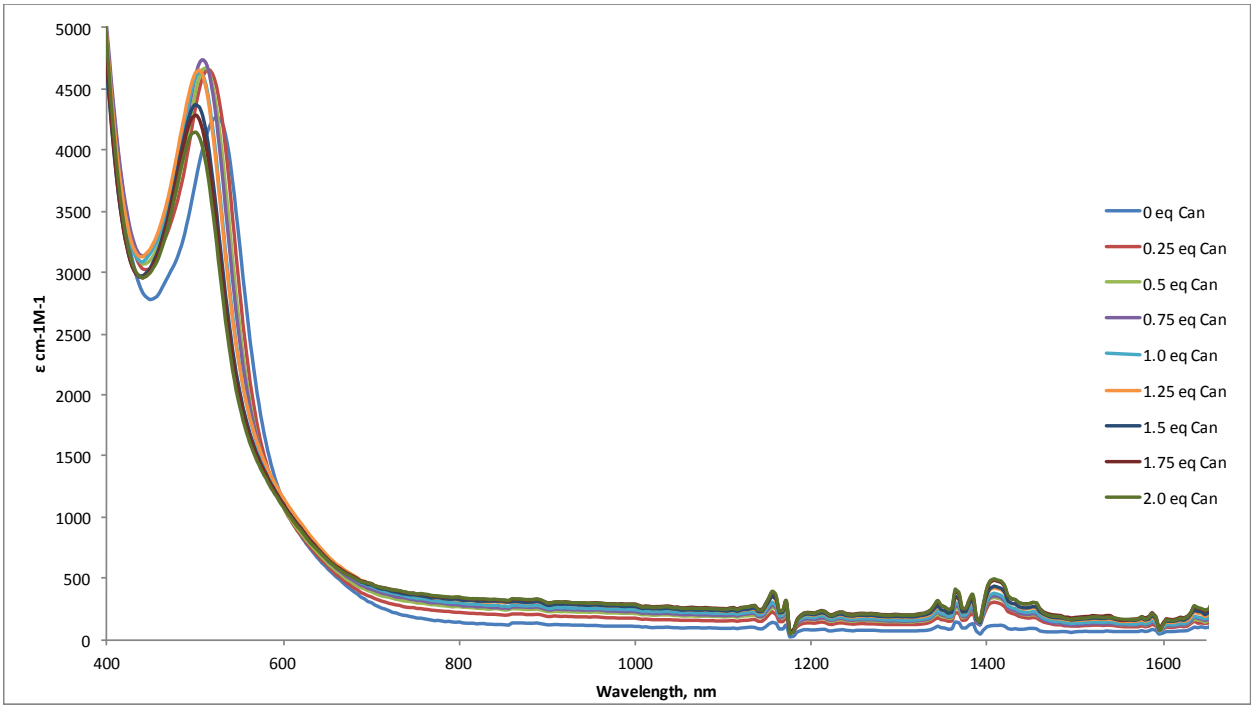

Figure 3-14: CAN titration of **25**.

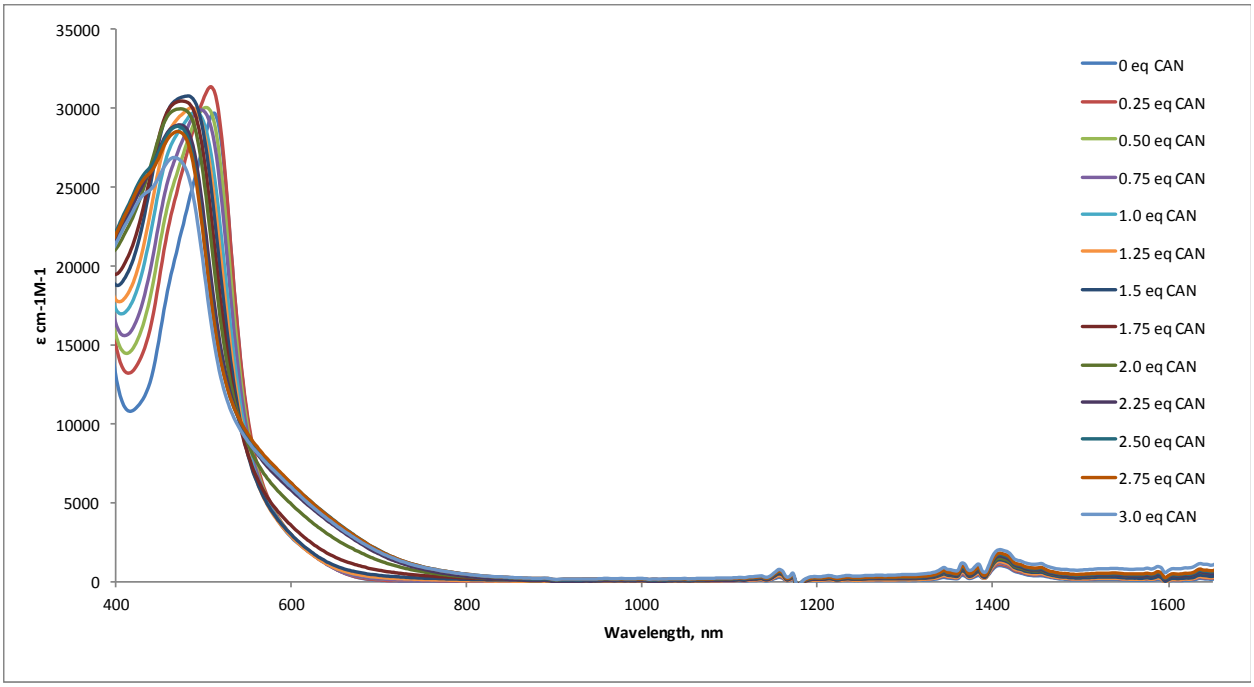

Figure 3-15: CAN titration of **26**.

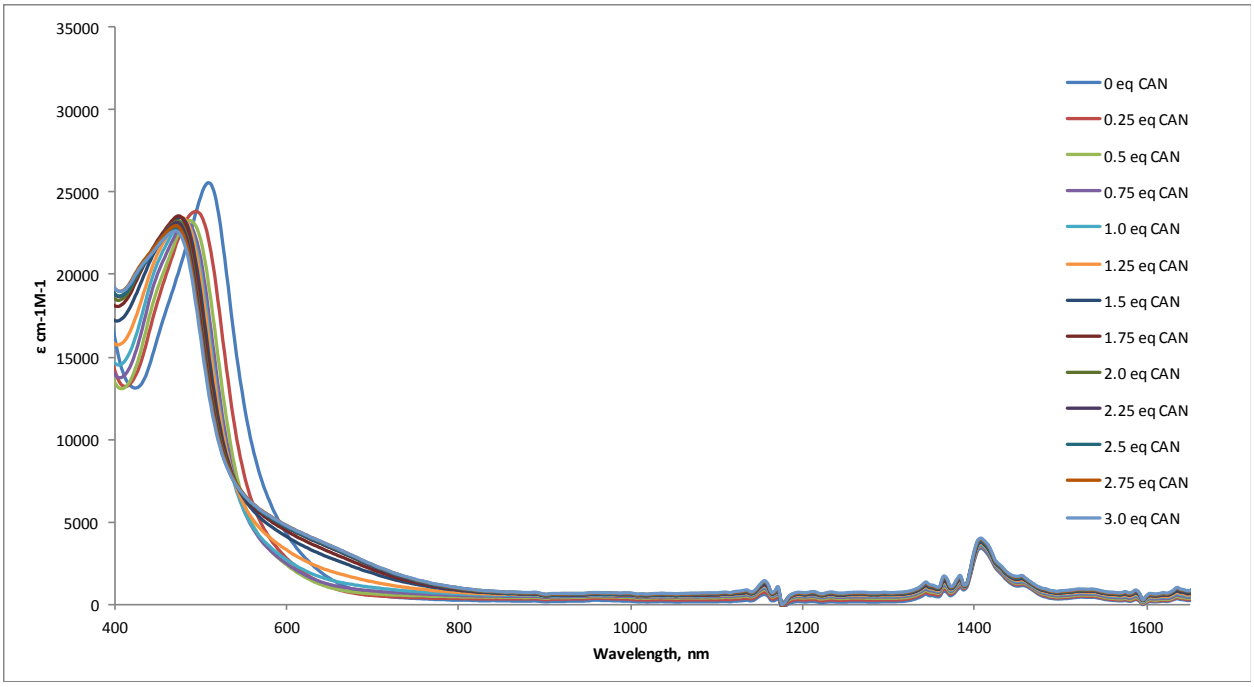

The CAN titrations for BPM-bridged **12**, **23**, and **24** are seen in Figures 3-16, 3-17, and 3-18 respectively. Each complex had a MLCT peak around 650-700 nm and a strong absorption below 450 nm. There is also an absorbance around 1325-1350 nm in each. This is present both at the start and at the completion of the titration. Through the titration, no major changes were seen in the absorption pattern in the bis-BPM bridged complexes. As mentioned in Chapter 2 of this dissertation, the mixed valence complex $[(BPY)_2Ru^{II}(BPM)Ru^{III}(NH_3)_4](PF_6)_5$ did not show a NIR absorption. It is likely CAN is not a strong enough oxidant to oxidize these complexes based on the results of similar TPPZ complexes described in chapter 4 of this dissertation.

Figure 3-16: CAN titration of **12.**

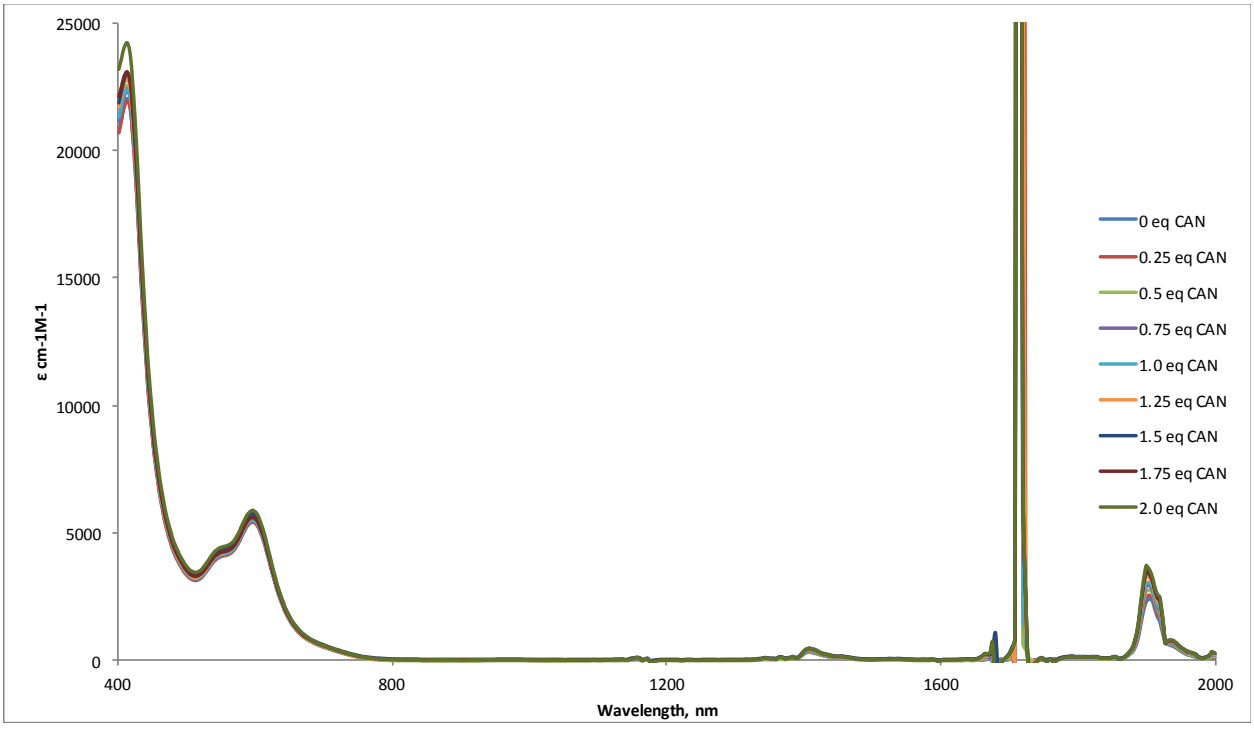

Figure 3-17: CAN titration of **23**.

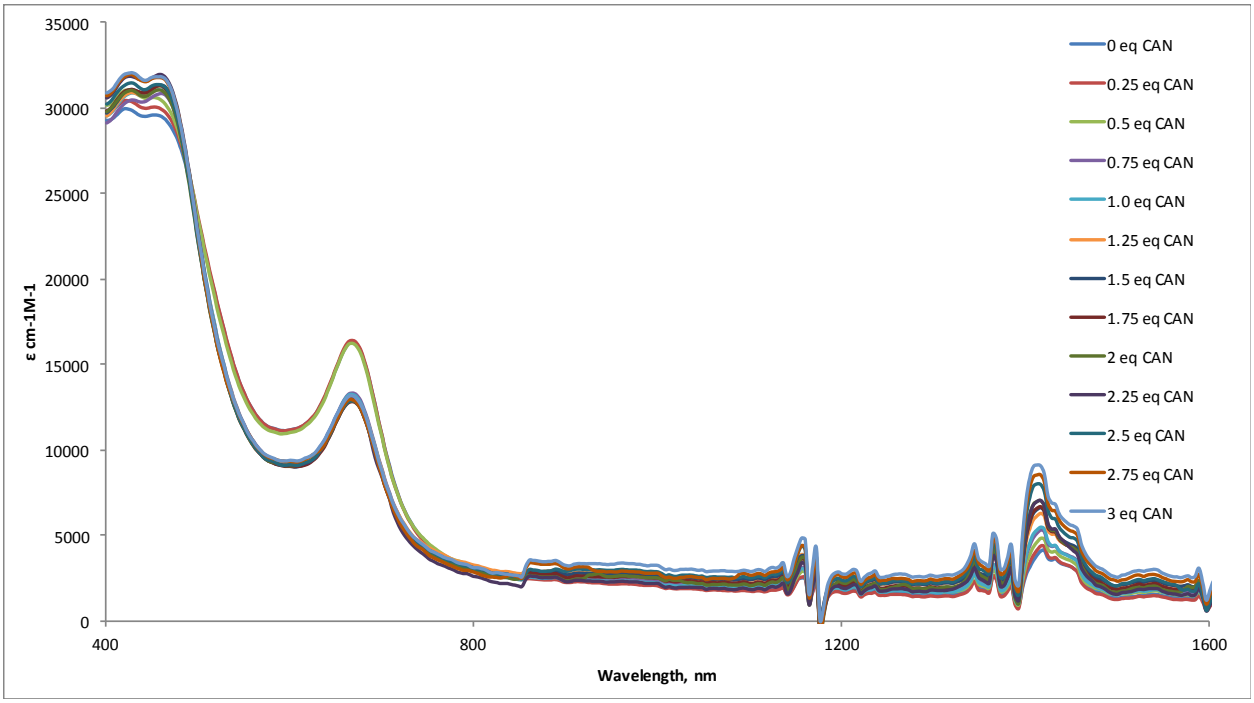

Figure 3-18: CAN titration of **24**.

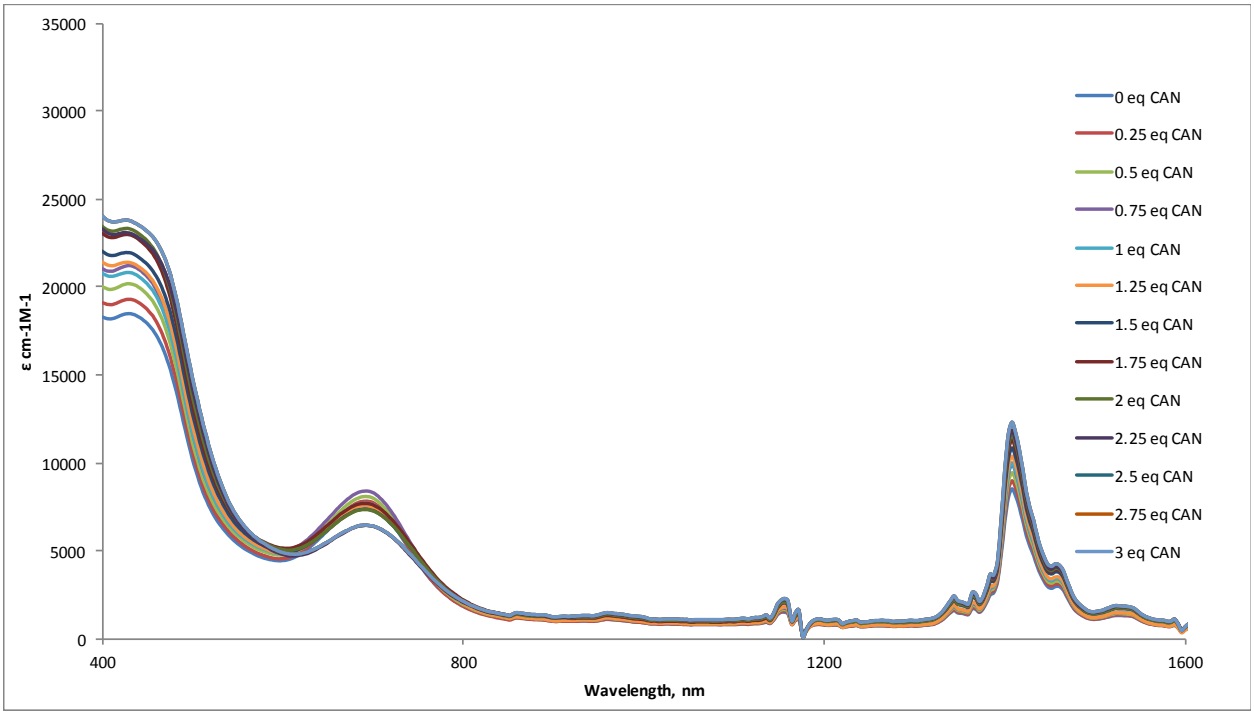

The CAN titrations for TPPZ-bridged **16** and **22** are seen in Figures 3-19 and 3-20 respectively. A strong peak is seen around 600 nm in both, arising from the ruthenium to TPPZ MLCT. There is a long tail extending to 1300 nm **16**. This complex is initially in the Ru (II)/Ru(III) mixed valence state and has no other major peaks in the NIR. In similar complexes, CAN was not a strong enough oxidization agent to oxide some TPPZ bridged ruthenium complexes, so it is likely the tail is a result of the mixed-valence transition in the initial complex which is not being oxidized.[13] The MLCT absorbance at **22** decreased as more CAN is added. This is likely the result of the central ruthenium, which was believed to be Ru(II), being oxidized. The initial complex was suspected to be in Ru(III)/Ru(II)/Ru(III) oxidation states. A NIR absorption would be seen before CAN was added if one was present. However, there was none.

Figure 3-19: CAN titration of **16**.

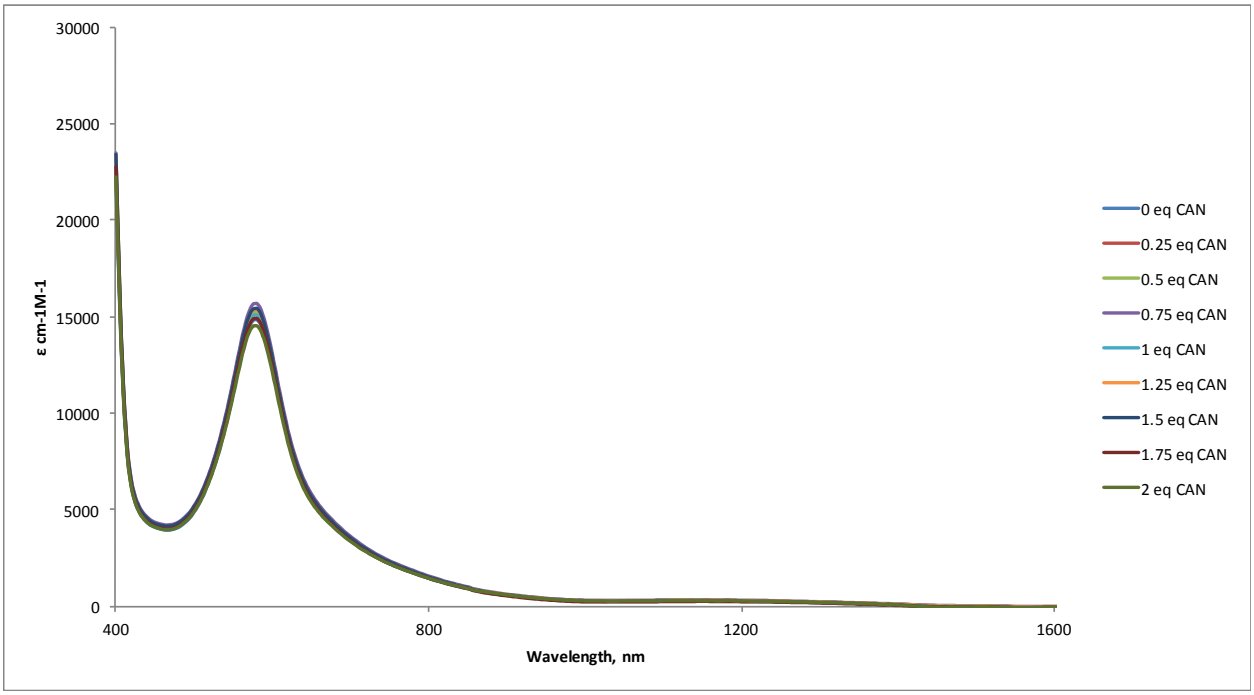

Figure 3-20: CAN titration of **22**.

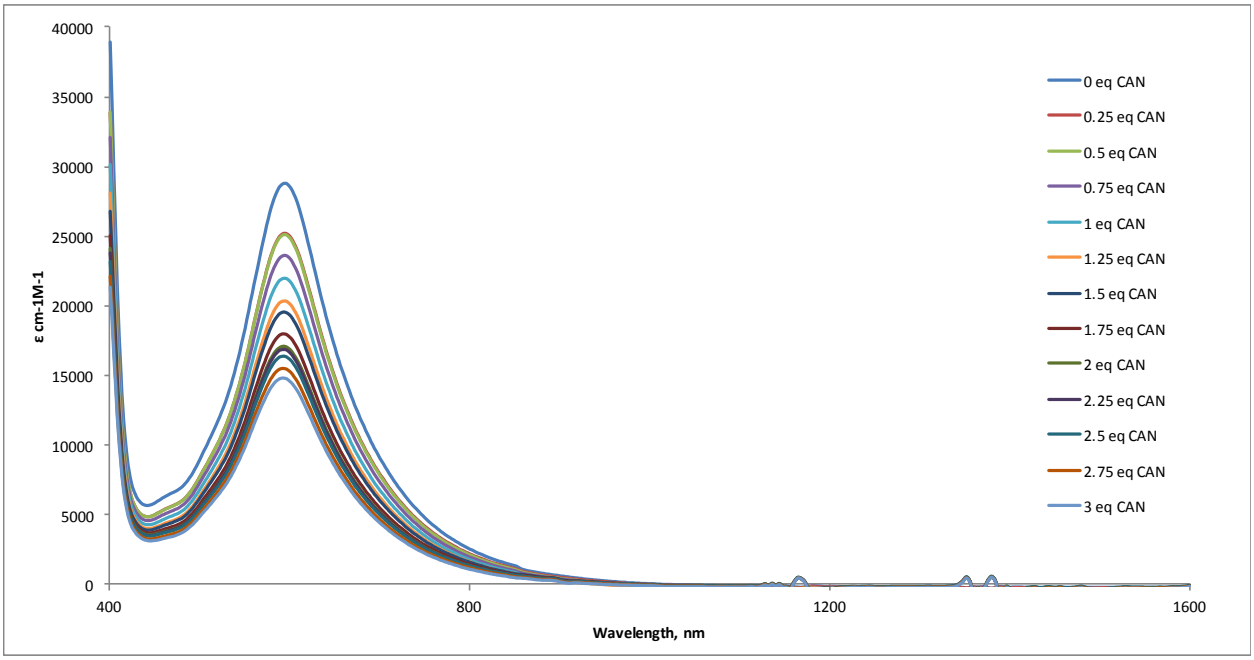

The CAN titrations for Ru-BPM-Ru-TPPZ-Ru complexes **19**, **20**, and **21** are seen in Figures 3-21, 3-22, and 3-23 respectively. All three contain a MLCT absorbance around 600 nm. This is most likely the MLCT absorbance that arises from the Ru-TPPZ transition as it is in the same location in the TPPZ bridged complexes seen in Figures 3-19 and 3-20. There is also an absorbance around 450 nm in each. This is the same location that the BPM and BPY ligands in the BPM bridged complexes in Figures 3-16 through 3-18 were seen. There was a peak that in the BPM bridged complexes around 600 nm that would also overlap with the TPPZ absorbance. In all three of **19**, **20**, and **21**, no NIR absorptions are seen and the absorption of the MLCT peaks drop as more CAN is added. This is likely a result of the ruthenium center around BPM being oxidized.

Figure 3-21: CAN titration of **19**.

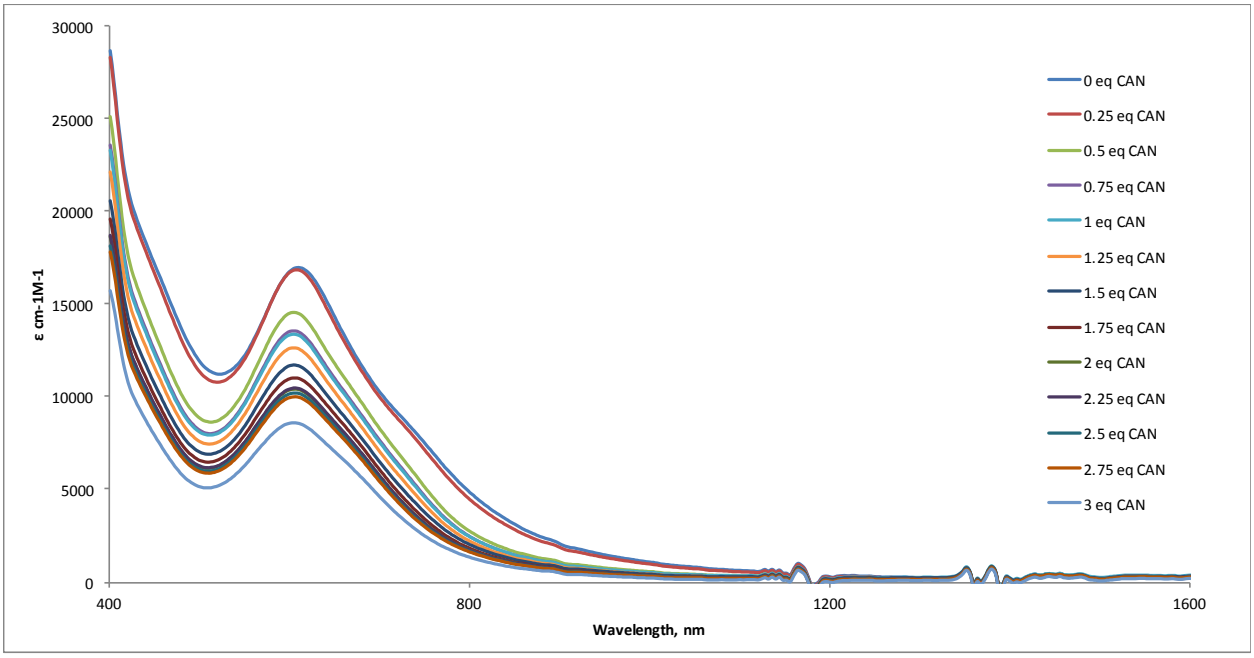

Figure 3-22: CAN titration of **20**.

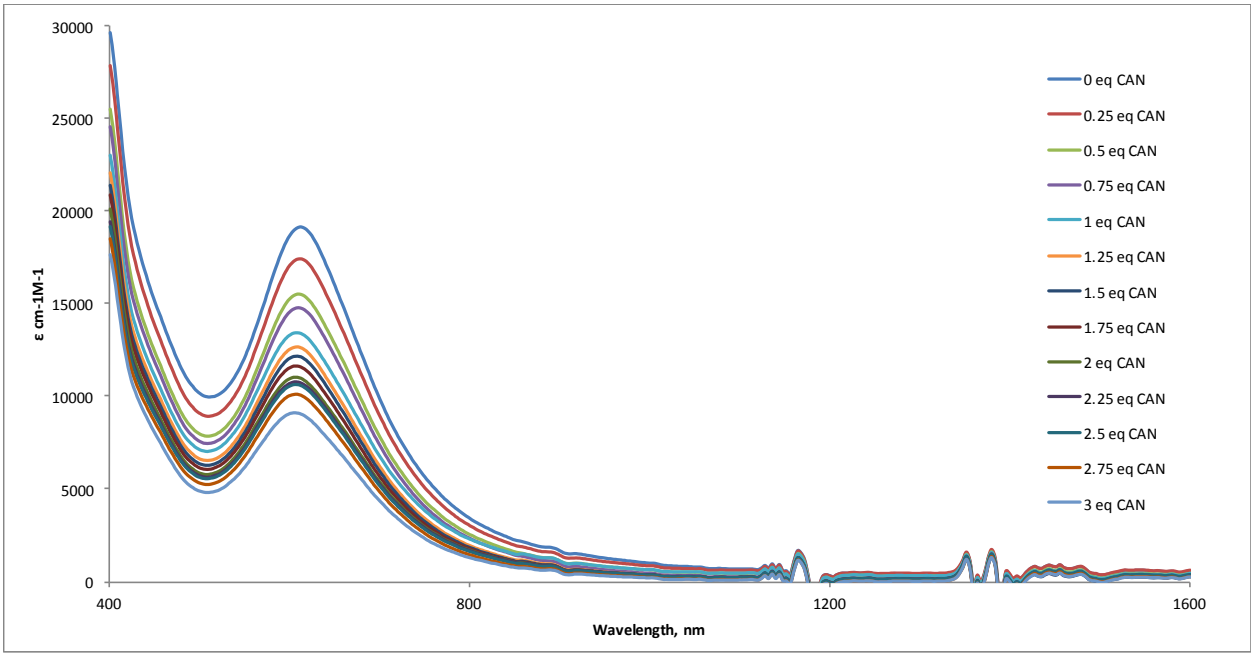

Figure 3-23: CAN titration of **21**.

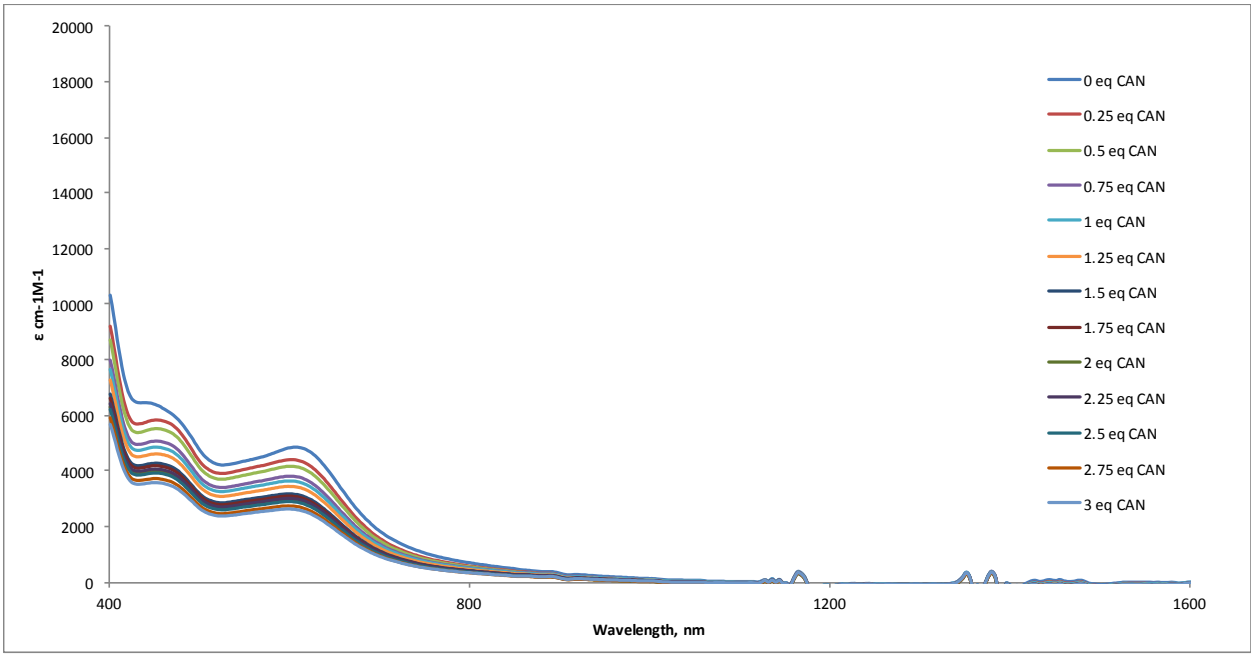

3.4 Conclusion

A number of triruthenium complexes were made with BPM, BIM, and TPPZ bridged centers. The complexes with two BPM and two TPPZ bridges did not display a NIR absorption in any oxidation state. The mixed bridge systems, with both one TPPZ and one BPM did not display a mixed-valence NIR state either. The two BIM bridged system had a slight mixed-valence absorption around the 700-800 nm mark, but it did not extend deep into the NIR. It was concluded that these bridging systems combined with Ru(II)/Ru(III) metal centers would not serve as good electron reservoirs. The next chapter described the modification of TPPZ to allow more electron density to be placed on the ruthenium centers, allowing the complex to reach a mixed-valence state with more ease. Each of these complexes were used as dyes in a DSSC and the results are described in Chapter 5 of this dissertation.

Chapter 4

Synthesis and characterization of an asymmetric cyclometalated diruthenium complex

4.1 Introduction

Ruthenium complexes containing isothiocyanate have long held an advantage over other types of dyes used in dye-sensitized solar cells.[1] However, the isothiocyanate ligand is often a weak point from a chemical stability standpoint.[1] The Ru-N bond of a nitrogen bound isothiocyanate is weak compared to multi-chelating polypyridine ligands[2, 3] At temperatures of 80-100 °C the isothiocyanate ligand can be freed by ligand exchange with 4-tertbutylpyridine, a common component of the electrolyte.[3] One option that has recently been explored to avoid use of isothiocyanate is the use of cyclometalated complexes.[4] A cyclometalated version of **N3**, bis(4,4'-dicarboxy-2,2'-bipyridine)-2-(2,4-difluorophenyl)pyridine ruthenium (II) (Figure 4-1) was made using 2-(2,4-difluorophenyl)pyridine in place of the isothiocyanate ligands was one the first cyclometalated complexes reported and it achieved an overall efficiency of 10.1%.[1] A large number of bipyridine derivatives, such as the previously mentioned 2-(2,4-difluorophenyl)pyridine, have been used as bidentate ligands that replace two isothiocyanate ligands.[4] A large number of similar terpyridine cyclometalated derivatives have also been used to replace the terminal ligands in complexes such as **Black Dye**.[4]

Figure 4-1: A cyclometalated version of **N3**, bis(4,4'-dicarboxy-2,2'-bipyridine)-2-(2,4-difluorophenyl)pyridine ruthenium (II).

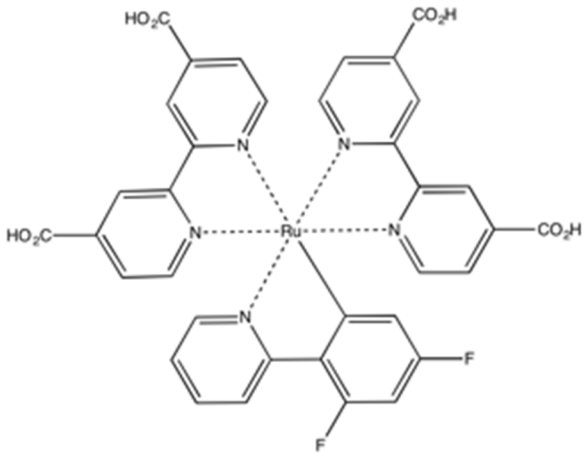

Bimetallic complexes containing the ligand 2,3,5,6-tetra-(2-pyridyl)pyrazine, TPPZ, have received quite a bit of attention due to the similarities to the Creutz-Taube ion.[5,6,7,8,9,10,11] TPPZ has a similar spacing between metal centers in bimetallic complexes while also containing a bis-tridentate coordination, providing much greater stability than seen in the Creutz-Taube ion.[6, 7] Complexes containing the bridging ligand TPPZ tend to exhibit metal-to-metal charge transfer peaks in the near-IR when in the mixed valence state.[7, 8] A variety of similar complexes (Figure 4-2) containing the bridging ligands 6',6"-di(2-pyridyl)-2,2';4',4":2",2"'-quaterpyridine, TPY-TPY, 2,3,5,6-tetra-(2-pyridyl)benzene, TPB, and 4'-(3,5-dipyridylphenyl)-2,2':6',2"-terpyridine, TPY-TBY, have also been synthesized and exhibit near-IR absorbances in their mixed-valence states.[4] Cyclometalated complexes made from ligands such as TPB and TPY-TBY tend to have much lower oxidation potentials on the metal center that is attached to through the carbon-metal bond compared to the similar metal centers with a nitrogen-metal bond.[4,12]

'

Figure 4-2: Counterclockwise from top left, TPPZ, TPB, TPY-TBY, and TPY-TPY.

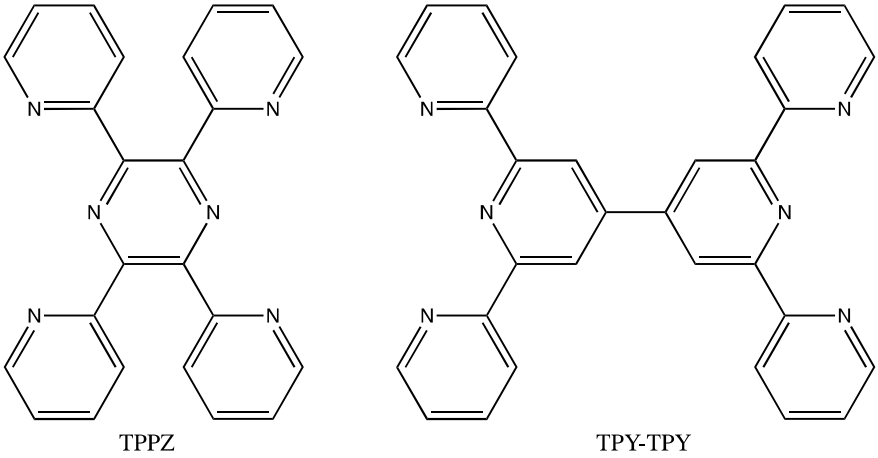

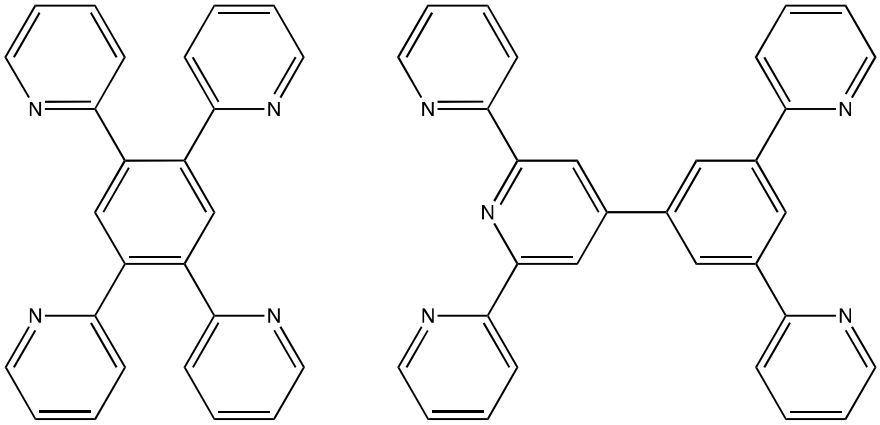

In this chapter, the synthesis of 2,3,5,6-tetra-(2-pyridyl)pyridine, TPPY, is described. When used to make a di-metallic complex, this ligand would have similar metal-to-metal distances as the Creutz-Taube ion, TPPZ, and TPB. However, a di-metallic complex made with TPPY would be asymmetric, similar to TPY-TBY and would contain a single carbon-metal bond, lowering the oxidation potential on one of the metal centers. The asymmetry in the molecule, potential mixed-valence absorbances, and similarities to other polypyridine ruthenium complexes would make it a good candidate as a bridging ligand for the electron reservoir strategy.

Figure 4-3: 2,3,5,6-tetra-(2-pyridyl)pyridine, TPPY.

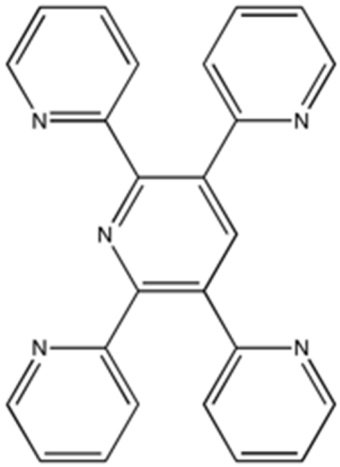

4.2 Experimental

All reactions were carried out under an atmosphere of dry nitrogen or in a glovebox unless otherwise noted. All NMR spectra were run using a 300 or 400 MHz Bruker NMR. All UV/Vis measurements were performed on a Perkin Elmer Lambda 950 UV/Vis spectrometer. All IR measurements were taken on a Thermo Nicolet IR200 FT-IR.

4.2.1 Synthesis of 2,6-diamino-3,5-dibromopyridine, 27

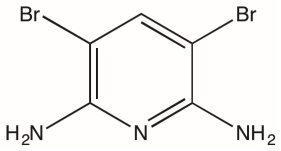

This reaction was performed according to a modified version of a literature procedure.[13] In a round bottom flask, 2,6-diaminopyridine (4.034 g, 36.97 mmol) was dissolved in 10 mL H_2O. Hydrobromic acid (9.0 mL, 48 %) was added followed by slow addition of H_2O_2 (7.0 mL, 30 %) over a 1 h period. The solution was then cooled in an ice bath and a 300-watt

incandescent light bulb was placed in close proximity. After 1 h, an additional 3 mL of HBr and 3 mL of H_2O_2 was added. After another 1 h, 1 M NaOH was added to bring the pH to 8, which caused a white solid to precipitate. The white solid was a mixture of the mono- and dibrominated products. These were separated by column chromatography on silica using an eluent mixture of 100:10:1 $CHCl_3$:MeOH:NH_3. A yield of 39.2% of **27** was obtained.

27 - ^{1}H NMR (DMSO-d_6, 300 MHz) δ 7.55 (s, 1H), 5.86 (s, 4H).

2,6-diamino-3-bromopyridine - ^{1}H NMR (DMSO-d_6, 300 MHz) δ 7.23 (d, 1H, J = 8.4 Hz), 5.65 (d, 1H, J = 8.4 Hz), 5.63 (s, 2H), 5.54 (s, 2H).

4.2.2 – Synthesis of 2,3,5,6-tetrabromopyridine, 28

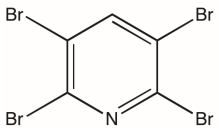

This reaction was performed according to a modified literature procedure.[13,14] In a round bottom flask, **27** (0.507 g, 1.90 mmol) was dissolved in a solution of 10 mL deionized H_2O and HBr (48 %, 1 ml) and cooled with an ice bath. Sodium nitrite (6.485 g, 76.30 mmol) dissolved in 10 ml water was added dropwise over a period of 1 h. A large amount of N_2 gas was given off right away. After 1 h at 0 °C, the reaction was allowed to warm to room temperature for 1 h and then the solution was heated at 50 °C for 8 h after which the solution was neutralized with 1 M NaOH. The aqueous solution was extracted three times with 50 mL $CHCl_3$. The solvent was vaporized under vacuum and the solid crude product was recrystallized from hexane. The product was obtained as a yellow solid (0.105 g, 0.266 mmol). After column chromatography on silica with $CHCl_3$ as the eluent, 0.0532 g of a yellow solid was collected for a yield of 7.1%. ^{1}H NMR ($CDCl_3$, 300 MHz) δ 8.07 (s); ^{13}C NMR ($CDCl_3$, 300 MHz) δ 145.5, 140.8, 123.2.

4.2.3 – Synthesis of 2,3,5,6–tetra-(2-pyridyl)pyridine, TPPY

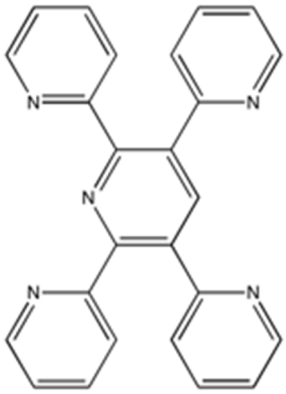

In a flame-dried vacuum flask, a solution was prepared by dissolving **28** (0.0501 g, 0.127 mmol) in 10 mL dried toluene. To this was added 2-(tributylstannyl)pyridine (0.464 g, 1.26 mmol), bis(triphenylphosphine)palladium(II) dichloride (0.023 g, 0.0327 mmol) and lithium chloride (0.107 g, 2.52 mmol) under a nitrogen atmosphere. The ratio of **28**:2-(tributylstannyl)pyridine:bis(triphenylphosphine)palladium(II) dichloride was 1: 9.9: 0.25. The reaction mixture was stirred under nitrogen and heated to 150 °C. The reaction vessel was sealed with a hand screwed Teflon stopcock and it was allowed to remain at 150 °C for 48 h. After cooling, the solvent was removed by vacuum. A column was performed using $CHCl_3$:MeOH:NH_4OH(aq) (100:10:1) as the eluent. The product was recrystallized by dissolving the solid in hot ethanol and allowing the solution to cool. The crystals were collected by vacuum filtration and used for X-ray crystallography. A total of 0.0360 g of a white/beige solid was collected for a yield of 73.1%. ^{1}H NMR ($CDCl_3$, 300 MHz) δ8.54 (dd, *J* = 5.4, 1.8, 2H), 8.23 (m, 3H), 7.86 (d, *J* = 7.8, 2H), 7.74 (td, *J* = 7.5, 1.8, 2H), 7.54 (td, *J* = 7.8, 1.5, 2H), 7.18 (m, 6H); ^{13}C NMR ($CDCl_3$, 300 MHz) δ157.8, 157.7, 155.1, 149.6, 148.9, 141.9, 136.5, 135.9, 135.4, 125.0, 124.8, 123.0, 122.1. A ^{1}H-^{1}H COSY was also performed and is discussed in section 4.3.

4.2.4 Synthesis of trichloro-2,2';6',2"-terpyridineruthenium, 29

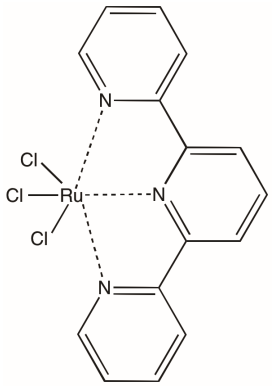

This complex was synthesized by following a literature procedure.[1] A total of 0.559 g was collected for a yield of 66%. The ^{1}H NMR had a very low signal to noise ratio and was not very clear due to the product being paramagnetic. There were broad, very low intensity multiplets in the 7-10 ppm range.

4.2.5 Synthesis of bis(2,2';6',2"-terpyridineruthenium)-μ-2,3,5,6-tetra-(2-pyridyl)pyridine, 30

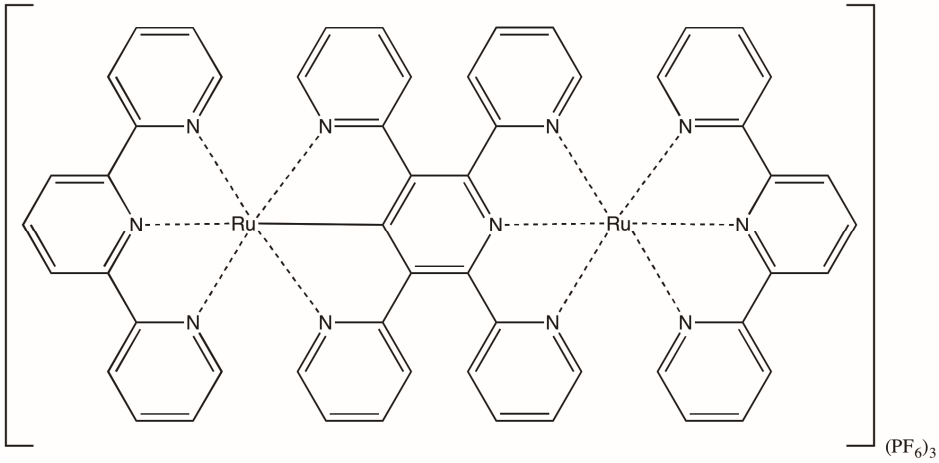

A solution of **29** (0.0853 g, 0.194 mmol) in 50 mL of DI water was prepared in a 50 mL round bottom flask. To this was added AgOTf (0.199 g, 0.776 mmol). This was stirred for 3 h at 50 °C and during this time, the solution changed from a black to a blue/purple color. After cooling, the solution was filtered to remove the solid silver chloride precipitate and the filtrate was collected and the water was evaporated. This left an amorphous purple product in the flask which was (TPY)Ru$(OTf)_3$. TPPY (0.0296 g, 0.764 mmol) in 50 mL of n-BuOH was added and the mixture was refluxed for 72 h. After cooling, the solvent was removed by vacuum. A column was performed using a 90:10 mixture acetonitrile/saturated $NaNO_3$ in H_2O on alumina. After collecting the fractions, a purple solid was collected by adding 10 mL of a saturated KPF_6 solution to make a purple precipitate. A total of 0.132 g was obtained for a yield of 84%. ^{1}H NMR (acetone-d_6, 300 MHz) δ 9.16 (d, *J* = 6.0 Hz, 2H), 9.12 (d, *J* = 6.0 Hz, 2H), 9.10 (d, *J* = 6.0 Hz, 2H), 8.90 (d, *J* = 6.0 Hz, 2H), 8.89 (d, *J* = 6.0 Hz, 2H), 8.84 (d, *J* = 6.0 Hz, 2H), 8.63 (t, *J* = 6.0 Hz, 1H), 8.56 (t, *J* = 6.0 Hz, 1H), 8.14 (td, *J* = 6.0, 1.0 Hz, 2H), 8.08 (d, *J* = 3.3 Hz, 2H), 7.98 (td, *J* = 6.0, 1.0 Hz, 2H), 7.96 (td, *J* = 6.0, 1.0 Hz, 2H), 7.80 (m, 6H), 7.65 (d, *J* = 6.0 Hz,

2H), 7.43 (td, *J* = 4.3, 1.0 Hz, 2H), 7.34 (td, *J* = 4.3, 1.0 Hz, 2H), 7.18 (td, *J* = 4.3, 1.0 Hz, 2H), 7.12 (td, *J* = 4.3, 1.0 Hz, 2H).

4.3 Results and Discussion

Synthesis of **30** began with the synthesis of the bridging ligand TPPY. The synthetic strategy for TPPY is shown in Scheme 4-1. Bromination of 2,6-diaminopyridine was achieved via radical bromination using HBr and H_2O_2.[13] The resulting **27** underwent a Sandmeyer reaction using $NaNO_2$ and HBr to give the tetrabromo product **28**.[13] A Stille coupling of the tetrabromo product with 2-(tributylstannyl)pyridine gave the desired product TPPY.[4]

Scheme 4-1: Synthesis of TPPY.

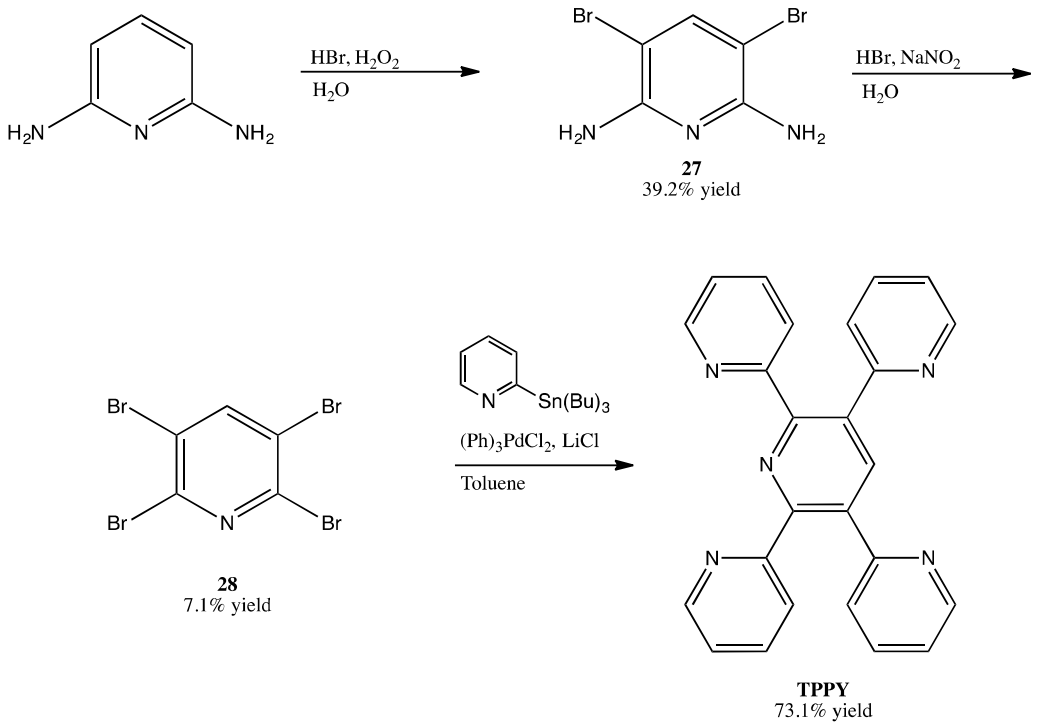

An X-ray crystal structure of TPPY was obtained, and the structure is shown in Figure 4-4. The rings had a non-planar arrangement in the crystal of TPPY with the nitrogens on the non-central pyridine rings facing towards each other. The C-C-N bond angles, which contain a carbon on the central pyridine and a nitrogen on the outer ring, have approximately 50° bond angles.

Figure 4-4: Crystal structure of TPPY.

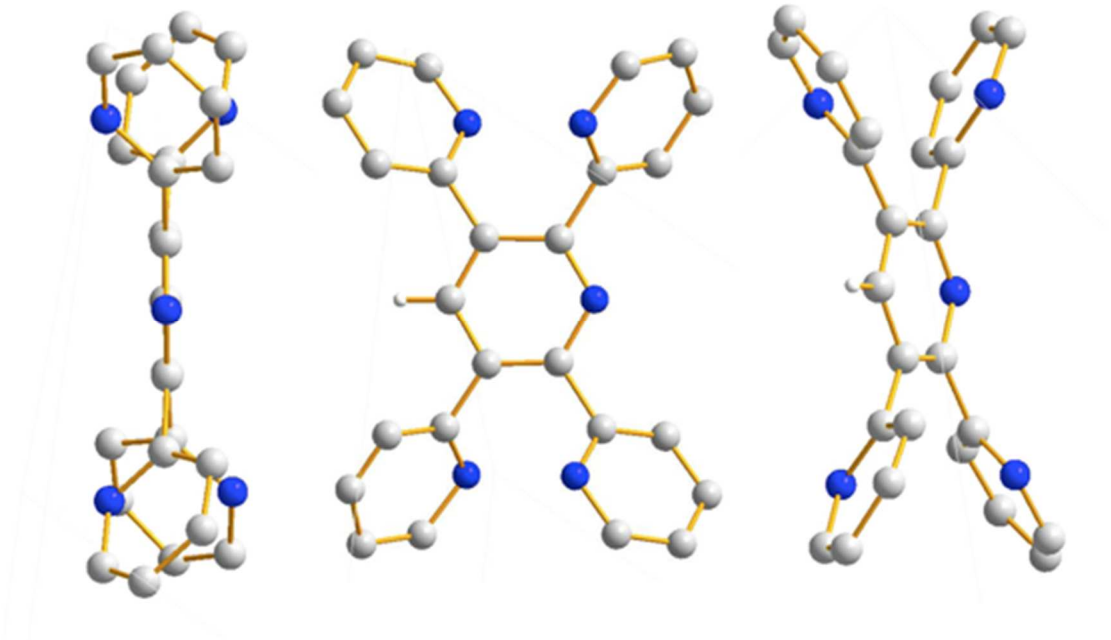

The synthesis of the diruthenium product (Scheme 4-2) was performed by first synthesizing **29** then treating it with silver triflate to make $(TPY)Ru(OTf)_3$. The $(TPY)Ru(OTf)_3$ was immediately dissolved in n-butanol and added to TPPY. Initially this reaction was performed in refluxing ethanol, but it resulted in a mixture of mono and di metallic products in a roughly 1:1 ratio as determined by ^1H NMR. When same procedure was repeated using refluxing n-BuOH as the solvent, this resulted in almost complete conversion to the diruthenium complex. Following column chromatography on alumina, the desired diruthenium complex, **30**, was

obtained as the hexafluorophosphate salt. The ^{1}H NMR of **30** showed a slight excess of the terminal ligands in the mixtures. The singles at 8.63 and 8.56 ppm are from the central hydrogen of the TPY ligands. ^{1}H-^{1}H COSY showed a correlation between these singlets and the doublets at 9.16 and 9.12 ppm. The integrations of these peaks were roughly double of what they should have been. Even though an excess of TPPY was used, it is likely that not all of it reacted and a large portion of the yield is due to excess KPF_6 which was used to precipitate the product. The ^{1}H NMR and ^{1}H-^{1}H COSY for **30** can be found in the Appendix, section 6.3.7.

Scheme 4-2: Synthesis of **30.**

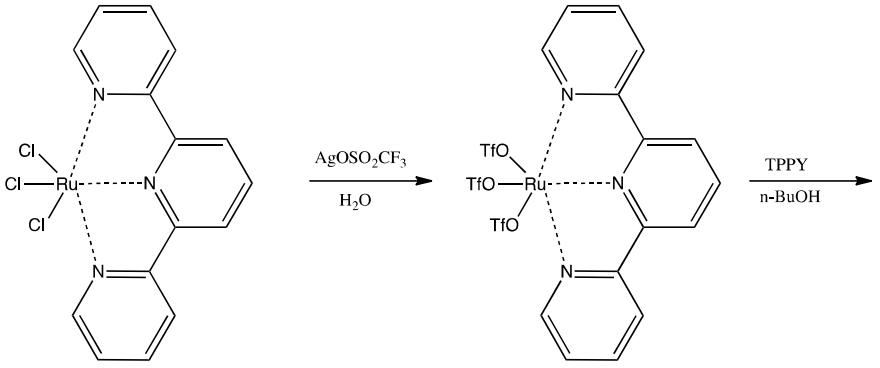

29

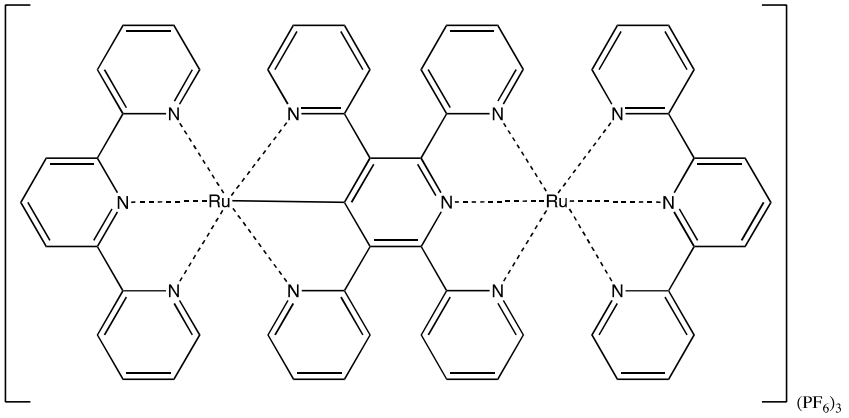

30
85% Yield

4.3.1 Ceric ammonium nitrate titration

Unlike the ruthenium complexes discussed in Chapter 3 of this dissertation, oxidation of **30** in acetonitrile with ceric ammonium nitrate, CAN was possible. Complex **30** was oxidized to the Ru (II)/Ru (III) state. The results of the CAN titration are seen in Figure 4-5 and 4-6. As seen in Figure 4-5, addition of CAN to the diruthenium product results in a decrease in the metal-to-ligand charge transfer peaks at 523 nm while a broad metal-to-metal charge transfer peak in the near-IR at 1370 nm arises with an extinction coefficient of 29831 $cm^{-1}M^{-1}$.

After 1 eq of CAN is added, no change is seen with increasing equivalents of CAN (Figure 4-6). Normally, it would be expected that the additional CAN would oxidize the Ru(II)/Ru(III) system to Ru(III)/Ru(III), resulting in a loss of the NIR peak with no concurrent rise in the MLCT peak. It likely that the initial oxidation occurs on the ruthenium containing the carbon-ruthenium bond, as seen in simlar complexes.[4,12] In a similar complex $[(TPY)Ru(TPPZ)Ru(TPY)](PF_6)_4$, CAN was not a strong enough oxidant to oxdize the ruthenium atoms. The ruthenium attached to the nitrogen side of TPPY in **30** is in an almost identical environment as $[(TPY)Ru(TPPZ)Ru(TPY)](PF_6)_4$ and this interpretation is consistant with the measured redox potentials in section 4.3.2.[3]

Figure 4-5: CAN oxidation of **30**$_3$, 0 to 1 eq.

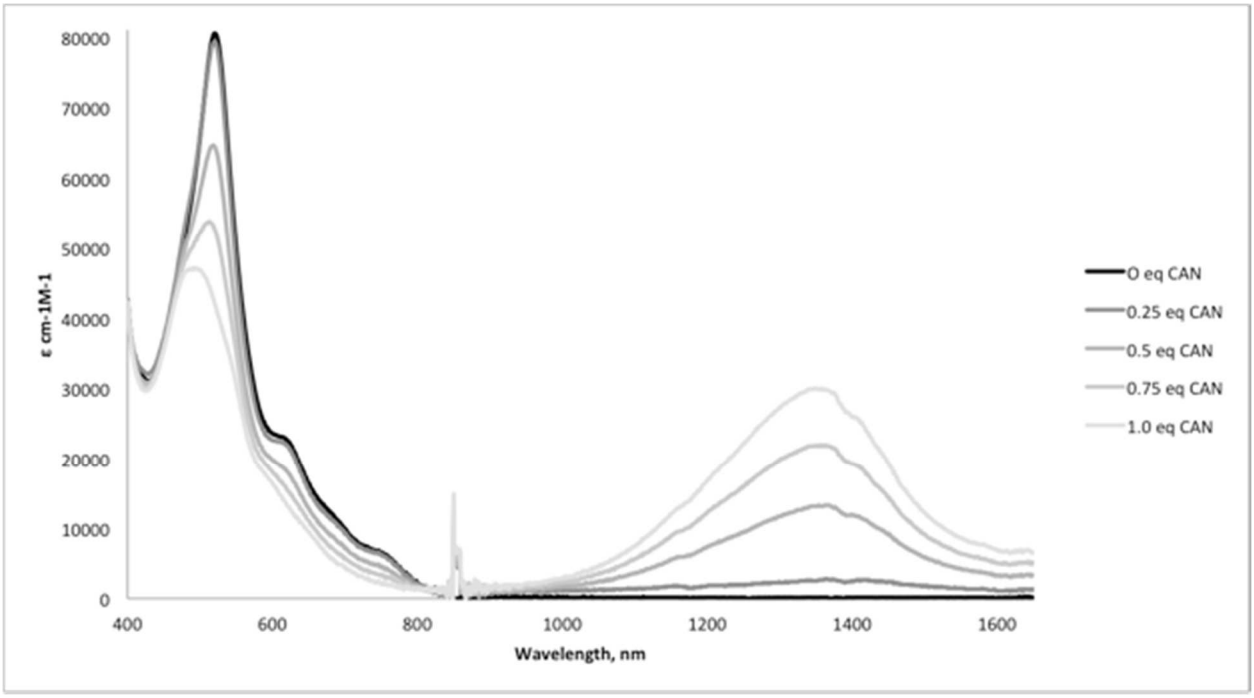

Figure 4-6: CAN oxidation of **30**, 1 to 3 eq.

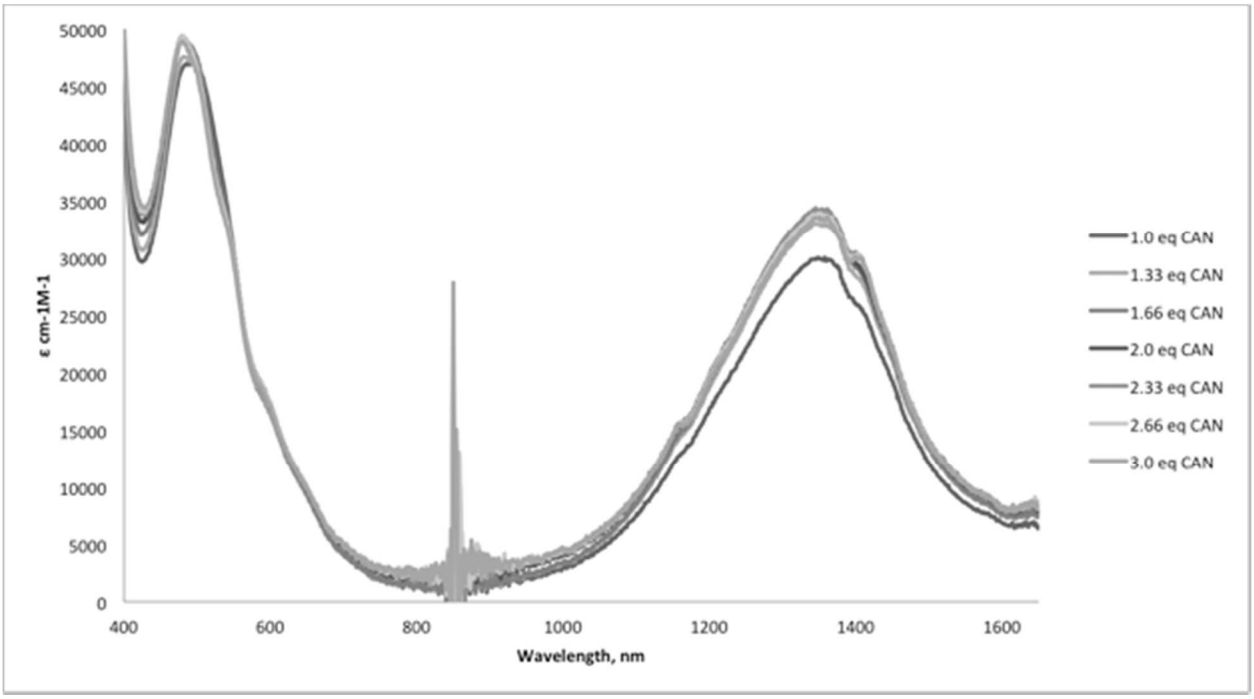

4.3.2 Electrochemical studies

A cyclic voltammetry scan was performed on **30** and the results are seen in Figure 4-7. There are several reductions and oxidations below zero volts which are from the polypyridine ligands in the complex.[3] There are two redox couples in the positive portion of the CV scan. These are highlighted in Figure 4-8. The redox couple at 0.58 V was assigned to the ruthenium bound to carbon while the redox couple at 1.14 V is assigned to the nitrogen coordinated ruthenium.

Figure 4-7: CV scan of **30** from -2.5 V to 2.5 V, scan rate of 0.1 V/s, and performed vs Ag/AgCl.

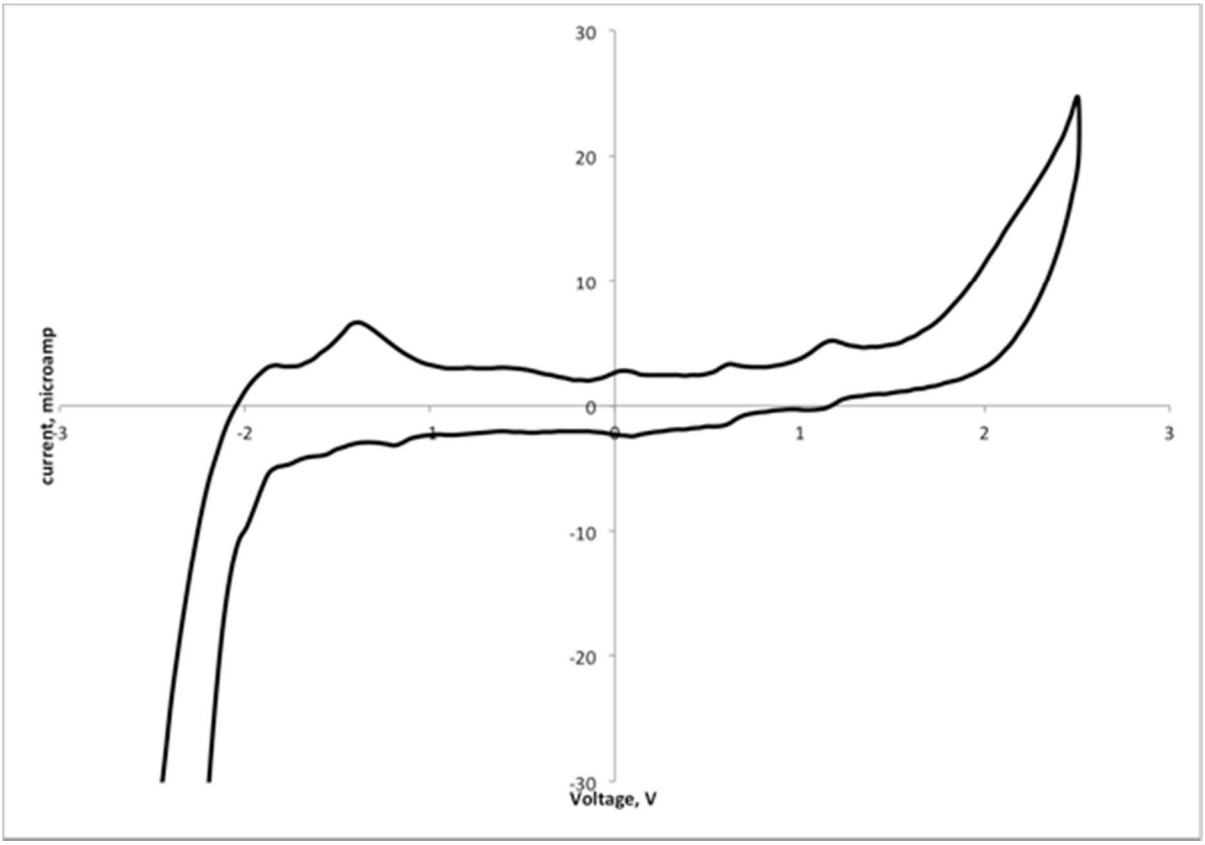

A monoruthenium complex containing, TPB, and a single TPY ancillary ligand, $[(TPB)Ru(TPY)]^+$ had a redox couple at 0.60V, which corresponds to the redox couple at 0.58 V in **30**.[1] The diruthenium complex $[(TPY)Ru(TPPZ)Ru(TPY)](PF_6)_4$ had an initial redox couple at +1.45 V vs Ag/AgCl. The redox couple at 1.14 V in **30** is 0.33 V lower, but this is likely attributed to greater electron density on the central ring of TPPY being donated to the opposing ruthenium as compared to TPPZ. The higher oxidation potential of the second ruthenium is also likely the reason CAN, which has an oxidation potential of 1.41 V vs Ag/AgCl, would not oxidize the mixed-valence system to the Ru(III)/Ru(III) system as readily.

Figure 4-8: CV scan of **30** from 0-1.5 V.

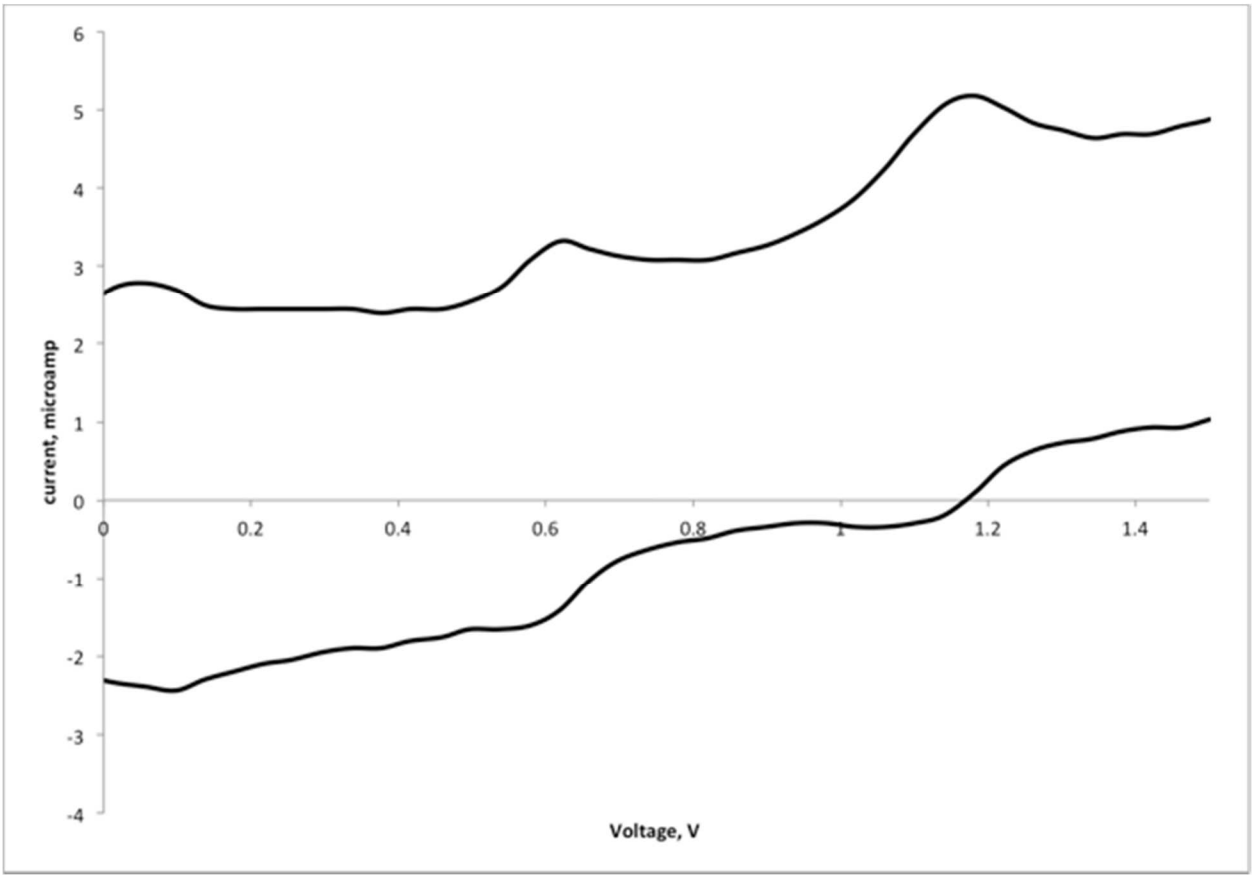

4.4 Conclusions

In this chapter, the synthesis of 2,3,5,6-tetra-(2-pyridyl)pyridine, TPPY, a ligand capable of asymmetrically binding two ruthenium centers, was performed. This novel ligand was used in the formation of a diruthenium complex, **30**, containing TPPY as a bridging ligand. The mixed-valence state of this complex has a strong NIR absorbance at 1370 nm. A triruthenium complex containing TPPY would likely be a good candidate for an electron reservoir complex. The complexes formed would be asymmetric, which could be used to promote directionality in the molecule. It would have strong coupling between the metal centers and a strong NIR absorbance. The lower oxidation potential of the ruthenium attached to the carbon of TPPY would allow the complex to reach its mixed-valence state more readily as well. The diruthenium complex would not be ideal for a reservoir dye because as mentioned in Chapter 1, a three-metal complex would be required, as a mixed-valence state would always need to be present. Photovoltaic performance for this complex is presented in Chapter 5.

Chapter 5

The fabrication and testing of dye-sensitized solar cells using mono-, di-, and triruthenium polypyridine complexes as dyes.

5.1 Introduction

The compounds prepared in the previous chapters were tested for their effectiveness in dye-sensitized solar cells by subjecting them to a variety of techniques. Characterization of solar cells is either done by analyzing the full area of the cell, to determine the effectiveness of the cell as a whole, or by using mapping or imaging techniques to investigate minor defects and imperfections.[1] Because the effectiveness of the dye as a whole is of more concern, all testing performed was done using a full area characterization.

Obtaining an *IV* curve (*I* = current, *V* = voltage) can elucidate the most basic and important solar cell measurements. An *IV* curve is obtained by subjecting the cell to varying bias voltages while measuring the corresponding current.[2] When performed under illumination, the *IV* curve obtained can give the following information:

1. Open-circuit voltage (V_{oc}) – The voltage across the terminals of the cell when disconnected from a circuit.
2. Short-circuit current (I_{sc}) – The current through the cell at 0 V, or when the cell is short-circuited.
3. Max Power (P_{max}) – Maximum value for V x I.
4. Max voltage and max current (V_{max}, I_{max}) –Voltage and current at maximum power.
5. Fill factor (*FF*) – The ratio of P_{max} to V_{oc} x I_{sc}.
6. Efficiency (η) – Overall percentage of solar energy converted to electricity.
7. Current density (*J*) – Current output per area of solar cell, either J_{sc} or J_{max}, can also be given.[2]

[2] 1 cm^2 cells were used, which makes the values for *I* in mA = the value of *J* in mA/cm^2 for the cells characterized herein.

A sample *IV* curve is presented in Figure 5-1 illustrating the parameters described above. V_{oc} is found at the point where the applied voltage is equal to the voltage generated by the cell, resulting in a net current of 0 A.[2] The I_{sc} is found at the point when applied voltage is at 0 V.[2] P_{max} can be found by multiplying the current by the corresponding voltage and determining the maximum value.[2] The voltage and current values at P_{max} are V_{max} and I_{max} respectively.[2] The fill factor can be found by finding the ratio of the product of the max voltage and current values to the product of the short-circuit current and open-circuit voltage as seen in Equation 5-1.[2]

Equation 5-1

$$FF = \frac{I_{max} \, x \, V_{max}}{I_{sc} \, x \, V_{oc}}$$

Figure 5-1: Sample *IV* and Power Curve.

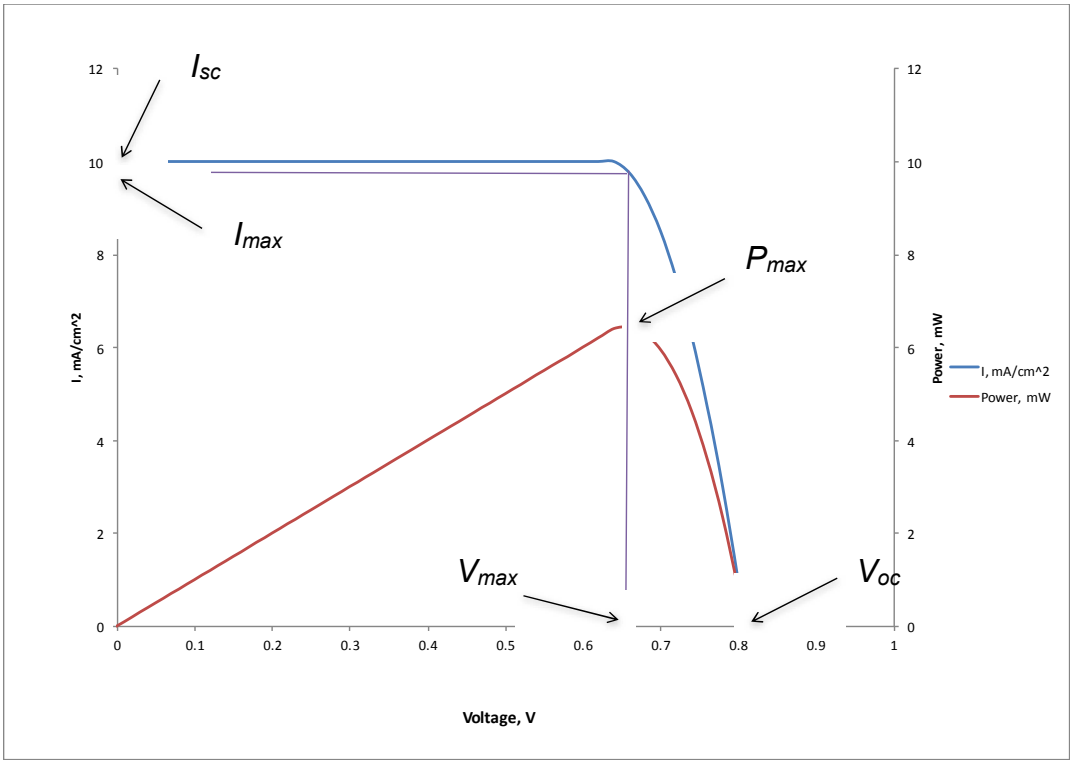

The overall efficiency of the cell is found by dividing P_{max} by the power of the incident light (P_{in}) as seen in Equation 5-2.[2] Efficiency is often presented in terms of open circuit voltage, short circuit current, and fill factor and Equation 5-3 represents this.

Equation 5-2

$$\eta\% = \frac{P_{max}}{P_{in}} x\ 100\% = \frac{I_{max}\ x\ V_{max}}{P_{in}}\ x\ 100\%$$

Equation 5-3

$$\eta\% = \frac{I_{sc}\ x\ V_{oc}\ x\ FF}{P_{in}}\ x\ 100\%$$

Industry standard solar cell characterization is done with solar simulators with a light intensity of 100 mW/cm^2 (1 kW/m^2, one-sun illumination).[1] All cells that were studied herein had areas of 1 cm^2, and light with power of 100 mW was impinged on the cell for all measurements. This simplifies Equation 5-2 to $\eta\% = P_{max}$ (Equation 5-4).

Equation 5-4

$$\eta\% = P_{max}$$

An IV curve can also be obtained in the absence of light. This can give important information about the overall integrity and construction of the solar cell. This can help determine whether performance problems are associated with the dye or with the cell fabrication.[2] A typical dark IV curve looks nearly identical in shape to one obtained in the light,

however there is little to no current through the voltage range up to V_{oc}, as obtained during illuminated scans (Figure 5-2). The little current that is present is called dark current. Most solar cells, including dye-sensitized solar cells, behave like diodes. As a result, the Ideal Diode Law, seen in Equation 5-5, can be applied.[2]

Figure 5-2: Sample dark current plot.

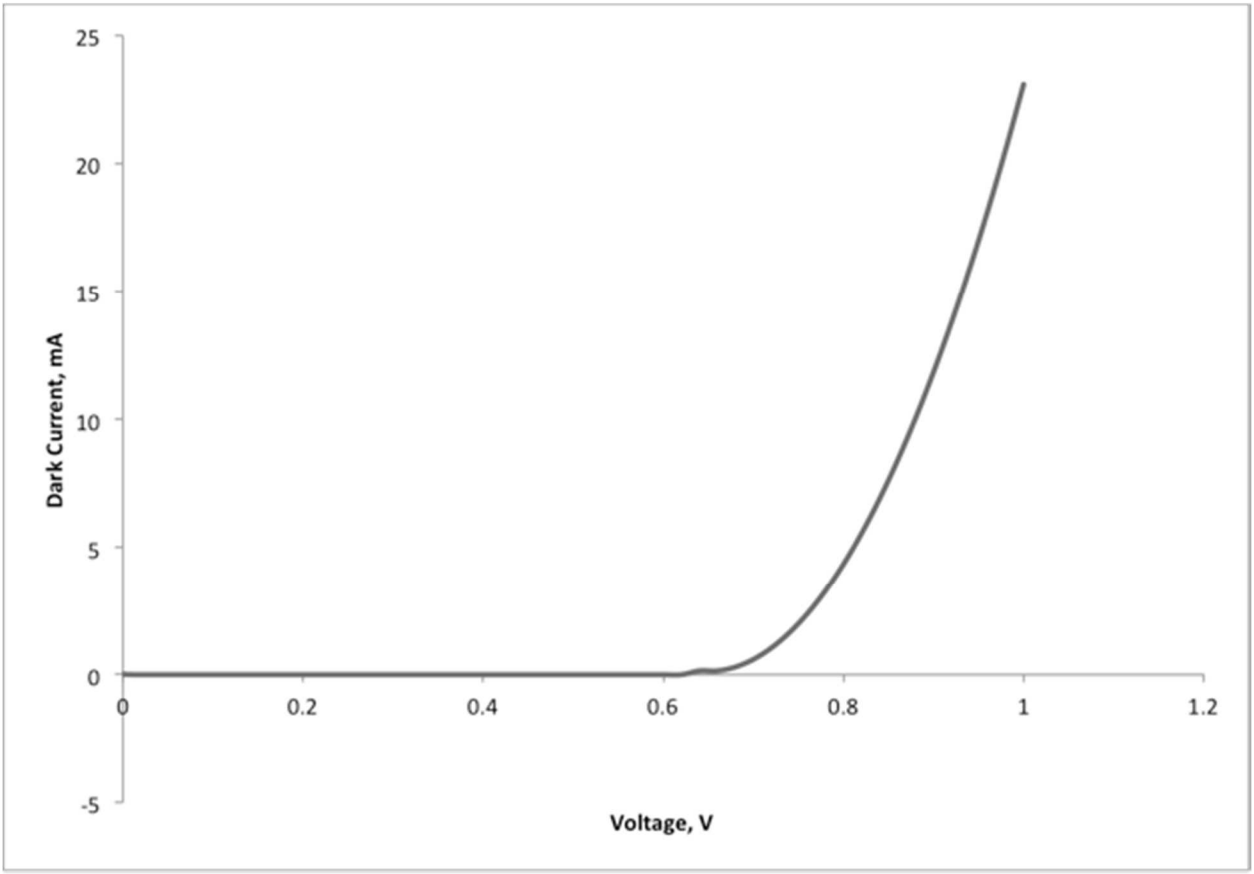

Equation 5-5

$$I = I_0(e^{\frac{qV}{kT}} - 1)$$

Here, I is the net current flowing through the diode, I_0 is the dark saturation current (**DCS**), or current flowing through the diode in the absence of light, V is the voltage applied

across the terminal, q is the absolute charge of an electron, 1.602 x 10^{-19} C, k is Boltzmann's constant, 1.381 x 10^{-23} J/K, and T is temperature in Kelvin.[2] Because a solar cell is an imperfect diode, an additional term in incorporated, n, called the ideality factor.[2] This is a measurement of the diode-like behavior of the solar cell. The ideality factor is incorporated into the Ideal Diode Law as seen in Equation 5-6.[2]

Equation 5-6

$$I = I_0(e^{\frac{qV}{nkT}} - 1)$$

Taking the natural log of each side of Equation 5-6 (when V > 50-100 mV, the -1 term can be neglected), Equation 5-7 is then obtained.[2] From this equation, it can be seen that plotting ln(I) vs voltage will give a linear graph with a slope equal to $q/(nkT)$ and an intercept equal to ln (I_0). As q, k and T are all constants, it is trivial to determine the ideality factor from the slope. An ideality factor close to 1 indicates low resistance in the cell and indicates good solar cell fabrication. A value of 2 or higher usually indicates some type of excessive resistance in the cell.[2]

Equation 5-7

$$ln\,(I) = ln(I_o) + \frac{qV}{nkT}$$

Solar cell data for all new complexes is presented in this chapter. All voltage and current measurements will be presented as well as an analysis of cell efficiencies.

5.2 Experimental

The TiO_2 layers, electrolyte, counter electrode, and cell construction were prepared using literature procedures using a commercial TiO_2 (aeroxide P25, Evonik Degussa),[3,4] as described below.

5.2.1 TiO_2 electrode preparation method

A solution was prepared by mixing acetylacetone (0.4 mL) and deionized water (4.0 mL). The solution (0.4 mL) was slowly added to the TiO_2 powder (1.2 g) and the mixture was ground with a mortar and pestle for 30 min. Deionized water (1.6 mL) was then added dropwise and the mixture was ground until a paste was achieved. A detergent (Triton X-100, 0.2 mL) was added to make the paste easier to spread on the transparent conducting oxide (TCO) glass. Fluorine doped tin oxide (FTO) coated pieces of glass from Pilkington Glass (2.5 cm x 2.5 cm, 12 Ω/cm^2) were used as the TCO. Two pieces of Scotch tape were applied parallel on opposite edges, followed by two additional pieces of Scotch tape perpendicular to these two creating a 1 cm $\times$ 1 cm square area surrounded by Scotch tape. A few drops of the TiO_2 paste were placed into the well created by the tape, and a glass rod was slid over the tape making a smooth layer, giving a film thickness of equal to the thickness of piece of tape, which is roughly 0.1 mm. After removing the tape, the plates were then heated at 450 °C in a tube furnace for 30 min to sinter the TiO_2. After sintering, the TiO_2 layered pieces of glass were placed in a freshly prepared 0.2 M solution of $TiCl_4$ in water and were allowed to sit overnight. After rinsing, the electrodes were heated again at 450 °C for 30 min.

5.2.2 Electrolyte for the solar cell

Iodine (0.245 g), lithium iodide (0.129 g), 4-tertbutylpyridine (0.680 g), and 1-methyl-3-propylimidazolium iodide (1.525g) were dissolved in acetonitrile and diluted to 10 mL to create a solution of 0.1 M I_2, 0.1 M LiI, 0.6 M 1-methyl-3-propylimidazolium iodide, and 0.5 M 4-tertbutylpyridine.

5.2.3 Counter electrode for solar cell

To create a thin platinum layer for the counter electrode, 0.21 mL of a solution of H_2PtCl_6 in isopropyl alcohol (0.05 mM) was placed on the conductive side of a 2.5 cm x 2.5 cm FTO plate. The solution covered the entirety of the electrode. The electrode was heated at 450 °C to leave a layer of approximately 0.010 mg of platinum and the electrode had a metallic sheen when completed.

5.2.4 Assembly and testing of Solar Cells

A TiO_2 coated electrode was placed in 5 mL of a 0.2 mM solution of the dye to be tested. This was allowed to soak for 18 h to make sure the dye was firmly bound to the TiO_2. After removing the electrode and rinsing with EtOH until the washes were colorless, the counter electrode was placed on top of the TiO_2 and the two were held together with small binder clips. A few drops of the electrolyte were placed near the edge between the plates and capillary action drew the electrolyte in between the plates. The cell was then attached to a Keithley 2400 source voltmeter via alligator clips. A voltage was applied in a sweep from -1 to 1 V in 0.02 V increments. This was done under both illumination and while in the dark to obtain the light and dark IV curves. Illumination was provided by a Newport solar simulator with a 150 W lamp.

The manufacturer states this provides 100 mW/cm^2 of intensity at the cell and it was assumed that the full 100 mW/cm^2 was applied. The lamp was 30 cm above the cell and a black curtain surrounded the setup.

5.3 Results and Discussion

5.3.1 Solar cell data of standards N3 and Black Dye

The industry standards, **N3** dye and **Black Dye**, were used to determine the overall quality of the solar cell fabrication. The results for the current density, power, dark current, and ln(dark current) are seen in Figures 5-3 through 5-6. The results for V_{oc}, J_{sc}, V_{max}, J_{max}, P_{max}, FF, η, ideality factor (IF), and dark current saturation (DCS) are listed in Table 5-1. The overall efficiency obtained using **N3** was 1.50% while **Black Dye** had an efficiency of 2.11%. The literature values for both of these complexes are listed at 10.4%.[5] The open circuit voltages obtained experimentally for **Black Dye** and **N3** were 0.65 V and 0.62 V respectively. These are close to their respective literature values of 0.72 V for **Black Dye** and 0.73 V for **N3**. The major difference in performance is due to the current output. The maximum reported current density for both dyes is listed at 20 mA/cm^2.[5] The current obtained experimentally, both short-circuit and max, were significantly lower than the literature values resulting in an overall lower power and efficiency.

Table 5-1: Solar data for **N3** and **Black Dye**.

Compound	V_{oc} (V)	J_{sc} (mA/cm^2)	P_{max} (mW)	FF (%)	η (%)	IF	DCS (mA)
N3	0.62	4.81	1.50	51	1.50	3.90	0.00169
Black Dye	0.65	6.24	2.11	52	2.11	4.28	0.004022

Figure 5-3: Current density and power plots for **N3**.

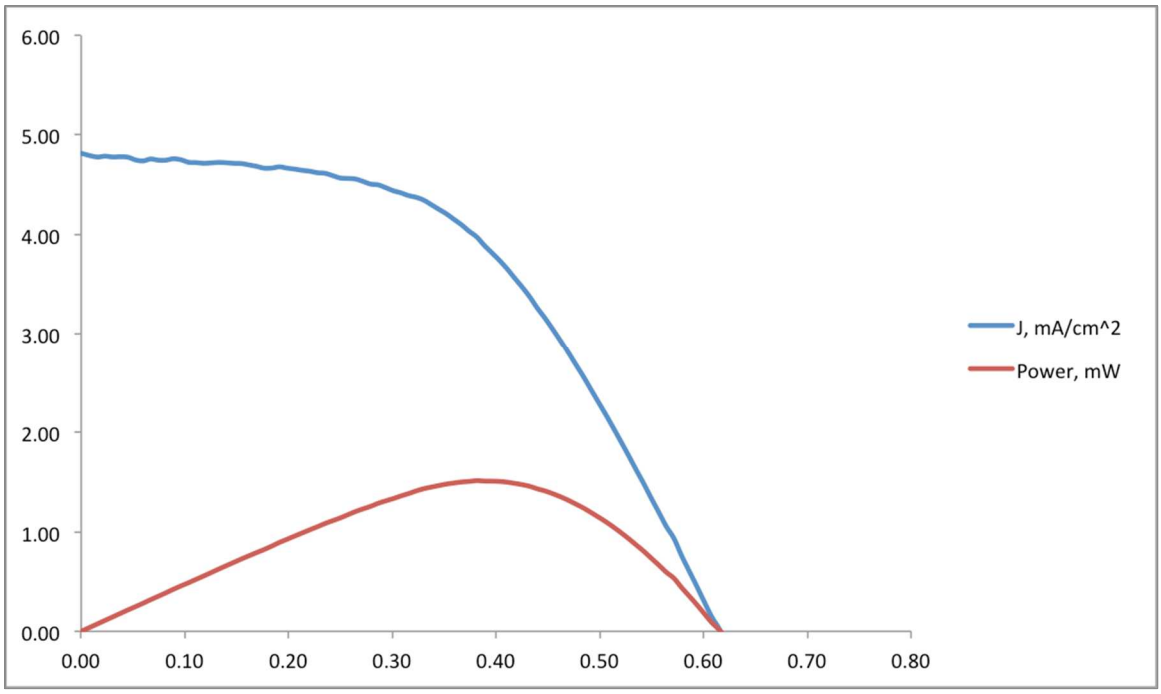

Figure 5-4: Dark current and dark current log plot for **N3**.

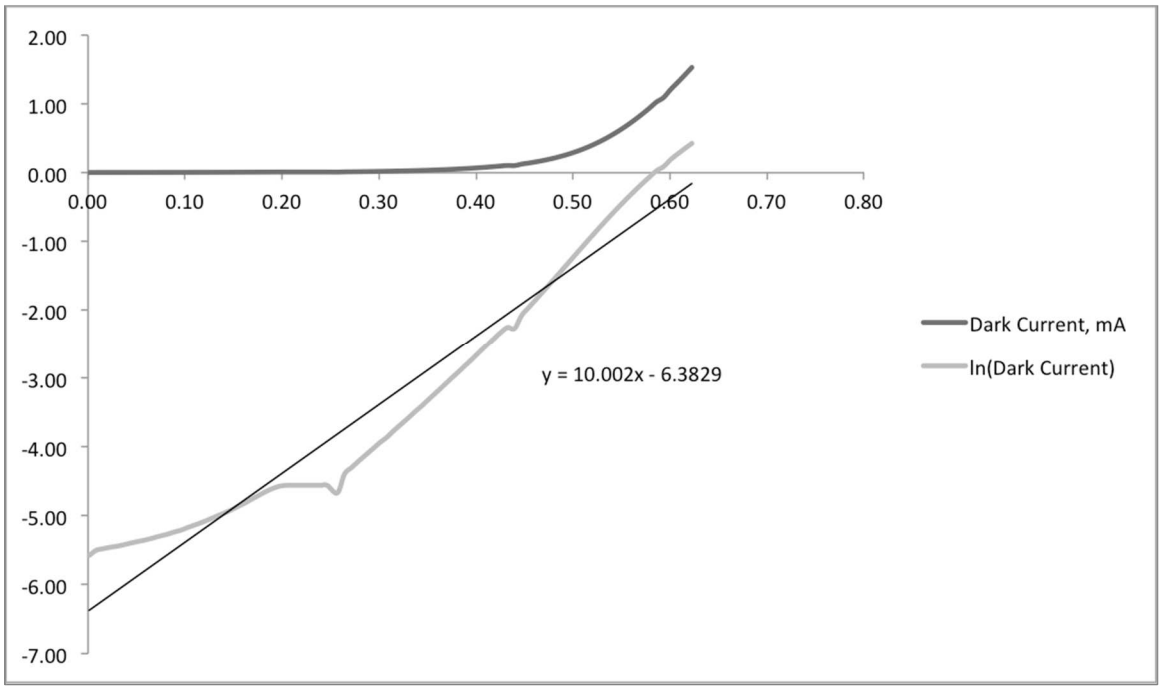

Figure 5-5: Current density and power plots for **Black Dye.**

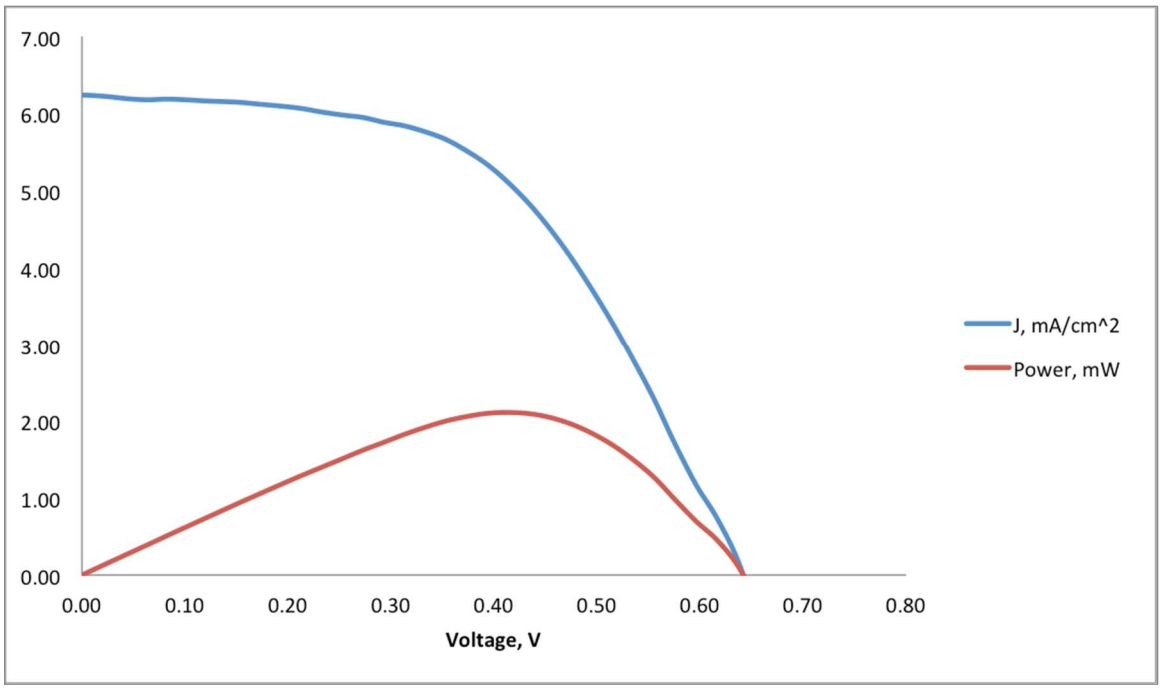

Figure 5-6: Dark current and dark current log plot for Black Dye.

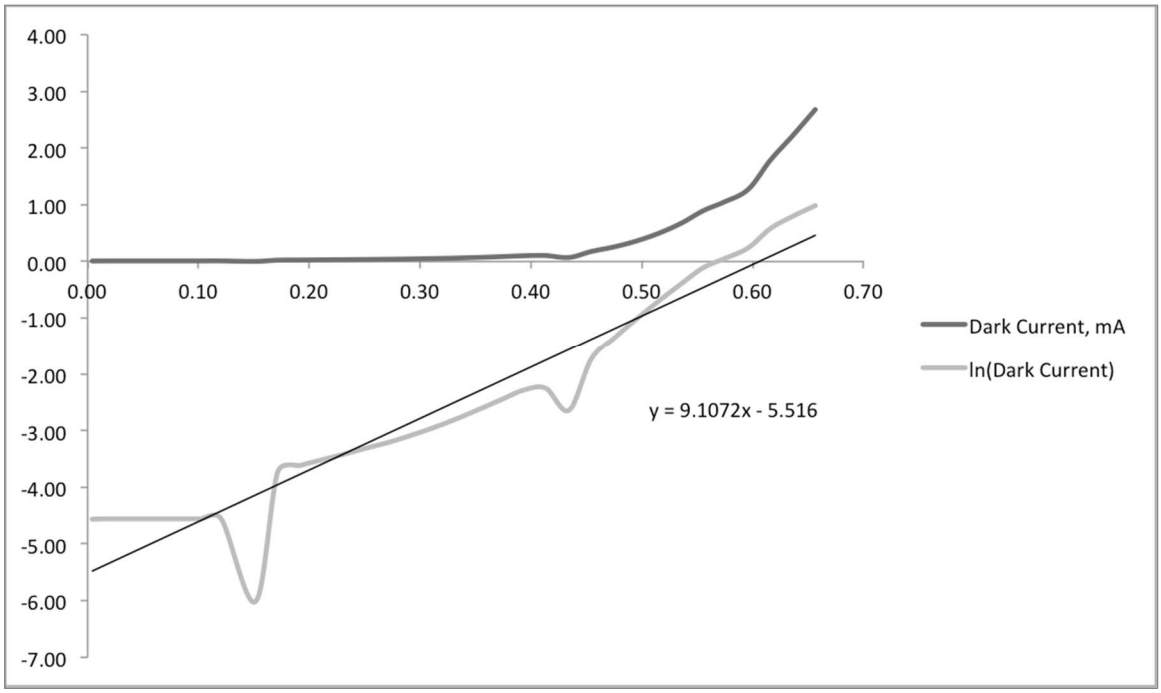

The literature value for the fill factor is around 70% for both standard dyes. Experimentally, 51% and 52% were obtained for **N3** and **Black Dye**. The dark current plot of the two revealed why the fill factor and overall current output was a lot lower than expected. An ideality factor around 4 was obtained for both dyes and this is quite indicative of excessive resistance in the cells.

When cells have a high series resistance, it is usually a problem with resistance of the cell material to current flow, particularly through the contacts.[6] In silicon cells, this is often seen as resistance between the metal contacts and the silicon as well as resistance in the metal contacts of the cell.[7] In dye-sensitized solar cells, resistance of the transparent conducting oxide on the glass plate is often the main cause.[8] In these cells, the series resistance likely comes from the resistance of the fluorine-doped tin oxide plates. The manufacturer's value for the resistance in the FTO plates used was listed as 12 Ω/cm^2. The Gratzel group reported that cells made with **Black Dye** using fluorine-doped tin oxide plates with a resistance of 1.8 Ω/cm^2 had efficiencies of 10.2%.[5] Since the FTO plates used in these experiments had 6.7 times the resistance of those of the Gratzel group, it is likely the cause of lower efficiencies. The effects of series resistance can be seen in the example data in Figure 5-7. The current output stays steady until reaching higher bias voltage, where a quicker drop in current is then seen.[2]

Figure 5-7: An example of increasing series resistance.

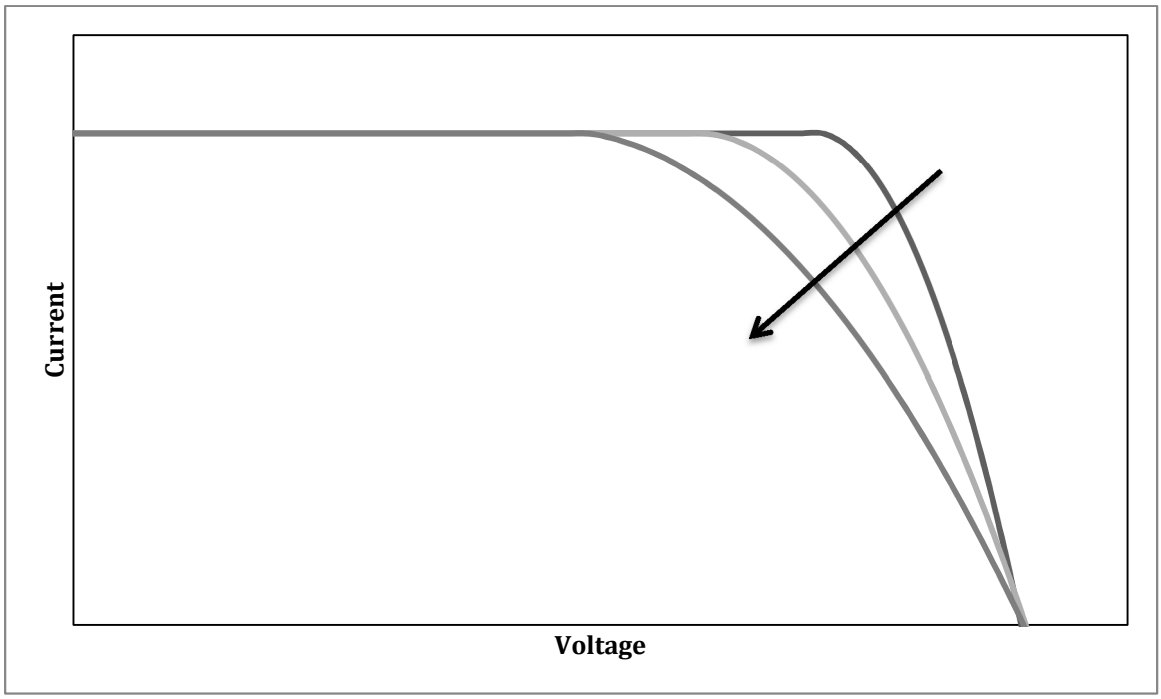

Parallel, or shunt resistance, arises from leakage of current through the cell, or around the cell edges.[2, 9] Slight defects in the semiconductor can also cause shunt resistance. Instead of following the expect current pathways, alternative routes are taken by the electrons back to the dye.[2, 9] The effects of parallel resistance can be seen in the example data in Figure 5-8.[2] The current slowly drops as bias voltage is increased, but drops normally at higher bias voltages. Figure 5-2 and 5-4 indicate that both parallel resistances are present in the cell.

Figure 5-8: An example of increasing parallel (shunt) resistance.

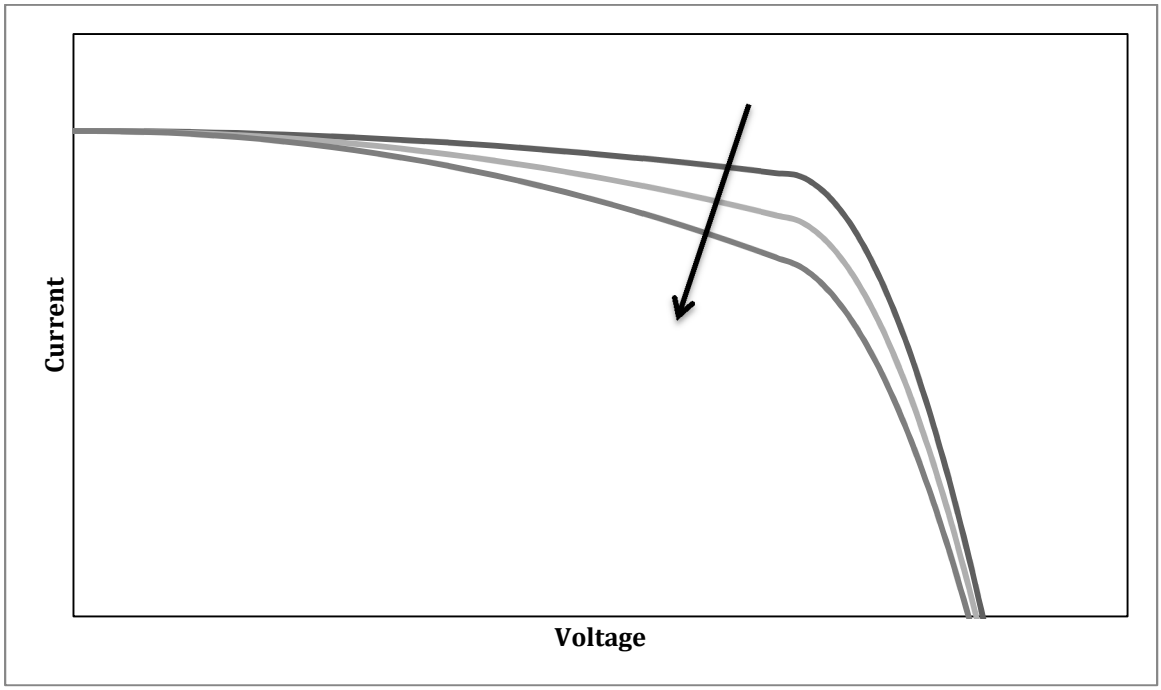

5.3.2 Solar cell data of TPPZ bridged and bis-TPPZ bridged complexes

The results for V_{oc}, J_{sc}, V_{max}, J_{max}, P_{max}, FF, η, ideality factor (IF), and dark current saturation (DCS) for the TPPZ bridged and bis-TPPZ bridged compounds are listed in Table 5-2. The current density and power plots for these complexes are seen in Figures 5-9 through 5-11. The efficiencies obtained are all less than 0.05% with the diruthenium complex **17** being exceptionally low. The cells experience the same series and parallel resistance seen in the **Black Dye** and **N3** cells. Given that these have no attaching ligands present, it is not surprising current generation is low. While the plates did have the green and green blue hue seen in the complexes, the color was not as intense as the color of the complexes which had attaching ligands.

Table 5-2: Solar data for the TPPZ bridged and bis-TPPZ bridged compounds.

Compound	V_{oc} (V)	J_{sc} (mA/cm^2)	P_{max} (mW)	FF (%)	η (%)	IF	DCS (mA)
15	0.19	0.38	0.021	29	0.02	12.93	0.086
17	0.04	0.018	0.00025	34	0.00025	4.78	0.015
22	0.19	0.29	0.020	36	0.020	2.92	0.012

Figure 5-9: Current density and power plots for **15**.

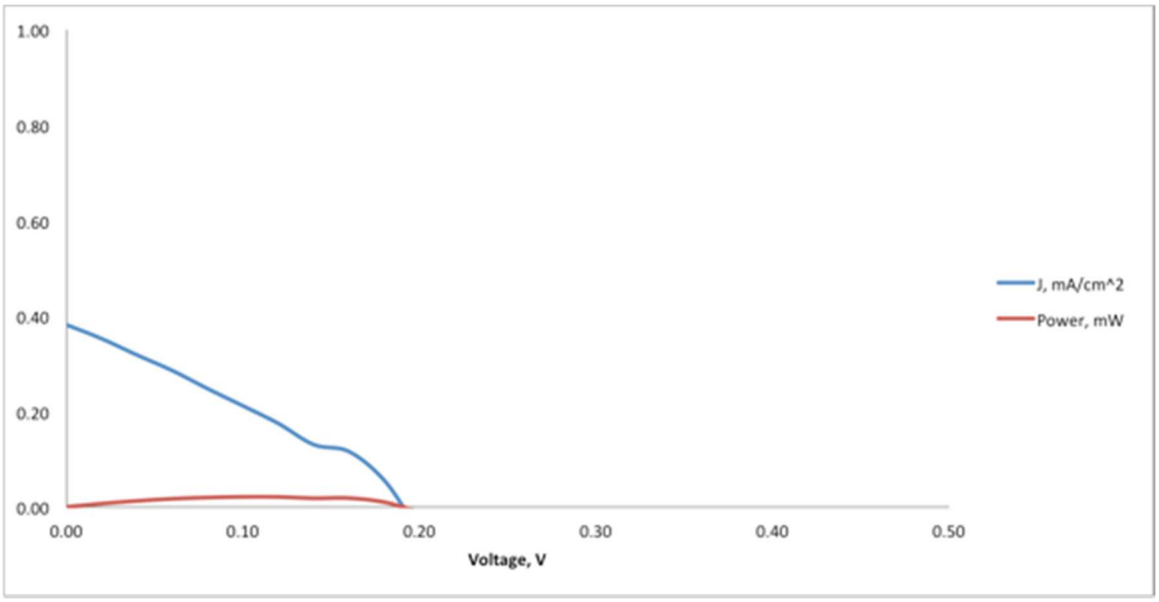

Figure 5-10: Current density and power plots for **17**.

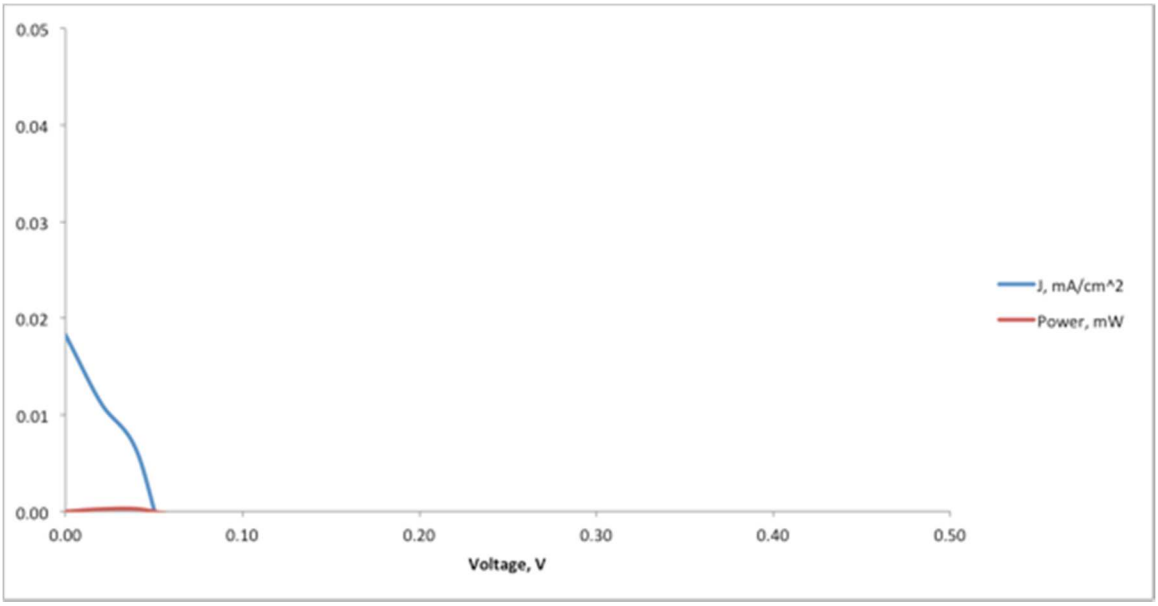

Figure 5-11: Current density and power plots for **22**.

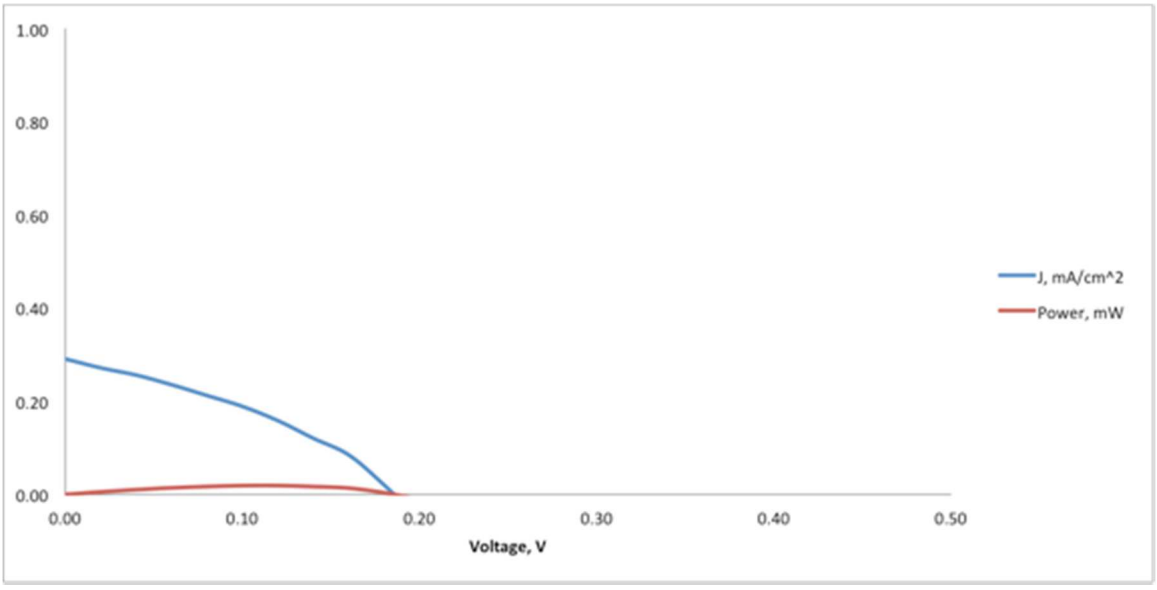

5.3.3 Solar cell data of BIM bridged and bis-BIM bridged complexes

The solar cell data for the BIM bridged and bis-BIM bridged compounds are listed in Table 5-3. The current density and power plots for these complexes are seen in Figures 5-12 through 5-14. The cells experience the same series and parallel resistance seen in the **Black Dye** and **N3** cells. The complex **26** has the highest efficiency of the three, 0.095%. This is likely due to the DEBPY ligands, as these would be adhered to the titanium dioxide much more strongly than BPY alone. The cell containing DEBPY was also a much more intense orange color. The dark current saturation is also significantly lower in that cell. It is possible that that cell was of much better quality than the others. The low ideality factor also suggests this.

Table 5-3: Solar cell data for the BIM bridged and bis-BIM bridged compounds.

Compound	V_{oc} (V)	J_{sc} (mA/cm^2)	P_{max} (mW)	FF (%)	η (%)	IF	DCS (mA)
11	0.20	0.20	0.018	33	0.018	8.44	0.0093
25	0.20	0.37	0.026	35	0.026	6.47	0.0462
26	0.27	1.01	0.095	35	0.095	1.11	0.0000081

Figure 5-12: Current density and power plots for **11**.

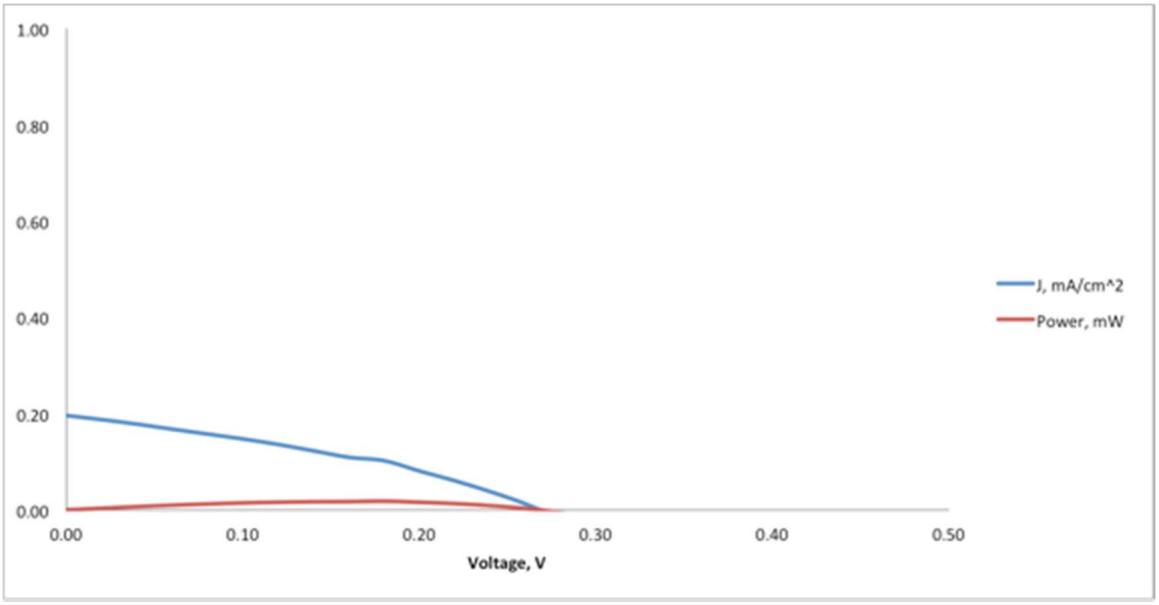

Figure 5-13: Current density and power plots for **25.**

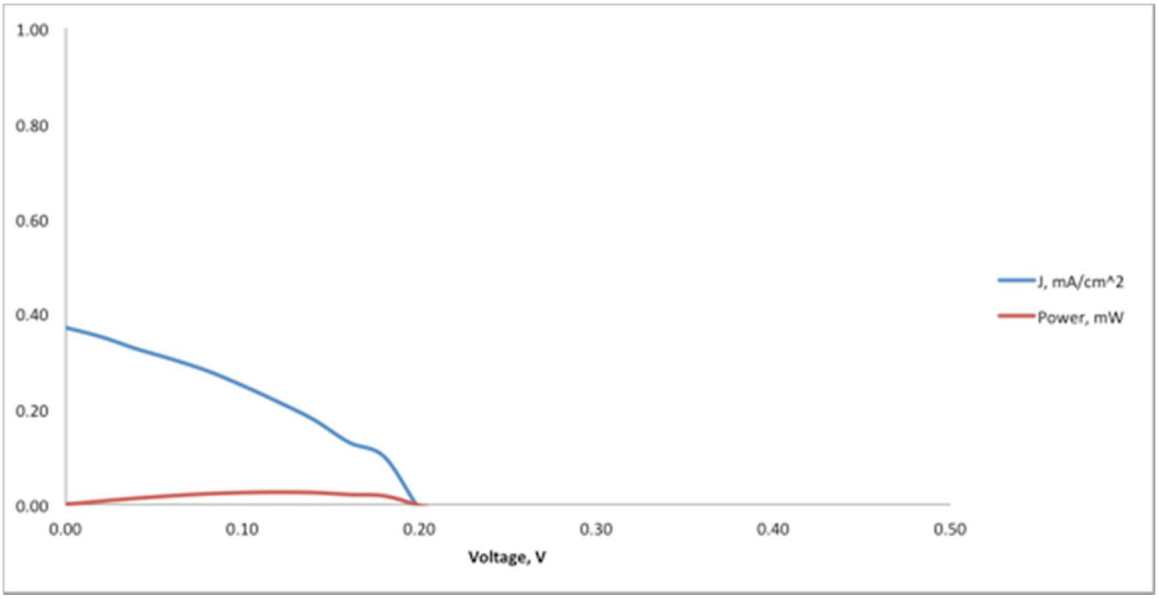

Figure 5-14: Current density and power plots for **26**.

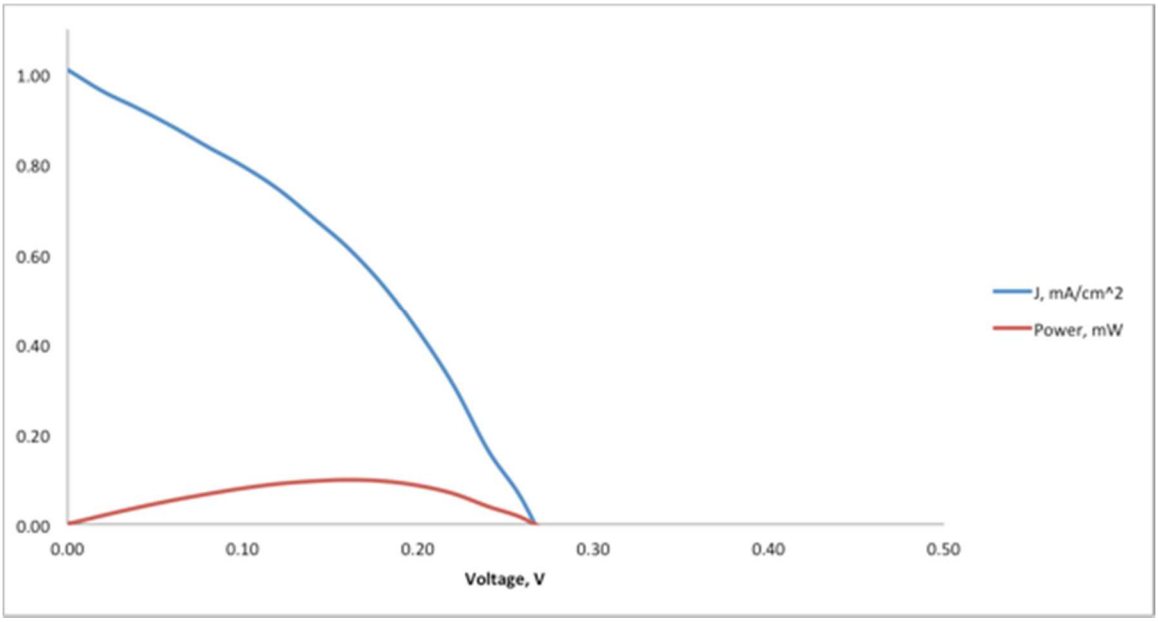

5.3.4 Solar cell data of BPM bridged and bis-BPM bridged complexes.

The solar cell data for the BPM bridged and bis-BPM bridged compounds are listed in Table 5-4. The current density and power plots for these complexes are seen in Figures 5-15 through 5-17. The cells experience the same series and parallel resistance seen in the Black Dye and N3 cells. The complex **23** has the highest efficiency of the three, 0.14%. It was expected that the complex with the DEBPY ligands would adhere more strongly to the TiO_2, providing a much stronger current. It is not entire clear why this is the case, although it might be attributed to a short-circuit in the cell.[10]

Table 5-4: Solar cell data for the BPM bridged and bis-BPM bridged compounds.

Compound	V_{oc} (V)	J_{sc} (mA/cm^2)	P_{max} (mW)	FF (%)	η (%)	IF	DCS (mA)
12	0.25	0.74	0.072	39	0.072	1.47	0.000090
23	0.40	0.86	0.14	38	0.14	2.35	0.00064
24	0.17	0.19	0.010	31	0.010	3.10	0.015

Figure 5-15: Current density and power plots for **12**.

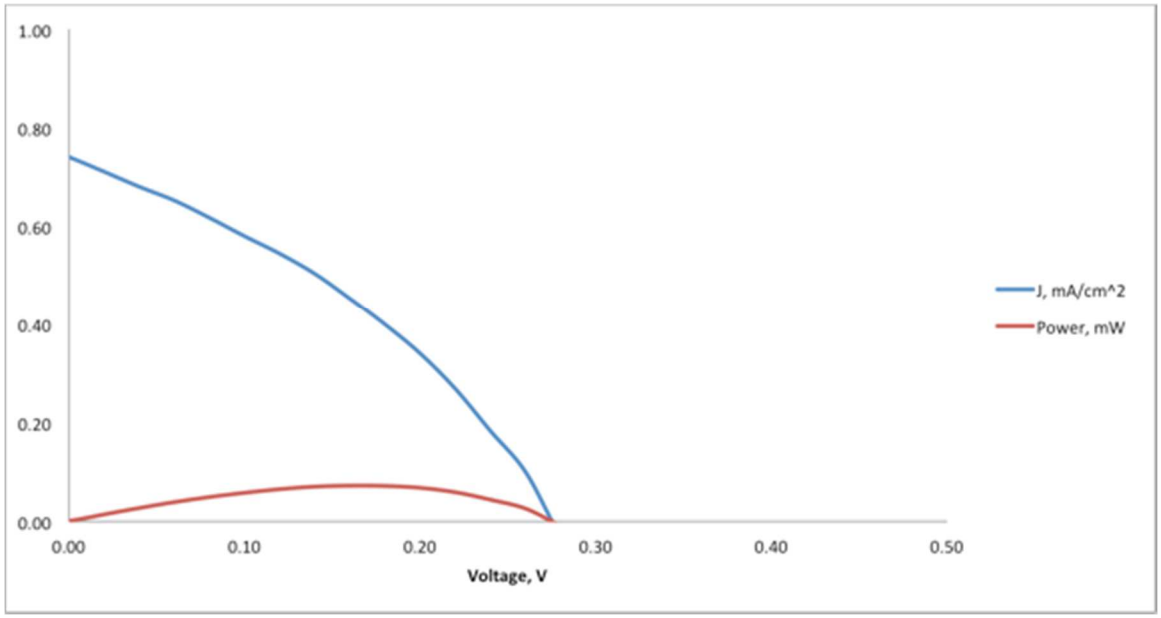

Figure 5-16: Current density and power plots for **23**.

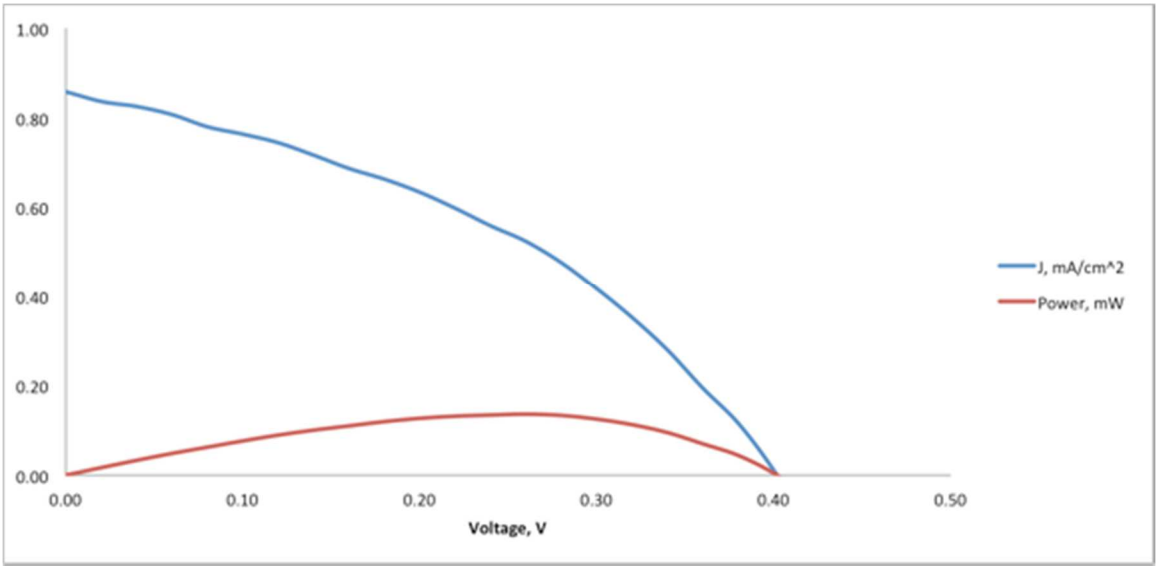

Figure 5-17: Current density and power plots for **24**.

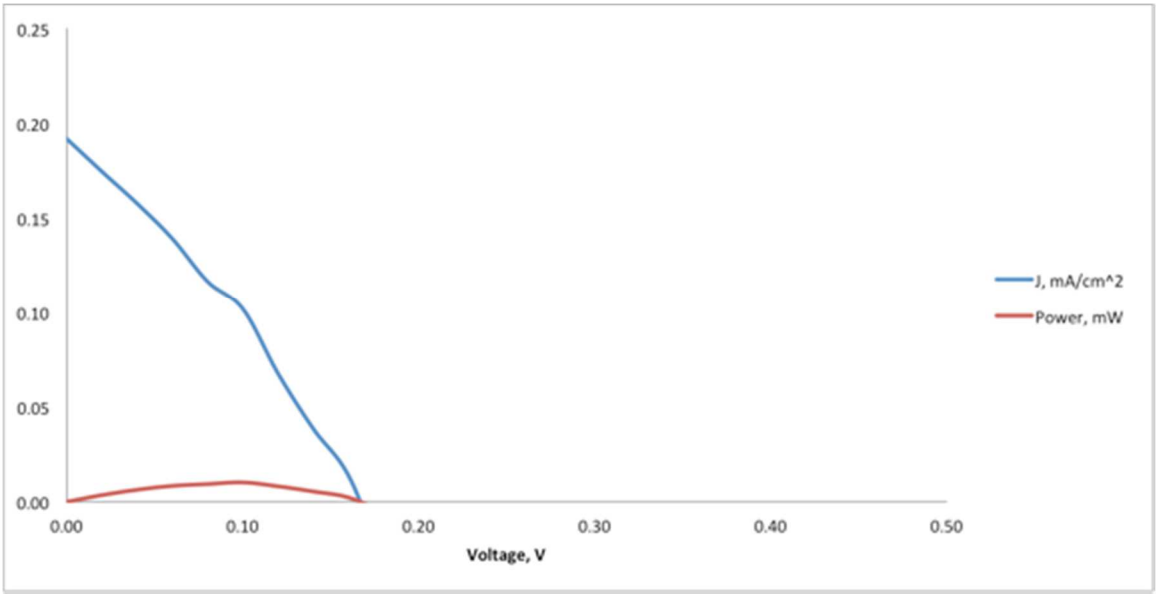

5.3.5 Solar cell data of mixed bridged complexes

The solar cell data for the mixed TPPZ and BPM bridged compounds are listed in Table 5-5. The current density and power plots for these complexes are seen in Figures 5-18 through 5-21. The cells experience the same series and parallel resistance seen in the Black Dye and N3 cells. The bis-DCBPY complex **21**, has the highest efficiency of the these at, 0.067%.

Table 5-5: Solar cell data for the mixed TPPZ and BPM bridged compounds.

Compound	V_{oc} (V)	J_{sc} (mA/cm^2)	P_{max} (mW)	FF (%)	η (%)	IF	DCS (mA)
19	0.26	0.39	0.036	36	0.036	4.72	0.024
20	0.22	0.35	0.025	32	0.025	5.22	0.028
21	0.44	0.39	0.067	39	0.067	7.64	0.014

Figure 5-18: Current density and power plots for **19.**

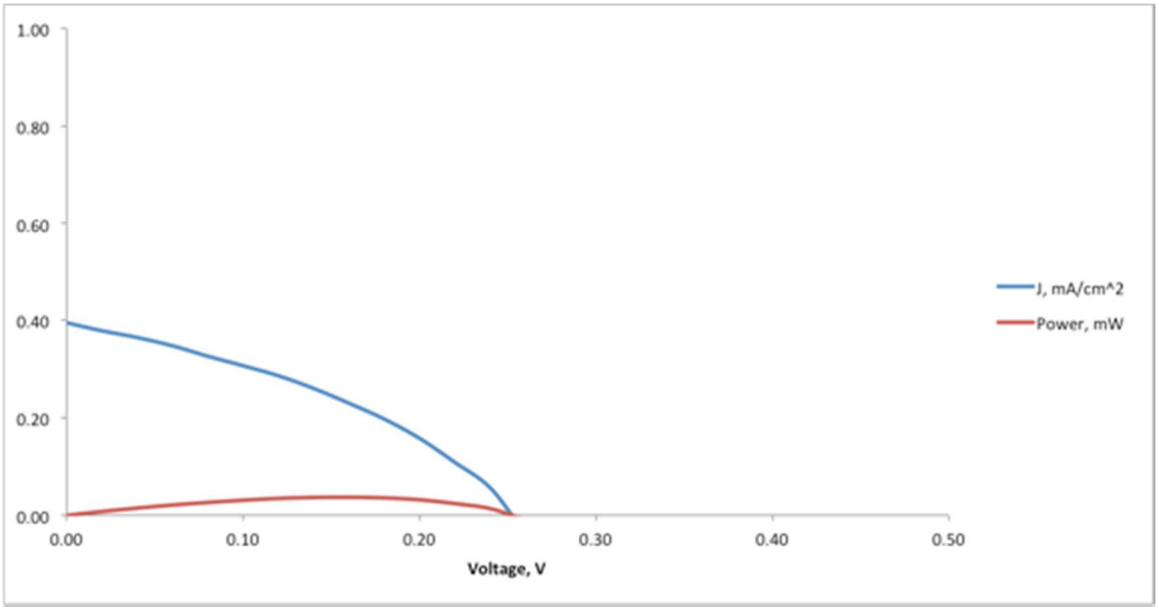

Figure 5-19: Current density and power plots for **20.**

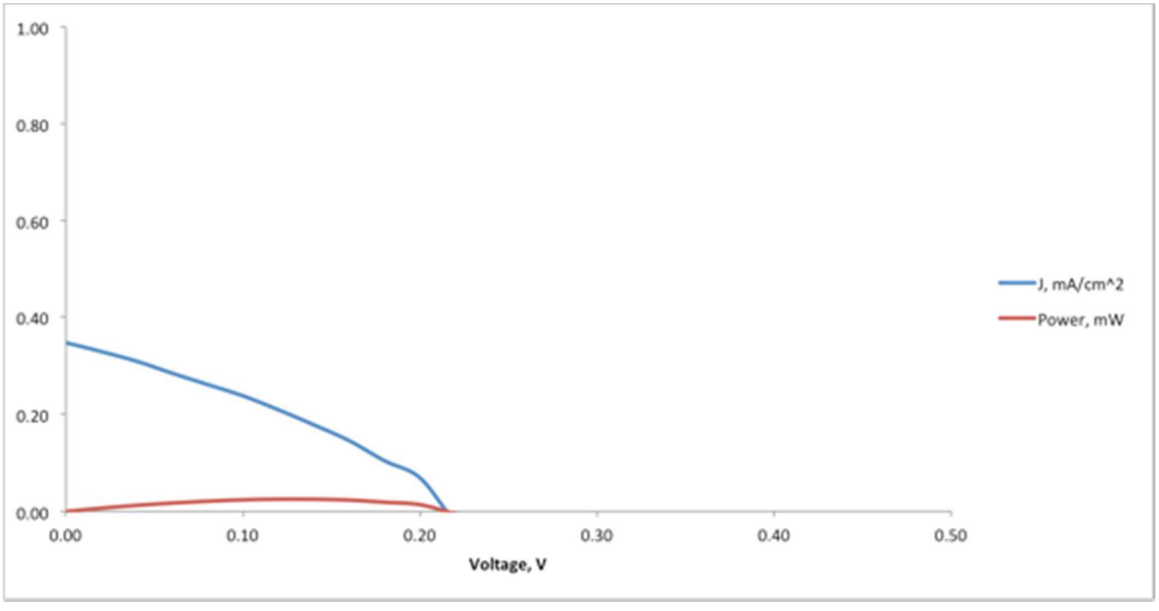

Figure 5-20: Current density and power plots for **21.**

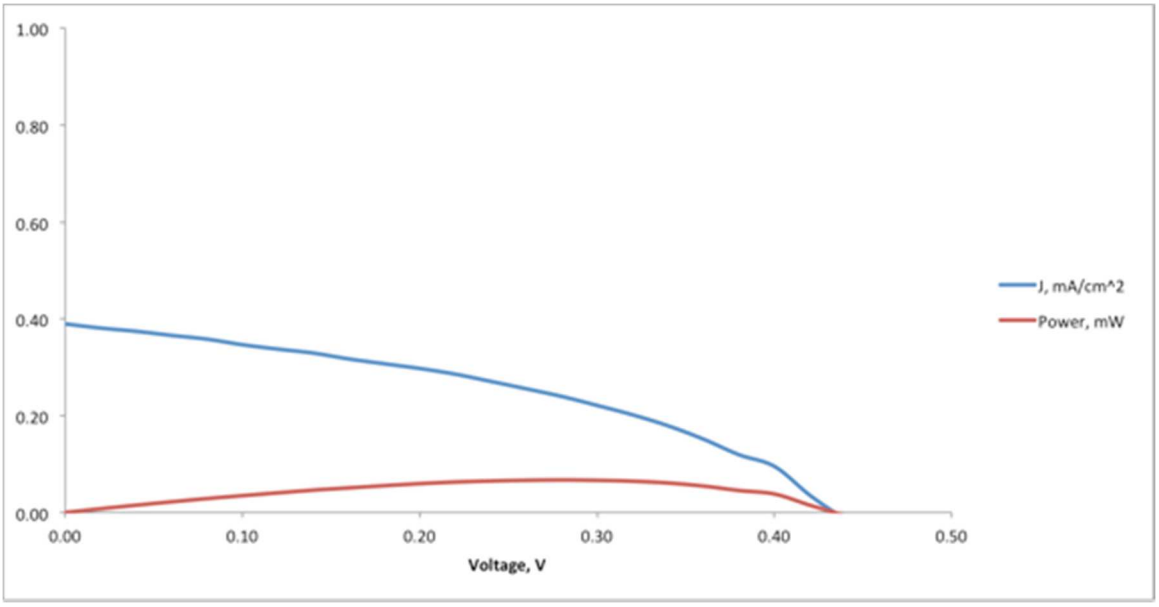

5.3.6 Solar cell data of TPY capped TPPZ and TPPY bridged complexes.

The solar cell data for the TPY capped TPPZ and TPPY bridged complexes are listed in Table 5-6. The current density and power plots for these complexes are seen in Figures 5-22 through 5-23. The cells experience the same series and parallel resistance seen in the Black Dye and N3 cells. The TPPZ bridged complex, had a slightly higher efficiency of 0.074%.

Table 5-6: Solar cell data for the TPY capped TPPZ and TPPY bridged complexes.

Compound	V_{oc} (V)	J_{sc} (mA/cm^2)	P_{max} (mW)	FF (%)	η (%)	IF	DCS (mA)
$[((TPY)Ru)_2(TPPZ)](PF_6)_4$	0.29	0.61	0.074	42	0.074	8.33	0.032
30	0.30	0.48	0.049	34	0.049	4.74	0.034

Figure 5-21: Current density and power plots for $[((TPY)Ru)_2(TPPZ)](PF_6)_4$.

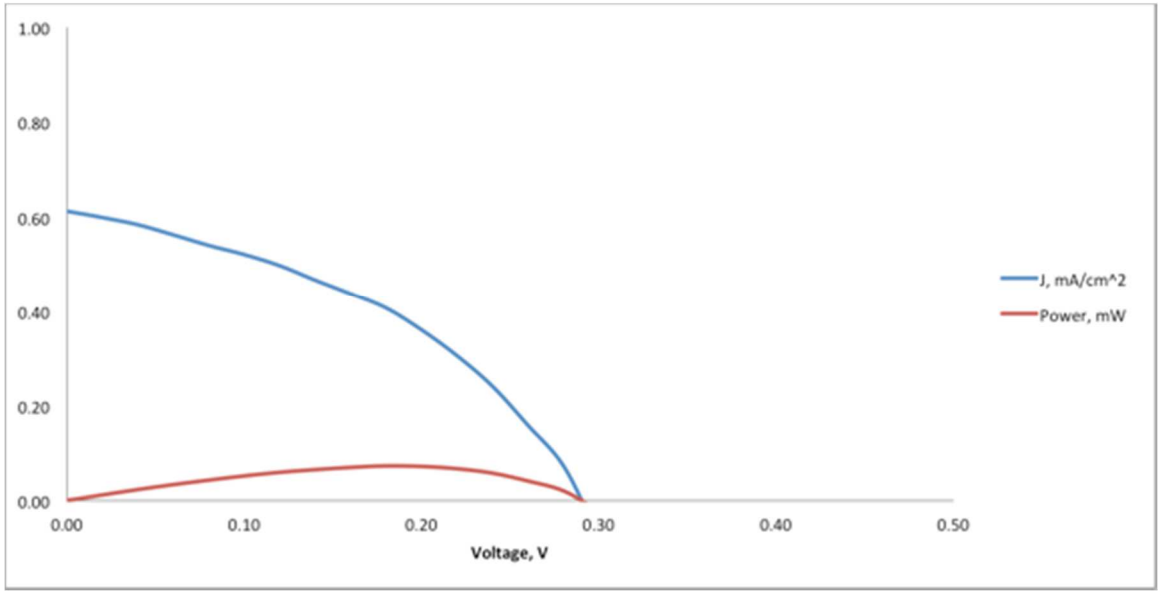

Figure 5-22: Current density and power plots for **30**.

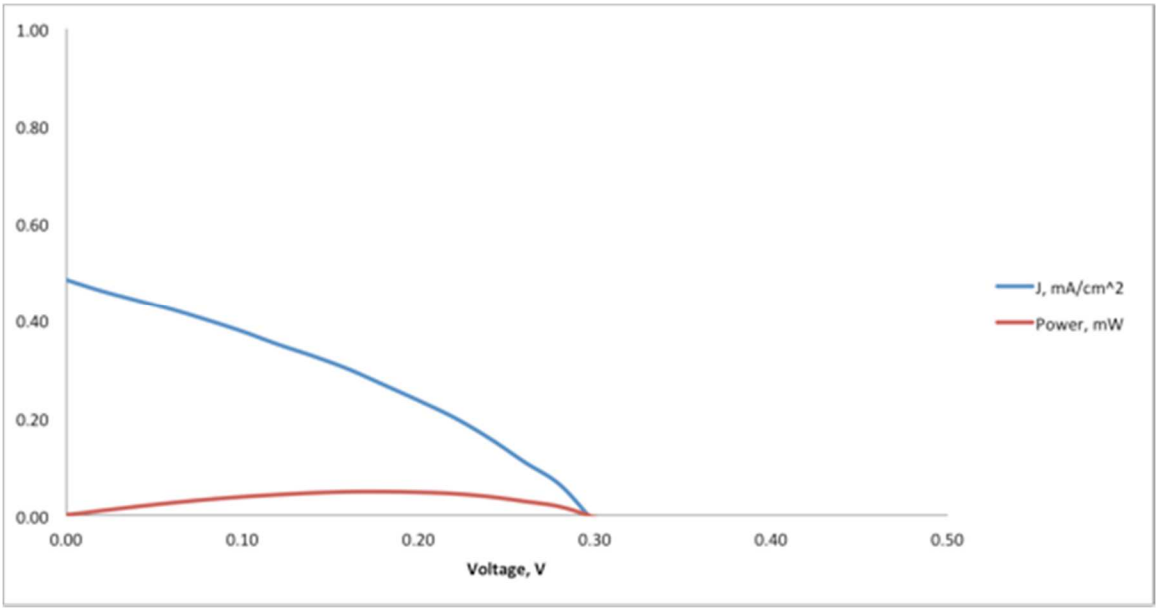

5.3.7 Summary of current density and power plots

Given that the sheet resistance of the FTO was around 6.7 times more resistance than seen in better performing cells, it is not surprising that all of the efficiencies were low. In general, resistance and current are inversely related as seen in Equation 5-8. If the voltage is considered constant, a 6.7 times decrease in resistance would result in a 6.7 times increase of current. This would in turn cause a 6.7 times increase in efficiency according the equation 5-3. Multiplying the efficiencies of **N3** and **Black Dye** by 6.7 would give efficiencies of 10.1% and 14.1% respectively. The 6.7 times multiplier is not exact, given that **Black Dye**'s highest reported efficiency is listed as 10.4%.

Equation 5-8

$$V = I\Omega$$

If the 6.7 times multiplier is applied to the efficiencies of all of the multi-metal dye solar cells, which were around 0.05-0.10%, this gives them a range of around 0.3 – 0.7%. The reported efficiency of a solar cell made with the dye $[Ru(TPY)_2]^{2+}$ is 0.5%.[11] Larger dendrimer ruthenium complexes, with either a carbomethoxy or carboxy attaching ligand and a hydrogen as the R group (Figure 5-24), had efficiencies of 0.01% and 0.1% respectively.[11] A series of *bis*-bipyridine complexes (Figure 5-25) has efficiencies of 0.009, 0.033, and 0.051% from left to right.[12] The cyclometalated diruthenium complex in Figure 5-26 had an efficiency of 1.13%.[13] These dyes are similar in structure to the dyes used in this chapter, and the cells made with these dyes all have efficiencies that are similar to the cells used in this chapter. It appears that larger multiruthenium dyes have lower efficiencies, while having higher molar absorptivity in the visible region.[11] This is seen in all of the complexes present in this dissertation as well.

Figure 5-23: Dendrimer ruthenium complexes, with either a carbomethoxy or carboxy attaching ligand.

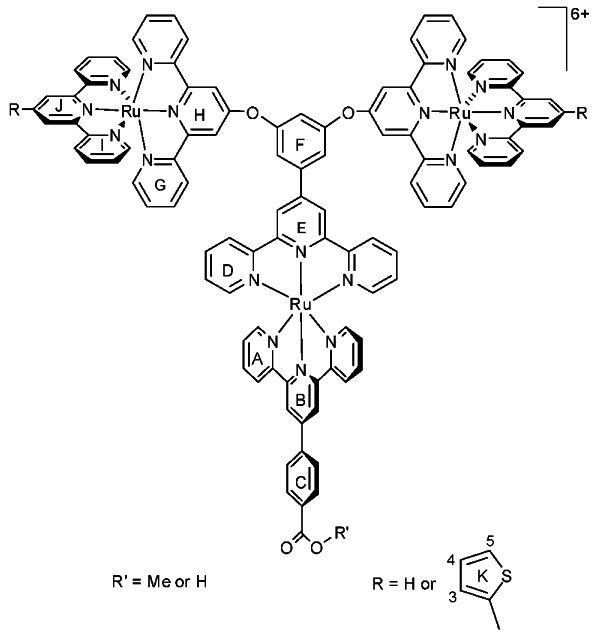

Figure 5-24: *Bis*-bipyridine complexes with efficiencies of 0.009, 0.033, and 0.051%.

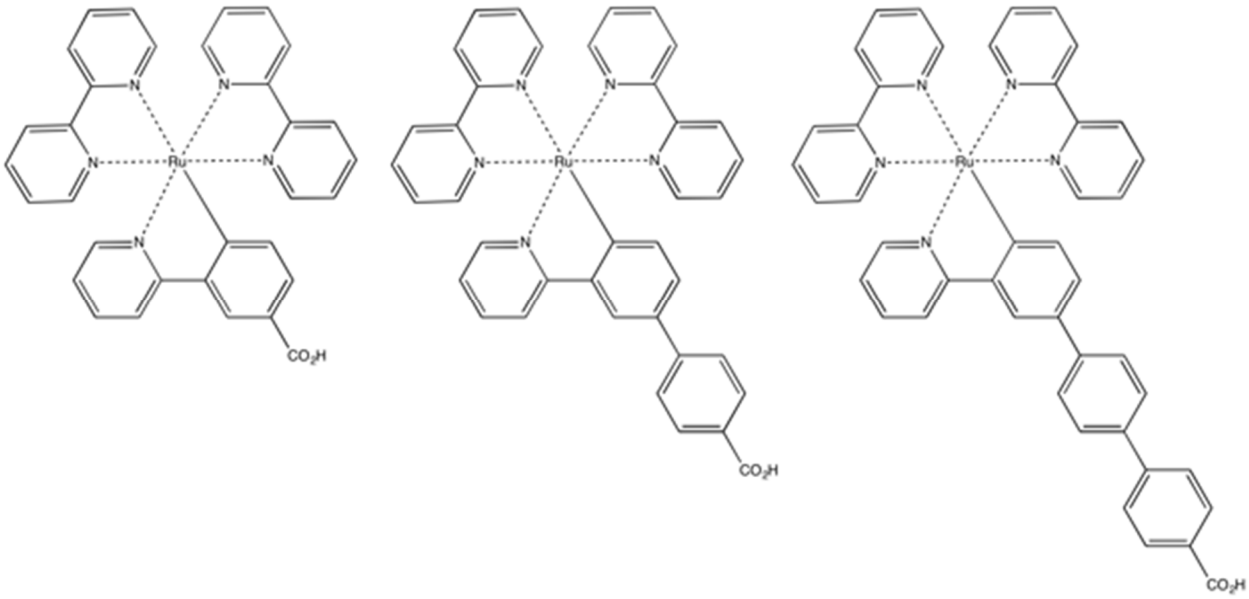

Figure 5-25: A cyclometalated diruthenium complex with an efficiency of 1.13%.

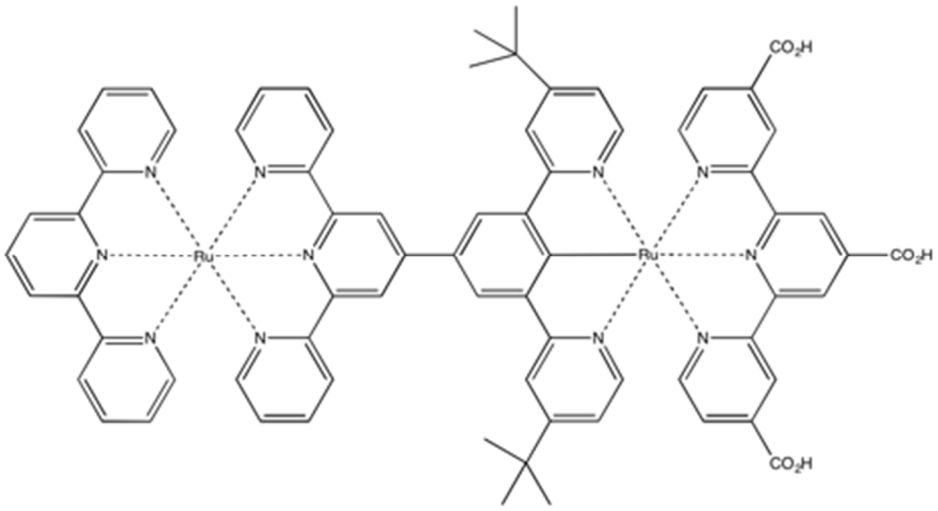

5.3.8 Solar cell data using filters to block light above 1200 nm

In Chapter 4, the NIR absorption of the mixed valance complex generated from **30** was seen. In order to see if this this NIR absorption would be seen in a dye-sensitized solar cell made with **30**, two square two by two inch Schott glass light filters were placed in the pathway from the solar illuminator and solar cell. The combined absorption pattern of the filters is seen in Figure 5-27. Almost all visible light is absorbed by the filters up to around 700 nm.

Figure 5-26: Absorption pattern of light filters.

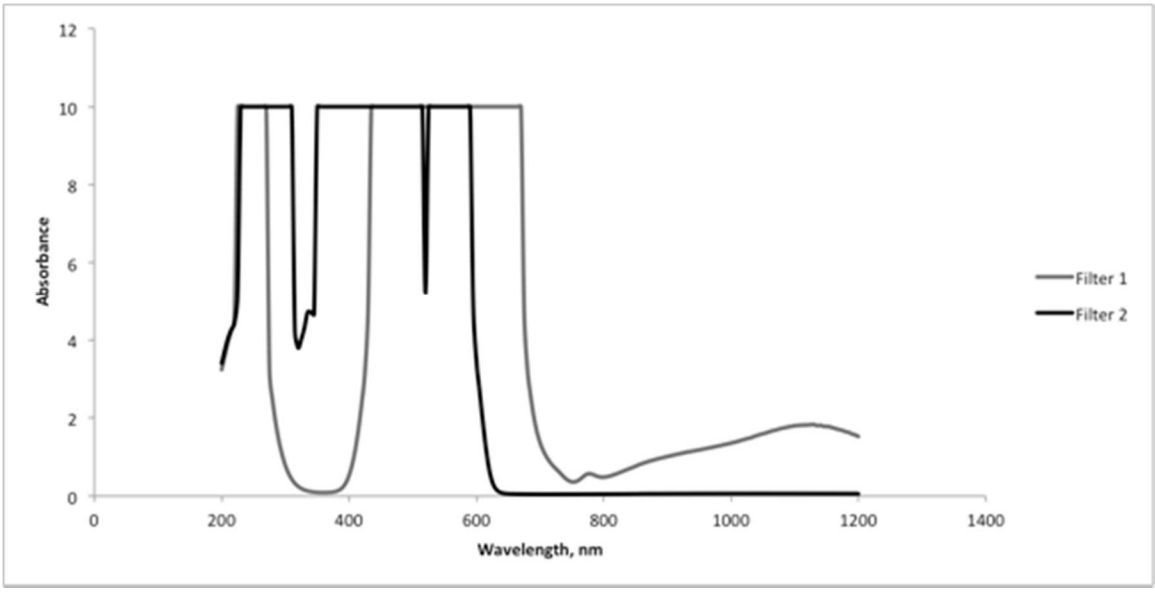

When the cell made **30** was tested with the filters in the pathway of the light, a dramatic drop in output was seen. The results are seen in Table 5-7 and Figure 5-24. The J_{sc} obtained with the filters present was 0.026 mA higher than the dark current seen in the cell without the filter and in the dark. This increase is most likely due to the light in the 700-800 nm range.

Table 5-7: Comparison of current with and without light filter.

Compound	V_{oc} (V)	J_{sc} (mA/cm^2)	P_{max} (mW)	FF (%)	η (%)
30 with a Filter	0.15	0.06	0.0037	41	0.0037
30 without a Filter	0.30	0.48	0.049	34	0.049

Figure 5-27: Current density and power plots for **30** with filters.

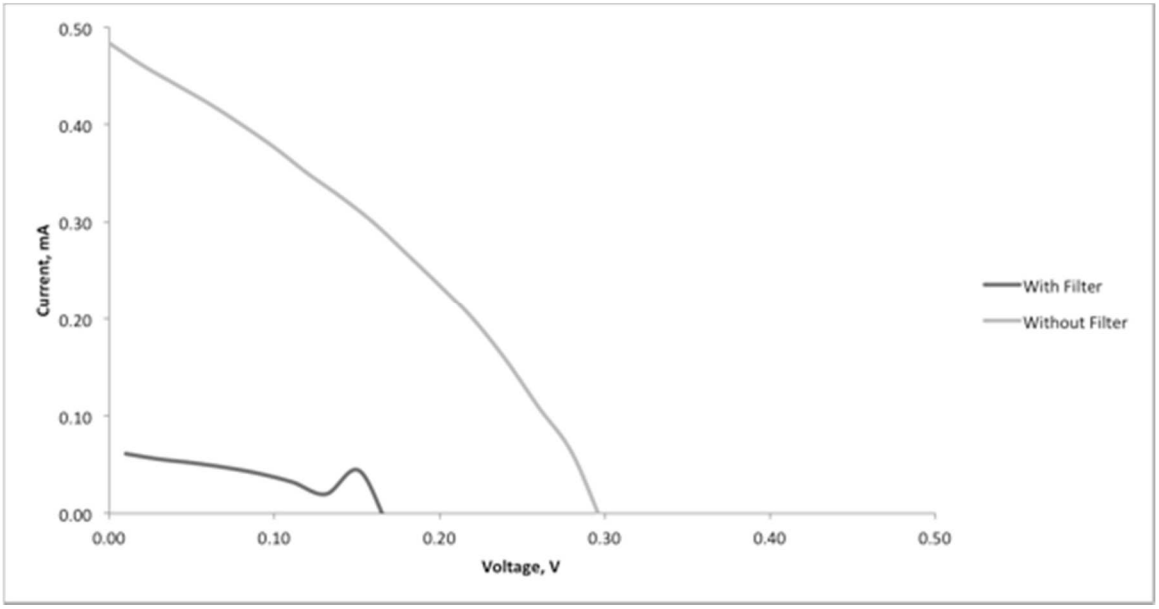

5.4 Conclusions

Solar cells were constructed with the di- and triruthenium dyes that were made in Chapters 2-4. There appears to be some resistance present in the cell, both from the fabrication of the cell and the choice of FTO used. This resistance is causing a drop in the measured efficiency of the cells.

The efficiencies of these cells made in this chapter were around 0.05 - 0.10%, or 0.3 - 0.7% if you take the excess resistance of the FTO into account. These efficiencies are consistent with similar compounds in the literature. No noticeable current is produced when **30** was tested in the absent of light in the visible region, suggesting the NIR absorbance is not a factor in the production of current.

6 Appendix

6.1 Chapter 2 spectra

6.1.1 ^{1}H NMR of 4

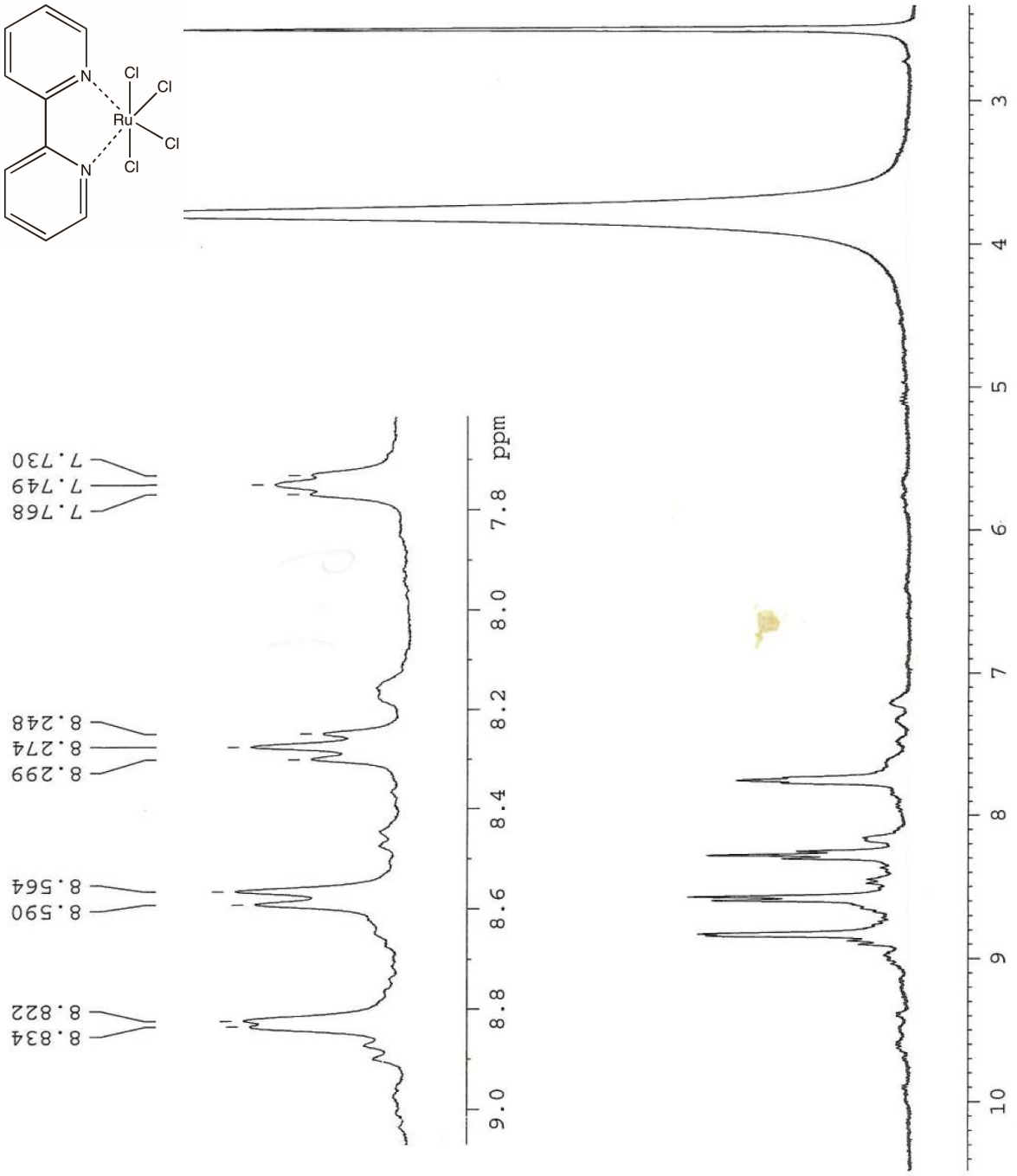

6.1.2 ^{1}H NMR of 1

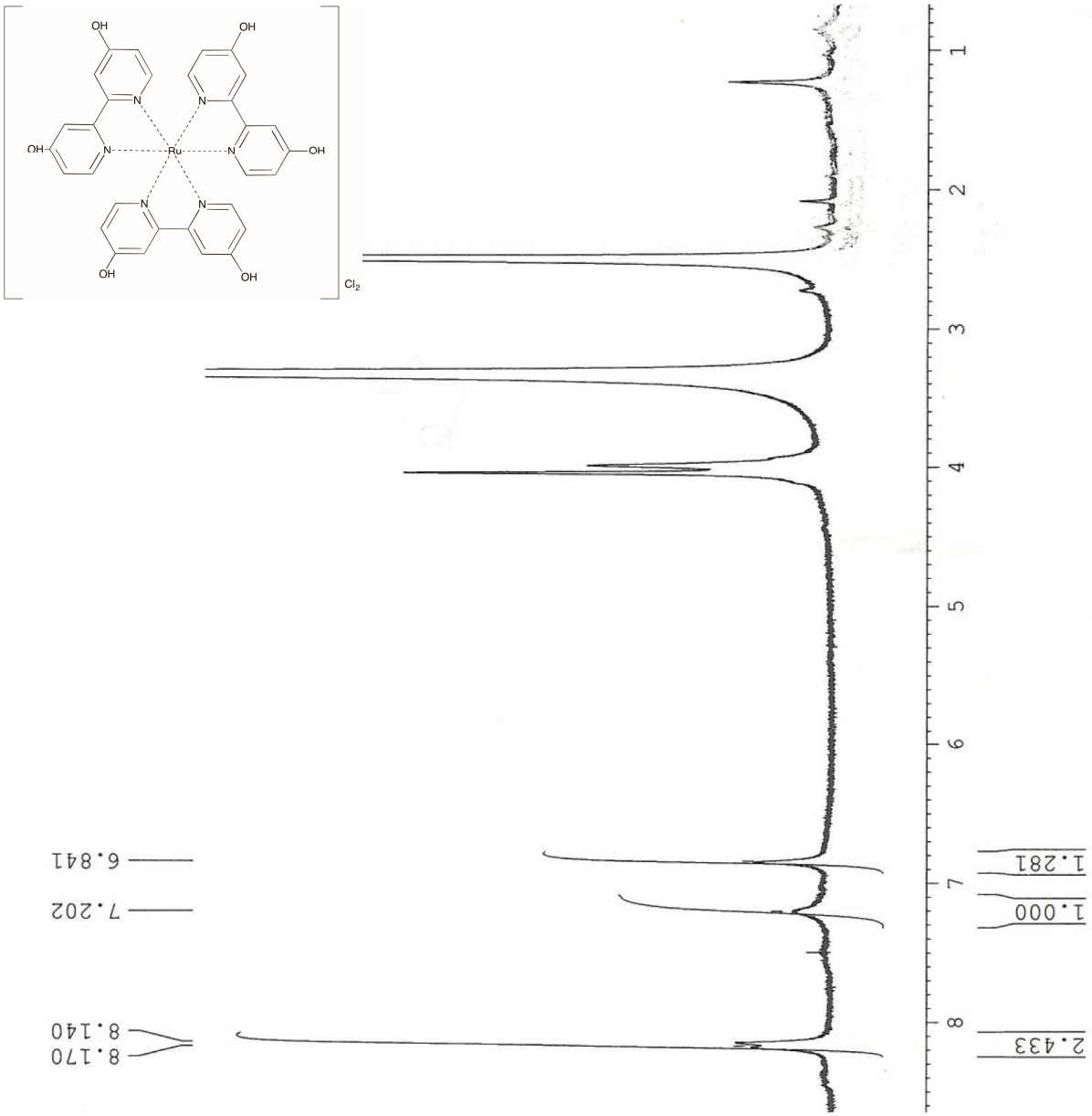

6.1.3 ^{1}H NMR of N3

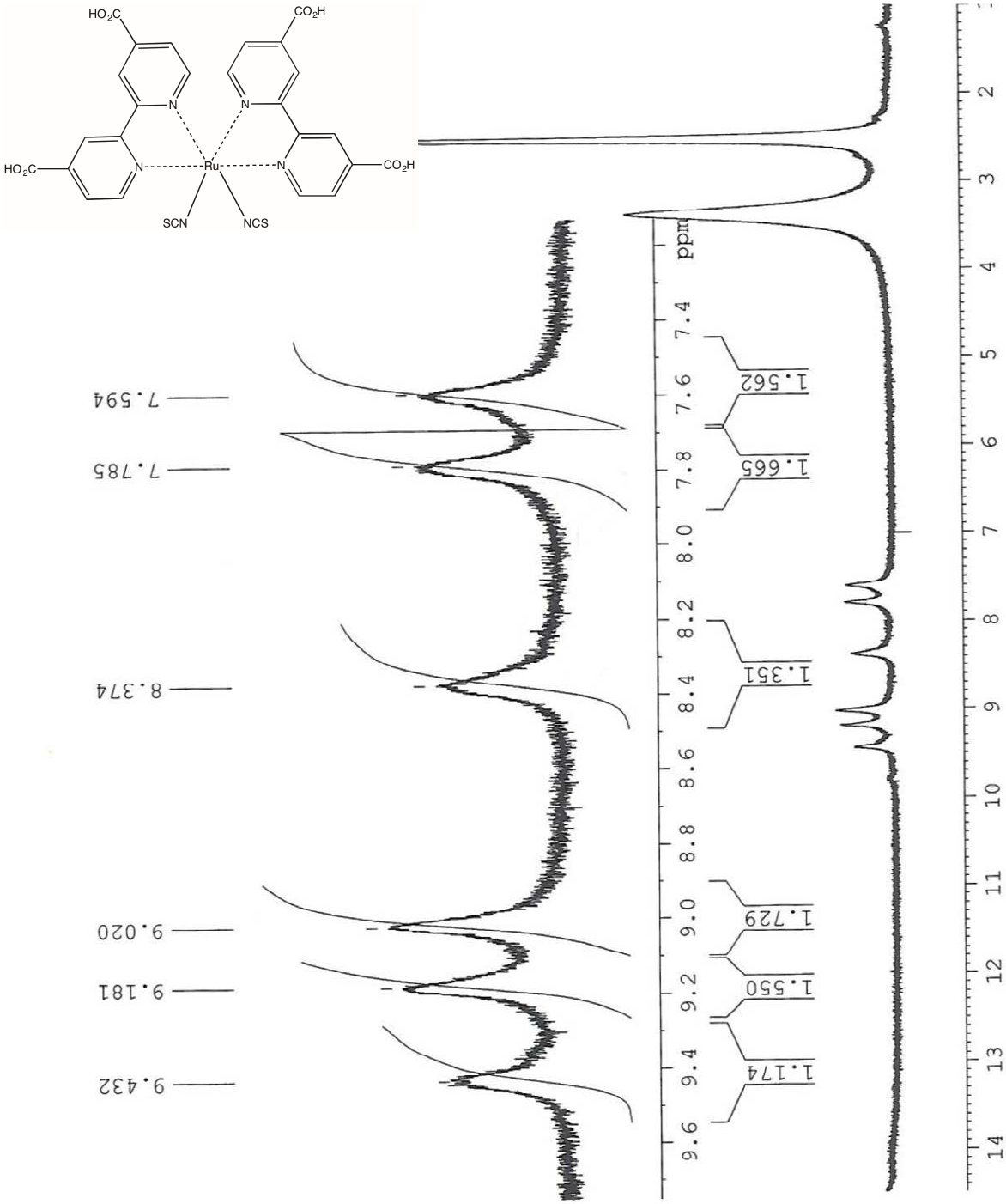

6.1.4 ^{1}H NMR of 10

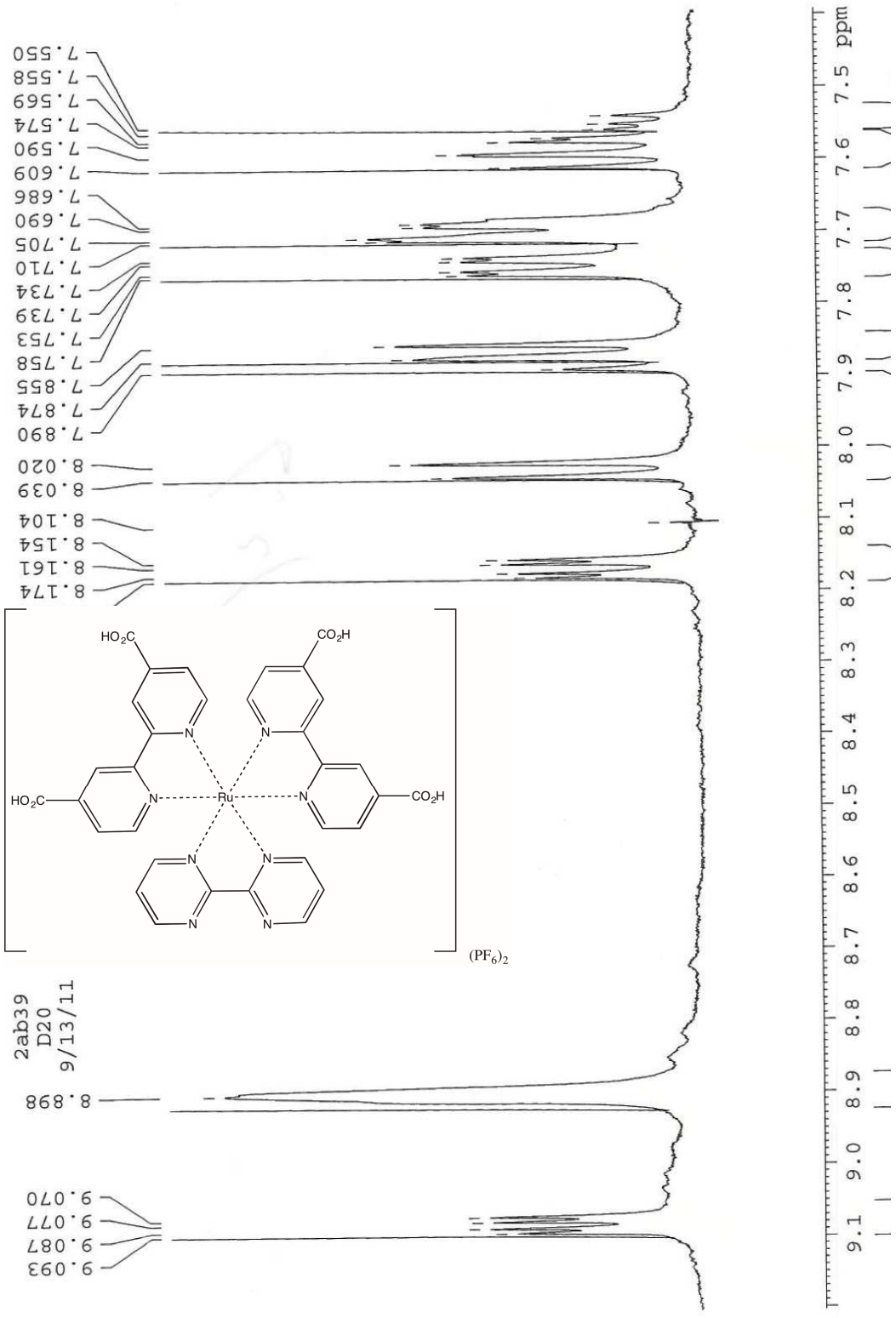

6.1.5 ^{1}H NMR of 5

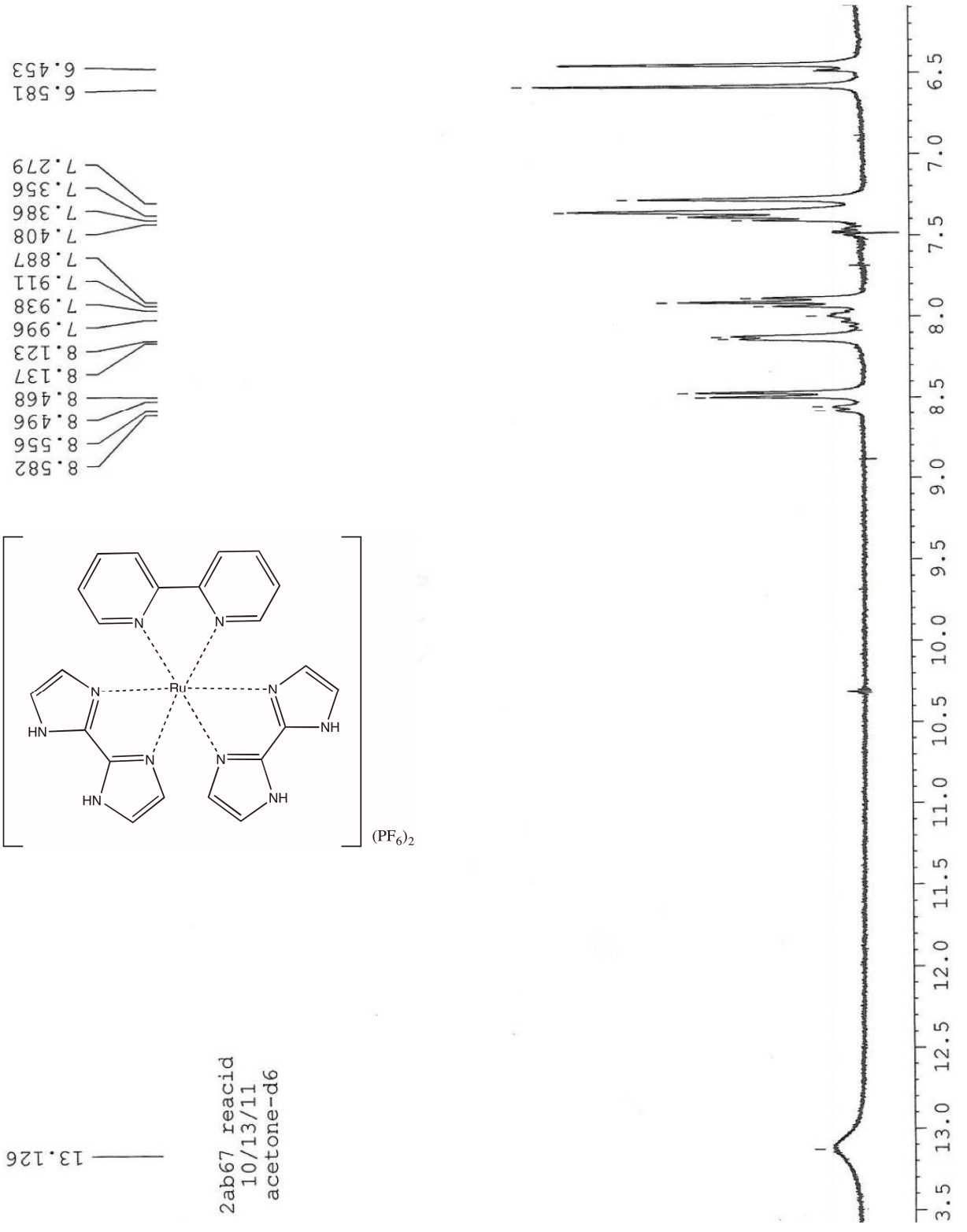

6.1.6 ^{1}H NMR of 6

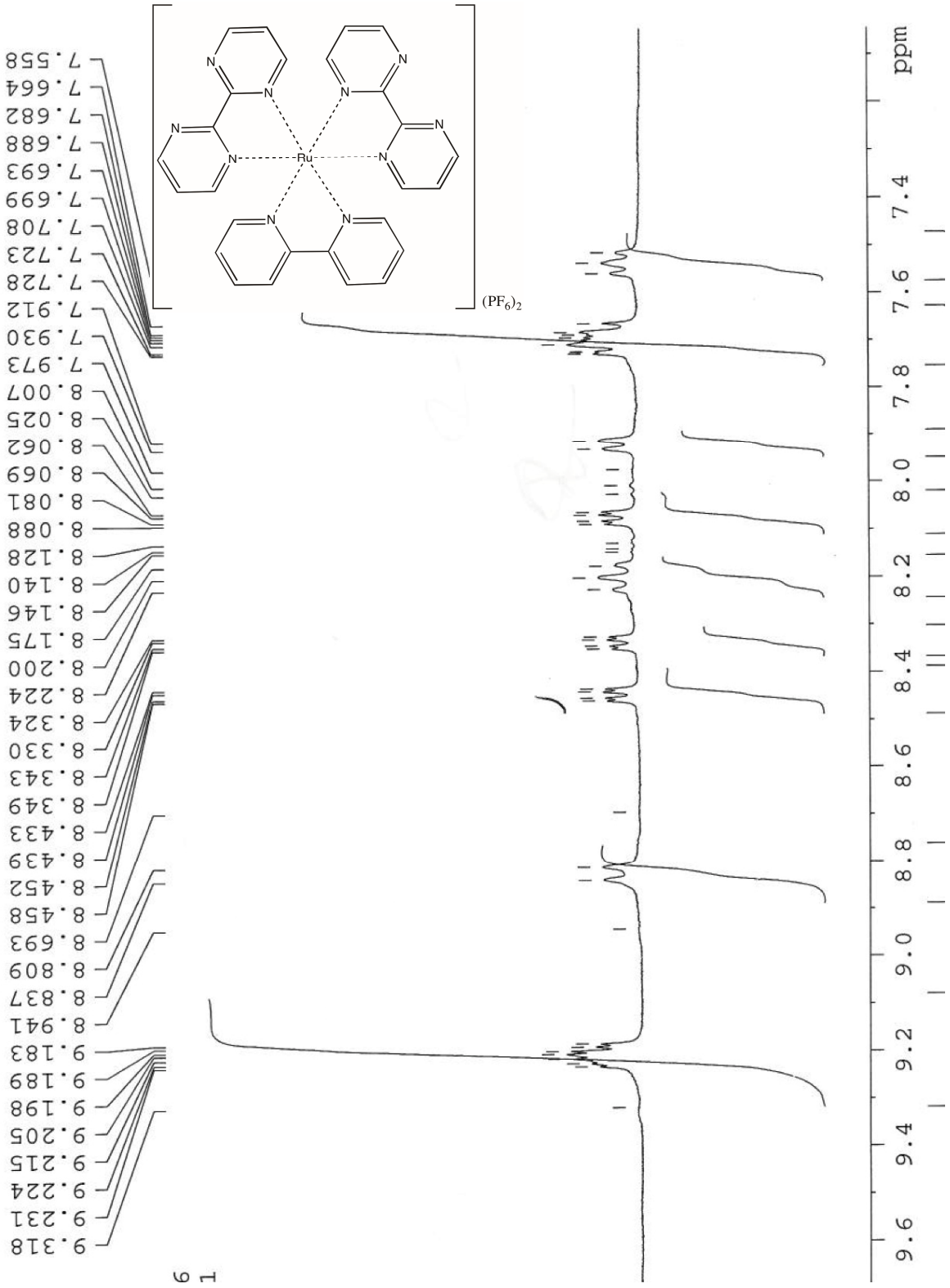

6.1.7 ^{1}H NMR of 7

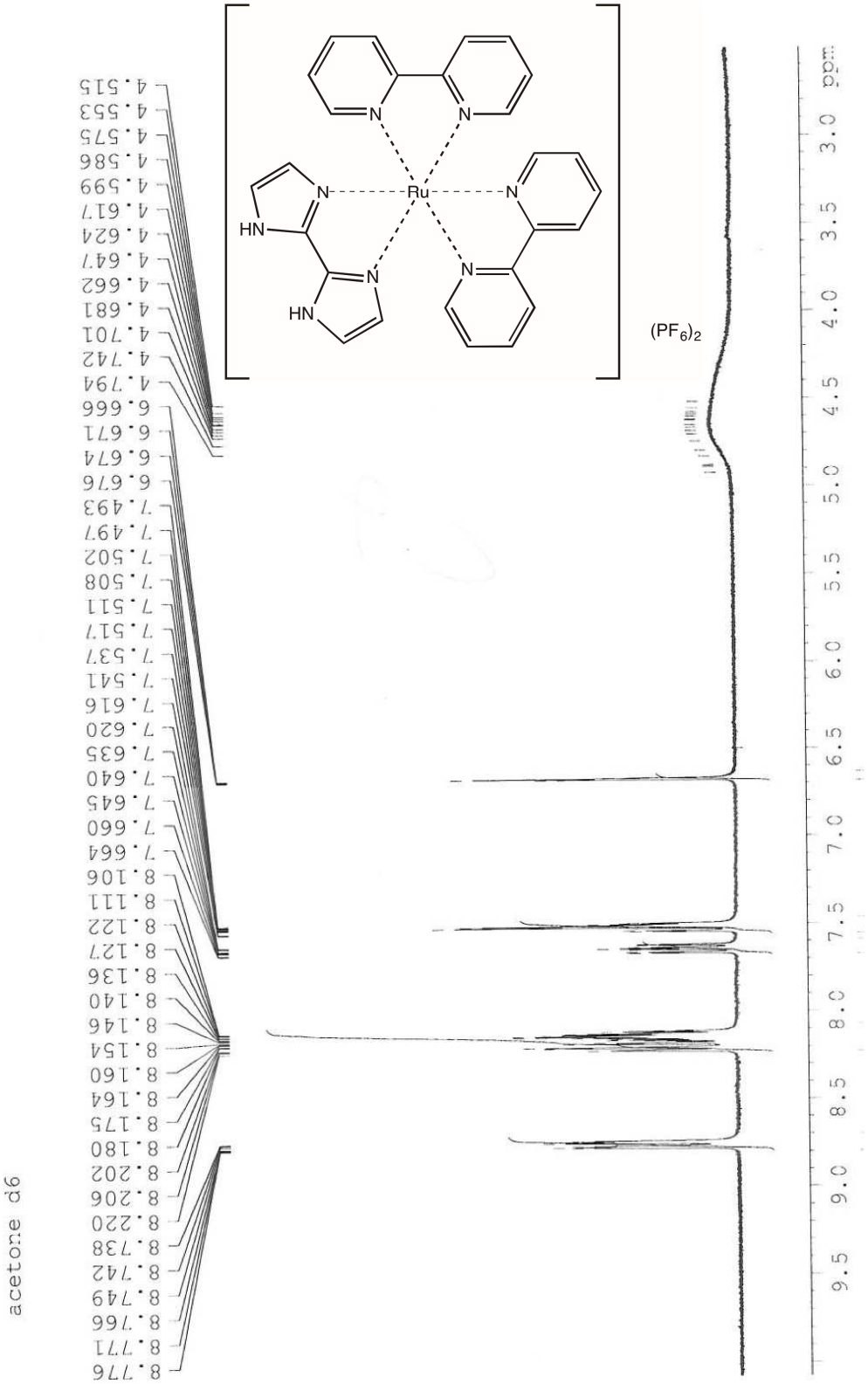

6.1.8 ^{1}H NMR of 8

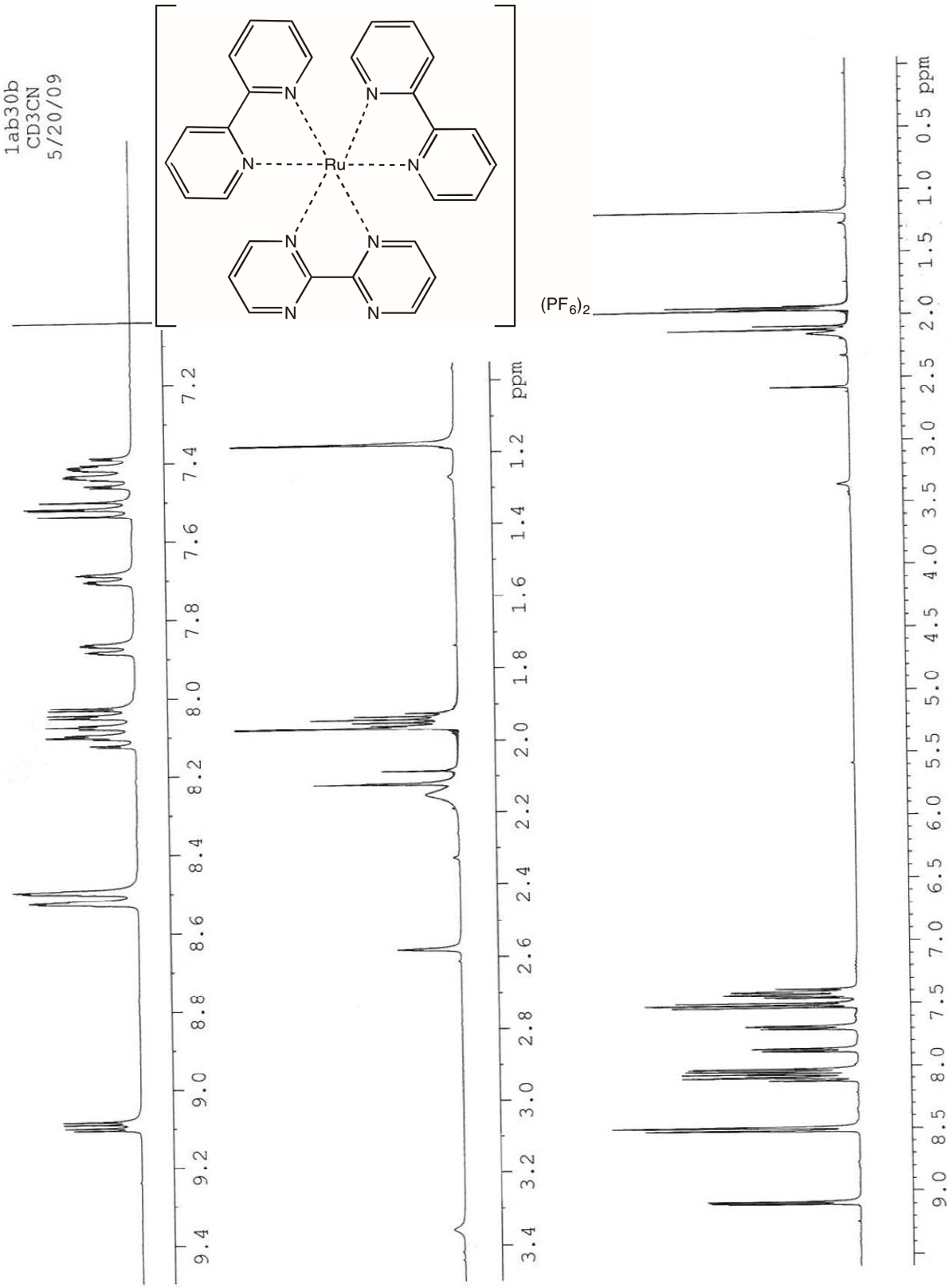

6.1.9 ^{1}H NMR of 11

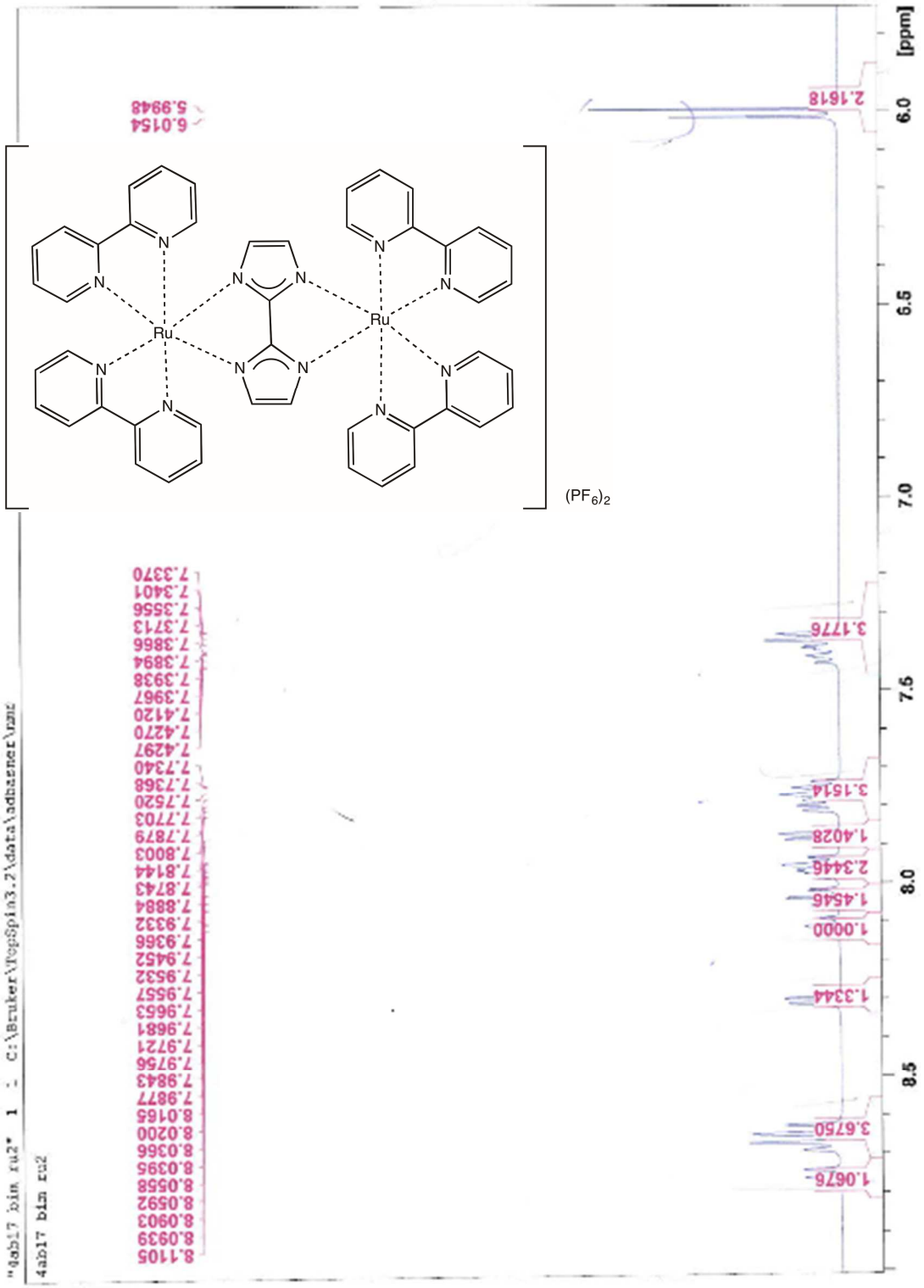

6.1.10 ^{1}H NMR of 12

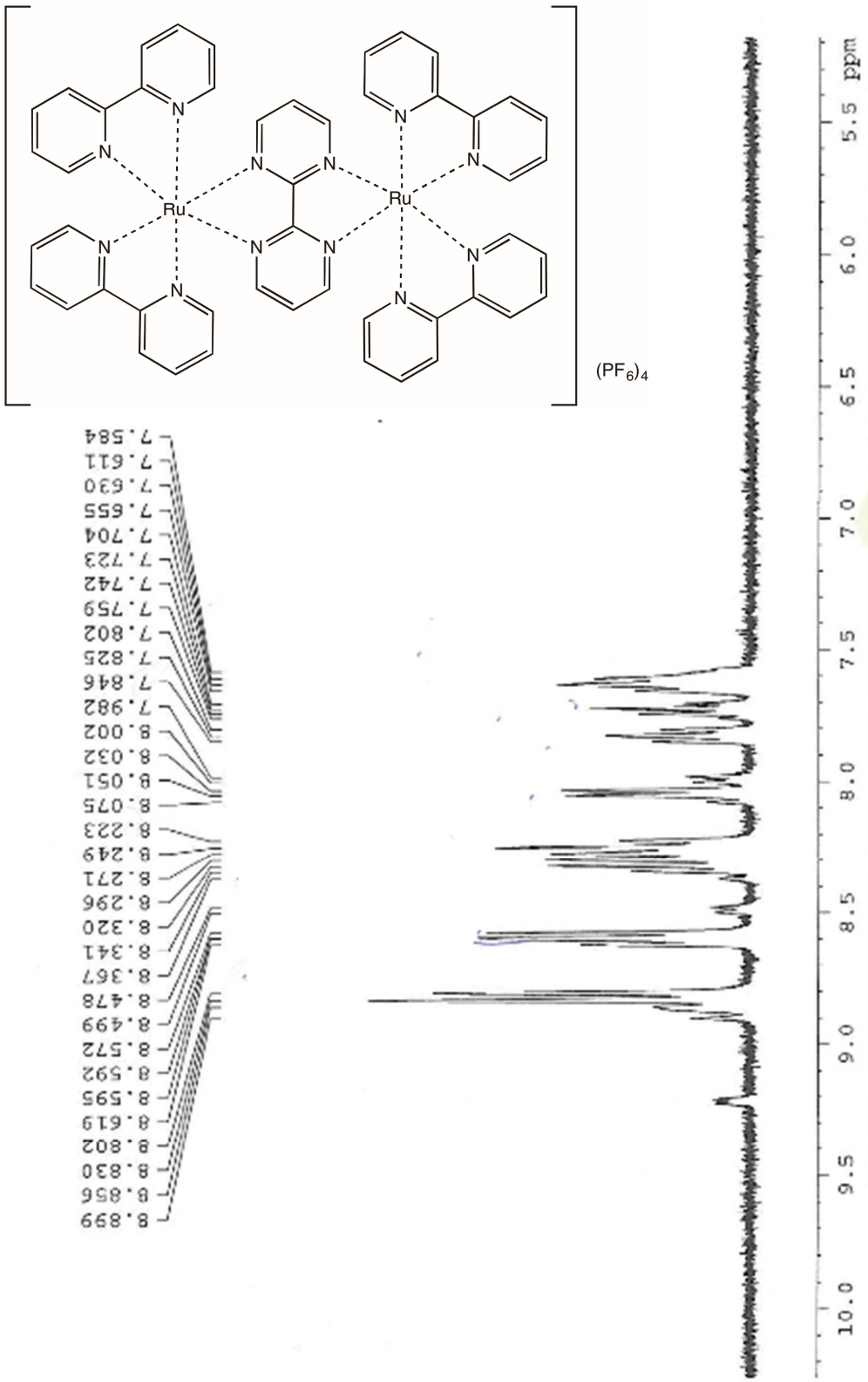

6.1.11 ^{1}H-^{1}H COSY of 12

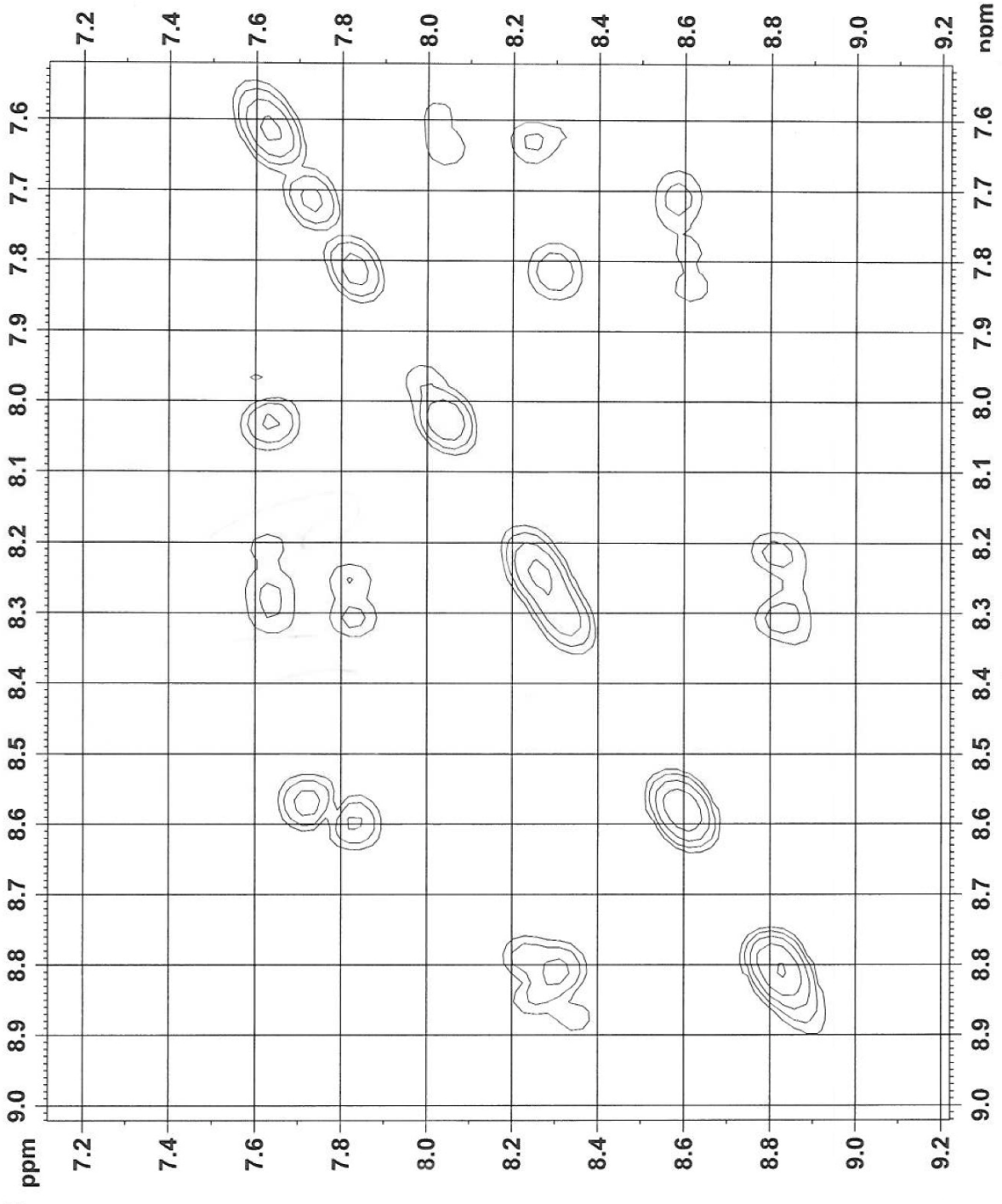

6.1.12 ^{1}H NMR of 13

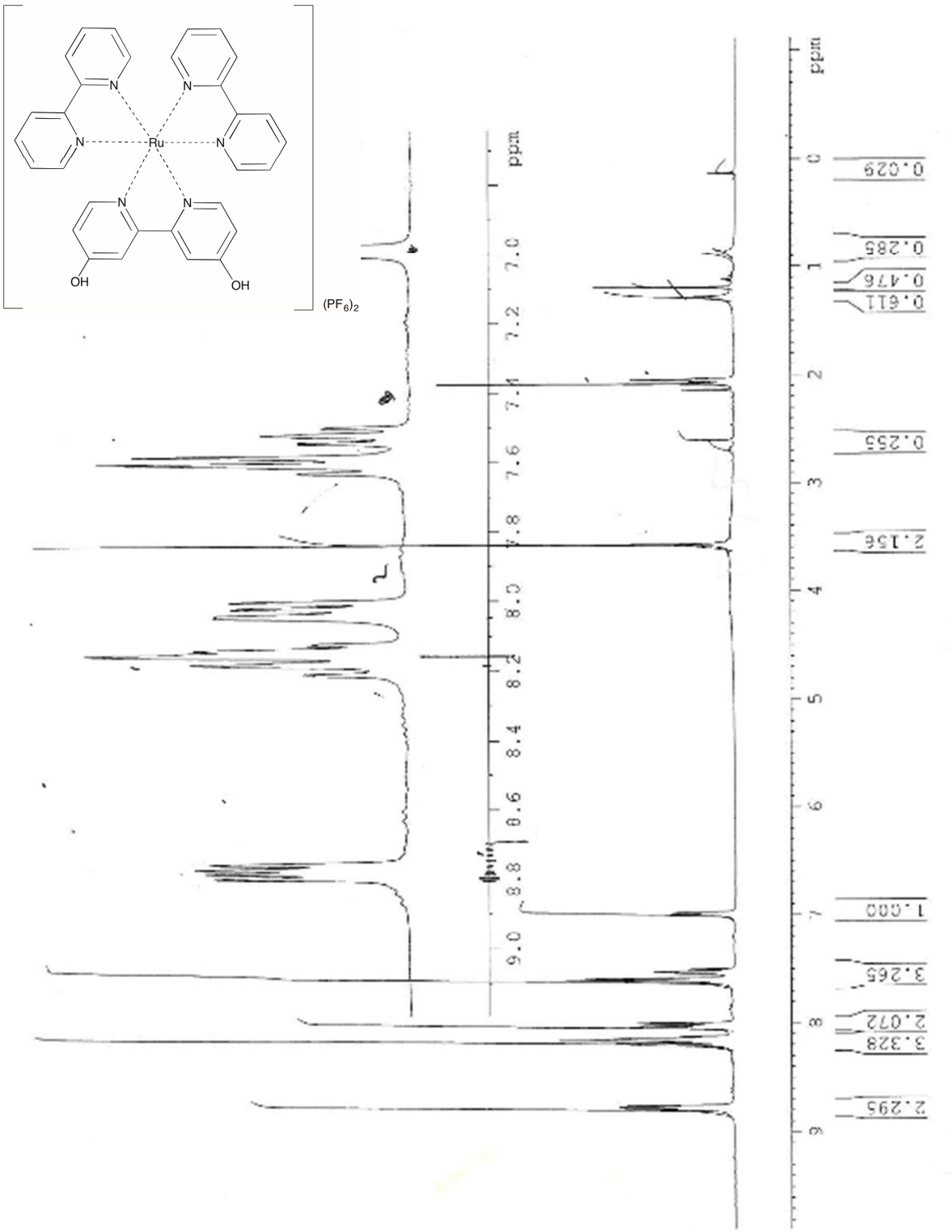

6.2 Chapter 3 spectra

6.2.1 ^{1}H NMR of 18

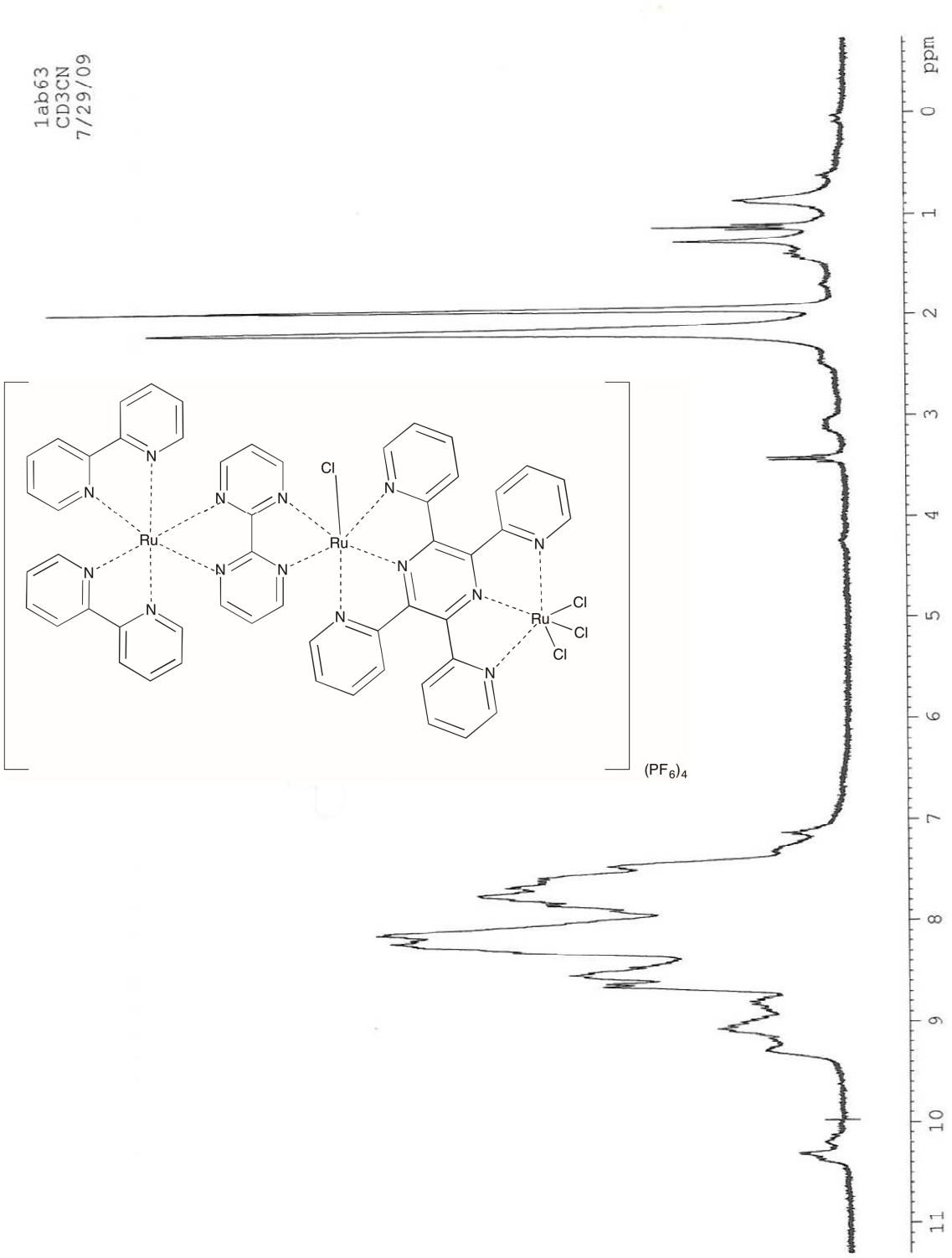

6.2.2 ^{1}H NMR of 19

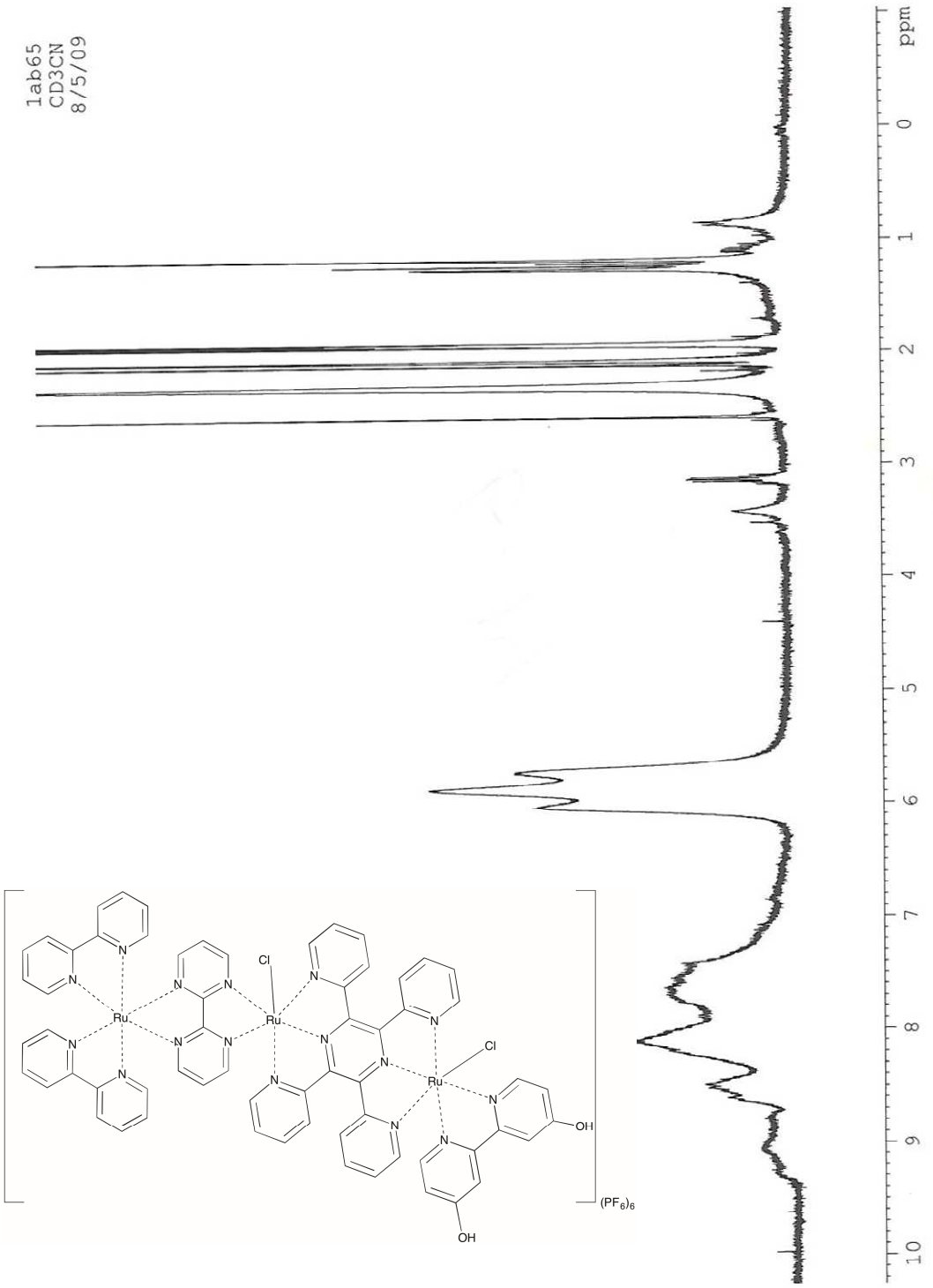

6.2.3 ^{1}H NMR of 20

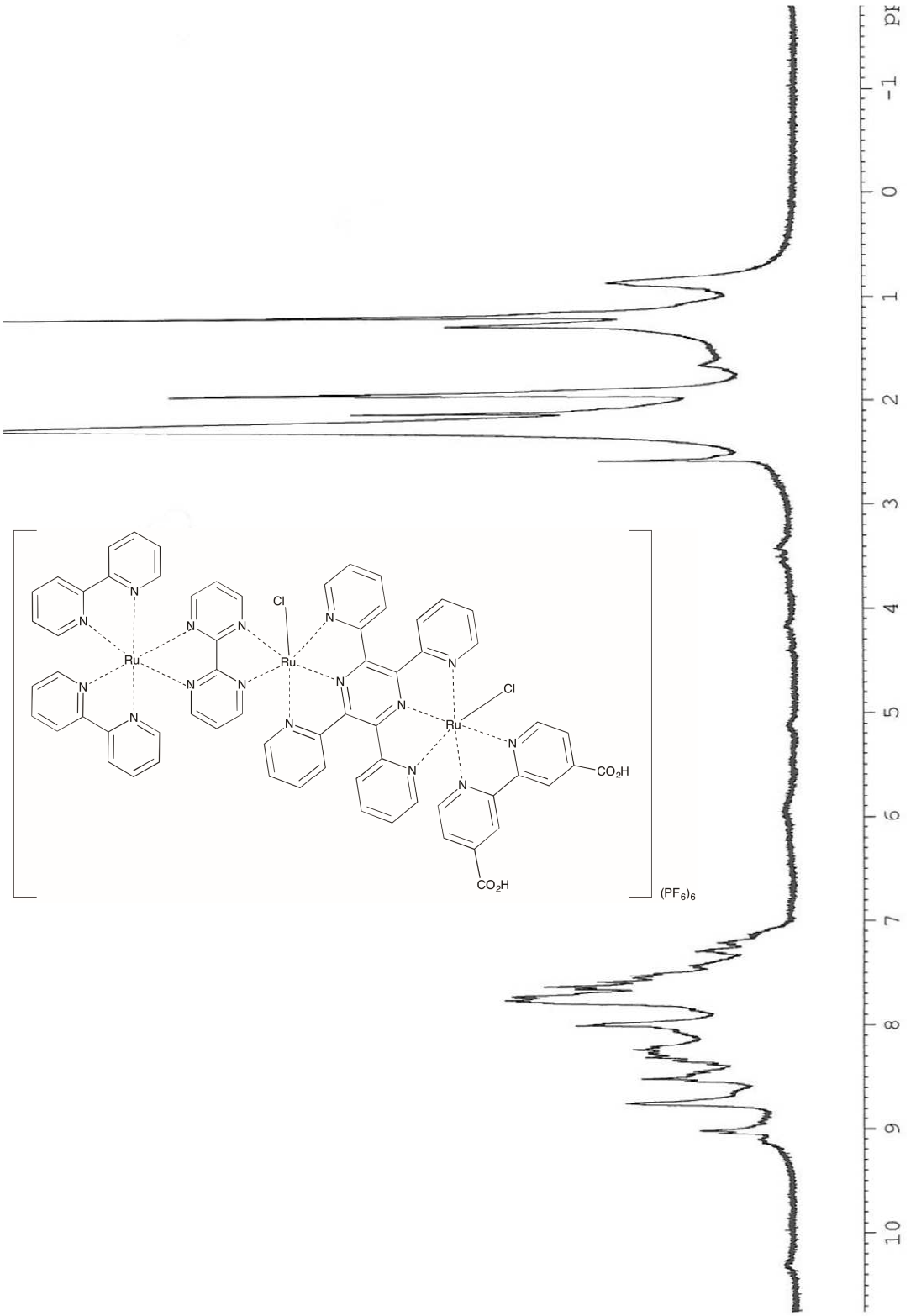

6.2.4 ^{1}H NMR of 23

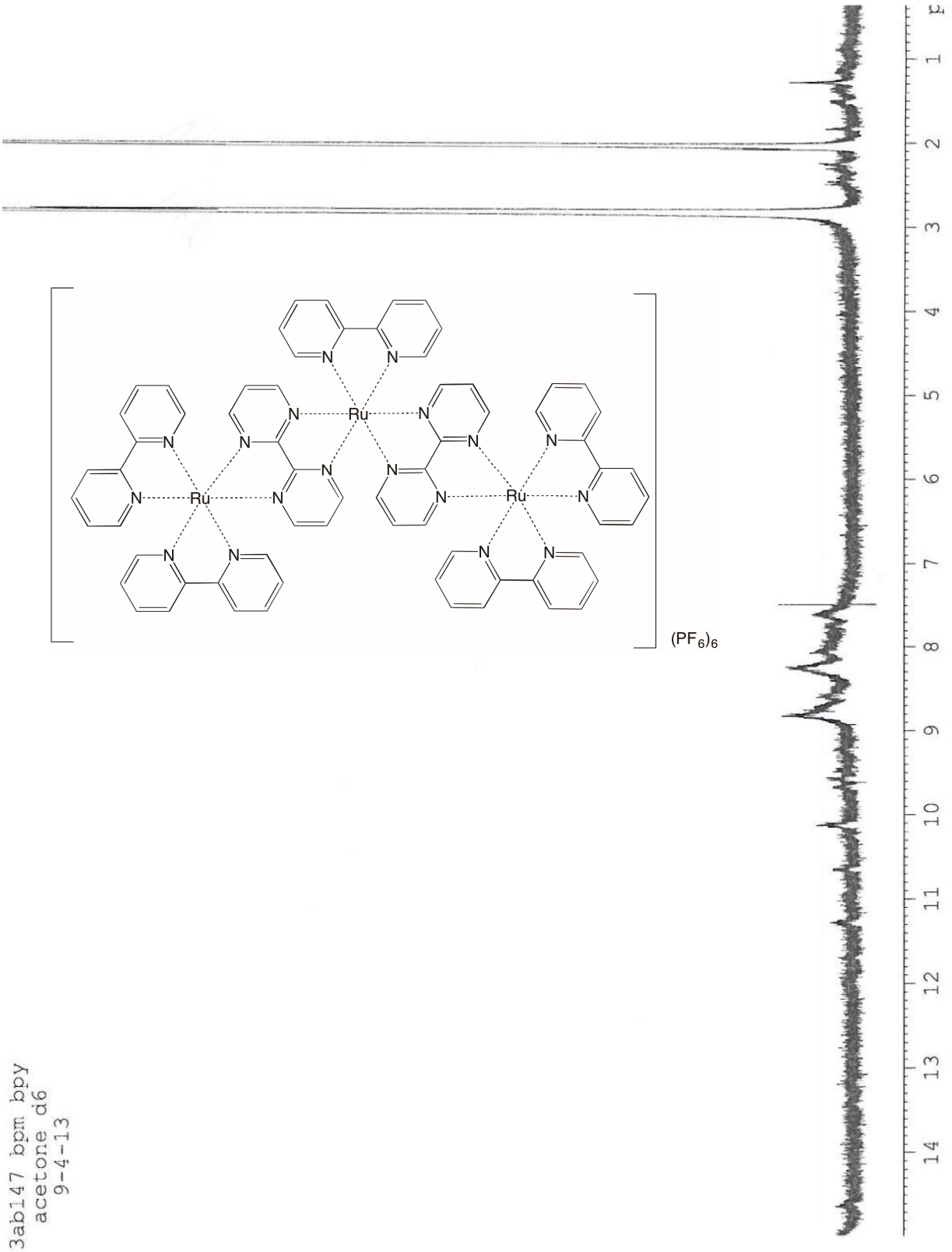

6.2.5 ^{1}H NMR of 24

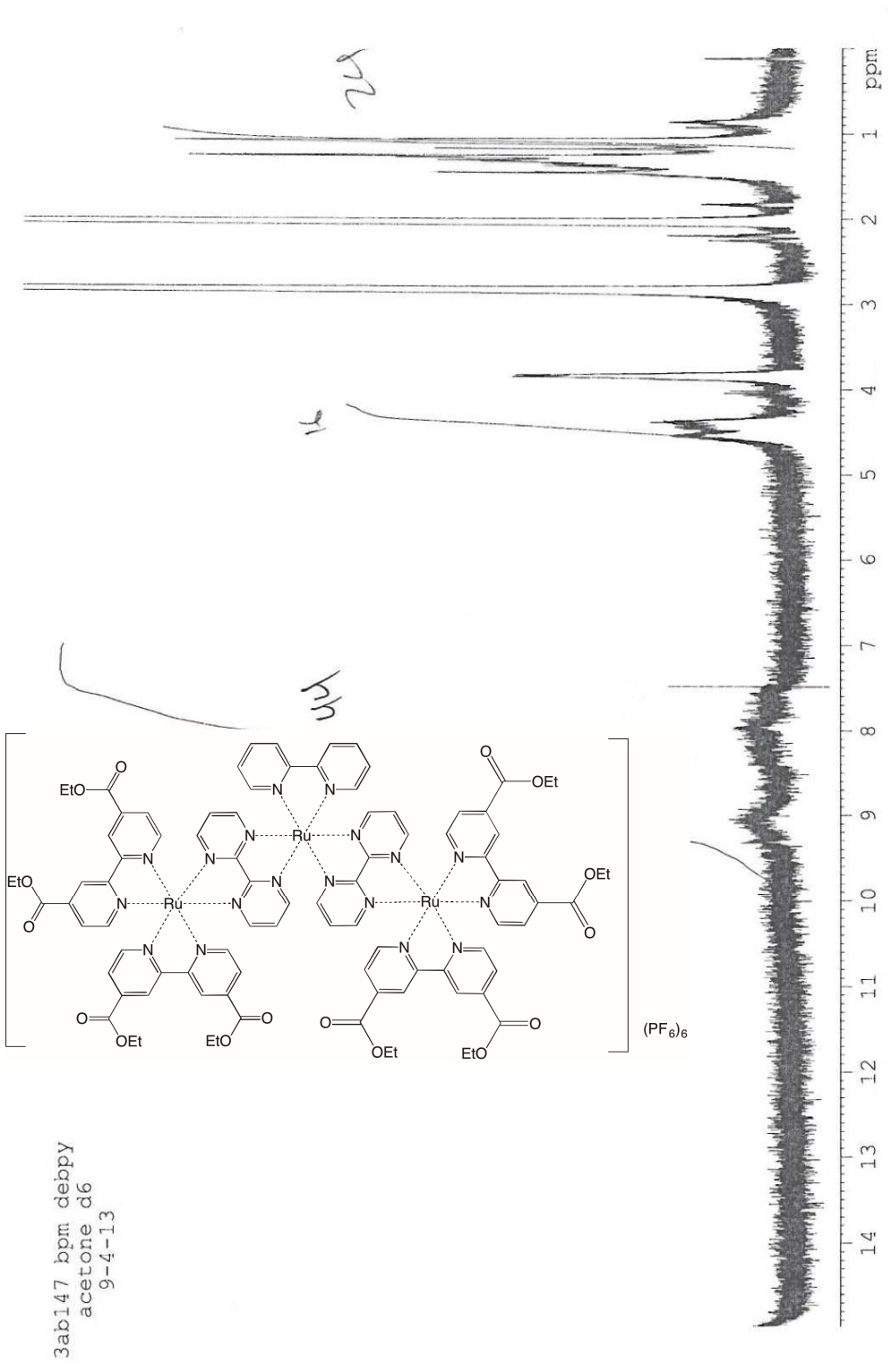

6.2.6 ^{1}H NMR of 25

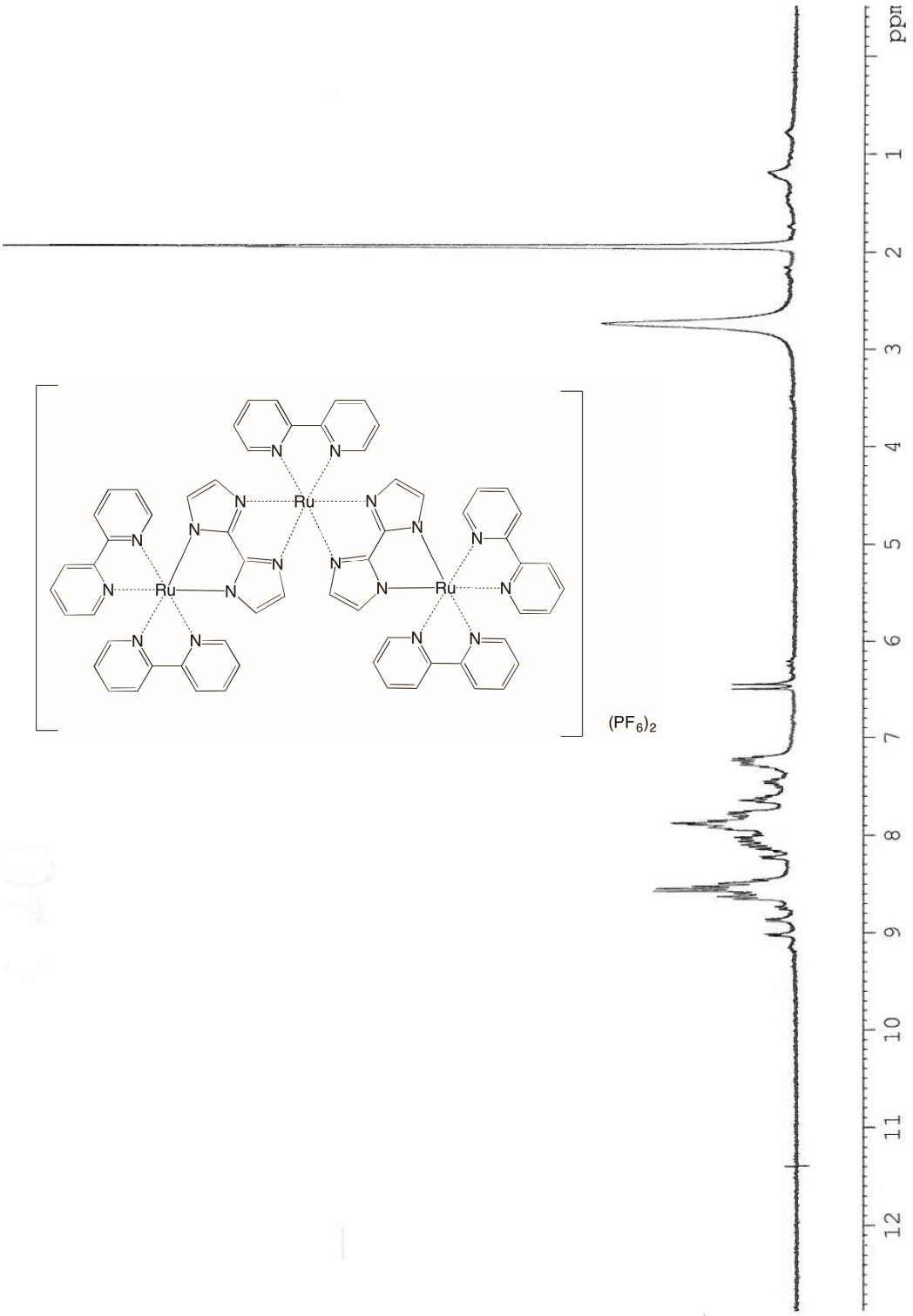

6.2.7 ^{1}H NMR of 26

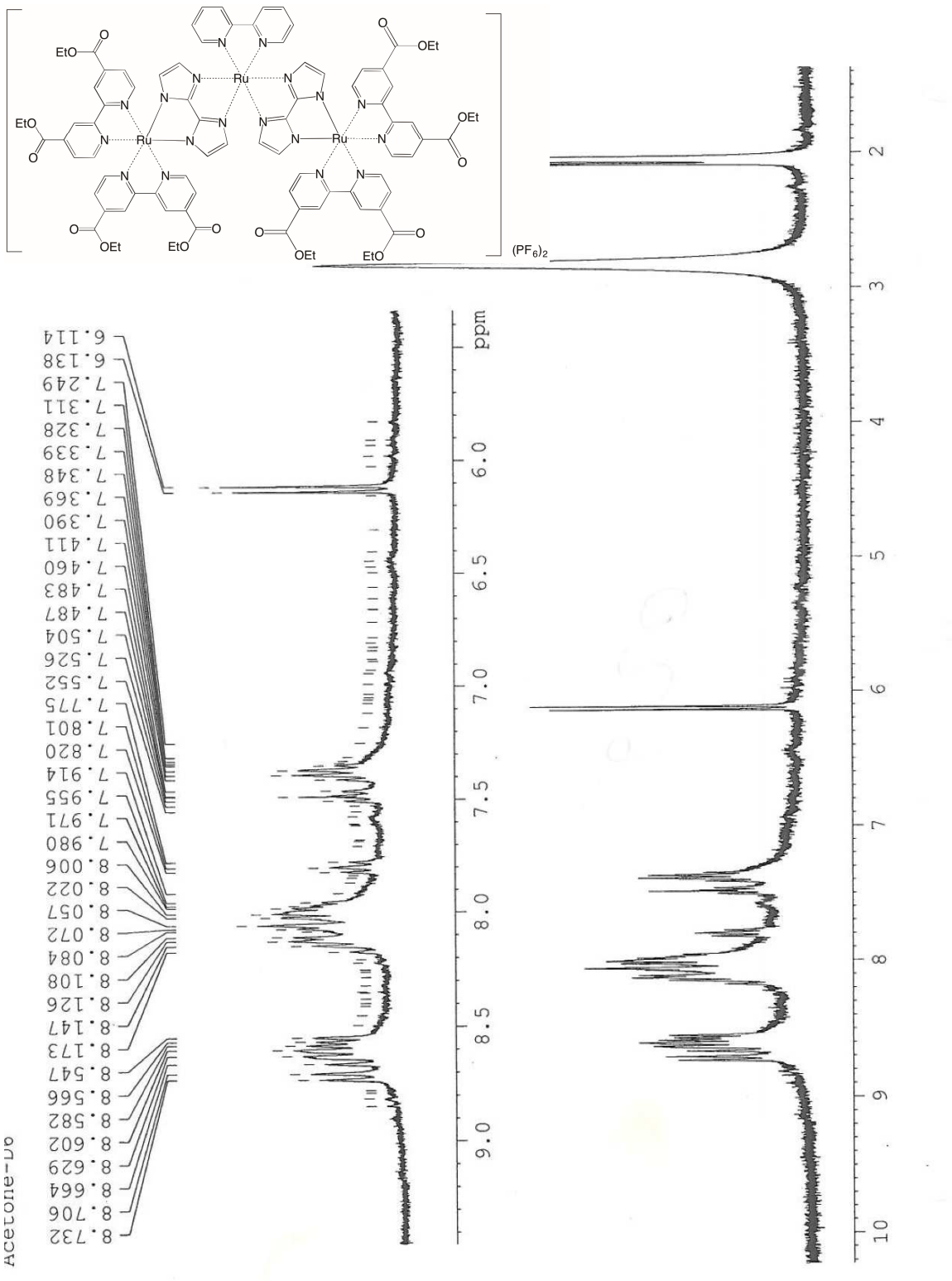

6.3 Chapter 4 spectra

6.3.1 ^{1}H NMR of 28

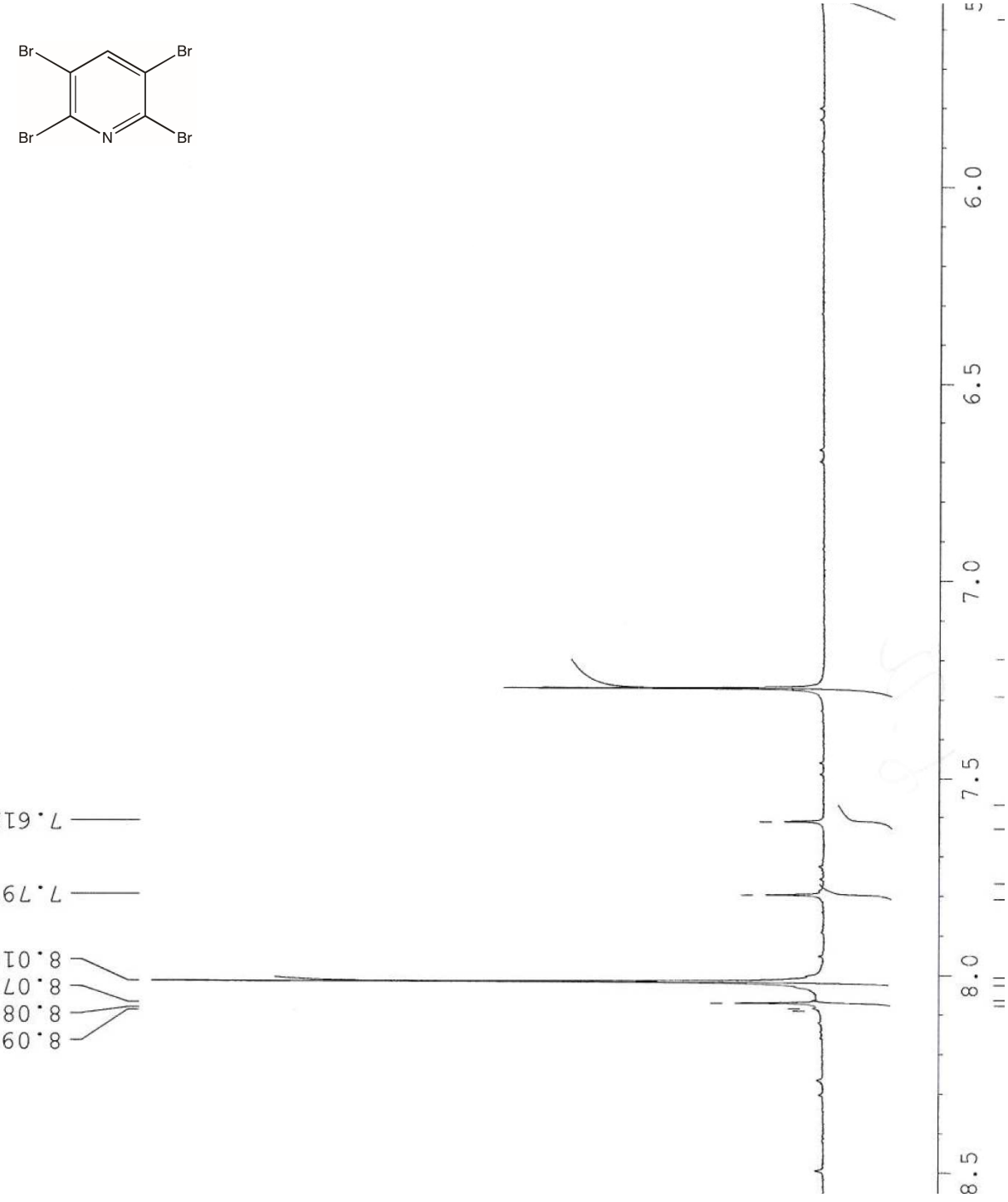

6.3.2 ^{13}C NMR of 28

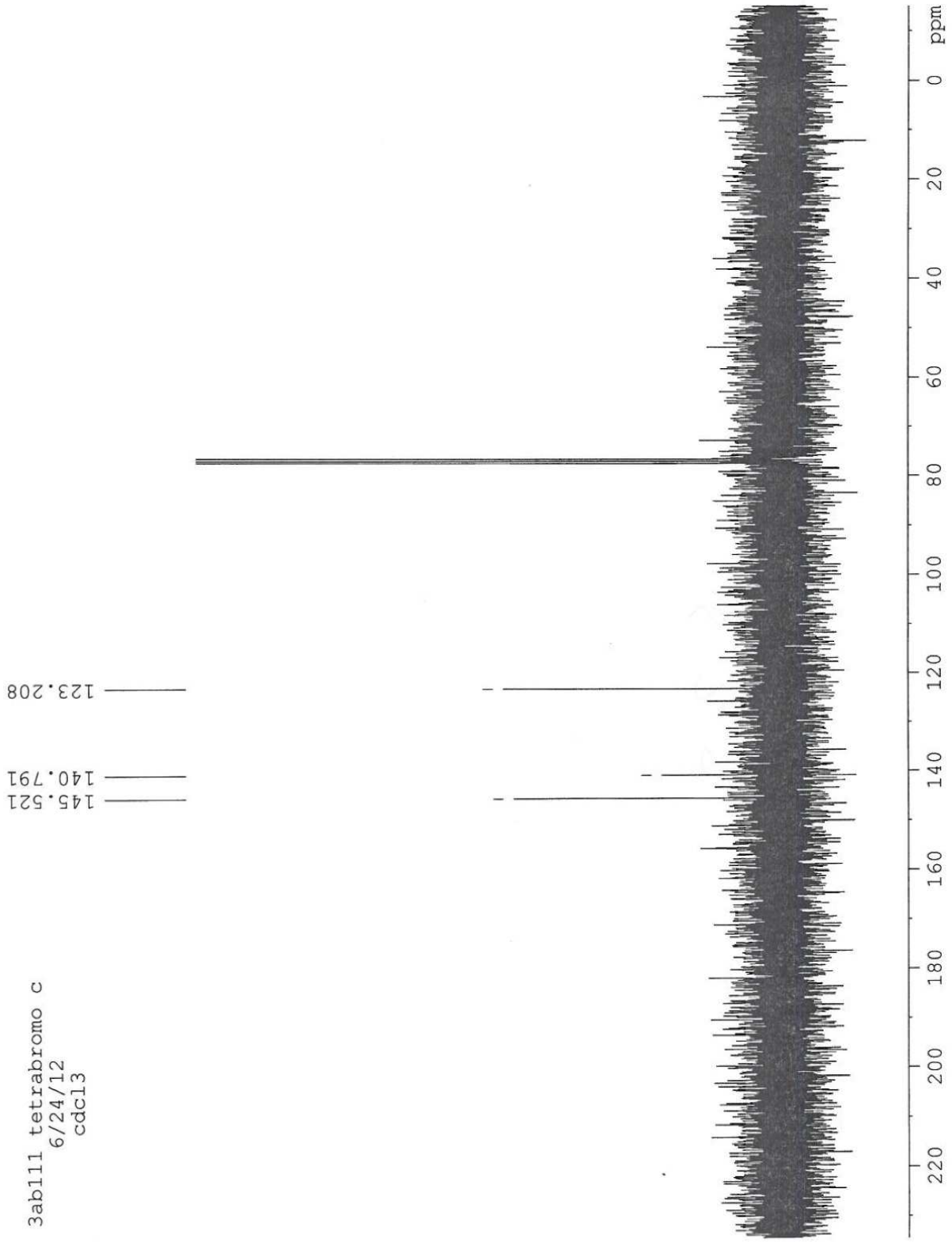

6.3.3 ^{1}H NMR of TPPY

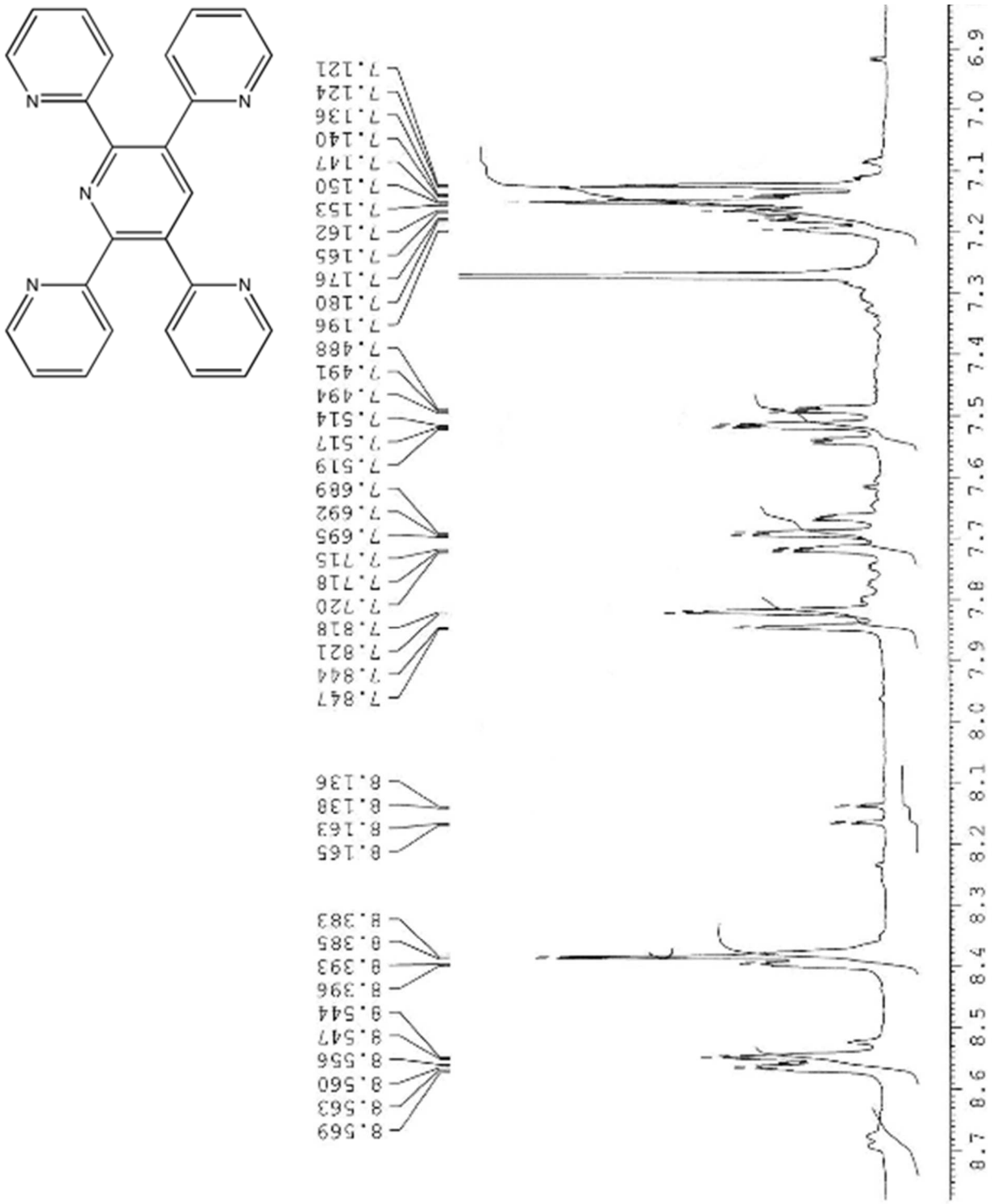

6.3.4 ^{13}C NMR of TPPY

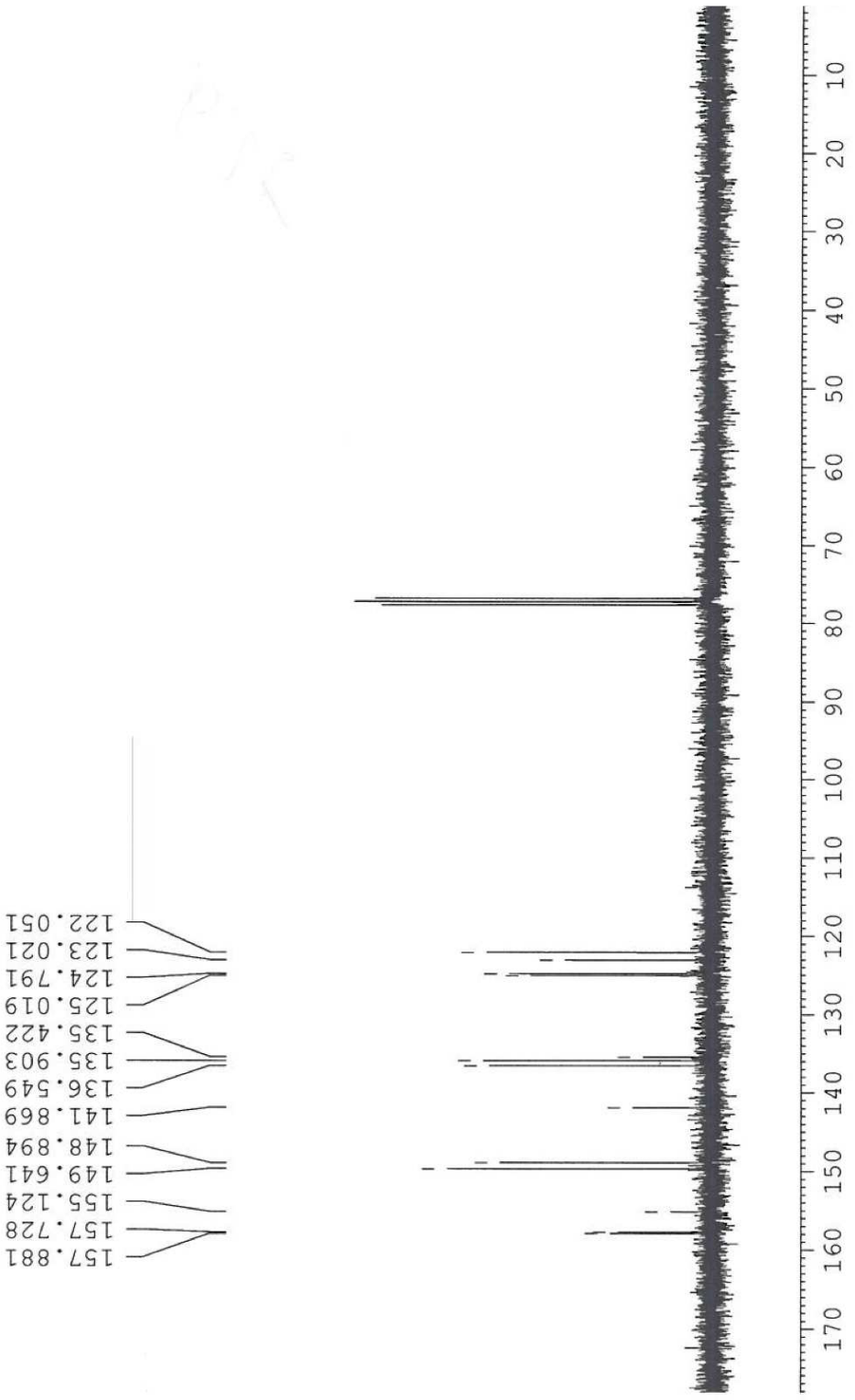

6.3.5 ^{1}H-^{1}H COSY of TPPY

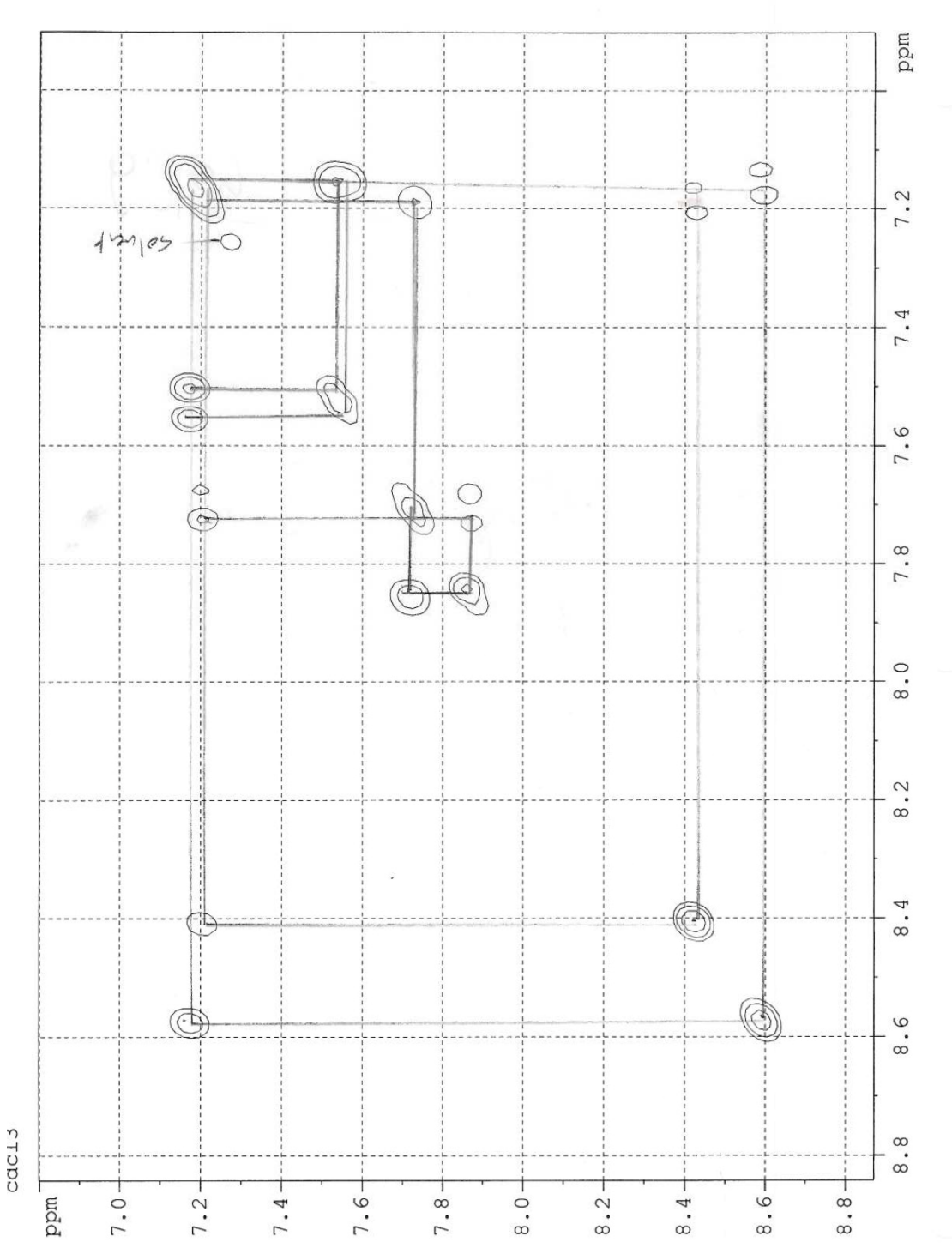

6.3.6 ^{1}H NMR of 30

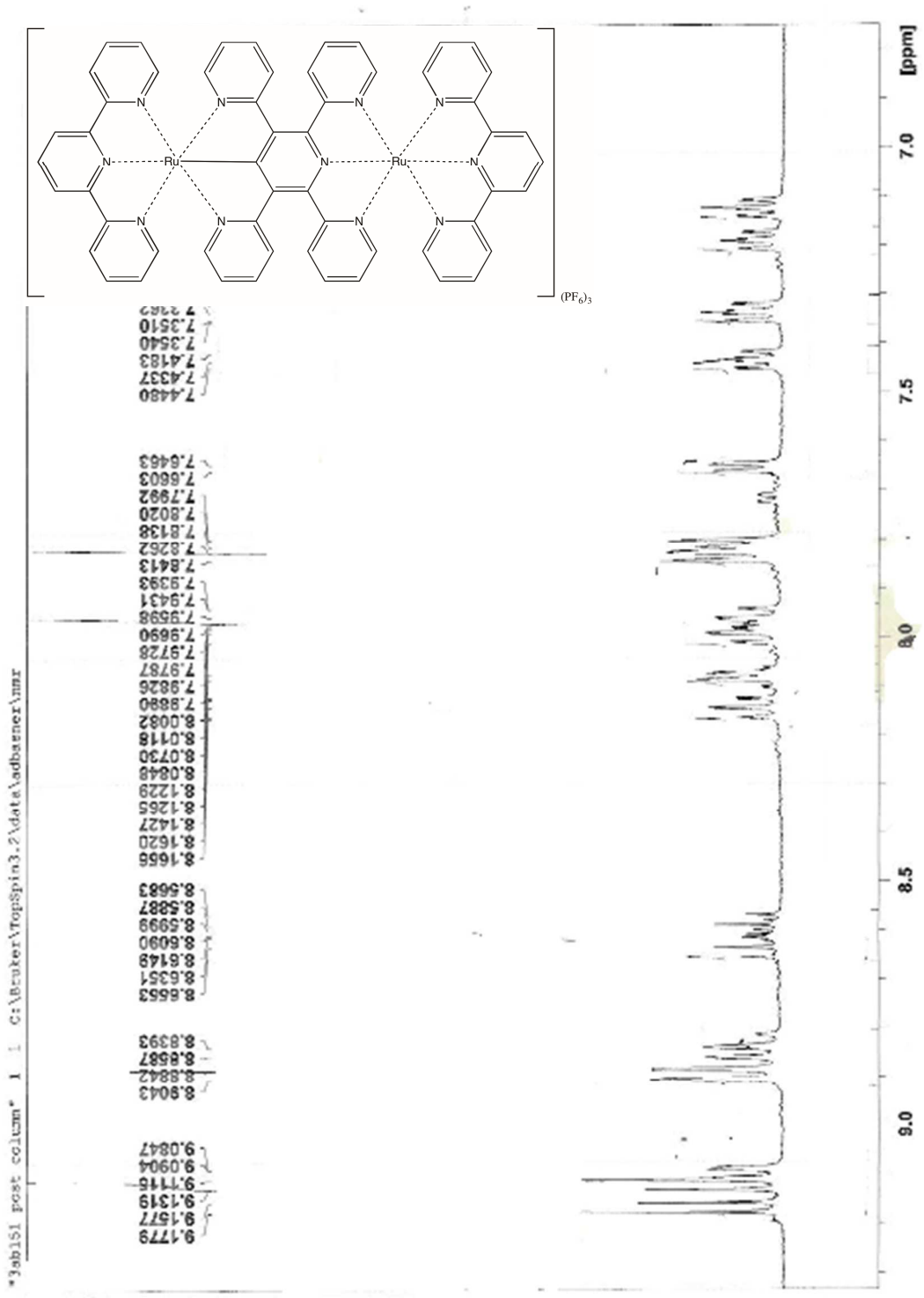

6.3.7 ^{1}H-^{1}H COSY of 30

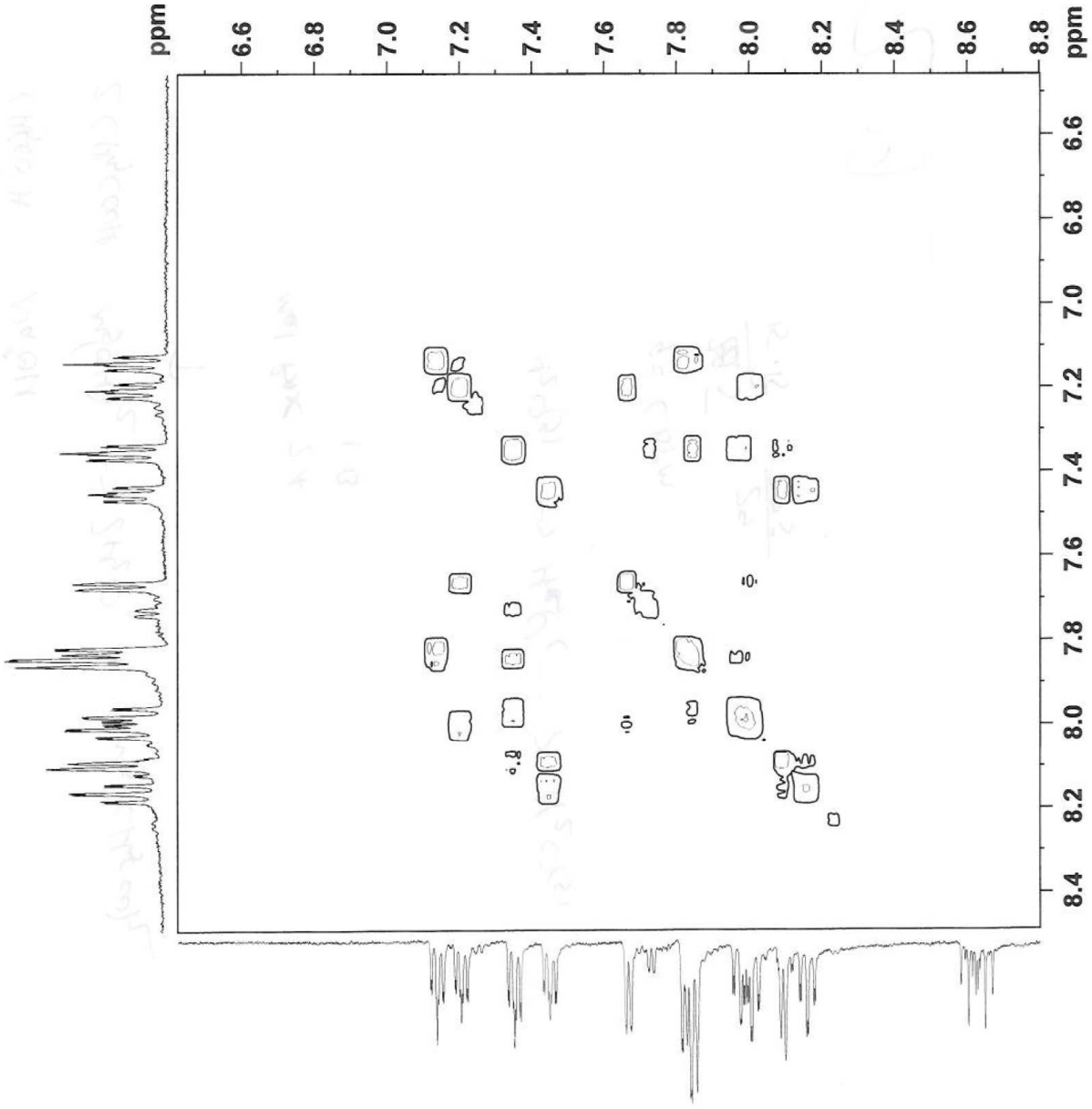

6.4 Crystallography files

6.4.1 Crystal data and structure refinement for 2,3,5,6-tetra-(2-pyridyl)pyridine, TPPY

Identification code	TPPY
Empirical formula	$C_{25}H_{17}N_5$
Formula weight	387.45
Temperature	90(2) K
Wavelength	0.71073 Å
Crystal system	Tetragonal
Space group	I 41/a
Unit cell dimensions	a = 17.229(2) Å α= 90°
	b = 17.229(2) Å β = 90°
	c = 13.1196(16) γ = 90°
Volume	3894.5(11) $Å^3$
Z	16
Density (calculated)	2.6432 g/cm^3
Absorption coefficient	0.099 mm^{-1}
F(000)	1966
Crystal size	0.2 x 0.2 x 0.1 mm^3
Theta range for data collection	1.951° to 30.247°
Index ranges	-22<=h<=22, -22<=k<=22, -17<=l<=17
Reflections collected	2644
Independent reflections	2100

Completeness to theta = 25.242°	99.9%
Absorption corrections	Multi-scan
Max. and min. transmission	0.8127 and 0.5871
Refinement method	Full-matrix least-squares on F^2
Data / restraints / parameters	2644 / 0 / 140
Goodness-of-fit on F^2	0.991
Final R indices [I>2sigma(I)]	0.0573
R indices (all data)	0.0749
Largest diff. peak and hole	0.429 -0.457 $e^-/Å^3$

Atomic Coordinates for TPPY. U(eq) is defined as one third of the trace of the orthogonalized U^{ij} tensor.

Atom	X	Y	Z	U(eq)
C1	0.15886(10)	0.37307(11)	0.66812(14)	0.0269(4)
C2	0.20193(11)	0.39993(12)	0.74988(15)	0.0332(4)
C3	0.16444(11)	0.43539(13)	0.83076(15)	0.0325(4)
C4	0.08393(10)	0.44369(10)	0.82683(12)	0.0215(3)
C5	0.04098(9)	0.47601(10)	0.91573(12)	0.0203(3)
C6	0.05917(9)	0.44637(9)	1.00938(11)	0.0169(3)

C7	-0.01886(9)	0.53045(10)	0.90630(12)	0.0199(3)
C8	-0.08625(15)	0.63706(12)	0.63232(15)	0.0418(6)
C9	-0.13843(13)	0.59696(15)	0.69237(16)	0.0422(6)
C11	-0.04125(10)	0.56682(10)	0.80766(12)	0.0215(3)
C12	0.01372(14)	0.60428(12)	0.75079(15)	0.0268(4)
C13	-0.00991(14)	0.64015(12)	0.66288(15)	0.0389(5)
C14	0.07924(10)	0.38482(10)	0.67046(13)	0.0244(4)
H1	0.1830	0.3475	0.6124	0.032
H2	-0.1027	0.6619	0.5714	0.050
H3	0.0268	0.6675	0.6226	0.047
H6	-0.1910	0.5939	0.6710	0.051
H7	0.0999	0.4096	1.0158	0.020
H9	0.0496	0.3673	0.6139	0.029
H10	0.2568	0.3941	0.7505	0.040
H11	0.1930	0.4537	0.8879	0.039

H20	0.0427(18)	0.6055(18)	0.763(2)	0.046(10)
N1	-0.11756(10)	0.56171(12)	0.78074(13)	0.0379(4)
N2	0.04137(8)	0.41938(8)	0.74738(11)	0.0215(3)

Bond lengths [Å] for TPPY

C(1)-C(2)	1.384(3)
C(1)-C(14)	1.387(2)
C(1)-H(1)	0.9500
C(2)-C(3)	1.384(3)
C(2)-H(10)	0.9500
C(3)-C(4)	1.396(2)
C(3)-H(11)	0.9500
C(4)-N(2)	1.341(2)
C(4)-C(5)	1.489(2)
C(5)-C(6)	1.367(2)
C(5)-C(7)	1.399(2)
C(6)-C(7)	1.366(2)

C(6)-H(7)	0.9500
C(7)-C(6)	1.366(2)
C(7)-C(11)	1.489(2)
C(8)-C(13)	1.376(3)
C(8)-C(9)	1.381(4)
C(8)-H(2)	0.9500
C(9)-N(1)	1.357(3)
C(9)-H(6)	0.9500
N(1)-C(11)	1.364(2)
C(11)-C(12)	1.368(3)
C(11)-H(20)	1.70(3)
C(12)-C(13)	1.370(3)
C(12)-H(20)	0.52(3)
C(13)-H(3)	0.9500
C(14)-N(2)	1.341(2)
C(14)-H(9)	0.9500

Bond angles [°] for TPPY

C(2)-C(1)-C(14)	117.67(16)
C(2)-C(1)-H(1)	121.2
C(14)-C(1)-H(1)	121.2
C(1)-C(2)-C(3)	119.44(17)
C(1)-C(2)-H(10)	120.3
C(3)-C(2)-H(10)	120.3
C(2)-C(3)-C(4)	118.73(17)
C(2)-C(3)-H(11)	120.6
C(4)-C(3)-H(11)	120.6
N(2)-C(4)-C(3)	122.69(15)
N(2)-C(4)-C(5)	116.99(14)
C(3)-C(4)-C(5)	120.21(15)
C(6)-C(5)-C(7)	119.92(14)
C(6)-C(5)-C(4)	116.78(14)
C(7)-C(5)-C(4)	123.18(14)
C(7)-C(6)-C(5)	120.15(14)
C(7)-C(6)-H(7)	119.9
C(5)-C(6)- H(7)	119.9

C(6)-C(7)-C(5)	119.93(15)
C(6)-C(7)-C(11)	116.69(14)
C(5)-C(7)-C(11)	123.37(14)
C(13)-C(8)-C(9)	118.39(18)
C(13)-C(8)-H(2)	120.8
C(9)-C(8)-H(2)	120.8
N(1)-C(9)-C(8)	122.61(19)
N(1)-C(9)-H(6)	118.7
C(8)-C(9)-H(6)	118.7
C(9)-N(1)-C(11)	116.58(19)
N(1)-C(11)-C(12)	123.83(17)
N(1)-C(11)-C(7)	116.59(16)
C(12)-C(11)-C(7)	119.56(16)
N(1)-C(11)-H(20)	139.2(10)
C(12)-C(11)-H(20)	15.3(10)
C(7)-C(11)-H(20)	104.2(10)
C(11)-C(12)-C(13)	117.8(2)
C(11)-C(12)-H(20)	121(4)

C(13)-C(12)-H(20)	121(4)
C(8)-C(13)-C(12)	120.8(2)
C(8)-C(13)-H(3)	119.6
C(12)-C(13)-H(3)	119.6
N(2)-C(14)-C(1)	124.23(16)
N(2)-C(14)-H(9)	117.9
C(1)-C(14)-H(9)	117.9
C(14)-N(2)-C(4)	117.22(14)

7 Bibliography

7.1 Chapter 1 References

[1] Renewable Energy Policy Network for the 21st Century. 2014 Global Energy Report. http://www.ren21.net/Portals/0/documents/Resources/GSR/2013 /GSR2013_lowres.pdf (accessed Jan 24, 2014).

[2] Perez, R.; Perez, M. A fundamental look at energy reserves for the planet. For publication in the IEA/SHC solar update. http://asrc.albany.edu/people/faculty/perez/Kit/pdf/a-fundamental-look-at%20the-planetary-energy-reserves.pdf (accessed Jan 26, 2014).

[3] Luque, Antonio; Hegedus, Steven. *Handbook of Photovoltaics*. 2nd ed.; John Wiley & Sons publishing: Hoboken, 2011.

[4] Cost of Solar is 2-100 times cheaper than you think. http://costofsolar.com/cost-of-solar-is-2-100-times-cheaper-than-you-think/ (accessed Jan 24, 2014).

[5] Saga, Tatsuo. Advances in crystalline silicon solar cell technology for industrial mass production. *NPG Asia Mater*. **2010**, *3*, 96-102.

[6] Green, M.A.; Emery, K.; Hishikawa, Y.; Warta, W.; Dunlop, E.D. Solar cell efficiency tables (version 43). *Prog. Photovol: Res. Appl.* **2014**, *22*, 1-9.

[7] Shockley, W.; Queisser, H. Detailed Balance Limit of Efficiency of p-n Junction Solar Cells. *J. Appl. Phys.* **1961**, *21*, 510-519.

[8] Luque, Antonio; Hegedus, Steven. *Handbook of Photovoltaics*. 1st ed.; John Wiley & Sons publishing: Hoboken, 2003.

[9] Gall, S.; Rech, B. Technological status of polycrystalline silicon thin-film solar cells on glass. *Solar Energy Materials & Solar Cells*. **2013**, *119*, 306-308.

[10] Sethi, V.K.; Pandey, M.; Shukla, P. Use of nanotechnology in solar PV cell. *Int. J. Chem. Eng. App.* **2012**, *2,* 77-88.

[11] Nowshad, A. Promises of Cu(In,Ga)Se_2 Thin Film Solar Cells from the Perspective of Material Properties, Fabrication Methods and Current Research Challenges. *J. Appl. Sci*. **2011**, *11*, 401-410.

[12] Okamoto, T. Current Status and Future Prospects of CdTe Solar Cells. *Journal of the Japan Institute of Energy* **2012**. *91*, 356-361.

[13] Tonezzer, M. *Solar Cell Nanotechnology,* 1st ed.; John Wiley & Sons, Hoboken, 2014. p293-315.

[14] O'Regan, B. Grätzel, M. A low-cost, high efficiency solar cell based on dye-sensitized colloidal TiO_2 films. *Nature* **1991**, *353*, 737-740.

[15] Amadelle, R.; Argazzi, R.; Bignozzi, A.; Sandola, F. Design of antenna-sensitizer polynuclear complexes. Sensitization of titanium dioxide with $[Ru(bpy)_2(CN)_2]_2Ru(bpy(COO)_2)_2^{2-}$. *J. Am. Chem. Soc.* **1990**, *112*, 7099-7103.

[16] Nazeeruddin, M.K.; Kay, A.; Rodicio, I.; Humphry-Baker, R.; Mueller, E.; Liska, P.; Vlachopoulos, N. Grätzel, M. Conversion of light to electricity by cis-X2bis(2,2'-bipyridyl-4,4'-dicarboxylate)ruthenium(II) charge-transfer sensitizers (X = Cl^-, Br^-, I^-, CN^-, and SCN^-) on nanocrystalline titanium dioxide electrodes. *J. Am. Chem. Soc.* **1993**, *115*, 6382-6390.

[17] Nazeeruddin, M.K.; Péchy, P.; Grätzel, M. Efficient panchromatic sensitization of nanocrystalline TiO_2 films by a black dye based on a trithiocyanato-ruthenium complex. *Chem. Commun.* **1997**, 1705-1706.

[18] Pickup of the Asian DCS activities. http://kuroppe.tagen.tohoku.ac.jp/~dsc/modules/company.htm (accessed Jun 23, 2014).

[19] Ikeda, N, Miyasaka, T. Plastic and Solid-state Dye-sensitized Solar Cells Incorporating Single-wall Carbon Nanotubes. *Chem. Lett.* **2007**, *36*, 466-467.

[20] Burschka, J.; Pellet, N.; Moon, S.; Humphrey-Baker, R.; Gao, P.; Nazeeruddin, M.K.; Grätzel, M. Sequential deposition as a route to high-performance perovskite-sensitized solar cells. *Nature*. **2013**, *499*, 316-319.

[21] Olsen, E.; Hagen, G; Eric Lindquist S. Dissolution of platinum in methoxy propionitrile containing LiI/I_2. *Sol. Energy Mater. Sol. Cells* **2000***, 63,* 267–273.

[22] Grätzel, M. Perspectives for dye-sensitized nanocrystalline solar cells. *Prog. Photovol: Res. Appl.* **2000**, *8*, 171-185.

[23] FG Glass Industry. http://www.fgglass.com/images/solar_spectrum1.jpg (accessed Jul 3, 2014).

[24] Green, M. *Third Generation Photovoltaics*, 1st ed.; Springer: Berlin, 2003.

[25] Marti, A.; Luque, A. *Next Generation Photovoltaics: High Efficiency through Full Spectrum Utilization.* Institute of Physics Publishing: Bristol, 2004.

[26] Karen, N.H.; Ermer, J. H.; King, R.R.; Hadda, M.; Cai, L.; Joslinn, D.E.; Krut, D. D.; Takahashi, M.; Eldredge, J.W.; Nishikawa, J.W.; Cavicchi, B.T. Lillington, D.R. *High efficiency $GaInP_2$/GaAs/Ge dual and triple junction solar cells for space applications*. Proceedings*,* 2nd World Conference on Photovoltaic Solar Energy Conversion*,* Vienna*,* July 6-10, 1998, 3535-3549.

[27] Yang, J.; Banerjee, A.; Lord, K.; Guha, S. *Correlation of component cells with high-efficiency amorphous silicon alloy triple junction solar cells and modules*. Proceedings, 2nd World Conference on Photovoltaic Solar Energy Conversion, Vienna, July 6-10, 1998, 387-930.

[28] Lin, C.; Han, H.; Chen, H.; Chen, K.; Tasi, Y.; Lin, W.; Kuo, H.; Yu, P. *J.* Highly Efficient Multiple-Layer CdS Quantum Dot Sensitized III-V Solar Cells. *Nanoscience and Nanotechnology*. **2014**, *14*, 1051-1063.

[29] Würfel, P. Solar energy conversion with hot electrons from impact ionisation. *Sol. Energy Mater. Sol. Cells* **1997**, *46*, 43-52.

[30] König, D.; Casalenuovo, K.; Takeda, Y.; Conibeer, G.; Guillemoles, J.F.; Patterson, R.; Huang, L.M.; and Green, M.A. Hot carrier solar cells: Principles, materials and design. *Physica E: Low-dimensional Systems and Nanostructures* **2012**, *42*, 2862-2866.

[31] Conibeer, G.J.; Jian, C.W.; König, D.; Shrestha, S.; Walsh, T.; Green, M.A. Selective energy contacts for hot carrier solar cells. *Thin Film Solids* **2008**, *516*, 6968-6973.

[32] Conibeer, G.; Ekins-Daukes, N.; Guillemoles, J.; König, D.; Cho, E.; Jiang, C.; Shrestha, S.; Green, M. Progress on hot carrier cells. *Sol. Energy Mater. Sol. Cells* **2009**, *93*, 713-719.

[33] Ross, R.; Nozik, A. Efficiency of hot-carrier solar energy converters. *J. Appl. Phys.* **1982**, *53*, 3813-3818.

[34] Kolodinski, S.; Werner, J.; Wittchen, T.; Queisser, H. Quantum efficiencies exceeding unity due to impact ionization in silicon solar cells. *Appl. Phys. Lett.* **1993,** *63*, 2405-2407.

[35] Wolf, M. *Limitations and possibilities for improvement of photovoltaic solar energy converters.* Proceedings of the IRE. 1960, *48*, 1246-1263.

[36] Guttler, G.; Queisser, J.J. Impurity photovoltaic effect in silicon. *Energy Conversion* **1970**, *10*, 51-55.

[37] Keeves, M. J.; Green, M. A. Efficiency improvements of silicon solar cells by the impurity photovoltaic effect. *J. Appl. Phys.* **1994**, *75*, 4022-4033.

[38] Wurful, P. Limiting efficiency for solar cells with defects from a three-level model. *Sol. Energy Mater. Sol. Cells* **1993**, *29*, 403-413.

[39] Brown, A. S.; Green, M. A. Limiting efficiencies for photovoltaic energy conversion in multigap systems. *Prog. In Photovoltaics* **2002**, *10*, 299-307.

[40] Luque, A.; and Martí, A. Increasing the Efficiency of Ideal Solar Cells by Photon Induced Transitions at Intermediate Levels. *Phys. Rev. Lett*. **1997**, *78*, 5014-5017.

[41] De Wile, J; Meijerink, A.; Rath, J.K.; van Sark, W.G.J.H.M.; Schropp, R.E.I. Upconverter solar cells: materials and applications. *Energy Environ. Sci*. **2011**, *4*, 4835.

[42] Richards, B.S.; Shalav, A. Enhancing the Near-Infrared Spectral Response of Silicon Optoelectronic Devices via Up-Conversion. *IEEE Trans. Electron Devices*. **2007**, *54*, 2679-2684.

[43] Shalav, A.; Richards, B.S.; Trupke, T.; Güdel, H.U. Application of $NaYF_4$: Er^{3+} up-converting phosphors for enhanced near-infrared silicon solar cell response. *Appl. Phys. Lett.* **2005**. *86*, 013505.

[44] Liu, M.; Lu, Y.; Zie, Z.B.; Chow, G.M. Enhancing near-infrared solar cell response using upconverting transparent ceramics. *Sol. Energy Mater. Sol. Cells*. **2011**, *95,* 800-803.

[45] Shan, G. B.; Demopoulos, G.P. Near-Infrared Sunlight Harvesting in Dye-Sensitized Solar Cells Via the Insertion of an Upconverter-TiO_2 Nanocomposite Layer. *Adv. Mater*. **2010**, *22*, 4373-4377.

[46] Partey, M.; Gluyas, J. B. G.; Fox, M. A.; Low, P. J.; Kaupp, M. Mixed-Valence Ruthenium Complexes Rotating through a Conformational Robin-Day Continuum. *Chem. Eur. J.* **2014**, *20*, 6895-6908.

[47] Giuffrida, G.; Campagna, S. Influence of peripheral ligands on the metal-metal interaction in dinuclear metal complexes with N-heterocyclic bridging ligands. *Coord. Chem. Rev.* **1994**, *135*, 517-531.

[48] Kaim, W.; Sarkar, B. Mixed valency in ruthenium complexes-Coordinative aspects. *Coord. Chem. Rev.* **2007**, *251*, 584-594.

[49] Demadis, K. D.; Hartshorn, C. M.; Meyere, T. J. The localized-to-delocalized transition in mixed-valence chemistry. The Localized-to-Delocalized Transition in Mixed-Valence Chemistry. *Chem. Rev.* **2001,** *101*, 2655-2685.

[50] Baranoff, E.; Collin, J. P.; Flamigni, L.; Sauvage, J. P. From ruthenium(II) to iridium(III): 15 years of triads based on bis-terpyridine complexes. *Chem. Soc. Rev.* **2004,** *33*, 147-155.

[51] De Cola, L.; Belser, P. Photoinduced energy and electron transfer processes in rigidly bridged dinuclear Ru/Os complexes. *Coord. Chem. Rev.* **1998,** *177*, 301-346.

[52] Low, P. J. Metal complexes in molecular electronics: progress and possibilities. *Dalton Trans.* **2005,** 2821-2824.

[53] Davis, W. B.; Sven, W. A.; Ratner, M. A.; Wasielewski, M. R. Molecular-wire behavior in p-phenylenevinylene oligomers. *Nature* **1998,** *396*, 60-63.

[54] Flores-Torres, S.; Hutchison G. R.; Soltzber, L. J.; Abruna, H. D. Ruthenium Molecular Wires with Conjugated Bridging Ligands: Onset of Band Formation in Linear Inorganic Conjugated Oligomers. *J. Am. Chem. Soc.* **2006**, *128*, 1513-1522.

[55] Fantacci, S.; De Angelis, F.; Wang, J. J.; Bernhard, S.; Selloni, A. A Combined Computational and Experimental Study of Polynuclear Ru-TPPZ Complexes: Insight into the Electronic and Optical Properties of Coordination Polymers. *J. Am. Chem. Soc.* **2004,** *126*, 9715-9723.

[56] De Cola, L. *Topics in Current Chemistry.* Springer: Berlin, 2005; Vol. 257.

[57] Solomon, E. I.; Brunold, T. C.; Davis, M. I.; Kemsley, J. N.; Lee, S. K.; Lehnert, N.; Neese, F.; Skulan, A. J.; Yang, Y. S.; Zhou, Y.J. Geometric and Electronic Structure/Function Correlations in Non-Heme Iron Enzymes. *Chem. Rev.* **2000,** *100*, 235-350.

[58] Wei, P. P.; Skulan, A. J.; Mitic, N.; Yang, Y. S.; Saleh, L.; Bollinger, J. M. Jr.; Solomon, E. I. Electronic and Spectroscopic Studies of the Non-Heme Reduced Binuclear Iron Sites of Two Ribonucleotide Reductase Variants: Comparison to Reduced Methane Monooxygenase and Contributions to O_2 Reactivity. *J. Am. Chem. Soc.* **2004,** *126*, 3777-3788.

[59] Wadman, S. H.; van Leeuwen, Y. M.; Havenith, R. W. A.; van Klink, G. P. M.; van Koten, G. A Redox Asymmetric, Cyclometalated Ruthenium Dimer: Towards Upconversion Dyes in Dye-Sensitized TiO_2 Solar Cells. *Organometallics* **2010,** *29*, 5635-5645.

[60] Chandrasekhar, P.; Zy, B. J.; Birur, G. D.; Rawal, S.; Pierson, E. A.; Kauder, L.; Swanson, T. Large, Switchable Electrochromism in the Visible Through Far-Infrared in Conducting Polymer Devices. *Adv. Funct. Mater.* **2002**, *12*, 95-103.

[61] Creutz, C.; Taube, H. Direct approach to measuring the Franck-Condon barrier to electron transfer between metal ions. *J. Am. Chem. Soc.* **1969,** *91*, 3988-3989.

[62] Creutz, C.; Taube, H. Binuclear complexes of ruthenium ammines. *J. Am. Chem. Soc.* **1973,** *95*, 1086-1094.

[63] Richardson, D. E.; Taube, H. Mixed-valence molecules: electronic delocalization and stabilization. *Coord. Chem. Rev.* **1984,** *60*, 107-129.

[64] Giuffrida, G.; Campagna, S. Influence of peripheral ligands on the metal-metal interaction in dinuclear metal complexes with N-heterocyclic bridging ligands. *Coord. Chem. Rev.* **1994**, *135*, 517-531.

[65] Balzani, V.; Juris, A. Photochemistry and photophysics of Ru(II) polypyrdine complexes in the Bologna group. From early studies to recent developments. *Coord. Chem. Rev.* **2001**, *211*, 97-115.

[66] Robin, M.B.; Day, P. Mixed-valence chemistry: a survey and classification. *Adv. Inorg. Chem. Radiochem.* **1967**, *10*, 247-422.

[67] Baxter, J.B. Commercialization of dye sensitized solar cells: Present status and future research needs to improve efficiency, stability, and manufacturing. *J. Vac. Sci. Technol. A.* **2012**, *30*, 020801.

[68] Macpherson, B.P.; Bernhardt, P.V.; Hauser, A.; Pages, S.; Vauthey, E. Time-Resolved Spectroscopy of the Metal-to-Metal Charge Transfer Excited State in Dinuclear Cyano-Bridged Mixed-Valence Complexes. *Inorg. Chem.* **2005**, *44*, 5530-5536.

[69] Gueymard, C. The sun's total and spectral irradiance for solar energy applications and solar radiation models. *Solar Energy*. **2004**, *74,* 423-453.

7.2 Chapter 2 References

[1] Kalyanasundaram, K.; Grätzel, M. Applications of functionalized transition metal complexes in photonic and optoelectronic devices. *Coord. Chem. Rev.* **1998**, 177, 347-414.

[2] Balzani, V.; Juris, A.; Venturi, M. Luminescent and Redox-Active Polynuclear Transition Metal Complexes. *Chem. Rev.* **1996**, *96*, 759-833.

[3] Arana, C. R.; Abruña, H. D. Monomeric and oligomeric complexes of ruthenium and osmium with tetra-2-pyridyl-1,4-pyrazine (TPPZ). *Inorg, Chem.* **1993,** *32*, 194-203.

[4] Constable, E. C.; Cargill Thompson, A. M. W. Strategies for the assembly of homo- and hetero-nuclear metallosupramolecules containing 2,2':6',2"-terpyridine metal-binding domains. *J. Chem. Soc. Dalton Trans.* **1995,** *10*, 1615-1627.

[5] Fantacci, S.; De Angelis, F.; Wang, J.; Bernhard, S.; Selloni, A. A Combined Computational and Experimental Study of Polynuclear Ru-TPPZ Complexes: Insight into the Electronic and Optical Properties of Coordination Polymers. *J. Am. Chem. Soc.* **2004**, *126*, 9715-9723.

[6] Flores-Torres, S.; Hutchison, G.; Soltzberg, L. J.; Abruña, H. D. Ruthenium Molecular Wires with Conjugated Bridging Ligands: Onset of Band Formation in Linear Inorganic Conjugated Oligomers. *J. Am. Chem. Soc.* **2006,** *128*, 1513-1522.

[7] Koley, M.; Sarkar, B.; Ghumann, S.; Bulak, E.; Fiedler, J.; Kaim, W.; Lahiri, G. K. Probing Mixed Valence in a New tppz-Bridged Diruthenium(III,II) Complex $\{(\mu\text{-tppz})[Ru(bik)Cl]_2\}^{3+}$ (tppz = 2,3,5,6-Tetrakis(2-pyridyl)pyrazine, bik = 2,2'Bis(1-methylimidazolyl)ketone): EPR Silence, Intervalence Absorption, and ν_{CO} Line Broadening. *Inorg. Chem.* **2007,** *46*, 3736-3742.

[8] Rocha, R. C.; Rein, F. N.; Jude, H.; Shreve, A.P.; Concepcion, J. J.; Meyer, T. J. Observation of Three Intervalence-Transfer Bands for a Class II-III Mixed-Valence Complex of Ruthenium. *Angew. Chem. Int. Ed.* **2008,** *47*, 503-506.

[9] Wadman, S. H.; Havenith, R. W. A.; Hartle, F.; Lutz, M.; Spek, A. L.; van Klink, G. P. M.; van Koten, G. Redox Chemistry and Electronic Properties of 2,3,5,6-Tetrakis(2-pyridyl)pyrazine-Bridged Diruthenium Complexes Controlled by *N,C,N'*-BisCyclometalated Ligands. *Inorg. Chem.* **2009,** *48*, 5685-5696.

[10] Thummel, R.P.; Goulle, V.; Chem, B. Bridged derivatives of 2,2'-biimidazole. *J. Org. Chem*. **1989**, *54*, 3057-3061.

[11] Walker, D.T.; Douglas, C.D.; MacLean, B.J. Synthesis, characterization, and surface studies of conjugated polymers possessing 2,2'-biimidazole moieties. *Can. J. Chem.* **2009**, *87*, 729-737.

[12] Rillema, D.P.; Sahai, R.; Matthews, P.; Edwards, K.; Shaver, R.J. Multimetallic ruthenium(II) complexes based on biimidazole and bibenzimidazole: effect of dianionic bridging ligands on redox and spectral properties. *Inorg. Chem*. **1990**, *29*, 167-175.

[13] Majumdar, P.; Peng, S.; Goswami, S. Biimidazole complexes of ML_2^{2+} [M = Ru or Os, L = 2-(phenylazo)pyridine]. Synthesis, structure and redox properties of mono- and di-nuclear complexes. *J. Chem. Soc., Dalton Trans.* **1998**, 1569-1574.

[14] Derossi, S.; Adams, H.; Ward, M.D. Hydrogen-bonded assemblies of ruthenium(II)-biimidazole complex cations and cyanometallate anions: structures and photophysics. *Dalton Trans.* **2007**, 33-36.

[15] Ji, Z.; Huang, S.D.; Guadalupe, A.R. Synthesis, x-ray structures, spectroscopic and electrochemical properties of ruthenium(II) complexes containing 2,2'-bipyrimidine. *Inorg. Chim. Acta.* **2000**, *305*, 127-134.

[16] Nallas, G.N.A.; Jones, S.W.; Brewer, K.J. Bipyrimidine-Bridged Mixed-Metal Trimetallic Complexes of Ruthenium(II) with Rhodium(III) or Iridium(III), $\{[(bpy)_2Ru(bpm)]_2MCl_2\}^{5+}$. *Inorg. Chem.* **1996,** *35*, 6974-6980.

[17] Thayumanavan, Sankaran. "Macromolecular Design and Syntheses for renewable Energy Applications." Colloquium, Syracuse University, **2009**, April 7th.

[18] Nantalaksakul, A; Mueller, A; Klaikherd, A; Bardeen, C.J.; Thayumanavan, S. Dendritic and Linear Macromolecular Architectures for Photovoltaics: A Photoinduced Charge Transfer Investigation. *J. Am. Chem. Soc.* **2009**, *131*, 2727-2738.

[19] Yoshikawa, N.; Yamabe, S.; Kanehisa, N.; Inoue, T.; Takashima, H.; Tsukahara, K. The key Cl^- ligand for metal-to-metal charge transfer in mononuclear terpyridine ruthenium(II) and binuclear ruthenium(II) tetrapyridylpyrazine complexes. *J. Phys. Org. Chem.* **2011**, *24*, 1110-1118.

[20] Park, H.; Bae, E.; Lee, J.; Park, J.; Choi, W. Effect of the Anchoring Group (Carboxylate vs Phosphonate) in Ru-Complex-Sensitized TiO_2 on Hydrogen Production under Visible Light. *J. Phys. Chem. B.* **2006**, *110*, 14792 14799.

[21] Nazeeruddin, M.K.; Kay, A.; Rodicio, I.; Humphry-Baker, R.; Mueller, E.; Liska, P.; Vlachopoulos, N. Grätzel, M. Conversion of light to electricity by cis-X2bis(2,2'-bipyridyl-4,4'-dicarboxylate)ruthenium(II) charge-transfer sensitizers (X = Cl^-, Br^-, I^-, CN^-, and SCN^-) on nanocrystalline titanium dioxide electrodes. *J. Am. Chem. Soc.* **1993**, *115*, 6382-6390.

[22] O'Regan, B.; Graetzel, M. A low-cast, high-efficiency solar cell based on dye-sensitized colloidal TiO_2 films. *Nature*. **1991**, *353*, 753-739.

[23] Privalov, T.; Boschloo, G.; Hagfeldt, A.; Svensson, P. H.; Kloo, L. A Study of the Interactions between I^-/I_3^- Redox Mediators and Organometallic Sensitizing Dyes in Solar Cells. *J. Phys. Chem. C*. **2009**, *113*, 783-790.

[24] Hou, Y.; Xie, P.; Kuiwang, W.; Wang, J.; Zhang, B.; Cao, Y. Synthetic control of the photophysical and photoelectrochemical properties. *Sol. Energy Mater. Sol. Cells*. **2001**, *70*, 131-139.

[25] Hong, R.; Gorman, C. Synthetic Approaches to an Isostructural Series of Redox-Active, Metal Tris(bipyridine) Core Dendrimers. *J. Org. Chem.* **2003**, *68*, 9019-9025.

[26] Maerker, G.; Case, F. The Synthesis of Some 4,4'-Disubstituted 2,2'-Bipyridines. *J. Am. Chem. Soc.* **1958**, *80*, 2745-2748.

[27] Smestad, G. P. Education and solar conversion: Demonstrating electron transfer. *Sol. Energy Mater. Sol. Cells*. **1998**, *55*, 157-178.

[28] Liska, P.; Vlachopoulos, N.; Zazeeruddin, M.K.; Comte, P.; Gratzel, M. cis-Diaquabis(2,2'-bipyridyl-4,4'-dicarboxylate)ruthenium(II) sensitizes wide band gap oxide semiconductors very efficiently over a broad spectral range in the visible. *J. Am. Chem. Soc.* **1988**, *110*, 3686-3687.

[29] Zapiter, J.M.D.; Tissue, B.M.; Brewer, K.J. Ruthenium and rhodium complexes anchored to europium oxide nanoparticles. *Inorg. Chem. Comm.* **2008**, *11*, 51-56

[30] Wolfbauer, G.; Bond, A.M.; MacFarlane, D.R. Electrochemical and Spectroscopic Studies on the Oxidation of the *cis*-$(Et_2dcbpy)_2RuX_2$ Series of Photovoltaic Sensitizer Precursor

Complexes (Et_2-dcbpy = 2,2'-Bipyridine-4,4'-diethoxydicarboxylic Acid, X = Cl^-, I^-, NCS^-, CN^-). *Inorg. Chem.* **1999**, *38*, 3836-3846

[31] Klein, C.; Baranoff, E.; Nazeeruddin, M.K., Grätzel, M. Convenient synthesis of functionalized 4,4'-disubstituted-2,2'-bipyridine with extended π-system for dye-sensitized solar cell applications. *Tet. Lett.* **2010**, *51*, 6161-6165

[32] Krause, R. A. Synthesis of mixed complexes of ruthenium(II) with 2,2'-dipyridyl. *Inorg. Chim. Acta*. **1977**, *22*, 209-213.

[33] Rillema, D.P.; Sahai, R.; Matthews, P.; Edwards, K.; Shaver, R.J.; Morgan, L. Multimetallic ruthenium(II) complexes based on biimidazole and bibenzimidazole: effect of dianionic bridging ligands on redox and spectral properties. *Inorg. Chem*. **1990**, *29*, 167-175.

[34] Ji, Z.; Huang, S.D.; Guadalupe, A.R. Synthesis, x-ray structures, spectroscopic and electrochemical properties of ruthenium(II) complexes containing 2,2'-bipyrimidine. *Inorg. Chim. Acta.* **2000**, *305*, 127-134.

[35] Sullivan, B. P.; Salmon, D. J.; Meyer, T. J. Mixed phosphine 2,2'-bipyridine complexes or ruthenium. *Inorg. Chem.* **1978**, *17*, 3334-3341.

[36] Holder, E.; Schoetz, G.; Schurig, V.; Lindner, E. Synthesis and enantiomer separation of a modified tris(2,2'-bipyridine)ruthenium(II) complex. *Tetrahedron: Asymmetry.* **2001**, *12*, 2289-2293.

[37] Rillema, D.P. Allen, G.; Meyer, T.J.; Conrad, D. Redox properties of ruthenium(II) tris chelate complexes containing the ligands 2,2'-bipyrazine, 2,2'-bipyrdine, and 2,2'bipyrimidine. *Inorg. Chem.* **1983**, *22*, 1617-1622.

[38] Hartshorn, C. M.; Daire, N.; Tondreau, V.; Loeb, B.; Meyer, T. J.; White, P. S. Synthesis and Characterization of Dinuclear Ruthenium Complexes with Tetra-2-pyridylpyrazine as a Bridge. *Inorg. Chem.* **1999**, *38*, 3200-3206.

[39] Gratzel, M.; Fraser, D.; Nazeeruddin, M.K.; Zakeeruddin, S.M. *PCT Int. Appl.* **1992**, 44.

[40] Fuentes, M.J.; Bognanno, R.J.; Dougherty, W.G.; Boyko, W.J. Kassel, W.S.; Dudley, T.J.; Paul, J.J. Structural, electronic, and acid/base properties of $[Ru(bpy(OH)_2)_3]^{2+}$ ($bpy(OH)_2$ = 4,4-dihydroxy-2,2'-bipyridine). *Dalton Trans.* **2012,** *41*, 12514

[41] Klein, S.; Dougherty, W.G.; Kassel, W.S.; Dudley, T.J.; Paul, J.J. Structural, Electronic, and Acid/Base Properties of $[Ru(bpy)_2(bpy(OH)_2)]^{2+}$ (bpy = 2,2'-Bipyridine, $bpy(OH)_2$ = 4,4-Dihydroxy-2,2'-bipyridine). *Inorg. Chem.* **2011**, *50*, 2754-2763.

[42] Bailey, A.J.; Griffith, W.P.; Savage, P.D. Oxo complexes of ruthenium with N,N'-donors as oxidation catalysts for alkenes, alkanes and alcohols, and their osmium analogues. *J. Chem. Soc. Dalton Trans.* **1995**, 3537-3542.

[43] Nazeeruddin, M.K.; Kay, A.; Rodicio, I.; Humphry-Baker, R.; Mueller, E.; Liska, P.; Vlachopoulos, N. Grätzel, M. Conversion of light to electricity by cis-X2bis(2,2'-bipyridyl-4,4'-dicarboxylate)ruthenium(II) charge-transfer sensitizers (X = Cl^-, Br^-, I^-, CN^-, and SCN^-) on nanocrystalline titanium dioxide electrodes. *J. Am. Chem. Soc.* **1993**, *115*, 6382-6390.

[44] Nazeeruddin, M.K.; Pechy, P.; Renouard, T.; Zakeeruddin, S.M.; Humphry-Baker, R.; Comte, P.; Liska, P.; Cevey, L.; Costa, E.; Shklover, V.; Spiccia, L.; Deacon, G.B.; Bignozzi, C.A.; Gratzel, M. Engineering of Efficient Panchromatic Sensitizers for Nanocrystalline TiO_2-Based Solar Cells. *J. Am. Chem. Soc.* **2001**, *123*, 1613-1624.

7.3 Chapter 3 References

[1] Rasheed, A.; Farhat, R. Combinatorial Chemistry: A Review. *IFPSR.* **2013,** *5,* 2502-2516

[2] Corbett, P.R.; Leclair, J.; Vial, L.; West, K.R.; Wietor, J.; Sanders, J.K.M.; Otto, S. Dynamic Combinatorial Chemistry. *Chem. Rev.* **2006**, *106*, 3652-3711.

[3] Stulz, E.; Scott, S.M.; Bond, A.D.; Teat, S.J.; Sanders, J.K.M. Selection and Amplification of Mixed-Metal Porphyrin Cages from Dynamic Combinatorial Libraries. *Chem.-Eur. J.* **2003**, *9,* 6039.

[4] Stulz, E.; Ng, Y.-F.; Scott, S.M.; Sanders, J.K.M. Amplification of cyclic mixed-metalloporphyrin tetramer from a dynamic combinatorial library through orthogonal metal coordination. *Chem. Commun.* **2002**, 524-525.

[5] Suar, I.; Severin, K. Selection Experiments with dynamic combinatorial libraries: the importance of the target concentration. *Chem. Commun*. **2005**, 1471-1473.

[6] Case, M. A.; McLendon, G.L. A Virtual Library Approach To Investigate Protein Folding and Internal Packing. *J. Am. Chem. Soc.* **2000**, *122*, 8089.

[7] Linton, B.; Hamilton, A.D. Formation of Artificial Receptors by Metal-Templated Self-Assembly. *Chem. Rev.* **1997**, *97*, 1669-1680.

[8] Ghadiri, M.R.; Case, M.A. De Novo Design of a Novel Heterodinuclear Three-Helix Bundle Metalloprotein. *Angew. Chem., Int. Ed.* **1993**, *32*, 1594-1597.

[9] Factacci, S.; Angelis, F.; Wang, J.; Bernhard, S.; Selloni, A. A Combined Computational and Experimental Study of Polynuclear Ru-TPPZ Complexes: Insight into the Electronic and Optical Properties of Coordination Polymers. *J. Am. Chem. Soc.* **2004**, *126*, 9715-9723.

[10] Nazeeruddin, M.K.; Kay, A.; Rodicio, I.; Humphry-Baker, R.; Mueller, E.; Liska, P.; Vlachopoulos, N. Gratzel, M. Conversion of light to electricity by cis-X2bis(2,2'-bipyridyl-4,4'-dicarboxylate)ruthenium(II) charge-transfer sensitizers (X = Cl^-, Br^-, I^-, CN^-, and SCN^-) on nanocrystalline titanium dioxide electrodes. *J. Am. Chem. Soc.* **1993**, *115*, 6382-6390.

[11] Rocha, R. C.; Rein, F. N.; Jude, H.; Shreve, A.P.; Concepcion, J. J.; Meyer, T. J. Observation of Three Intervalence-Transfer Bands for a Class II-III Mixed-Valence Complex of Ruthenium. *Angew. Chem. Int. Ed.* **2008,** *47*, 503-506.

[12] Thummel, R.P.; Goulle, V.; Chem, B. Bridged derivatives of 2,2'-biimidazole. *J. Org. Chem*. **1989**, *54*, 3057-3061.

[13] Arana, C. R.; Abruña, H. D. Monomeric and oligomeric complexes of ruthenium and osmium with tetra-2-pyridyl-1,4-pyrazine (TPPZ). *Inorg, Chem.* **1993,** *32*, 194-203.

7.4 Chapter 4 References

[1] Bessha, T.; Yoneda, E.; Yum, J.; Guglielmi, M.; Tavernelli, I.; Imai, H.; Rothlisberger, R.; Nazeeruddin, M.K.; Gratzel, M. New Paradigm in Molecular Engineering of Sensitizers for Solar Cell Applications. *J. Am. Chem. Soc.* **2009**, *131*, 5930-5934.

[2] Funaki, T.; Funakoshi, H.; Kitao, O.; Onozawa-Komatsuzaki, N.; Kasuga, K.; Sayama, K.; Sugihara, H. Cyclometalated Ruthenium(II) Complexes as Near-IR Sensitizes for High Efficiency Dye-Sensitized Solar Cells. *Angew. Chem. Int. Ed.* **2012**, *51*, 7528-7531.

[3] Dragonetti, C.; Valore, A.; Colombo, A.; Roberto, D.; Trifiletti, V.; Manfredi, N.; Salamone, M.M.; Ruffo, R.; Abbotto, A. A new thiocyanate-free cyclometallated ruthenium complex for

dye-sensitized solar cells: Beneficial effects of substitution on the cyclometallated ligand. *J. Organ met. Chem*. **2012,** *714*, 88-93.

[4] Bombed, P.G.; Robson, K.; Chivito, B.; Briquette, C. Photophysical, electrochemical and photovoltaic properties of dye sensitized solar cells using a series of pyridyl functionalized porphyrin dyes. *Coord. Chem. Rev.* **2012,** *256*, 1438-1450.

[5] Arana, C. R.; Abruña, H. D. Monomeric and oligomeric complexes of ruthenium and osmium with tetra-2-pyridyl-1,4-pyrazine (TPPZ). *Inorg, Chem.* **1993,** *32*, 194-203.

[6] Constable, E. C.; Cargill Thompson, A. M. W. Strategies for the assembly of homo- and hetero-nuclear metallosupramolecules containing 2,2':6',2"-terpyridine metal-binding domains. *J. Chem. Soc. Dalton Trans.* **1995,** *10*, 1615-1627.

[7] Fantacci, S.; De Angelis, F.; Wang, J.; Bernhard, S.; Selloni, A. A Combined Computational and Experimental Study of Polynuclear Ru-TPPZ Complexes: Insight into the Electronic and Optical Properties of Coordination Polymers. *J. Am. Chem. Soc.* **2004**, *126*, 9715-9723.

[8] Flores-Torres, S.; Hutchison, G.; Soltzberg, L. J.; Abruña, H. D. Ruthenium Molecular Wires with Conjugated Bridging Ligands: Onset of Band Formation in Linear Inorganic Conjugated Oligomers. *J. Am. Chem. Soc.* **2006,** *128*, 1513-1522.

[9] Koley, M.; Sarkar, B.; Ghumann, S.; Bulak, E.; Fiedler, J.; Kaim, W.; Lahiri, G. K. Probing Mixed Valence in a New tppz-Bridged Diruthenium(III,II) Complex $\{(\mu\text{-tppz})[Ru(bik)Cl]_2\}^{3+}$ (tppz = 2,3,5,6-Tetrakis(2-pyridyl)pyrazine, bik = 2,2'Bis(1-methylimidazolyl)ketone): EPR Silence, Intervalence Absorption, and ν_{CO} Line Broadening. *Inorg. Chem.* **2007,** *46*, 3736-3742.

[10] Rocha, R. C.; Rein, F. N.; Jude, H.; Shreve, A.P.; Concepcion, J. J.; Meyer, T. J. Observation of Three Intervalence-Transfer Bands for a Class II-III Mixed-Valence Complex of Ruthenium. *Angew. Chem. Int. Ed.* **2008,** *47*, 503-506.

[11] Wadman, S. H.; Havenith, R. W. A.; Hartle, F.; Lutz, M.; Spek, A. L.; van Klink, G. P. M.; van Koten, G. Redox Chemistry and Electronic Properties of 2,3,5,6-Tetrakis(2-pyridyl)pyrazine-Bridged Diruthenium Complexes Controlled by *N,C,N'*-BisCyclometalated Ligands. *Inorg. Chem.* **2009,** *48*, 5685-5696.

[12] Arana, C. R.; Abruña, H. D. Monomeric and oligomeric complexes of ruthenium and osmium with tetra-2-pyridyl-1,4-pyrazine (TPPZ). *Inorg, Chem.* **1993,** *32*, 194-203.

[13] Chen, T.K.; Flowers, W.T. A convenient synthesis of 2,3,4,5-tetrahalogenopyridines and of 3,5-bis(alkylthio)pyridines from 2,6-diaminopyridine. *Chem. Comm.* **1980**, *23*, 1139-1140.

[14] Collins, I.; Suschitzky, H. Polyhalogeno-aromatic compounds. Part XIV. Nucleophilic substitution and peroxy-acid oxidation of pentabromopyridine and some of it *NN*-dialkylamino- and bis-(*NN*-dialkylamino)-derivatives. *J. Chem. Soc. C.* **1970,** 1523-1530.

[1] Leising, R.A.; Kubow, S.A.; Takeuchi, K.J. Synthesis and characterization of (nitro)ruthenium complexes that utilize identical trans-positioned tertiary phosphine ligands. *Inorg. Chem.* **1990**, *29*, 4569-4574.

[1] Wei, P. P.; Skulan, A. J.; Mitic, N.; Yang, Y. S.; Saleh, L.; Bollinger, J. M. Jr.; Solomon, E. I. Electronic and Spectroscopic Studies of the Non-Heme Reduced Binuclear Iron Sites of Two Ribonucleotide Reductase Variants: Comparison to Reduced Methane Monooxygenase and Contributions to O_2 Reactivity. *J. Am. Chem. Soc.* **2004,** *126*, 3777-3788.

7.5 Chapter 5 References

[1] Luque, Antonio; Hegedus, Steven. *Handbook of Photovoltaics*. 2nd ed.; John Wiley & Sons publishing: Hoboken, 2011.

[2] Nelson, Jenny. *The Physics of Solar Cells*. 1st ed.; Imperial College Press: London, 2004.

[3] Smestad, G. P. Education and solar conversion: Demonstrating electron transfer. *Sol. Energy Mater. Sol. Cells*. **1998**, *55*, 157-178.

[4] Nazeeruddin, M.K.; Kay, A.; Rodicio, I.; Humphry-Baker, R.; Mueller, E.; Liska, P.; Vlachopoulos, N. Gratzel, M. Conversion of light to electricity by cis-X2bis(2,2'-bipyridyl-4,4'-dicarboxylate)ruthenium(II) charge-transfer sensitizers (X = Cl^-, Br^-, I^-, CN^-, and SCN^-) on nanocrystalline titanium dioxide electrodes. *J. Am. Chem. Soc.* **1993**, *115*, 6382-6390.

[5] Gratzel, M. Perspectives for dye-sensitized nanocrystalline solar cells. *Prog. Photovolt. Res. Appl.* **2000**, *8*, 171-185.

[6] Pysch, D.; Metta, A; Glunz, S.W. A review and comparison of different methods to determine the series resistance of solar cells. *Sol. Energy Mater. Sol. Cells*. **2007**, *6*, 1698-1706.

[7] Series Resistance. http://www.pveducation.org/pvcdrom/solar-cell-operation/series-resistance (accessed Aug 2, 2014).

[8] Han, L.; Koide, N.; Chiba, Y.; Islam, A.; Komiya, R.; Fuke, N.; Fukui, A.; Yamanaka, R. Improvement of efficiency of dye-sensitized solar cells by reduction of internal resistance. *Appl. Phys. Lett.* **2005**. *86*. 213501.

[9] Shunt Resistance. http://www.pveducation.org/pvcdrom/solar-cell-operation/shunt-resistance (accessed Aug 2, 2014).

[10] Ito, S.; Liska, P.; Comte, P.; Charvt, R.; Pechy, P.; Bach, U.; Schmidt-Mende, L.; Zakeeruddin, S.M.; Kay, A.; Nazeeruddin, M.; Gratzel M. Control of dark current in photoelectrochemical (TiO_2/I^-- I_3^-) and dye-sensitized solar cells. *Chem. Commun.* **2005**, *34*, 4351-4353.

[11] Bozic-Weber, B.; Constable, E.C.; Figgemeier, E.; Housecroft, C.E.; Kylberg, W. Evaluation of polynuclear dendrons as photosensitizers for dye-sensitized solar cells. *Energy Environ. Sci*. **2009**, *2*, 299-305.

[12] Ji, Z.; Natu, G.; Huang, Z.; Kokhan, O.; Zhang, X.; Wu, Y. Synthesis, Photophysics, and Photovoltaic Studies of Ruthenium Cyclometalated Complexes as Sensitizers for p-Type NiO Dye-Sensitized Solar Cells. *J. Phys. Chem. C.* **2012**, *116*, 16854-16863.

[13] Wadman, S. H.; van Leeuwen, Y. M.; Havenith, R. W. A.; van Klink, G. P. M.; van Koten, G. A Redox Asymmetric, Cyclometalated Ruthenium Dimer: Toward Upconversion Dyes in Dye-Sensitized TiO_2 Solar Cells. *Organometallics* **2010,** *29*, 5635-5645.

VITA

Andrew Basner
1300 Academy Rd
Culver, IN 46511

EDUCATION

PhD, Organometallic Chemistry, Syracuse University

Syracuse, NY, anticipated Spring 2016

Dissertation Title: "Synthesis of Triruthenium Complexes as Electron Reservoirs for use in Dye-Sensitized Solar Cells."

Advisor: Professor Michael B. Sponsler.

BS, IUPUI (Indiana University-Purdue University of Indianapolis)

Indianapolis, IN, May 2008

Graduated Dec. 2007 (3.61/4.00 GPA) with an A.C.S. certified BS in chemistry with a biological chemistry concentration.

Advisors: Dr. Kyungsoo Oh, Keith Anliker

TEACHING EXPERIENCE

Culver Academies

Senior Instructor, Aug. 2014 - Present

Syracuse University, Syracuse, NY

Adjunct Faculty Member, Aug. 2013-Aug. 2014

SUNY Cortland

Adjunct Lecturer, Jan. 2014 - May 2014

Syracuse University, Syracuse, NY

Graduate Teaching Assistant, Aug. 2008-Aug. 2013

Indiana University-Purdue University of Indianapolis, Indianapolis, IN

Laboratory Instructor and Recitation Leader, 2006-2008

Peer Led Team Learning Workshop Leader, 2005-2007

Undergraduate and Master Students Mentored

Stefan Holler, B.S. (2012) Graz University of Technology, Graz, Austria

Bernhard Műller, B.S. (2011) Graz University of Technology, Graz, Austria.

Chiara Gstrein, M.S. (2011) Graz University of Technology, Graz, Austria

Catherine DeSarle, B.S. (2010) Syracuse University, Syracuse, NY

RESEARCH EXPERIENCE

Graduate Research, Syracuse University, Syracuse, NY, Aug. 2008 – Aug. 2016

Developed new organometallic and inorganic dyes for use in dye-sensitized solar cells.

Synthesized and characterized new ruthenium based catalysts.

Helped develop new hydrogel based sensors for detection of infectious diseases resulting in a NSF I-Corps grant to pursue potential commercialization.

Undergraduate Research, IUPUI, Indianapolis, IN, 2006-2008

Investigated new methods for carbon-carbon bond formation using AIBN radical reactions.

Developed new video based lab tutorial videos for general chemistry students.

AFFILIATIONS

American Chemical Society, 2008-present

GRANTS AND HONORS

NSF I-Corps grant #1242505 IIP Division of Industrial Innovation and Partnerships

Eagle Scout award, Boy Sounds of America, 1998.

PUBLICATIONS AND PATENTS

Luk, Y.L.; Burton, E. A.; Simon, K. A.; Shetye, G. S.; Weldon, M. P.; Basner, A., Biosensor Based on Chemically Woven Hydrogel. U.S. Patent 0196309, Aug 1, 2013.

CONFERENCE AND POSTER PRESENTATIONS

American Chemical Society National Meeting, Indianapolis, IN, September 8th, 2013

Presentation Title – *Synthesis and characterization of polyruthenium dyes for solar cells*

Presentation Title – *Commercializing your research and finding focus for your start-up using the teachings of the NSF I-Corps program*

Poster Title – *Synthesis and characterization of polyruthenium dyes for solar cells and ruthenium catalysts based on Grubbs' first and second-generation catalyst*

Buffalo Chemistry Graduate Student Symposium, University of Buffalo, Buffalo, NY, May 15th, 2013

Presentation Title - *Commercializing Your Research and Finding Focus for your Small Chemical Business*

American Chemical Society Northeastern Regional Meeting, Rochester, NY, Sept. 30th, 2012

Presentation Title - *The NSF I-Corps Experience – Turning your ideas into a business*

American Chemical Society 2012 National Meeting, Philadelphia, PA, August 19th, 2012

Poster Title - *Synthesis of Tri-Ruthenium Complexes to Act as Electron Reservoirs for use in Dye-Sensitized Solar Cells*

Buffalo Chemistry Graduate Student Symposium, University of Buffalo, Buffalo, NY, May 16th, 2012

Poster Title - *Synthesis of Tri-Ruthenium Complexes to Act as Electron Reservoirs for use in Dye-Sensitized Solar Cells*